TECHNISCHE
UNIVERSITÄT
DARMSTADT

Collective Behavior in Inertial Active Matter

Kollektives Verhalten in träger aktiver Materie

vom Fachbereich Physik
der Technischen Universität Darmstadt

zur Erlangung des akademischen Grades

Doctor rerum naturalium
(Dr. rer. nat.)

genehmigte Dissertation von

Lukas Hecht, M.Sc.

Erstgutachter: Prof. Dr. Benno Liebchen
Zweitgutachter: Prof. Dr. Thomas Palberg

Darmstadt 2024

Collective Behavior in Inertial Active Matter
Kollektives Verhalten in träger aktiver Materie

Genehmigte Dissertation von Lukas Hecht

Tag der Einreichung: 14.10.2024
Tag der Prüfung: 27.11.2024

Darmstadt, Technische Universität Darmstadt

Publications

In the following, I provide a list of my publications. This thesis is based on publications 1–5 and 7.

Preprints:

1. L. Hecht, K.-R. Dormann, K. L. Spanheimer, M. Ebrahimi, M. Cordts, S. Mandal, A. K. Mukhopadhyay, and B. Liebchen, "AMEP: The Active Matter Evaluation Package for Python", arXiv:2404.16533 [cond-mat.soft] (2024).
2. L. Hecht, J. C. Ureña, and B. Liebchen, "An Introduction to Modeling Approaches of Active Matter", arXiv:2102.13007 [cond-mat.soft] (2021). [This article will be published by Springer as part of the book "Active Matter — Theory, Simulation, and Experiments" in the Springer Series Soft and Biological Matter. Editors: Giovanni Volpe, Nuno Araújo, Agnese Callegari, and Giorgio Volpe.]

Published:

3. L. Hecht, I. Dong, and B. Liebchen, "Motility-Induced Coexistence of a Hot Liquid and a Cold Gas", *Nat. Commun.* **15**, 3206 (2024) (featured as an Editor's Highlight in Applied Physics and Mathematics). [Impact factor: 14.7*]
4. L. Hecht, L. Caprini, H. Löwen, and B. Liebchen, "How to Define Temperature in Active Systems?", *J. Chem. Phys.* **161**, 224904 (2024). [Impact factor: 3.1*]
5. N. Möller†, L. Hecht†, R. Niu, B. Liebchen, and T. Palberg, "Writing Into Water", *Small* **19**, 2303741 (2023). [Impact factor: 13.0*]
6. H. Bonart, F. Gebhard, L. Hecht, T. Roy, B. Liebchen, and S. Hardt, "Detecting Isotachophoresis Zones Hidden in Noise Using Signal Processing", *Anal. Chem.* **95**, 7575 (2023). [Impact factor: 6.7*]
7. L. Hecht, S. Mandal, H. Löwen, and B. Liebchen, "Active Refrigerators Powered by Inertia", *Phys. Rev. Lett.* **129**, 178001 (2022). [Impact factor: 8.1*]
8. R. Horstmann, L. Hecht, S. Kloth, and M. Vogel, "Structural and Dynamical Properties of Liquids in Confinements: A Review of Molecular Dynamics Simulation Studies", *Langmuir* **38**, 6506 (2022). [Impact factor: 3.7*]
9. L. Hecht, R. Horstmann, B. Liebchen, and M. Vogel, "MD Simulations of Charged Binary Mixtures Reveal a Generic Relation between High- and Low-Temperature Behavior", *J. Chem. Phys.* **154**, 024501 (2021). [Impact factor: 3.1*]
10. M. Becher, S. Becker, L. Hecht, and M. Vogel, "From Local to Diffusive Dynamics in Polymer Electrolytes: NMR Studies on Coupling of Polymer and Ion Dynamics across Length and Time Scales", *Macromolecules* **52**, 9128 (2019). [Impact factor: 5.1*]

*2023 Journal Impact Factor, *Journal Citation Reports* (Clarivate, 2024)
†These authors contributed equally to this work.

Abstract

Active matter consists of particles which consume energy to convert it into directed motion. Due to this local energy conversion, active matter is intrinsically out of equilibrium. This manifests in striking collective phenomena. For example, active particles can phase separate into a dense and a dilute phase without any attractive interactions by motility-induced phase separation, or they can form stationary or moving patterns. In stark contrast to systems in thermodynamic equilibrium, active particles can even self-assemble into clusters in which they feature a persistently lower kinetic temperature, i.e., mean kinetic energy, compared to particles in their environment. This phenomenon requires inertia and raises the general question of how inertia influences collective behavior in active matter. In particular, the influence of inertia on the emergence of coexisting temperatures is not fully understood. More generally, it is under debate how to define temperature in an active system at all. The aim of this thesis is to provide fundamental insights into these questions. As a key non-equilibrium phenomenon, we explore the emergence of coexisting temperatures in inertial active Brownian particles, which undergo motility-induced phase separation, by using Brownian dynamics simulations. First, we show that the effect of inertia on the phase transition line and the emergence of coexisting kinetic temperatures allows designing a mechanism of a “refrigerator” for active particles. Without requiring any isolating walls, it is able to decrease their kinetic temperature by two orders of magnitude compared to the environment. Second, we observe coexisting kinetic temperatures even in mixtures of overdamped active and inertial passive particles, when they undergo motility-induced phase separation. We show that the liquid-like phase can be not only colder but also hotter than the gas-like phase. Finally, we show that these results are robust against the used “thermometer”. In particular, we compare different possibilities to calculate temperature in active systems by applying well-established thermodynamic relations. This comparison yields the existence of two temperature classes. In both classes, we identify methods that are independent of tracer properties or external confinements, and hence, are suited for measuring the temperature of active matter. We further investigate control mechanisms for particle self-assembly by developing a minimal model for assembling colloidal particles in the trail of an ion-exchange resin bead. Our simulations describe the experiments well, both qualitatively and quantitatively. The numerical investigation of the explored systems requires a wide range of data analysis tools. Thus, we developed the Active Matter Evaluation Package for the analysis of the simulation data. This Python library allows for quickly calculating observables which provide insights into the structural and dynamical properties of the investigated systems. It is the first tool that is specifically designed for the analysis of active matter systems. The results of this thesis provide routes to control self-assembly and temperature in active systems, and the detailed comparison of different temperature definitions can serve as a starting point towards a thermodynamic theory for active matter. The explored colloidal self-assembly could be applied as a new technique to write lines and letters into water, and finally, the developed Python library is publicly available as open-source software and provides essential tools to study phase separation, pattern formation, and critical phenomena in active matter systems and beyond.

Zusammenfassung

Aktive Materie besteht aus Teilchen, die Energie aufnehmen und in eine gerichtete Bewegung umwandeln. Aufgrund dieser lokalen Energieumwandlung befinden sich aktive Systeme intrinsisch im Nichtgleichgewicht. Dies äußert sich in eindrucksvollen kollektiven Phänomenen. Aktive Teilchen können beispielsweise ohne jegliche anziehende Wechselwirkung in eine dichte flüssige und eine gasartige Phase separieren (Motility-Induced Phase Separation, MIPS) oder sie können stationäre oder bewegte Muster bilden. Im Gegensatz zu Systemen im thermodynamischen Gleichgewicht können sich aktive Teilchen sogar selbst zu Clustern zusammenschließen, in denen sie im Vergleich zu Teilchen in ihrer Umgebung eine dauerhaft niedrigere kinetische Temperatur, d.h. mittlere kinetische Energie, aufweisen. Letzteres setzt voraus, dass die Teilchen träge sind und wirft die allgemeine Frage auf, wie Trägheit das kollektive Verhalten aktiver Teilchen beeinflusst. Insbesondere ist der Einfluss der Trägheit auf die Entstehung koexistierender Phasen mit unterschiedlichen Temperaturen nicht vollständig geklärt. Ganz allgemein wird außerdem diskutiert, wie man Temperatur in einem aktiven System überhaupt definieren kann. Ziel dieser Arbeit ist es, grundlegende Erkenntnisse zu diesen Fragen zu gewinnen. Als zentrales Nichtgleichgewichtsphänomen wird die Entstehung koexistierender Temperaturen in Systemen aus trägen aktiven Brownschen Teilchen, die MIPS zeigen, mit Brownschen Dynamik-Simulationen untersucht. Zunächst wird gezeigt, dass die Auswirkung der Trägheit auf die Phasenübergangslinie und das Auftreten koexistierender kinetischer Temperaturen die Entwicklung eines Mechanismus für einen “Kühlschrank” für aktive Teilchen ermöglicht. Ohne isolierende Wände zu benötigen, ist dieser in der Lage, die kinetische Temperatur der aktiven Teilchen im Vergleich zur Umgebung um zwei Größenordnungen zu senken. Zweitens wird gezeigt, dass koexistierende kinetische Temperaturen sogar in Mischungen aus überdämpften aktiven und trägen passiven Teilchen auftreten, wenn sie in eine flüssige und eine gasartige Phase separieren. Hierbei kann die flüssige Phase nicht nur kälter, sondern auch heißer sein als die koexistierende gasartige Phase. Schließlich wird gezeigt, dass diese Ergebnisse robust gegenüber der Art des verwendeten “Thermometers” sind. Insbesondere werden verschiedene Methoden zur Berechnung der Temperatur in aktiven Systemen, die auf etablierten thermodynamischen Beziehungen basieren, systematisch miteinander verglichen. Dieser Vergleich zeigt die Existenz von zwei Temperaturklassen. In beiden Klassen können Temperaturen identifiziert werden, die unabhängig von den Eigenschaften eines Testteilchens oder von externen Potentialen sind und sich daher für die Messung der Temperatur aktiver Materie eignen. Darüber hinaus werden Kontrollmechanismen für die Selbstorganisation von Partikeln untersucht. Dazu wird ein Minimalmodell für das Ansammeln kolloidaler Partikel in der Spur eines Ionenaustauschers entwickelt. Die numerischen Ergebnisse beschreiben die Experimente sowohl qualitativ als auch quantitativ gut. Die numerische Untersuchung der betrachteten Systeme erfordert eine breite Palette von Datenanalysewerkzeugen. Daher wurde das Active Matter Evaluation Package für die Analyse der Simulationsdaten entwickelt. Diese Python-Bibliothek ermöglicht die schnelle Berechnung von Observablen, die Aufschluss über die strukturellen und dynamischen Eigenschaften der untersuchten Systeme geben. Sie ist die erste Python-Bibliothek, die speziell für die Analyse aktiver

Materie entwickelt wurde. Die Ergebnisse dieser Arbeit zeigen, wie die Bildung von Clustern und deren Temperatur in aktiven Systemen kontrolliert werden kann und der detaillierte Vergleich verschiedener Temperaturdefinitionen liefert einen Ausgangspunkt für die Entwicklung einer thermodynamischen Theorie für aktive Materie. Die erforschte Selbstorganisation kolloidaler Partikel kann als neue Technik eingesetzt werden, um Linien und Buchstaben in Wasser zu schreiben und die entwickelte Python-Bibliothek ist als Open-Source-Software öffentlich zugänglich und bietet wesentliche Werkzeuge zur Untersuchung von Phasenseparation, Musterbildung und kritischen Phänomenen in aktiver Materie und darüber hinaus.

Acronyms

A-IEX	Anionic ion-exchange resin bead.
ABP	Active Brownian particle.
AMB+	Active model B+.
AMEP	Active Matter Evaluation Package.
AOUP	Active Ornstein-Uhlenbeck particle.
API	Application Programming Interface.
Appx.	Appendix.
BD	Brownian dynamics.
C-IEX	Cationic ion-exchange resin bead.
CAP	Chiral active particle.
Chap.	Chapter.
DO	Diffusio-osmotic.
DP	Diffusio-phoretic.
DPD	Dissipative-particle dynamics.
Eq.	Equation.
FDR	Fluctuation-dissipation relation.
Fig.	Figure.
fps	Frames per second.
FWHM	Full width at half maximum.
GIF	Graphics Interchange Format.
HDF	Hierarchical Data Format.
HDW	Hydrodynamic writing.
IEX	Ion-exchange resin bead.
LBM	Lattice-Boltzmann method.
MD	Molecular dynamics.
MIPS	Motility-induced phase separation.
MPCD	Multi-particle collision dynamics.

MSD	Mean-square displacement.
MSLE	Mean-squared logarithmic error.
OA	Optical axis.
OACF	Orientational autocorrelation function.
PBP	Passive Brownian particle.
RDF	Radial distribution function.
Ref.	Reference.
RTP	Run-and-tumble particle.
Sec.	Section.
Subsec.	Subsection.
Tab.	Table.
UV	Ultraviolet.
VACF	Velocity autocorrelation function.
WCA	Weeks-Chandler-Anderson.

Symbols

A	Area of a two-dimensional simulation box.
χ	Susceptibility.
C_v	Spatial velocity correlation function.
d	Number of spatial dimensions.
D_r	Rotational diffusion coefficient.
D_t	Translational diffusion coefficient.
γ_r	Rotational drag coefficient.
γ_T	Translational tracer drag coefficient.
γ_t	Translational drag coefficient.
I	Moment of inertia.
k_B	Boltzmann constant.
l_p	Persistence length.
m_a	Mass of active particles.
m	Particle mass.
m_T	Tracer mass.
m_p	Mass of passive particles.
φ	Packing fraction.
Pe	Péclet number.
ψ_6	Hexagonal order parameter.
r_c	Cutoff radius.
Re	Reynolds number.
σ	Particle diameter.
τ_p	Persistence time.
T_b	Bath temperature.
T_conf	Configurational temperature.
T_eff	Effective temperature.

T_{Ein}	Einstein temperature.
θ	Orientation angle.
ϑ	Tilt angle.
T_{kin}	Kinetic temperature.
T_{kin4}	Fourth-moment kinetic temperature.
T_{MB}	Maxwell-Boltzmann temperature.
T_{osc}	Oscillator temperature.
T_{vir}	Virial temperature.
v_0	Self-propulsion speed.
v_{IEX}	Speed of an ion-exhange resin bead.
x_{a}	Number fraction of active particles.
ζ	Zeta potential.

Contents

1 Introduction

Active matter consists of "agents" which consume energy to propel themselves. Such agents are an essential component of our ecosystem. For example, molecular motors help to assemble the cytoskeleton and drive cell division processes,[1–3] bacteria self propel to search for nutrients and to avoid toxins in order to survive,[4–6] and cells migrate to build up the human body during embryogenesis or to control our immune response.[7–9] Also on larger scales, living organisms collectively perform certain tasks. Ant colonies build up giant anthills or underground nests,[10,11] locusts self-organize in swarms,[12] fishes and birds collectively move in form of flocks and schools, respectively,[13–17] and even human crowds are representatives of active matter systems.[18,19] All these active agents have in common that they consume energy from their environment and convert it into work, which allows them to propel themselves.[20–22] This local energy conversion leads to the breakdown of detailed balance on the level of the individual agents, and hence, active systems are intrinsically out of equilibrium.[23–25]

The research on active matter has become a popular branch of soft matter physics over the last two decades. This is also reflected in the high number of publications in that field, which has amounted to more than 500 review articles in the last ten years.[26] These cover a broad field of research that ranges from biology, medicine, and ecology to statistical physics.[21,22,27–32] This highly interdisciplinary research has helped to understand the motion of bacteria,[21] the swarming and flocking of insects and birds, respectively,[12,16,17,33] as well as to develop efficient vaccination and disease mitigation strategies.[34–36] It opens the route to many future applications such as swarming drones,[37,38] microrobots,[39–44] bacteria-driven microgears,[45–47] or smart materials.[48,49] In contrast to equilibrium systems, active matter shows a large variety of non-equilibrium collective phenomena. These range from dynamic clustering and non-equilibrium phase separation as observed for bacteria and active colloids[50–59] to the formation of stationary and moving patterns as found in actin filaments driven by molecular motors,[60,61] bacteria,[62,63] or nematodes.[64] These collective phenomena can be controlled by the interactions between the active agents, their possibilities to communicate with each other, and their self-propulsion speed for example. They made active matter to a prime example of non-equilibrium systems.[15,65–75] To understand the underlying mechanisms in detail, one can exploit various minimal models for active matter.[76–79] These are typically studied using numerical simulation techniques such as Brownian dynamics simulations.[80–82] Such simulations allow us to systematically modify the interactions between the active agents as well as system parameters such as the self-propulsion speed or the number density. Accordingly, they provide fundamental insights into structural and dynamical properties of active matter systems and allow us to systematically investigate their state diagrams.[31,78,83,84] In addition, theoretical approaches like a systematic coarse-graining of the underlying Langevin equations,[85–89] dynamical density functional theory,[90–92] mode-coupling theories,[93,94] and theories which

explicitly account for hydrodynamic interactions[27,95–98] have been frequently used to provide a deep understanding of active matter systems.

Beside dynamic clustering and the formation of stationary or moving patterns, it has been found that active particles can undergo a phase separation into a dense and a dilute phase even without any attractive interactions. This phenomenon is known as motility-induced phase separation (MIPS) and constitutes a prime example of non-equilibrium phenomena in active matter.[83,85,86,99–102] This is also reflected in the remarkable finding that the active particles feature persistently lower kinetic temperatures, i.e., mean kinetic energies, in the dense phase compared to the dilute phase if they are inertial.[103] While simulation studies of active matter systems have been mostly focused on overdamped active particles during the last decades of research,[21,31,53,72,76,99,104–118] the influence of inertia is currently under debate.[119–161] The example of a persistent kinetic temperature difference in coexisting phases in particular shows that MIPS is fundamentally different from a liquid-gas phase separation in equilibrium. Especially, it demonstrates that inertial active particles show a collective behavior that is fundamentally different from equilibrium physics. These results raise the general question how inertia influences collective behavior in active matter. How does inertia influence the emergence of coexisting temperatures? More generally, they raise the question of how we can understand the concept of temperature in the framework of non-equilibrium active matter. While the kinetic temperature is commonly used as a measure for the temperature of active systems,[103,123,162–168] other possibilities to define temperature exist.[123,169–171] In contrast to systems in thermodynamic equilibrium, these possibilities typically lead to different temperature values when they are applied to active matter.[172–174] Accordingly, the universality of temperature, which allows us to measure temperature with different types of thermometers, applies exclusively in thermodynamic equilibrium but not to systems far from equilibrium such as active matter.[175–177]

The aim of this thesis is to develop a fundamental understanding of the role of inertia for collective behavior in active matter systems. To reach this goal, we split this thesis into several parts that cover different aspects: As a key non-equilibrium phenomenon, we explore the emergence of coexisting temperatures in systems that undergo MIPS. First, the observation of different kinetic temperatures in coexisting phases raises the question of how we can control the self-assembly of cold active-particle clusters. To answer this, we exploit Brownian dynamics simulations of inertial active Brownian particles and explore their state diagram in terms of activity and particle density. We show that these insights allow us to design a “refrigerator” for inertial active particles, which exploits MIPS to cool down active particles in a predefined cooling domain. Inertia is a key ingredient for their design, but common active matter experiments are based on microswimmers that move at low Reynolds numbers, and hence, are overdamped. Accordingly, as a second part, we explore temperature differences in mixtures of overdamped active and inertial passive particles that undergo MIPS. This also requires the analysis of their state diagram in terms of activity and composition. The results are highly beneficial for designing related experiments based on microswimmers. Third, we discuss the fundamental question of how to define temperature in active systems. We systematically compare different possibilities to define temperature in order to explore their relevance for measuring temperature in inertial active systems. To reach these objectives, we need to develop tools to analyze

collective phenomena in inertial active systems. Therefore, we develop the Active Matter Evaluation Package (AMEP), which is a Python library for the analysis of structural and dynamical properties from simulation data. We then use these tools to analyze a colloidal system in which self-assembly is used to write into water.

This thesis is organized as follows: In Chap. 2, we introduce the considered active-particle models and explain the mechanism leading to MIPS and coexisting temperatures in inertial active matter. Next, in Chap. 3, we introduce AMEP, which has been developed as part of this thesis and provides all observables used to analyze the Brownian dynamics simulations. In Chap. 4, we explore different possibilities to define temperature in active systems, and we present design principles of a refrigerator for active particles in Chap. 5. In Chap. 6, we present our study of mixtures of overdamped active and inertial passive Brownian particles. Finally, in Chap. 7, we show how colloidal particles can be assembled in a fluid to write lines and letters into water, and we summarize the main results of this thesis and its future perspectives in Chap. 8.

2 Scientific Background

The following chapter provides an overview of the field of active matter physics and introduces all models used in this PhD thesis. A central and commonly-used model for active particles is the active Brownian particle (ABP) model as sketched in Fig. 2.1 and introduced in Subsec. 2.2.1. Most of the paragraphs and figures which are related to the modeling of active matter are taken verbatim from my publication "An Introduction to Modeling Approaches of Active Matter" published as a preprint on *arXiv* (2021) and licensed under CC BY 4.0.[77] For this publication, I have created all new figures related to continuum theories, I wrote the original draft for all sections about the continuum theories and hydrodynamic models, and I contributed to the writing of the sections about particle-based models.

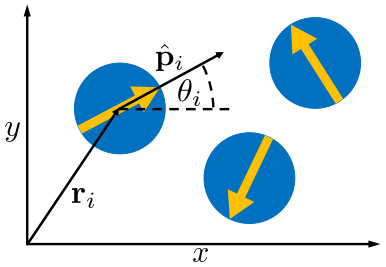

Fig. 2.1 Active Brownian particle model. Sketch of an active Brownian particle (ABP) in two spatial dimensions with particle index i at position $\mathbf{r}_i$ surrounded by two other ABPs. It's self-propulsion direction $\hat{\mathbf{p}}_i$ and orientation angle θ_i are indicated.

2.1 What is active matter?

By active matter we mean systems which consist of "agents" that consume energy to convert it into mechanical work resulting in directed motion or so-called self propulsion.[21,22,28,178] Such self-propelling agents can be found across scales from the microscale to the macroscale in the form of living and synthetic agents. For instance, microscopic entities comprise bacteria, algae, and synthetic microswimmers,[4,59,74,179–185] while active agents on the macroscale comprise fishes, birds, sheep, drones, and human crowds.[12,14,15,17,19,34,186–189] Therefore, the field of active matter covers multiple disciplines ranging from biology, medicine, and ecology to soft-matter and statistical physics.[21,27–29] For example, research in active matter investigates how biological cells such as bacteria perform directed motion to search for nutrients or to avoid toxins,[21] how the swarming of insects can be described,[12] or how a flock of birds forms.[16,17,33] Accordingly, research in active matter helps to control and design swarming drones and robots that can perform tasks such as cargo delivery, area exploration, or surveillance.[37,38] However, these are dual-use applications that could also be used for military purposes with all its advantages and disadvantages.[190] Active matter research is also relevant for controlling the movement of human crowds, and therefore, it helps to develop efficient evacuation strategies for mass events.[18,19] On the microscale, understanding the self-propulsion mechanisms of biological microswimmers such as bacteria or algae allows designing robotic microswimmers.[191] These could be used to remove

contaminants from liquids or to monitor the quality of water for instance.[192] Such robotic microswimmers may also be used for therapeutic applications such as targeted drug delivery in the future.[39–42] Related to medical applications, investigating active matter systems has also helped to develop efficient vaccination and disease mitigation strategies as recently relevant for combating the Covid-19 pandemic.[34–36]

From a more fundamental viewpoint, active matter systems have become a prime example for non-equilibrium systems over the last decades. Due to the local energy conversion of each agent, detailed balance is broken at the level of the individual agents and the system is intrinsically in a non-equilibrium state, i.e., the trajectories of each agent are irreversible.[23–25,193] Such breakdown of time-reversal symmetry can be measured by entropy production.[24,25,194] The fact that detailed balance is broken can lead to striking collective phenomena that have been studied in experiments, simulations, and theory over the last two decades.[4,21,27,28,31–33,43,76,78,83,195–200] Examples are non-equilibrium phase separations,[53,54,72,83,85,86,152,201–203] the formation of patterns with a characteristic length scale,[112,196,204–208] or ordering transitions such as flocking characterized by a (long-range) orientational order.[16,120,187,209] Nowadays, analytical and numerical approaches used to understand and model active matter are frequently complemented with machine-learning techniques.[210] Examples range from solving optimal navigation problems,[211–213] extracting partial differential equations from particle-based simulations and experiments,[210,214–217] and investigating bacterial foraging strategies[218] to quantifying entropy production,[219] efficiently sampling state points for generating phase diagrams,[220] or classifying phases and predicting phase transitions.[221,222]

In this PhD thesis, we use minimal models to simulate the dynamics of active matter systems. Figure 2.2 shows some examples of biological and artificial active matter systems ranging from the microscale to meter-sized active agents by which these minimal models, which we will introduce below, are inspired.

2.2 Modeling active matter

To describe the motion of active agents, various mathematical models have been developed. Particle-based models define an equation of motion for each individual particle. In contrast, continuum models describe an active system on coarse-grained scales and provide equations of motion for the particle density and orientation field for example.[76–78] These models can be classified into “wet” models, which include an explicit model of a solvent in addition to the equations of motion of the active agents, and “dry” models, which consider the active agents only. In the latter class, the impact of the solvent is modeled effectively. The solvent provides

(i) *fluctuations and dissipation:* Active particles are typically orders of magnitude larger than the molecules of the surrounding solvent and are subject to collisions with the latter. This leads to fluctuations in their motion, analogously to Brownian motion of passive colloids in equilibrium (cf. trajectory in Fig. 2.3a). The trajectory of an isolated active particle is then typically given by the combination of ballistic motion due to self propulsion and fluctuations due to collisions with the solvent molecules. As can be seen in Fig. 2.3b, the motion of an active particle is not straight because the collisions of the solvent molecules with the active particles feature both a radial and a

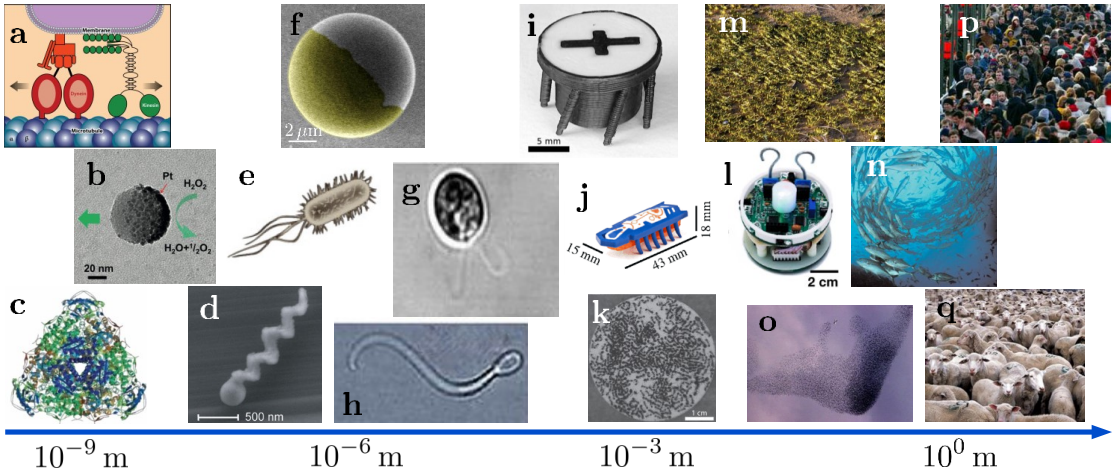

Fig. 2.2 Examples of active matter ordered by the agent size. **a** Sketch of a kinesin motor protein moving along a microtubule (reprinted with permission of Annual Reviews, Inc. from Ref. [223]; permission conveyed through Copyright Clearance Center, Inc.). **b** Silica Janus nanoparticle half coated with platinum (reprinted from Ref. [224]. © 2018, with permission from Elsevier). **c** Sketch of the enzyme urease self-propelling due to a catalytic reaction leading to chemotaxis (reprinted with permissions of Annual Reviews, Inc. from Ref. [225]; permission conveyed through Copyright Clearance Center, Inc.). **d** Artificial microswimmer made of a glass screw and driven by a magnetic field (reprinted with permission from Ref. [226]. © 2009 American Chemical Society). **e** Sketch of a self-propelling Escherichia coli bacterium (reprinted with permission from Ref. [21]. © 2016 by the American Physical Society). **f** Micrometer-sized Janus colloid made of a silica sphere half-coated with gold (reprinted with permission of the Royal Society of Chemistry from Ref. [227]; permission conveyed through Copyright Clearance Center, Inc.). **g**,**h** Self-propelling Chlamydomas alga and bull spermatozoa, respectively (reprinted with permission from Ref. [228]). **i** Millimeter-sized vibrot self-propelling on a vibrated plate (reprinted from Ref. [229], licensed under CC BY 3.0. © 2016, IOP Publishing Ltd and Deutsche Physikalische Gesellschaft). **j** Centimeter-sized vibration-driven vehicle (reprinted with permission from Ref. [156]. © 2017 by the American Physical Society). **k** Ants collectively forming clusters (reprinted from Ref. [230], licensed under CC BY 4.0). **l** Centimeter-sized robot (reprinted with permission from Ref. [231]. © 2021 by the American Physical Society). **m–q** Marching locusts, a swarm of fish, a flock of birds, a human crowd, and a herd of sheep, respectively, are examples of active matter at large length scales (reprinted from Ref. [13]. © 2012, with permission from Elsevier).

tangential component. The latter induces a stochastic turn of the particle orientation, and hence, reorientation of the self-propulsion direction, which is called rotational Brownian motion or rotational diffusion. Following the fluctuation-dissipation theorem, these fluctuations are necessarily linked to dissipation occurring, e.g., in the form of Stokes drag for spherical particles. For microswimmers, i.e., for active particles at the microscale, dissipation normally dominates over inertia. Hence, the motion is overdamped. These effects of the solvent, namely translational diffusion, rotational diffusion, and dissipation, are the only effects of the solvent which are typically taken into account in “dry” models such as the active Brownian particle (ABP) model, which we will introduce further below.

(ii) *momentum conservation:* Physically, in the absence of external fields or boundaries, the overall momentum of an active system has to be conserved. For example, when a microorganism or an active Janus colloid moves forward, there is necessarily a counter-propagating solvent flow such that the overall momentum of the active particle and the surrounding solvent is conserved (swimming in vacuum is impossible). Thus, the solvent not only acts as a bath providing fluctuations and drag but also ensures momentum conservation.

(iii) *hydrodynamic interactions:* The solvent mediates hydrodynamic interactions among different active particles. These arise because the flow pattern induced by each active particle as a consequence of its swimming acts onto all other particles in the system. These solvent-mediated interactions are often long-ranged. In particular, in the absence of external forces, they often decay as $1/r^2$ for force-dipole swimmers such as various bacteria or algae (explicit measurements of the flow field exist, e.g., for *E. coli* bacteria),[232] and as $1/r^3$ for source-dipole swimmers such as *Paramecium*[233] or (idealized) Janus colloids with a uniform surface mobility.[234,235] However, they can be weakened or decay faster in the presence of a substrate or other boundaries.[236]

(iv) *hydrodynamic boundary effects:* If the active particles are in contact with boundaries such as a glass substrate, which is frequently used in experiments with active colloids, or another liquid-solid or liquid-air interface, the solvent can lead to additional interesting effects. An example of these is constituted by osmotic flows at fluid-solid interfaces such as those induced by auto-phoretic particles[237] or by some modular swimmers involving ion-resins.[238,239] At fluid-air interfaces, active particles can cause Marangoni flows,[195,240–242] which act on all particles in the system and can elicit interesting collective behaviors.[243–246]

In the following, we introduce commonly used models for active systems. We focus on "dry" particle-based and continuum models in Subsecs. 2.2.1 and 2.2.2, respectively, and we briefly discuss how to model a solvent explicitly in Subsec. 2.2.3.

2.2.1 Particle-based models

Particle-based models are commonly used as a minimal model to describe the motion of an active particle, i.e., a particle that features a generic self-propulsion mechanism, which drives the particle forward. Motivated by Brownian motion, these models are typically based on a Langevin equation for each particle, in which the solvent is treated as a bath that provides fluctuations and drag only without accounting for momentum conservation (and usually without accounting for hydrodynamic interactions). Therefore, particle-based models typically belong to the class of "dry" models. They are based on the Langevin equation of a passive Brownian particle (PBP) of mass m_p, whose position $\mathbf{r}_i$ evolves according to $\mathrm{d}\mathbf{r}_i(t)/\mathrm{d}t = \mathbf{v}_i(t)$, and its velocity $\mathbf{v}_i$ evolves as[247,248]

$$m_\mathrm{p}\frac{\mathrm{d}\mathbf{v}_i(t)}{\mathrm{d}t} = -\gamma_\mathrm{t}\mathbf{v}_i(t) - \sum_{\substack{j=1\\ j\neq i}}^{N} \boldsymbol{\nabla}_{\mathbf{r}_i} u\left(r_{ij}\right) + \sqrt{2k_\mathrm{B}T_\mathrm{b}\gamma_\mathrm{t}}\boldsymbol{\eta}_i(t). \tag{2.1}$$

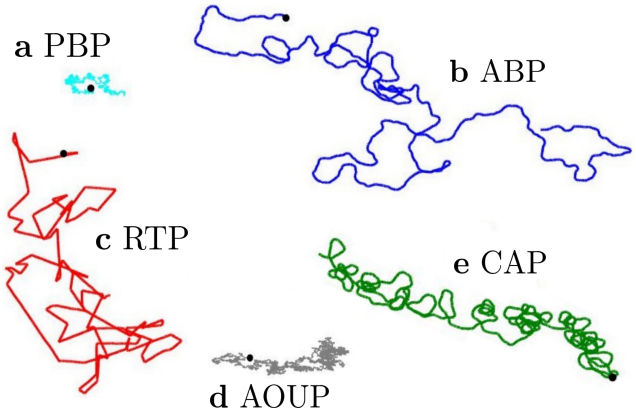

Fig. 2.3 Exemplary trajectories. Exemplary trajectory obtained from simulations in the overdamped regime: **a** passive Brownian particle (PBP; Eq. (2.1)), **b** active Brownian particle (ABP; Eqs. (2.4) and (2.5)), **c** run-and-tumble particle (RTP; Eqs. (2.9) and (2.10)), **d** active Ornstein-Uhlenbeck particle (AOUP; Eq. (2.11)), and **e** chiral active particle (CAP; Eq. (2.12)). Note that an isolated AOUP is equivalent to an inertial PBP with $m_\mathrm{p}/\gamma_\mathrm{t} = \tau_\mathrm{p}$ (see Subsec. 2.2.1).

Here, i denotes the particle index, γ_t the translational drag coefficient, and $u(r_{ij})$ with $r_{ij} = |\mathbf{r}_i - \mathbf{r}_j|$ represents a pairwise interaction potential. The fluctuations are represented by a Gaussian white noise process $\boldsymbol{\eta}_i$ with zero mean and unit variance, whose strength is given by the bath temperature T_b, and k_B is the Boltzmann constant.

Active Brownian particle model

The active Brownian particle (ABP) model is one of the simplest and most popular models to describe active particles that self propel in a certain direction, which smoothly changes due to rotational diffusion.[77,103,110,119,133,146,152,249–251] Within this model, each particle is represented by a (slightly soft) disk/sphere of diameter σ, mass m, and moment of inertia I. The ABP model does not explicitly describe the mechanism leading to self propulsion. In contrast, it simply replaces it with an effective self-propulsion force $\mathbf{F}_{\mathrm{SP},i} = \gamma_\mathrm{t} v_0 \hat{\mathbf{p}}_i(\theta_i)$, where the self-propulsion direction is represented by $\hat{\mathbf{p}}_i(t) = (\cos\theta_i(t), \sin\theta_i(t))$ in two-dimensional space, and v_0 denotes the self-propulsion speed (Fig. 2.1). Microscopically, this is not correct because, as discussed above, microswimmers are force free, but it leads to a simple generic model for the dynamics of active particles, which stays agnostic on many details of the specific underlying realization. The interactions between the particles are governed by an excluded-volume repulsive interaction potential u. The evolution of the particles' positions $\mathbf{r}_i$ and orientations θ_i adheres to the Langevin equations[103,119,133,165,252]

$$m\frac{\mathrm{d}^2\mathbf{r}_i(t)}{\mathrm{d}t^2} = -\gamma_\mathrm{t}\frac{\mathrm{d}\mathbf{r}_i(t)}{\mathrm{d}t} - \sum_{\substack{j=1\\ j\neq i}}^{N} \boldsymbol{\nabla}_{\mathbf{r}_i} u\left(r_{ij}\right) + \gamma_\mathrm{t} v_0 \hat{\mathbf{p}}_i(t) + \sqrt{2k_\mathrm{B}T_\mathrm{b}\gamma_\mathrm{t}}\boldsymbol{\eta}_i(t), \tag{2.2}$$

$$I\frac{\mathrm{d}^2\theta_i(t)}{\mathrm{d}t^2} = -\gamma_\mathrm{r}\frac{\mathrm{d}\theta_i(t)}{\mathrm{d}t} + \sqrt{2k_\mathrm{B}T_\mathrm{b}\gamma_\mathrm{r}}\xi_i(t). \tag{2.3}$$

Here, $\boldsymbol{\eta}_i$ and ξ_i denote Gaussian white noise with zero-mean and unit variance, T_b represents the bath temperature, γ_t and γ_r denote the translational and rotational drag

coefficients, respectively, k_B is the Boltzmann constant, and N denotes the total number of active particles. The overdamped limit can be obtained using $m/\gamma_\mathrm{t} \to 0$ and $I/\gamma_\mathrm{r} \to 0$ and leads to the well-known overdamped ABP model

$$\frac{\mathrm{d}\mathbf{r}_i(t)}{\mathrm{d}t} = v_0\hat{\mathbf{p}}_i(t) - \frac{1}{\gamma_\mathrm{t}}\sum_{\substack{j=1\\j\neq i}}^{N}\boldsymbol{\nabla}_{\mathbf{r}_i}u\left(r_{ij}\right) + \sqrt{2D_\mathrm{t}}\boldsymbol{\eta}_i(t), \tag{2.4}$$

$$\frac{\mathrm{d}\theta_i(t)}{\mathrm{d}t} = \sqrt{2D_\mathrm{r}}\xi_i(t). \tag{2.5}$$

Here, $D_\mathrm{t} = k_\mathrm{B}T_\mathrm{b}/\gamma_\mathrm{t}$ and $D_\mathrm{r} = k_\mathrm{B}T_\mathrm{b}/\gamma_\mathrm{r}$ denote the translational and rotational diffusion coefficients, respectively.

It is instructive to first consider a single overdamped ABP, i.e., Eqs. (2.4) and (2.5) with $u = 0$. Different from an overdamped PBP (Fig. 2.3a), the trajectory of an overdamped ABP is characterized by an initial period of directed motion followed by a randomization of the self-propulsion direction due to rotational diffusion (Fig. 2.3b). The initial directed motion persists for a time $\tau_\mathrm{p} = 1/D_\mathrm{r}$ (persistence time) over a distance $l_\mathrm{p} = v_0\tau_\mathrm{p}$ (persistence length). Accordingly, the average displacement of an overdamped ABP reads[21,119,253]

$$\langle\mathbf{r}_i(t) - \mathbf{r}_i(0)\rangle = l_\mathrm{p}\left(1 - e^{-t/\tau_\mathrm{p}}\right)\hat{\mathbf{p}}_i(0). \tag{2.6}$$

Therefore, an ABP moves, on average, over a distance l_p along its initial orientation $\hat{\mathbf{p}}_i(0)$ before its orientation is randomized. Additionally, the mean square displacement (MSD) of an overdamped ABP (in two-dimensional space) reads[21,119,181,253]

$$\left\langle\left(\mathbf{r}_i(t) - \mathbf{r}_i(0)\right)^2\right\rangle = 2l_\mathrm{p}^2\left(\frac{t}{\tau_\mathrm{p}} - 1 + e^{-t/\tau_\mathrm{p}}\right) + 4D_\mathrm{t}t, \tag{2.7}$$

which provides valuable insight into the different dynamical regimes of the ABP model. Three regimes are observed when expanding Eq. (2.7) for short, intermediate, and long times. The motion of an overdamped ABP is initially diffusive with diffusion coefficient D_t for $t \ll D_\mathrm{t}/v_0^2$. For $D_\mathrm{t}/v_0^2 \ll t \ll \tau_\mathrm{p}$, a ballistic regime, which represents directed motion due to the activity of the particle comes about. Finally, for $t \gg \tau_\mathrm{p}$, the motion is again diffusive with effective diffusion coefficient $D_\mathrm{eff} = D_\mathrm{t} + l_\mathrm{p}^2/(2\tau_\mathrm{p})$. These three regimes are shown in Fig. 2.4. The relative importance of activity in comparison with diffusion can be characterized by the Péclet number $\mathrm{Pe} = v_0/\sqrt{2D_\mathrm{r}D_\mathrm{t}}$, which is one of the main control parameters for a system of multiple ABPs.[21]

In this thesis, we primarily use the ABP model and solve the system of Langevin equations numerically by using LAMMPS.[254,255] The interaction between two particles i and j is modeled by the purely repulsive Weeks-Chandler-Anderson (WCA) potential[256]

$$u(r_{ij}) = \begin{cases} 4\epsilon\left[\left(\frac{\sigma}{r_{ij}}\right)^{12} - \left(\frac{\sigma}{r_{ij}}\right)^{6}\right] + \epsilon, & r_{ij}/\sigma \leq 2^{1/6} \\ 0, & \text{else} \end{cases}, \tag{2.8}$$

with $r_{ij} = |\mathbf{r}_i - \mathbf{r}_j|$, particle diameter σ, and strength ϵ.

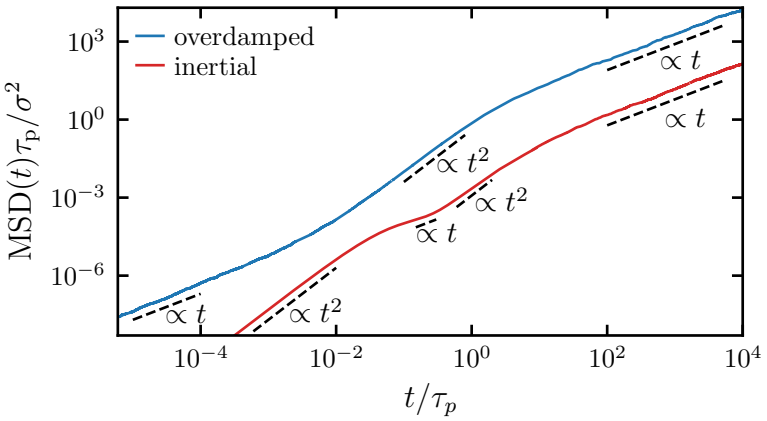

Fig. 2.4 Mean-square displacement of an active Brownian particle. Mean-square displacement $\mathrm{MSD}(t) = \langle(\mathbf{r}_i(t) - \mathbf{r}_i(0))^2\rangle$ of an overdamped ABP (blue; Eqs. (2.4) and (2.5)) and an inertial ABP (red; Eqs. (2.2) and (2.3)) of mass $m/(\gamma_\mathrm{t}\tau_\mathrm{p}) = 0.05$ at $\mathrm{Pe} = 20$. The inertial ABP features an additional ballistic regime at short times.

Alternatives to the ABP model

Several alternative models have been designed that have a similar scope to that of the ABP model in the sense that they also treat the solvent as a bath which only provides fluctuations and drag rather than accounting for momentum conservation and hydrodynamic interactions. We introduce some of these alternative models in the following.

Run-and-tumble particle model: The run-and-tumble particle (RTP) model was originally introduced to describe the characteristic motion patterns of certain bacteria such as *E. coli*,[6,257,258] but it has now advanced to a standard model for the description of active particles.[99,259–261] In fact, the first theory for motility-induced phase separation was formulated for RTPs.[259] In contrast to ABPs, RTPs alternate running periods, during which the self-propulsion direction remains unchanged, with idealized tumbling events, in which the orientation of the particles is randomized (Fig. 2.3c). The equations of motion for an RTP with particle index i read

$$\frac{\mathrm{d}\mathbf{r}_i(t)}{\mathrm{d}t} = v_0\hat{\mathbf{p}}_i(t) - \frac{1}{\gamma_\mathrm{t}}\sum_{\substack{j=1\\j\neq i}}^{N}\boldsymbol{\nabla}_{\mathbf{r}_j}u\left(r_{ij}\right), \tag{2.9}$$

$$\frac{\mathrm{d}\theta_i(t)}{\mathrm{d}t} = \sum_n \Delta\theta_n\delta(t - T_n). \tag{2.10}$$

The values of $\Delta\theta_n$ are uniformly distributed between 0 and 2π, with tumbling events taking place at discrete times T_n.[261] In practice, the times T_n are chosen either randomly with $\langle T_{\mathrm{n}+1} - T_\mathrm{n}\rangle = \lambda_\mathrm{t}^{-1}$ (and, e.g., tumbling events following a Poisson distribution, which leads to exponentially distributed times between tumbling events, as originally found for *E. coli*)[262] or equally spaced. In any case, the (mean) tumbling rate λ_t is fixed, yielding a persistence time $\tau_\mathrm{p} = 1/\lambda_\mathrm{t}$, which plays the role of the (mean) time between tumbling

events. Remarkably, the many-particle dynamics following from the RTP and the ABP models turn out to be equivalent at coarse-grained scales if $(d-1)D_\mathrm{r} = \lambda_\mathrm{t}$, where $d > 1$ is the spatial dimension.[99,260]

Active Ornstein-Uhlenbeck particle model: Another alternative to the ABP model is the active Ornstein-Uhlenbeck particle (AOUP) model,[263–266] which has certain advantages compared with the ABP model regarding the theoretical description of the many-body dynamics of dry active particles. This is due to the fact that the AOUP model avoids the strongly nonlinear dependence of the center-of-mass motion on the particle orientation, which is present in the ABP model, by using colored noise to generate self propulsion. In particular, the translational degrees of freedom still follow Eq. (2.2), but the orientation vector $\hat{\mathbf{p}}_i$ is replaced by a vector $\mathbf{p}_i$ (without the "hat"), which evolves in time through an Ornstein-Uhlenbeck process:[158,267]

$$\frac{\mathrm{d}\mathbf{p}_i}{\mathrm{d}t} = -\frac{\mathbf{p}_i}{\tau_\mathrm{p}} + \sqrt{\frac{1}{\tau_\mathrm{p}}}\boldsymbol{\xi}_i(t). \tag{2.11}$$

Here, τ_p is the persistence time and $\boldsymbol{\xi}_i$ is Gaussian white noise with unit variance and zero mean. In contrast to the ABP model, where $\hat{\mathbf{p}}_i$ is a unit vector with fixed modulus, $\mathbf{p}_i$ has a fluctuating modulus. Consequently, the velocity components of an isolated AOUP are represented by colored noise. However, both the ABP and the AOUP model share the same autocorrelation function of the orientation vectors $\hat{\mathbf{p}}_i$ and $\mathbf{p}_i$, respectively, with an exponential shape, i.e., $\langle \hat{\mathbf{p}}_i(t)\cdot\hat{\mathbf{p}}_i(0)\rangle = \langle \mathbf{p}_i(t)\cdot\mathbf{p}_i(0)\rangle = \exp(-t/\tau_\mathrm{p})$, and thus, also the same equal-time second moment $\langle \hat{\mathbf{p}}_i^2\rangle = \langle \mathbf{p}_i^2\rangle = 1$.[263,267] The difference between the two models is visible in the higher-order moments and the full-shape of the active-force distribution. Indeed, the latter is Gaussian in the case of AOUPs, but it is characterized by a constant modulus in case of ABPs.[267] Note that a single overdamped AOUP, i.e., $u = 0$ and $m = 0$ in Eq. (2.2), is formally identical to an inertial PBP with $m_\mathrm{p}/\gamma_\mathrm{t} = \tau_\mathrm{p}$.

Since it involves colored noise, the AOUP model does not permit formulation of an exact Fokker-Planck equation for the corresponding probability distribution. However, it is still possible to derive an approximate Fokker-Planck equation for the many-body dynamics, which does not depend on the particle orientation but only on the particle positions.[263,265,266,268] Motility-induced phase separation has also been reported for the AOUP model suggesting that it provides a useful alternative for the description of the many-body dynamics of active particles although the single-particle properties significantly differ from those of the ABP and RTP model.[264,266]

Chiral active particles: A further class of models describes chiral active particles (CAPs),[82,118,119,205,269–274] which experience an additional effective torque arising from an anisotropy in their shape or propulsion mechanism. For an isolated CAP, this leads to circular trajectories in the limit of zero noise. In the presence of noise, the orientation angle θ_i of the i-th CAP moving in two spatial dimensions evolves according to

$$\frac{\mathrm{d}\theta_i(t)}{\mathrm{d}t} = \omega + \sqrt{2D_\mathrm{r}}\xi_i(t) \tag{2.12}$$

in the overdamped limit. Here, ω is a constant angular velocity. As in the ABP model, the position $\mathbf{r}_i$ of the i-th CAP generally evolves with time according to Eq. (2.4) in the overdamped regime. An exemplary trajectory of a CAP is shown in Fig. 2.3e. Examples of such circle swimmers include *E. coli* bacteria near surfaces and interfaces,[275,276] sperm cells,[277,278] and artificial microswimmers such as L-shaped particles,[279] "spherical-cap particles" near a substrate,[280] and asymmetric Quincke rollers.[281]

Models with explicit alignment interactions: Thus far, we have focused our discussion on active particles without explicit alignment interactions. The most popular model for describing dry active particles with polar alignment interactions is the Vicsek model,[282,283] which accounts for self-propelled particles that align their orientation with that of their neighbors such as observed for birds.[187] A generalized continuous-time variant of the Vicsek model comprising overdamped CAPs with alignment interactions can be defined by

$$\frac{\mathrm{d}\mathbf{r}_i(t)}{\mathrm{d}t} = v_0\hat{\mathbf{p}}_i(t) + \sqrt{2D_\mathrm{t}}\boldsymbol{\eta}_i(t), \tag{2.13}$$

$$\frac{\mathrm{d}\theta_i(t)}{\mathrm{d}t} = \omega + \frac{K}{\pi R_0^2}\sum_{j\in S_{R_0}^{(i)}}\sin(\theta_j-\theta_i) + \sqrt{2D_\mathrm{r}}\xi_i(t), \tag{2.14}$$

where ω is an angular velocity, K is the strength of the alignment interactions (for $K=0$ this model reduces to the CAP model) and the sum is calculated over all particles within a circle $S_{R_0}^{(i)}$ of radius R_0 centered at the position of particle i.[204,205,284,285] The hallmark of this model is that particles tend to follow the orientation of their neighbors, which can induce polar order, e.g., in the form of the traveling bands shown in Fig. 2.5a for $\omega=0$. When considering CAPs with polar interactions (Eq. (2.14) with $\omega>0$), one finds two remarkable phenomena: The formation of rotating macrodroplets with late-time sizes comparable to the system size, which is indicative of phase separation, at low angular velocity (Fig. 2.5b), and a pattern of rotating microflocks exhibiting phase synchronization and a self-selected length scale at high angular velocity (Fig. 2.5c).

Another class of models with alignment interactions accounts for nematic alignment interactions,[27,286–288] which arise in systems of head-tail symmetric particles such as (self-propelled) rods featuring apolar interactions.[31]

Applicability regime of "dry" active particle models

The ABP model and its alternatives are commonly used to perform particle-based simulations of active particles and also as a starting point for the formulation of continuum theories, as we shall discuss hereunder. These models have proven useful when applied to, e.g., the following problems concerning active particles:

(i) When we are concerned with the dynamics of a single active particle, the ABP model has been very successful, e.g., to predict correlation functions in close agreement with experiments of Janus colloids.[185]

(ii) When hydrodynamic interactions play a minor role such as for certain active colloids, their many-body behavior is reasonably well described by ABPs.[53] Similarly, when

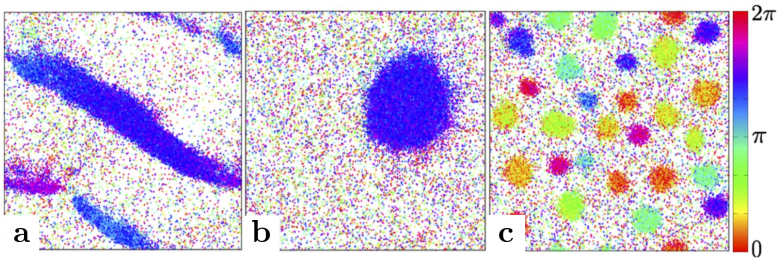

Fig. 2.5 Active particles with alignment interactions. Simulation snapshots of active particles with alignment interactions (cf. Eqs. (2.13) and (2.14)) for $D_\mathrm{t} = 0$ and **a** $\omega = 0$ (smooth variant of the Vicsek model) and **b**, **c** $\omega > 0$ (chiral active particles). Colors represent particle orientation angles such that equally colored particles are aligned or phase-synchronized (reprinted with permission from Ref. [205]. © 2017 by the American Physical Society).

hydrodynamic interactions are dominated by other interactions such as phoretic interactions of autophoretic colloids with a near-uniform surface mobility, the ABP model serves as a useful starting point for the derivation of simple models with effective phoretic pair interactions.[235]

(iii) When a solvent is absent but fluctuations are still relevant as, e.g., for granular particles on vibrating plates, where quasi-deterministic chaos arises and leads to effective randomness, which can be described as Brownian noise, the ABP model can be used as a numerical model.[289,290]

(iv) The ABP model is also useful for fundamental theoretical explorations, e.g., when we are more interested in the fundamental consequences of activity on the collective behavior of active particles rather than in the specific link to experimental realizations.

Advantages and limitations

Compared with most "wet" models, a key advantage of the ABP model and its alternatives is their simplicity from both a conceptual and a computational viewpoint. In particular, these models allow one to simulate very large ensembles of active particles (state-of-the-art simulations often use $10^5 - 10^7$ particles).[72,103,110,291–293] One key limitation of these models regarding the description of soft active matter systems is that they do not account for momentum conservation and often not for hydrodynamic interactions either. This can be particularly relevant for the description of collective behavior or for describing single microswimmers near walls. The ABP model is popular when simulating the collective behavior of autophoretic active colloids as well. Here, beside hydrodynamic interactions, also phoretic interactions can play a crucial role and are also neglected by the standard ABP model,[235] which can however be extended to take them into account.[74,112,115,294–297]

2.2.2 Continuum models

To understand the collective behavior of (dry) active particles, one often uses continuum models, which can be used for a purely theoretical analysis or a numerical analysis based

on continuum simulations. In general, one can distinguish between (i) phenomenological and (ii) microscopic theories:

(i) *Phenomenological theories:* This class is often based on an identification of the relevant "slow variables" (e.g., the density field $\rho(\mathbf{r},t)$ in the case of isotropic active systems with particle number conservation or the density field and polarization density for polar active systems with polar alignment interactions) and on writing down all terms which are allowed by symmetry and conservation laws up to a certain order. Accordingly, these theories are sometimes called Landau theories. A key advantage of phenomenological theories is that they predict the structure of the field equations essentially based on symmetry, conservation laws, and dimensionality of the system without requiring any reference to the details of the underlying particle system (such as the precise form of the interactions). Thus, these field theories are sometimes called "generic" in this sense and can even be formulated (and numerically solved) if no underlying particle-based model is known. However, phenomenological field theories do not provide information about the values of the coefficients. Thus, one often treats all occurring coefficients as independent parameters and studies the phenomenology of the field equations as a function of all these parameters. A related important drawback of this approach is that it then remains unclear if there is an underlying particle-based model or realization which leads to the corresponding parameter values. A specific example of a phenomenological theory is discussed further below.

(ii) *Microscopic theories:* In contrast to phenomenological theories, microscopic theories involve a systematic derivation of the field equations typically from the underlying equations of motion for the individual active particles. This approach yields equations of motion for the relevant fields, which directly follow from the underlying particle-based model. Thus, in contrast to the former class of theories, one advantage of this second approach is that one obtains, in addition to the structure of equations, an explicit link between the coefficients of the particle-based model and the continuum theory. This typically leads to a (much) smaller number of independent parameters than one would obtain from phenomenological approaches. Another advantage is that, following the microscopic approach, terms which are allowed by symmetry cannot be missed, which has happened for various standard models of active matter in the past when following the phenomenological approach.

In the following, we will illustrate both approaches based on specific examples for isotropic and polar active systems.

Phenomenological theory for isotropic active matter — the active model B+

Collective phenomena of isotropic active matter such as phase separation can be described, e.g., by the phenomenological active model B+ (AMB+), which is based on the common model B that describes phase separation in equilibrium systems.[298] Here, the density field $\rho(\mathbf{r},t)$ is assumed to be the only slow variable of the system and the order parameter ϕ is related to it by the linear transformation $\phi = (2\rho - \rho_{\mathrm{H}} - \rho_{\mathrm{L}})/(\rho_{\mathrm{H}} - \rho_{\mathrm{L}})$, where ρ_{H} and ρ_{L}

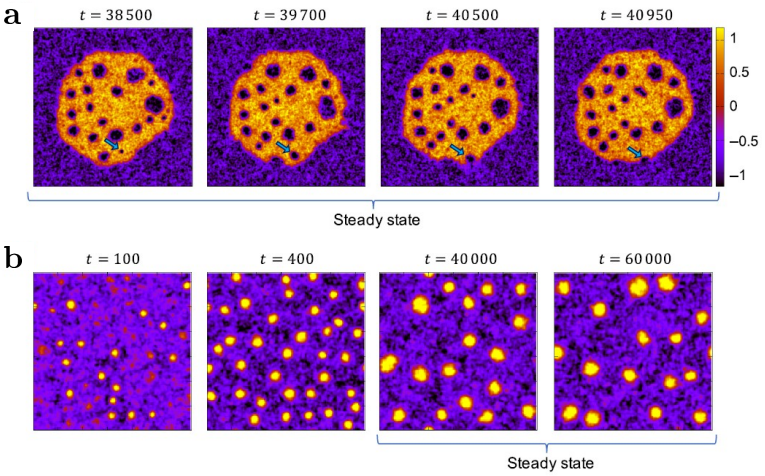

Fig. 2.6 Numerical results of the active model B+. a Coexistence of a liquid phase (yellow to red colors) comprising continuously created vapor bubbles and a gas phase (black and purple). **b** Phase separation into a dense (yellow to red colors) and a dilute phase (black and purple). Dense clusters stabilize at a certain cluster size in the steady state (reprinted from Ref. [300] licensed under CC BY 4.0).

denote the density at the low-density and the high-density critical point, respectively.[76,299] The active model B+ is given by the equations[300]

$$\frac{\partial \phi}{\partial t} = -\boldsymbol{\nabla} \cdot \left[-M \boldsymbol{\nabla} \left(\frac{\delta \mathcal{F}}{\delta \phi} + \lambda |\boldsymbol{\nabla} \phi|^2 \right) + \zeta M \left(\nabla^2 \phi \right) \boldsymbol{\nabla} \phi + \sqrt{2 k_\mathrm{B} T M} \boldsymbol{\Lambda} \right], \tag{2.15}$$

$$\mathcal{F}[\phi] = \int \mathrm{d}^3 r \left[\frac{a}{2} \phi^2 + \frac{b}{4} \phi^4 + \frac{K}{2} |\boldsymbol{\nabla} \phi|^2 \right]. \tag{2.16}$$

Here, the free-energy functional $\mathcal{F}$ is approximated up to the order ϕ^4 and up to square-gradient terms, and $\boldsymbol{\Lambda}(\mathbf{r}, t)$ denotes Gaussian white noise with zero mean and unit variance. The mobility is denoted by M, the temperature is given by $k_\mathrm{B}T$ with Boltzmann constant k_B, and a, b, K, ζ, λ are free parameters of the model. Equation (2.15) has the form of a continuity equation, and hence, it ensures particle number conservation, whereas reaction terms are not allowed in Eq. (2.15). For active particles, the time-reversal symmetry (TRS) is broken locally. This fact is included in the AMB+ by the additional terms proportional to λ and ζ. The AMB+ describes the phase separation behavior of isotropic active matter and predicts two types of patterns apart from MIPS: The first one is characterized by phase separation into a dense and a dilute phase and the additional occurrence of vapor bubbles inside the dense phase, which are continuously created and move to the surface of the dense phase (Fig. 2.6a). The second pattern is characterized by the emergence of dense clusters that do not grow beyond a certain characteristic size (Fig. 2.6b). The coefficients a, b, K, λ, ζ are not known in this phenomenological approach and are treated as parameters of the model. Thus, there is no obvious connection to particle-based models such as the ABP model, whereas in microscopic theories all parameters are directly related to the underlying particle-based model, as we will discuss next.

Microscopic theories for isotropic active matter

There are several approaches to developing microscopic theories. To exemplify one of them, we consider a system of N active particles without alignment interactions. Then, we write down the Smoluchowski equation for the N-particle probability density and integrate out variables to obtain the one-particle density field. This approach has been used, for instance, to formulate a microscopic theory of MIPS for overdamped ABPs with positions $\mathbf{r}_i$ and orientations θ_i.[301] Let $\mathbf{X} = \{\mathbf{r}_1, ..., \mathbf{r}_N, \theta_1, ..., \theta_N\}$ denote the state of the N-particle system. The corresponding Smoluchowski equation for the joint probability distribution $\psi_N(\mathbf{X}, t)$ reads[302]

$$\frac{\partial \psi_N}{\partial t} = \sum_{k=1}^{N} \boldsymbol{\nabla}_{\mathbf{r}_k} \cdot \left[\frac{(\boldsymbol{\nabla}_{\mathbf{r}_k} U)}{\gamma_\mathrm{t}} - v_0 \hat{\mathbf{p}}_k + D_\mathrm{t} \boldsymbol{\nabla}_{\mathbf{r}_k} \right] \psi_N + D_\mathrm{r} \sum_{k=1}^{N} \frac{\partial^2 \psi_N}{\partial \theta_k^2}, \tag{2.17}$$

with $U = \sum_{k<k'} u\left(|\mathbf{r}_k - \mathbf{r}_{k'}|\right)$, interaction potential $u(r)$, and self propulsion along $\hat{\mathbf{p}}_k$ with self-propulsion speed v_0. The Smoluchowski equation ensures probability conservation and its physical interpretation is illustrated in Fig. 2.7. Starting from Eq. (2.17), one usually derives an equation of motion for the one-particle probability distribution $\psi_1(\mathbf{r}_1, \theta_1, t)$ by integration. Due to the pair interactions, the resulting equation still contains terms which include the two-particle probability distribution. Similarly, one can derive an equation for the two-particle probability distribution, which then includes the three-particle distributions, and so on, leading to a hierarchy of coupled differential equations that has to be closed by a suitable closure scheme.[303,304] Afterward, an equation of motion for the particle density $\rho(\mathbf{r}, t)$ can be derived by integrating over the orientation θ, which typically couples again to higher moments and leads to a second hierarchy of equations, which has again to be closed using a suitable closure scheme. To study phase separation, one possible approximation to avoid the first type of hierarchy is to assume that the density varies slowly in space such that the local density is constant within the range of the interaction potential resulting in an effective self-propulsion speed $v(\rho) = v_0 - \zeta\rho$ with constant ζ. This density-dependent self-propulsion speed effectively accounts, to some extent, for the net effect of the repulsive interactions, namely the slowdown of active particles in regions of high density. The result of this microscopic approach fits well to computer simulations of ABPs and predicts MIPS in overdamped ABPs.[301]

An alternative approach, sometimes called the "Dean approach",[305] is based on an explicit coarse-graining of the Langevin equations for the individual particles. This approach has been applied in several works, e.g., to describe MIPS in systems of RTPs,[259] pattern formation in self-propelled particles with alignment interactions,[204] collective phenomena in systems of CAPs,[205], pattern formation in systems of phoretically interacting active colloids,[294] or active systems showing nematic order.[306] Here, one uses Itô calculus to deduce a stochastic differential equation, which involves multiplicative noise, for the (fluctuating) combined probability $f(\mathbf{r}, \theta, t) = \sum_{i=1}^{N} \delta(\mathbf{r}_i(t) - \mathbf{r})\delta(\theta_i - \theta)$ to find one particle with orientation θ at position $\mathbf{r}$ at time t.[305,307,308] To derive the one-particle density field $\rho(\mathbf{r}, t)$, one can then, for example, choose to neglect the multiplicative noise term (mean field) and derive a hierarchy of equations in a similar way to the Smoluchowski approach.

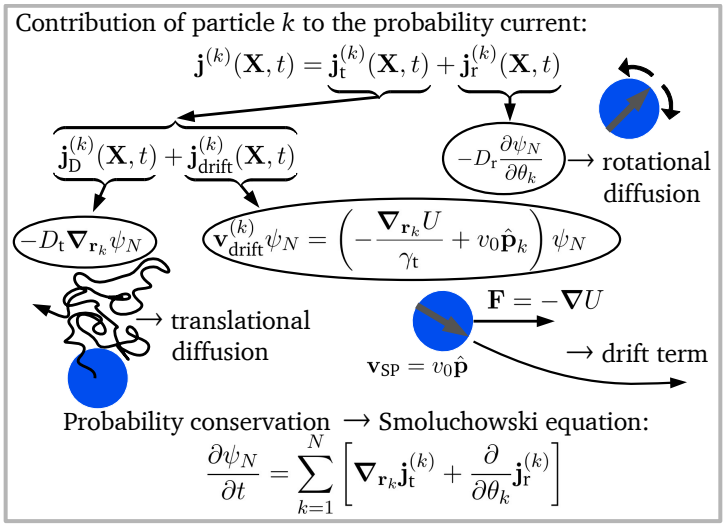

Fig. 2.7 Interpretation of the Smoluchowski equation. Interpretation of Eq. (2.17) as probability conservation law. The contribution of each particle to the probability current can be decomposed into a translational and a rotational current. The former includes translational diffusion and a drift term due to the interaction potential as well as the self-propulsion velocity, whereas the latter considers rotational diffusion. The Smoluchowski equation can then be interpreted as a continuity equation ensuring probability conservation.

Microscopic theories for polar active matter

The aforementioned continuum theories for dry active matter were focused on isotropic active matter that can be described by only considering the density field. However, if the particles feature alignment interactions such as in the Vicsek model, polar order can arise. Thus, describing these systems additionally requires the consideration of the mean local orientation of the particles by means of a polarization density $\mathbf{P}(\mathbf{r},t)$. Corresponding theories for the density field and the polarization density can be derived based on the Smoluchowski approach or the Dean approach. Another approach, which is aimed at describing the collective behavior of the Vicsek model (which is discrete in time in its original formulation) and is given by Ref. [309], is based on the Liouville equation for the N-particle probability density $\psi_N(\mathbf{X},t)$ and applied to the well-known Vicsek model.[282] Within this model, the particles only interact during a collision event by aligning their orientation to that of their next neighbors and the orientation is subject to Gaussian white noise. Under the assumption that the particles are uncorrelated prior to a collision, the N-particle density is written as a product of one-particle densities, which is a good approximation if the noise strength is large and if the mean-free path between two collisions is larger than the interaction radius. Then, the one-particle probability distribution is obtained by integration. However, the solution contains complicated collision integrals that are approximated using the Chapman-Enskog expansion,[310] which takes the stationary state as a reference and expands around it in powers of the gradients. Finally, this leads to a set of two coupled differential equations for ρ and $\mathbf{P}$. This set of equations is similar to that of the phenomenological Toner-Tu model except for additional gradient terms, which occur only in the microscopic approach.[16]

Independently of whether a theory is phenomenological or microscopic, the relevant field equations can then be studied based on various analytical and numerical techniques ranging from perturbation theories, linear stability analyses, or dynamical renormalization group calculations in the presence of additional noise terms to explicit numerical solutions based on, e.g., finite difference, finite volume, or finite element methods.

2.2.3 Modeling hydrodynamics of microswimming

The ABP model and its alternatives do not resolve the self-propulsion mechanism, but instead, they involve an effective force to phenomenologically model the resulting directed motion. To understand and describe the self-propulsion mechanism of a microswimmer, one has to explicitly model the flow field produced by the microswimmer and its interaction with the body of the swimmer.

Microhydrodynamics

Let us now briefly discuss the basic equations which are involved in the modeling of a single microswimmer. While swimming at the macroscale involves inertia and leads to flow fields which are described by the Navier-Stokes equation, microswimmers have to employ swimming mechanisms which work even in the absence of inertia since viscous effects dominate over inertial effects at the microscale. This is quantified by the Reynolds number, which measures the relative importance of inertial and viscous forces and is given by $\mathrm{Re} = (\rho L v)/\eta$, where the numerator represents the product of the fluid density ρ, a characteristic length scale L, and a typical flow speed v, whereas the denominator contains the solvent viscosity η. For microswimmers, $\mathrm{Re} \ll 1$: For *E. coli* bacteria in water, for example, we have $L \sim 3\,\mu\mathrm{m},\ v \sim 30\,\mu\mathrm{m/s},\ \eta = 0.001\,\mathrm{Pa\ s}$, and $\rho = 1\,\mathrm{g/cm^3}$.[21] Thus, $\mathrm{Re} \sim 10^{-5} - 10^{-4} \ll 1$ and inertial effects can safely be neglected. For comparison, phenomena occurring at high Reynolds numbers such as turbulence often occur at $\mathrm{Re} \sim 10^3 - 10^4$.[311]

At low Reynolds number, the Navier-Stokes equation reduces to the Stokes equation, which describes "creeping flow" and reads

$$\eta \nabla^2 \mathbf{u} - \boldsymbol{\nabla} p + \mathbf{f} = 0, \tag{2.18}$$

where $\mathbf{u}(\mathbf{r}, t)$ and $p(\mathbf{r}, t)$ are the solvent velocity field and the pressure field, respectively, and $\mathbf{f}(\mathbf{r}, t)$ is the force density representing the forces exerted by the microswimmers on the solvent. The Stokes equation is typically complemented by the incompressibility condition $\boldsymbol{\nabla} \cdot \mathbf{u} = 0$ leading to a complete set of equations to determine $\mathbf{u}(\mathbf{r}, t)$ and $p(\mathbf{r}, t)$ for a given $\mathbf{f}(\mathbf{r}, t)$ and given boundary conditions. Notably, the Stokes equation does not contain any time derivatives, and therefore, the solvent responds instantaneously to the applied forces (no motion would take place once the forcing term is switched off), which reflects the absence of inertia. Accordingly, the swimming mechanism of scallops, which move by periodically opening and closing their shells, would not work at low Reynolds number (Fig. 2.8a). Likewise, any other mechanism based on reciprocal motions would not lead to directed motion. This is Purcell's scallop theorem.[312]

The general procedure to model microswimmers which move by body-shape deformations (or squirmers) at low Reynolds numbers consists in solving the Stokes equation

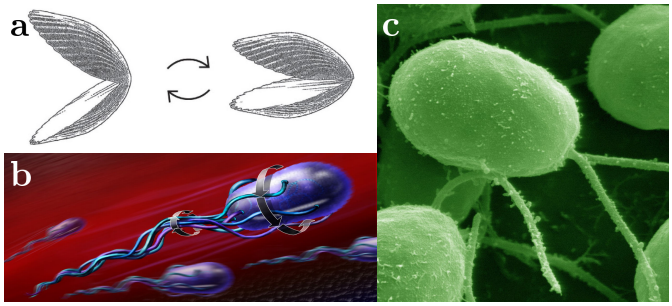

Fig. 2.8 Self-propelling at low Reynolds number. **a** Motion of a scallop. By quickly closing and slowly opening the two shells, the scallop produces a net flow and starts moving. At low Reynolds number, the net displacement is zero for this reciprocal motion (reprinted from Ref. [313] licensed under CC BY 4.0, © 2014 Macmillan Publishers Limited). **b** Schematic of the non-reciprocal motion of an *E. coli* bacterium (reprinted from Ref. [314], by Nicolle Rager Fuller, National Science Foundation). **c** Electron microscope image of *Chlamydomonas reinhardtii* algae showing the flagella producing self propulsion by non-reciprocal motion (reprinted from Ref. [315], by Louisa Howard, Dartmouth College).

with appropriate boundary conditions for the solvent velocity field $\mathbf{u}$ on the surface of the microswimmers. This yields the solvent velocity field $\mathbf{u}$, from which the stress tensor $\boldsymbol{\sigma} = \eta \left(\boldsymbol{\nabla} \otimes \mathbf{u} + (\boldsymbol{\nabla} \otimes \mathbf{u})^{\mathrm{T}} \right)$ can be obtained, where $\otimes$ denotes the dyadic product. The latter allows one to calculate the total force $\mathbf{F} = \int_S \mathrm{d}S\, \boldsymbol{\sigma}(\mathbf{r}, t)\hat{\mathbf{n}}$ and the torque $\mathbf{T} = \int_S \mathrm{d}S\, \mathbf{r} \times (\boldsymbol{\sigma}(\mathbf{r}, t)\hat{\mathbf{n}})$ which act on the microswimmer, where S and $\mathrm{d}S$ denote the surface of the microswimmer and a differential element of it, respectively. Then, for a solid particle, the rigidity condition

$$\mathbf{u}(\mathbf{r}) = \mathbf{v} + \boldsymbol{\omega} \times \mathbf{r}, \quad \mathbf{r} \in S \tag{2.19}$$

is typically assumed to apply at the surface S of the particle and links the particle velocity $\mathbf{v}$ and angular velocity $\boldsymbol{\omega}$ to $\mathbf{F}$ and $\mathbf{T}$. Finally, the torque-free ($\mathbf{T} = 0$) and force-free ($\mathbf{F} = 0$) conditions allow one to solve for $\mathbf{v}$ and $\boldsymbol{\omega}$.[21,32] Since microswimmers often deform in a cyclic way, the net displacement during one cycle of period T is given by $\int_0^T \mathrm{d}t\, \mathbf{v}(t)$, which is zero for reciprocal movement in the regime of low Reynolds numbers.[236] Thus, non-reciprocal body-shape deformations are required to produce directed motion. Two examples of biological microswimmers that self propel by non-reciprocal motion are demonstrated in Fig. 2.8b,c. A minimal microswimmer model can be constructed, e.g., based on three spheres connected by two arms, which periodically change their length (three-sphere swimmer)[316–320] or based on two spheres which can contract or expand radially and are connected by an elastic arm.[317,321,322]

Modeling hydrodynamics at the many-particle level

In ensembles of microswimmers, each of them generates a specific flow pattern which typically decays slowly in space and leads to long-ranged hydrodynamic cross interactions among different microswimmers as well as to hydrodynamic (self) interactions with walls and interfaces. These hydrodynamic interactions are typically not included in models of dry active matter such as the ABP model and its alternatives. One way of simulating

several interacting microswimmers is to explicitly model the detailed self-propulsion mechanism of each microswimmer, i.e., to alternately solve the Stokes equation with the microswimmer-solvent boundary conditions for all swimmers simultaneously and to propagate the swimmers based on the force- and torque-free conditions. While such an approach is conceptually relatively simple and accurate in principle, it creates a huge numerical effort and typically becomes unfeasible even for moderately large microswimmer ensembles. In the following, we briefly discuss some alternative approaches, which allow for more efficient numerical descriptions of microswimmer ensembles.

Minimal models and hydrodynamic far-field interactions: To model the dynamics of large microswimmer ensembles, an explicit modeling of the solvent flow including the detailed particle-solvent boundary conditions occurring in real microswimmers is often numerically so demanding that very large system sizes remain unreachable. Therefore, one often looks for a compromise between the ABP model, which neglects hydrodynamic interactions and momentum conservation altogether, and an explicit modeling of the self-propulsion mechanism of all interacting microswimmers in a given ensemble. One common approach involves formulating hydrodynamically consistent minimal models for the collective behavior of microswimmers, where one does not explicitly describe the self-propulsion mechanism of each microswimmer but replaces each microswimmer with a simpler representative that creates a similar (far-field) flow pattern. To this end, one uses a multipole expansion of the flow field (similar to that used, e.g., in electrodynamics) and only considers the leading-order terms.[96,323–325] In the simplest case, these are the so-called "singularity solutions" of the Stokes equation (e.g., the flow field of a force dipole), which are then used to replace the flow field created by each microswimmer and are equivalent to the far-field flow pattern generated by the actual microswimmer to be modeled. For example, it is well known that *E. coli* bacteria produce essentially the same far-field flow pattern as a force dipole (pusher)[232] and *Chlamydomonas* algae produce a far-field flow pattern which can be represented by the flow field produced by an oscillatory force dipole.[326] Let us briefly discuss three common singularity solutions of the Stokes equation:

(i) *Point force ("Stokeslet"):* The flow generated by a point force $\mathbf{f}_\mathrm{p} = f\hat{\mathbf{e}}\delta(\mathbf{r}-\mathbf{r}_0)$ placed at position $\mathbf{r}_0$ and pointing along the direction $\hat{\mathbf{e}}$ is similar to the far-field flow of a particle that is driven by an external force.[32,324] By setting $\mathbf{f} = \mathbf{f}_\mathrm{p}$ in the Stokes equation (cf. Eq. (2.18)), the resulting velocity field reads

$$\mathbf{u}_\mathrm{PF}(\mathbf{r}) = \frac{f}{8\pi\eta r}\left[\hat{\mathbf{e}} + (\hat{\mathbf{r}}\cdot\hat{\mathbf{e}})\,\hat{\mathbf{r}}\right], \tag{2.20}$$

where $r = |\mathbf{r}|$, $\hat{\mathbf{r}} = \mathbf{r}/r$, and η denotes the viscosity of the solvent. The velocity field is shown in Fig. 2.9a. Since microswimmers are force free (momentum conservation), the Stokeslet solution alone is unsuitable to represent them.

(ii) *Force dipole:* The far-field solution of the Stokes equation in the presence of two point forces $\mathbf{f}_+ = f\hat{\mathbf{e}}\delta(\mathbf{r}-\mathbf{r}_0-(l/2)\hat{\mathbf{e}})$ and $\mathbf{f}_- = -f\hat{\mathbf{e}}\delta(\mathbf{r}-\mathbf{r}_0+(l/2)\hat{\mathbf{e}})$, which are separated by a distance l, reads

$$\mathbf{u}_\mathrm{FD}(\mathbf{r}) = \frac{fl}{8\pi\eta r^2}\left[3\,(\hat{\mathbf{e}}\cdot\hat{\mathbf{r}})^2 - 1\right]\hat{\mathbf{r}} \tag{2.21}$$

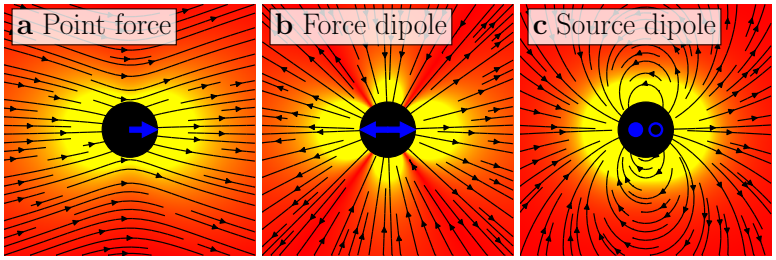

Fig. 2.9 Singularity solutions of the Stokes equation. Illustration of the velocity field $\mathbf{u}(\mathbf{r})$ of **a** a point force, **b** a force dipole, and **c** a source dipole. The black arrows indicate the direction of the flow field and the background color indicates its magnitude, where yellow denotes a large magnitude and (dark) red a small magnitude. The blue arrows represent the point forces and the filled and empty blue circles a source and sink, respectively.

in the limit $l \to 0$ or at distances $r \gg l$, and it is represented in Fig. 2.9b for $f > 0$.[32,324] These force dipoles push fluid molecules in the forward and backward directions. Hence, microswimmers that show this kind of far-field flow pattern are called "pushers", whereas the case of $f < 0$, where all flow field lines are reverted, corresponds to a "puller".

(iii) *Source dipole:* The point-force and force-dipole solutions are obtained by solving the Stokes equation together with the incompressibility condition $\boldsymbol{\nabla} \cdot \mathbf{u} = 0$. In the presence of sources of solvent molecules, the Stokes equation is unchanged, but the incompressibility condition changes to $\boldsymbol{\nabla} \cdot \mathbf{u}(\mathbf{r}) = s(\mathbf{r})$, where $s(\mathbf{r})$ denotes the source density.[324] While a point source is of limited relevance (it would lead to a net flow of solvent molecules entering or leaving the domain), the source dipole is an important singular solution to the Stokes equation. Its source density consists of two point sources $s_+(\mathbf{r}) = Q\delta(\mathbf{r} - \mathbf{r}_0 - (l/2)\hat{\mathbf{e}})$ (source of solvent molecules) and $s_-(\mathbf{r}) = -Q\delta(\mathbf{r} - \mathbf{r}_0 + (l/2)\hat{\mathbf{e}})$ (sink of solvent molecules) that are separated by a distance l, where $Q > 0$ denotes the magnitude of the source densities. The corresponding solution to the Stokes equation in the limit $l \to 0$ reads[324]

$$\mathbf{u}_{\mathrm{SD}}(\mathbf{r}) = \frac{Ql}{4\pi r^3} \left[3\left(\hat{\mathbf{e}} \cdot \hat{\mathbf{r}}\right)\hat{\mathbf{r}} - \hat{\mathbf{e}}\right] \tag{2.22}$$

and its velocity field is demonstrated in Fig. 2.9c.

Since self-propelled particles are force free, the simplest representation of active particles by singularity solutions of the Stokes equation is given by source and force dipoles. Examples of simulations of microswimmer models based on these singularity solutions comprise, e.g., studies of motile suspensions of active rod-like particles,[327] of the dynamics of a single molecule composed of microswimmers,[328] of RTPs with hydrodynamic interactions,[329] or of microswimmers near boundaries.[330]

To simulate microswimmers based on singularity solutions of the Stokes equation, one often models the external fluid velocity field $\mathbf{u}$ as a sum of all microswimmer singularity solutions and applies certain boundary conditions on the surface of each microswimmer. The velocity $\mathbf{v}$ of each microswimmer is then calculated using the force-free and torque-free conditions based on the stress tensor, as previously discussed for a single microswimmer,

via numerical integration. To obtain self propulsion, one shifts the force or source dipole away from the center of the particles.[327,328] Moreover, one can also combine the singularity solutions with numerical solvers such as the Lattice-Boltzmann method discussed below.[331] Beside simulations, the force and source dipole models are used to develop continuum theories for active matter with hydrodynamic interactions, which we will briefly discuss in the last part of this section.

Squirmer models: An alternative (not necessarily unrelated) approach to formulate hydrodynamically consistent models of microswimmers is to consider squirmers, i.e., spherical particles with a prescribed solvent flow along the surface (without explicitly modeling the origin of the latter).[201,323,332–340] On the surface of the squirmer particle, the vertical fluid velocity is set to zero and the tangential surface velocity is prescribed by a series of first derivatives of Legendre polynomials, which can be used, e.g., to model the net effect of autophoresis, which leads to a slip velocity across the surface of Janus particles.[341] The squirmer model has been used in several works, e.g., in combination with the lattice-Boltzmann method[338,342,343] or multi-particle collision dynamics simulations.[201,332,333,335–337,339,340]

In contrast to the ABP model and its alternatives, microswimmer models based on combinations of singularity solutions of the Stokes equation or on squirmers are momentum conserving and can correctly describe hydrodynamic interactions at large inter-particle distances for a given active system. However, they do not necessarily account for the correct hydrodynamic near-field interactions and are therefore mainly useful to model active systems at low density (squirmer models may serve as an exception when they are used to representing Janus particles; they are expected to correctly describe hydrodynamic interactions down to distances on the order of the slip length).[341] These effective models are often used also as a starting point for continuum theories as briefly discussed further below.

Explicit simulations of the solvent: In the following, we briefly introduce several numerical methods which are frequently used in active matter physics to explicitly determine the flow field and to simulate hydrodynamic interactions, often beyond the far-field approximation.

(i) *Lattice-Boltzmann method:* One popular method to solve fluid dynamics problems is the lattice-Boltzmann method (LBM), where one solves the Boltzmann equation instead of the (Navier-)Stokes equation and exploits the fact that the latter equation can be derived from the former.[98,338,344–349] Interestingly, the Boltzmann equation is numerically often more convenient when combined with suitable approximations. It describes the particle distribution function $f(\mathbf{r}, \mathbf{v}, t)$, which is the density of particles with velocity $\mathbf{v}$ at position $\mathbf{r}$ and time t. With the so-called collision operator $\Omega(f)$, the Boltzmann equation reads[345,350]

$$\frac{\partial f}{\partial t} + \mathbf{v} \cdot \boldsymbol{\nabla}_{\mathbf{r}} f + \frac{\mathbf{F}}{m} \cdot \boldsymbol{\nabla}_{\mathbf{v}} f = \Omega(f), \tag{2.23}$$

where m denotes the mass of the particles and $\mathbf{F}$ is the external force field acting on them. The second term on the left-hand side describes advection of the particles with

velocity $\mathbf{v}$, whereas the third term describes external forces acting on the solvent particles and affecting their velocity. The source term on the right-hand side of Eq. (2.23) describes the local redistribution of the solvent particles due to collisions. This collision operator is often approximated by $\Omega(f) = -(f - f_{\text{eq}})/\tau$, which describes the relaxation of the distribution f towards the equilibrium distribution f_{eq} on the timescale τ and is known as the Bhatnagar–Gross–Krook (BGK) collision operator.[351] In the LBM, the continuous Boltzmann equation (i.e., Eq. (2.23)) is discretized in position, velocity, and time and numerically solved on a lattice with spacing Δx at discrete times with time step Δt. The velocity $\mathbf{v}$ can only take discrete values $\mathbf{c}_i$, which are given by a discrete set $\{\mathbf{c}_i, w_i\}$ with weights w_i. The discretized Boltzmann equation is then solved numerically as discussed, e.g., in Ref. [345]. To simulate microswimmers that, e.g., create directed motion through body-shape deformations, one often describes the microswimmer surface as a set of boundary links that define a closed surface and solves the discretized Boltzmann equation together with suitable boundary conditions.[345]

(ii) *Multi-particle collision dynamics:* Another popular approach to simulate the dynamics of microswimmers is based on multi-particle collision dynamics (MPCD), where, in contrast to the LBM, the solvent is represented by point-like particles which have continuous positions and velocities.[352–358] To model active particles, one usually combines the MPCD method for the solvent molecules with molecular dynamics (MD) simulations of the active particles, which are coupled to the solvent and are represented either as a single particle or by a quasi-continuous distribution of particles which are connected with (time-dependent) springs and represent the surface of a (deformable) microswimmer.[359] The MPCD method has been used in several works to investigate, e.g., chemotactic Janus colloids,[360] active particles with phoretic interactions,[361] dynamics of active particles in chemically active media,[362] the motion of squirmers,[333,337,339] the influence of hydrodynamic interactions on phase separation in systems of microswimmers,[201] collective behavior of sperm cells,[67] and active particles in filament networks.[182]

(iii) *Dissipative-particle dynamics:* Another coarse-grained approach to modeling the solvent is given by dissipative-particle dynamics (DPD) simulations. Here, each DPD particle represents a small solvent region and, similar to the MPCD simulations, the positions and velocities of the DPD particles take continuous values. The DPD particles interact via three types of effective forces: A weak conservative force models the soft repulsion of the solvent molecules, a dissipative force models the friction, and a random force accounts for thermal fluctuations. Knowing these forces, Newton's equation of motion is solved for the DPD particles to obtain the hydrodynamics of the solvent.[363–365] This model has been adapted, e.g., to active suspensions[366] and to model the self-propulsion of Janus colloids.[367]

(iv) *Microscopic solvent simulations:* Finally, beside the previously discussed mesoscale-simulation methods, particle-based simulations of the solvent molecules based on direct MD simulations, which allow one to resolve very small spatial and temporal scales, are possible. Nevertheless, these simulations are computationally very intense, which makes it impossible to study systems of the microscale over time scales

of seconds, which are relevant to most active matter systems. Still, this explicit modeling of the solvent has been successfully used to model a self-propelled particle in a Lennard-Jones solvent.[368]

Overall, the LBM, MPCD, and the DPD methods are mesoscale simulation methods, which can be applied to many hydrodynamic problems in soft and active matter physics and beyond. Since the DPD method is based on particles moving in continuous space, it avoids lattice artifacts and allows simulations capturing much larger length and time scales than typically possible in MD simulations. However, DPD simulations include many parameters in order to model the different forces, which have to be chosen carefully. The MPCD method, on its part, which models the net effect of individual collisions rather than accounting for every collision event, is computationally very efficient and can be efficiently parallelized. This applies also to the LBM, which numerically solves the Boltzmann equation and is well suited, e.g., for implementing complex (moving) boundaries.[345]

Continuum theories of microswimmers with hydrodynamic interactions

Based on the previously discussed effective microswimmer models, continuum theories for large ensembles of particles can be formulated which explicitly account for hydrodynamic interactions at least at low density. These theories describe wet active matter and can be formulated, e.g., based on the puller and pusher solutions of the Stokes equation. One popular approach to account for hydrodynamic far-field interactions is to write down the (overdamped) equations of motion for the position and orientation of each microswimmer, which couple with the overall fluid velocity field. The contribution of each microswimmer to the overall velocity field is modeled by singularity solutions of the Stokes equation such as force or source dipoles (which can be superimposed due to the linearity of the Stokes equation). One then derives a continuity equation for the N-particle probability density, which typically takes the form of a Fokker-Planck equation.[206,369–371] From here, one can proceed similarly to microscopic theories for dry active matter in order to derive an equation of motion for the one-particle density. Since the described approach to formulate continuum theories for wet active matter is based on the singularity solutions of the Stokes equation, which only describe the far-field flow pattern of active particles, near-field hydrodynamic effects are not included in this approach. However, although complicated in practice, one can go beyond the far-field regime in principle, e.g., by using superimposed singularity solutions to represent the near-field flow pattern of each swimmer or by starting with squirmer models.

Let us finally mention that one can alternatively formulate phenomenological minimal models of wet active matter. Following a similar spirit to the case of dry active matter, these models are generic in the sense that they are largely based on considerations of symmetry, conservation laws, and dimensionality, and they do not refer to details such as the specific self-propulsion mechanism, which is employed by the microswimmers. One example of such a minimal model for wet active matter is given by the phenomenological active model H,[97] which accounts for momentum conservation. It is based on the active model B[299] and is closely related to the model H for equilibrium systems.[298] The active model H addresses the phase separation behavior of wet active matter and couples the generalized density field $\phi(\mathbf{r}, t)$ to the velocity field $\mathbf{u}(\mathbf{r}, t)$ of the solvent. The general idea is that diffusive

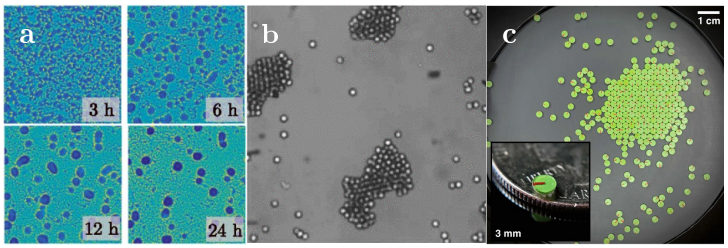

Fig. 2.10 Examples of motility-induced phase separation. Evolution of motility-induced phase separation in **a** *Myxococcus xanthus* bacteria (reprinted with permission from Ref. [59]. © 2019 by the American Physical Society), **b** diffusiophoretic Janus particles (reprinted with permission from Ref. [53]. © 2013 by the American Physical Society), and **c** in millimeter-sized bristle bots (reprinted from Ref. [373]. © 2022 IEEE).

dynamics of the active particles take place in the moving frame of the solvent and the velocity field of the solvent is given by the corresponding Navier-Stokes equation. There are also phenomenological models for specific phenomena such as bacterial turbulence, which are based on phenomenological equations to describe the fluid velocity field.[372] More generally, there are also many alternative approaches to formulating continuum theories such as discussed in Refs. [27, 236, 323].

2.3 Motility-induced phase separation

The fact that active matter systems are intrinsically out of equilibrium manifests in striking collective phenomena. Besides phenomena such as flocking or pattern formation, motility-induced phase separation (MIPS) denotes a remarkable example of non-equilibrium phenomena: Active particles with purely repulsive interactions can phase separate similar to a liquid-gas phase separation. For passive particles, this is impossible unless they have attractive interactions. The mechanism that leads to this phase separation in active systems is known as MIPS. The motility of the individual particles leads to the formation of small clusters that coarsen over time leading to the formation of a dense phase that is surrounded by a dilute gas of active particles. This phenomenon can be observed in different experimental systems such as bacteria,[59] Janus colloids,[53] or millimeter-sized bristle bots (Fig. 2.10).[373]

On the level of the particles, MIPS can be understood as the formation of small clusters that grow and coarsen over time until the system has formed a single dense cluster that is surrounded by a dilute gas. The formation of small clusters is visualized in Fig. 2.11e. Here, three particles block each other. This configuration can be resolved if at least one particle changes its orientation due to rotational diffusion. This typically happens on a timescale of the persistence time τ_p. If the mean time between collisions is smaller than τ_p, small clusters can grow. This situation appears if the active particles are fast (large Péclet number) and if the particle density is large enough (high packing fraction). Then, the time between collisions becomes small, and the uniform state loses stability. The clusters move, merge, and coarsen such that they finally lead to a dense liquid-like phase that coexists with a dilute gas-like phase. This process is visualized in the snapshots shown in Fig. 2.11a–d. On coarse-grained scales, MIPS can be understood as a consequence of a

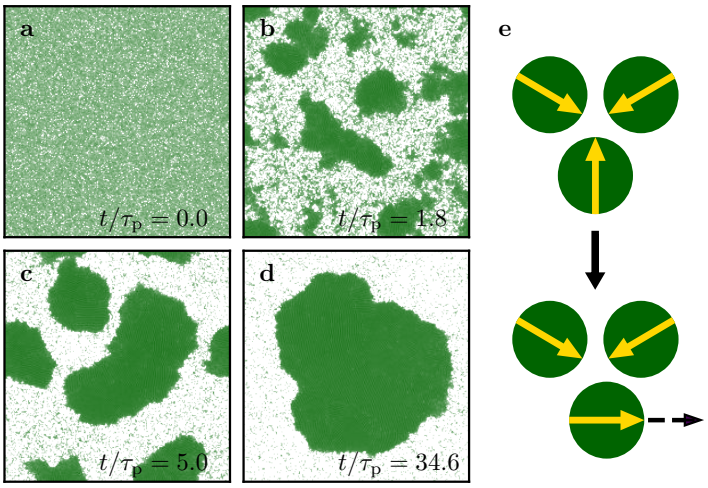

Fig. 2.11 Mechanism of motility-induced phase separation. a–d Evolution of motility-induced phase separation for an ensemble of $N = 39\,200$ overdamped ABPs (Eqs. (2.4) and (2.5)) at packing fraction $\varphi_\mathrm{tot} = 0.47$ and $\mathrm{Pe} = 200/\sqrt{2}$. The ABPs interact purely repulsively via the Weeks-Chandler-Anderson potential as defined in Eq. (2.8) with strength $\epsilon = 10\,k_\mathrm{B}T_\mathrm{b}$. **e** Sketch of the mechanism leading to MIPS. A self-trapped configuration (top) can be resolved after a typical time τ_p, after which the orientation changes due to rotational diffusion. Yellow arrows denote the self-propulsion direction.

positive feedback: First, active particles tend to accumulate in regions where their directed motion is restricted. On coarse-grained scales, they move more slowly within these regions. Second, active particles move more slowly on coarse-grained scales where the local particle density is large. Accordingly, a positive feedback between the accumulation, which is induced by slowly moving particles, and the accumulation-induced slowdown finally leads to MIPS.[83,259]

In the overdamped limit, it has been shown that on coarse-grained scales, MIPS can be mapped onto equilibrium liquid-gas phase separation in passive particles with attractive interactions.[83,110,374] Correspondingly, the length scale $L(t)$ of clusters coarsens in time as $L(t) \propto t^{1/3}$ similar to a passive phase-separating system undergoing diffusive coarsening.[83] In contrast, when we consider inertial active particles, the system also undergoes MIPS, but the coarsening process is slower. In particular, it follows $L(t) \propto t^{1/5}$.[103] Additionally, the dense and the dilute phase feature different kinetic temperatures (defined as the mean kinetic energy per particle; Fig. 2.12b). This kinetic temperature difference persists even in the steady state, which would not be possible in equilibrium systems.[103,119,123] As a consequence, systems of inertial active particles cannot be mapped on an effective equilibrium system on coarse-grained scales.[103]

To explain the emergence of the kinetic temperature difference between the dense and the dilute phase, we have to understand what happens when two active particles collide. In the overdamped limit, the two particles block each other and their directed motion stops immediately (Fig. 2.12c). The blocked configuration is resolved after a typical time τ_p, after which the particles change their self-propulsion direction due to rotational diffusion. However, their instantaneous speed is still dominated by the self-propulsion

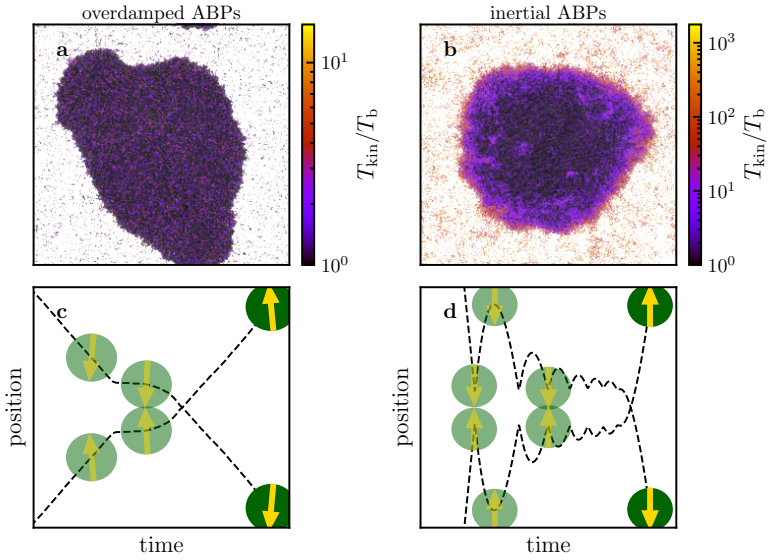

Fig. 2.12 Motility-induced temperature difference. Snapshots of BD simulations of ABPs **a** in the overdamped limit ($m/(\gamma_{\mathrm{t}}\tau_{\mathrm{p}}) = 5 \times 10^{-5}$) and **b** with $m/(\gamma_{\mathrm{t}}\tau_{\mathrm{p}}) = 5 \times 10^{-2}$ at $\mathrm{Pe} = 200/\sqrt{2}$. The colors denote the kinetic temperature $k_{\mathrm{B}}T_{\mathrm{kin}} = 0.5m\langle v^2\rangle$ of the particles. **c** Sketch of a collision between two repulsively interacting overdamped ABPs moving towards each other along the x direction in two spatial dimensions. The visualized trajectories (black dashed lines) show their position in x direction over time. The frontally colliding overdamped ABPs stay almost touching but maintaining an instantaneous speed of v_0 until they reorient due to rotational diffusion after a time τ_{p}. Then, they glide past each other. **d** Same sketch as in panel c but for two repulsively interacting inertial ABPs. The particles bounce back multiple times and do not reach their self-propulsion speed v_0 anymore before they reorient and glide past each other. Accordingly, they slow down. Yellow arrows denote the direction of the self-propulsion velocity.

speed v_0. Consequently, even though the particles in the cluster are densely packed, both the dense and the dilute phase have the same kinetic temperature. In contrast, inertial active particles bounce back elastically when they collide (Fig. 2.12d). After each collision, they move back against their self-propulsion force to a turning point at a decreased distance. From this turning point, they accelerate again until they touch each other again, but they have less space to accelerate. Consequently, the particles are not able to reach their self-propulsion speed v_0 anymore unless they reorient due to rotational diffusion and move away from each other. In the dilute phase, collisions are rare and the particles can reach their self-propulsion speed v_0 between two subsequent collisions. In the dense phase, frequent collisions slow down the particles. Especially, when an inertial active particle enters the dense phase, it slows down due to successive collisions with other particles. Accordingly, the self-propulsion power is significantly smaller in the dense phase compared to the dilute phase.[103] This leads to the kinetic temperature difference between the two phases. The temperature difference is maintained by the continuous energy conversion of the active particles that leads to their self propulsion.

3 Active Matter Evaluation Package

Fig. 3.1 Active Matter Evaluation Package (AMEP) logo.

To gain detailed insights into the dynamics and the structure of systems simulated using particle-based or continuum simulations as described in the previous chapter, various observables can be calculated from simulation data to gain insights into dynamical and structural properties of the investigated system. Examples especially relevant for active matter systems range from the mean-square displacement and the structure factor to cluster-size distributions, binder cumulants, and growth exponents. To analyze the simulation data used in this PhD thesis and to provide a powerful and simple interface for calculating and visualizing a broad variety of observables that are relevant to active matter systems, we created the Active Matter Evaluation Package (AMEP; Fig. 3.1), which is a Python library for analyzing simulation data of particle-based and continuum simulations. AMEP is written in pure Python and it is based on powerful libraries such as NumPy,[375,376] SciPy,[377] Matplotlib,[378] and scikit-image.[379] It provides the first unified framework for handling both particle-based and continuum simulation data and therefore, it can also be used to analyze simulations that combine particle-based and continuum techniques such as used to study the motion of bacteria in chemical fields or for modeling particle motion in a flow field for example.

This chapter gives an overview about the design and the features of AMEP and defines the observables used in this PhD thesis. The code examples are based on AMEP version 1.0.0. The content of this chapter is taken from my publication "AMEP: The Active Matter Evaluation Package for Python" published as a preprint on *arXiv* (2024),[380] and the majority of this chapter is taken verbatim from it. For this publication, I wrote the majority of the first version of the software, created most of the simulation data, contributed to acquiring funding for computational resources, coordinated and managed the data analysis, and wrote the original draft with input from all co-authors.

3.1 Introduction

Computer simulations are a powerful method to investigate and understand the physical properties of soft matter and biological systems. In particular, molecular dynamics (MD) simulations stand out as an indispensable tool to determine the microscopic dynamics and structural properties of molecular systems comprising bio-molecules,[381–383] polymer electrolytes,[384–386] liquid crystals,[387–389] or confined liquids for example.[390–393] These

systems exhibit notable relevance in both industrial and medical applications.[394–396] Expanding beyond atomistic and systematically coarse-grained MD simulations involving suitable force fields, Brownian dynamics (BD) simulations have extensively been used over the past two decades especially also for modeling active matter systems. In such systems, the individual constituents consume energy from their environment and use it to self propel and navigate through complex surroundings.[21,397] Examples of active matter systems can be observed across scales from microscopic entities such as bacteria, algae, and synthetic microswimmers[4,59,74,179–185] to fishes, birds, drones, and human crowds on the macroscale.[12,14,15,17,19,34,186–188] These out-of-equilibrium systems exhibit striking collective phenomena such as phase separation (where the system selects a density),[53,54,72,83,85,86,152,201–203] non-equilibrium pattern formation (where the system selects a length scale),[112,196,204–208] or other ordering transitions such as flocking showing (long-range) orientational ordering.[16,120,187,209]

To effectively model active matter systems, different computational approaches provide distinct advantages.[76,77] Particle-based models such as the active Brownian particle (ABP) model as introduced in Eqs. (2.2) and (2.3),[249] solved numerically using BD simulations for example, have proven valuable for investigating collective phenomena such as motility-induced phase separation (MIPS; cf. Sec. 2.3)[72,83,103,110,165,259,374,398–405] as well as the dynamics and local order of the involved individual particles.[4,142,143,146,162,250,406–408] Conversely, continuum models such as the active model B+ (Eq. (2.15))[300] enable us to understand collective phenomena over larger length and time scales by studying the evolution of particle densities.[97,112,120,207,292,300,374,409–411] Therefore, it is a common approach to start from a particle-based model and subsequently derive a continuum model via coarse-graining techniques.[66,90,205,209,259,293,302,305,412–414] Moreover, the integration of particle-based and continuum models has emerged as a promising approach,[68,74,75,204,294,415–417] especially for scenarios such as modeling the interaction of active particles with a surrounding fluid or another medium that is quasi-continuous on the scale of the considered particles, as exemplified by the motion of bacteria or synthetic Janus colloids in a self-produced concentration field.[75,294–296,416–418] These approaches are also particularly important for modeling artificial microswimmers such as active colloids in the presence of chemical fields,[65,78] exhibiting phenomena such as chemotaxis.[79,410,417,419]

To gain physical insights from the data resulting from numerical solutions, a comprehensive array of analysis techniques is required. The mean-square displacement and time correlation functions such as the orientational autocorrelation function are popular observables to achieve insights into the dynamical aspects,[133,143,148,158,420–426] while spatial correlation functions such as the radial/pair distribution function and the structure factor are frequently considered to provide information about spatial structures.[203,427–430] Other observables such as entropy production and kinetic temperature are also considered frequently to analyze the collective behavior of the system under investigation,[24,103,125,144,162,163,165,166,252,431–441] and together with statistical analysis tools such as binder cumulants used in finite size scaling analyses[72,442–445] and cluster analyses including cluster growth exponents,[55,103,146,152,291,293,299,446] these observables allow us to characterize the non-equilibrium phase diagram and critical dynamics of active matter systems. Additionally, local order analyses such as local density and bond orientational order parameters offer insights into the system's local structure

and symmetries.[72,110,250,398,447–450] While existing analysis packages such as freud,[451] MDAnalysis,[452,453] VMD,[454] MDTraj,[455] Ovito,[456] Pytim,[457] LOOS,[458,459] and MMTK[460] offer the possibility to calculate such observables, they are mostly inspired by and optimized for the MD simulation community and fall short in capturing all relevant observables for active matter systems in a single package. Additionally, they lack the possibility to handle continuum simulation data. Therefore, a new library is required that (i) consolidates the essential observables needed to analyze active matter simulation data, (ii) provides a unified platform for analyzing both particle-based and continuum simulation data, and (iii) seamlessly integrates data formats widely-used in computational physics through an application programming interface (API).

In this chapter, we introduce the Active Matter Evaluation Package (AMEP), a unified framework for analyzing MD simulation, BD simulation, and continuum simulation data with a specific focus on soft and active matter systems. AMEP provides an optimized framework for loading, storing, and evaluating simulation data based on particle trajectories and the time evolution of continuum fields. This framework is based on an optimized HDF5 file format[461,462] which is optimal for long-term storage purposes and for handling data of large-scale simulations.[462–464] Computationally expensive methods are parallelized and AMEP selectively loads only the data into the main memory which is necessary for the current computational step. This ensures efficient operation on high-performance computing architectures, workstations, and laptops. AMEP is written in pure Python and provides a user-friendly, easy-to-learn Python API that interfaces with common tools used in computational physics via NumPy arrays.[375,376] Based on common Python libraries such as NumPy,[375,376] SciPy,[377] Matplotlib,[378] and scikit-image,[379] AMEP provides a powerful toolbox for calculating spatial and temporal correlation functions, visualizing and animating simulation results, and coarse-graining particle-based simulations, which makes it possible to easily analyze the dynamics and structure of both particle-based and continuum simulation data.

This chapter is organized as follows: We first demonstrate a minimal example on how to use AMEP to load, analyze, and visualize simulation data in Sec. 3.2. Second, we give a brief overview on the structure and design of AMEP in Sec. 3.3. Finally, in Secs. 3.4 and 3.5, we apply a selection of analysis functions provided by AMEP to particle-based simulations of the ABP model and to continuum simulations of the active model B+, respectively, and briefly discuss the results.

3.2 How to use AMEP

AMEP is designed with a user-focused mindset to simplify the access to simulation data within a few lines of Python code. Before discussing the general design of AMEP and various examples on how to apply it to particle-based and continuum simulation data, we will demonstrate its general usage with a minimal example. For a quick start with AMEP, we recommend downloading the demo files at https://github.com/amepproject/amep/tree/main/examples and to run them part by part while reading this section.

3.2.1 Installing AMEP

AMEP is a Python library that requires Python 3.10 or higher. To use AMEP, we recommend installing Python via Anaconda[a]. If Anaconda is installed, one can create a new environment, activate it, and install AMEP through the terminal (Linux/macOS) or the Anaconda Prompt (Windows):

```
conda create -n amepenv python=3.10
conda activate amepenv
conda install conda-forge::amep
```

Alternatively, AMEP can also be installed via `pip install amep`. Now, one can start the Python interpreter to import and use AMEP:

```
python
>>> import amep
>>>
```

Alternatively, we recommend to use Jupyter notebooks.[b]

3.2.2 Analyzing simulation data using AMEP

Now, we use AMEP to calculate the mean-square displacement (MSD), the diffusion coefficient, and the orientation autocorrelation function (OACF) of a single ABP and the radial distribution function (RDF) of multiple interacting ABPs using the ABP model as introduced in Subsec. 2.2.1 and solved numerically using LAMMPS.[255] At the end of this section, we visualize the results in a combined plot. Exemplary code and data of the relevant BD simulations is available at https://github.com/amepproject/amep/tree/main/examples.

First, we import AMEP and load the simulation data of non-interacting overdamped ABPs:

```
import amep
traj_nonint = amep.load.traj(
    "/path/to/non_interacting_ABPs",
    mode = "lammps"
)
```

The function amep.load.traj creates an HDF5 file (`traj.h5amep`) in the background that contains all the simulation data and returns a ParticleTrajectory object which allows to easily access the data for further processing. Since the data has been produced using LAMMPS,[255] we load it using mode = *"lammps"*. To save useful information for long-term storage, we add the author to the trajectory object, which will save this information within the linked HDF5 file:

```
traj_nonint.add_author_info(
    "Lukas Hecht",
    "affiliation",
    "Technical University of Darmstadt"
```

[a] See https://docs.anaconda.com/free/anaconda/install/index.html for instructions on how to install Anaconda.

[b] For more information about Jupyter notebooks, see https://jupyter.org/.

```
)
traj_nonint.add_author_info(
    "Lukas Hecht",
    "email",
    "lukas.hecht@pkm.tu-darmstadt.de"
)
```

This information can be accessed by calling traj_nonint.get_author_info("Lukas Hecht"), returning

```
{'affiliation': 'Technical University of Darmstadt',
 'email': 'lukas.hecht@pkm.tu-darmstadt.de'}
```

while traj_nonint.authors returns a list of all authors. AMEP provides several methods to add more information to trajectory objects (ParticleTrajectory or FieldTrajectory) such as software information, simulation scripts, log files, or simulation parameters for a comprehensive and reproducible set of information about the simulation (see online documentation available at https://amepproject.de and Fig. 3.2).

Next, we calculate the MSD, which is defined as

$$\mathrm{MSD}(t) = \frac{1}{N}\sum_{i=1}^{N}\left[\mathbf{r}_i(t) - \mathbf{r}_i(0)\right]^2, \tag{3.1}$$

where $\mathbf{r}_i(0)$, $\mathbf{r}_i(t)$ denote the position of particle i at time 0 and $t \geq 0$, respectively. For a single overdamped ABP, it can be shown analytically that the MSD can be written as (cf. Eq. (2.7))

$$\begin{aligned}\mathrm{MSD}(t) &= 2l_p^2\left(\frac{t}{\tau_p} - 1 + e^{-t/\tau_p}\right) + 4D_\mathrm{t}t \\ &\xrightarrow{t\gg\tau_p} 4D_\mathrm{eff}t\end{aligned} \tag{3.2}$$

with effective diffusion coefficient $D_\mathrm{eff} = D_\mathrm{t} + l_\mathrm{p}^2/(2\tau_\mathrm{p})$.[77,181,253] Here, $\tau_\mathrm{p} = 1/D_\mathrm{r}$ denotes the persistence time, which signifies the time after which the directed motion of an ABP is randomized due to rotational diffusion, and $l_\mathrm{p} = v_0\tau_\mathrm{p}$ denotes the persistence length, which is the distance an ABP moves on average before its direction of motion is randomized. $D_\mathrm{t} = k_\mathrm{B}T_\mathrm{b}/\gamma_\mathrm{t}$ and $D_\mathrm{r} = k_\mathrm{B}T_\mathrm{b}/\gamma_\mathrm{r}$ are the translational and rotational diffusion coefficients, respectively, and v_0 is the self-propulsion speed of the ABP. To calculate the MSD with AMEP, we create a MSD object via

```
msd = amep.evaluate.MSD(
    traj_nonint
)
```

which calculates the MSD for all frames and performs the average over all particles. The MSD object contains all information about the MSD, and we can access the times via msd.times and the value for each individual frame via msd.frames for example. The returned objects are NumPy arrays and can therefore easily be used also elsewhere in Python.

To get the effective diffusion coefficient D_eff from the MSD in the late time limit, we define the fit function f with the fit parameters as keyword arguments and create a corresponding Fit object:

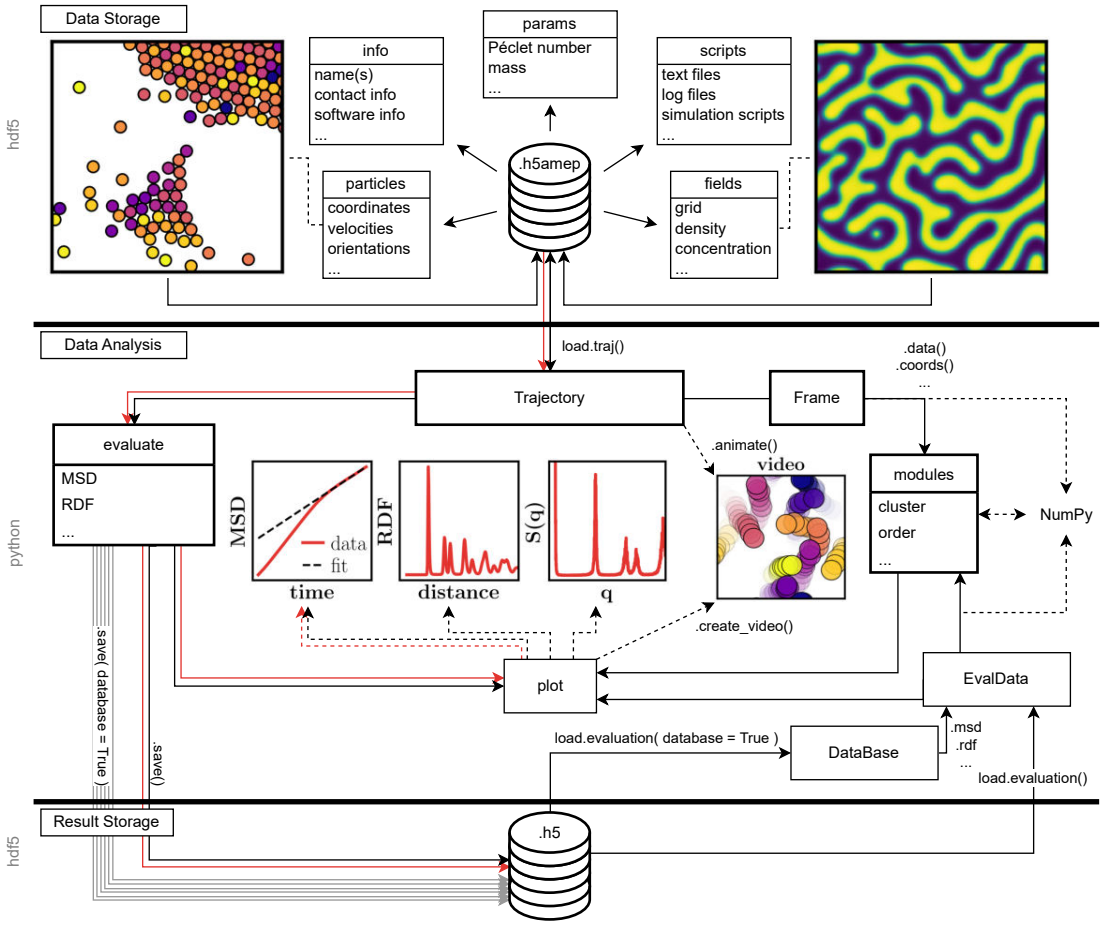

Fig. 3.2 AMEP flow chart: Schematic of the design of AMEP. The first layer "Data Storage" represents the loading and storage of data from particle-based or continuum simulations, which is stored in HDF5 files (`.h5amep`) together with various metadata the user can add. The central part of the Python interface (layer "Data Analysis") is the `Trajectory` object which acts as a list of `Frame` objects and gives access to the data stored in the HDF5 file. The `Trajectory` object can be used with the evaluate classes (module `evaluate`) which give simple access to many observables calculated over whole trajectories. Alternatively, the data can be returned as NumPy array through the `Frame` objects and can be analyzed using the individual AMEP modules, also in combination with self-written Python code to perform additional operations beyond AMEP. The `plot` module allows visualizing analysis results and simulation data in form of figures or videos. Finally, the results can be stored in an HDF5-based data format again (layer "Result Storage"). It is possible to save and load one or more results in one HDF5 file. Later, the results can be imported as `DataBase` (for multiple results) or `EvalData` objects (one result in a file or one result selected from a `DataBase` object). The red arrows follow the path of our first minimal example as discussed in Sec. 3.2. The design itself is explained in more detail in Sec. 3.3.

```
def f(t, D = 1.0):
    return 4*D*t
Dfit = amep.functions.Fit(f)
```

By calling the object's `fit` method, which uses the `scipy.odr` package in the background, with the data to fit and an initial guess (using the `p0` keyword), we obtain the optimal parameters. Here, we only want to fit the long-time behavior, and hence, we only consider data for $t > 10^1 \tau_\mathrm{p}$. The optimal parameters and their errors can then be retrieved from the `Fit` object:

```
mask = msd.times > 1e1
Dfit.fit(
    msd.times[mask],
    msd.frames[mask],
    p0 = [900]
)
print(
    f"D={Dfit.params[0]:0.2f}, "\
    f"D-error={Dfit.errors[0]:0.2f}"
)
```

```
D=885.32, D-error=0.59
```

This is fairly close to the expected value of $D_\mathrm{eff} = 883$ as obtained from Eq. (3.2) for overdamped ABPs with $l_\mathrm{p} = 1.0$, $\tau_\mathrm{p} = 1.0$, $v_0 = 42$, and $D_\mathrm{t} = 1.0$ as used in this example.

Next, we use the same simulation data to calculate and fit the OACF, which is given by

$$\langle \hat{\mathbf{p}}(0) \cdot \hat{\mathbf{p}}(t) \rangle = \frac{1}{N} \sum_{i=1}^{N} \hat{\mathbf{p}}_i(0) \cdot \hat{\mathbf{p}}_i(t) \tag{3.3}$$

and is equal to $e^{-D_\mathrm{r} t}$ for overdamped ABPs.[133] Here, $\hat{\mathbf{p}}_i$ is the orientation vector of the effective self-propulsion force of particle i. Again, by creating the corresponding evaluate and fit objects, we can analyze the OACF in a few lines of Python code. For the correct normalization, we specify the plane in which the OACF is to be calculated with `direction = "xy"`:

```
oacf = amep.evaluate.OACF(
    traj_nonint,
    direction = "xy"
)
def f(t, Dr = 1.0):
    return np.exp(-Dr*t)
Tfit = amep.functions.Fit(f)
Tfit.fit(oacf.times, oacf.frames)
print(
    f"Dr={Tfit.params[0]:0.4f}, "\
    f"Dr-error={Tfit.errors[0]:0.4f}"
)
```

```
Dr=0.9890, Dr-error=0.0021
```

Again, we obtain a value close to the expected one of $D_\mathrm{r} = 1.0$.

Next, we calculate the RDF. For that, we load simulation data of $N = 10^5$ interacting overdamped ABPs moving in a two-dimensional periodic simulation box with a total packing fraction of $\varphi = 0.5$ and create a RDF evaluate object. Note that a corresponding exemplary dataset is available at https://github.com/amepproject/amep/tree/main/examples. Here, we only want to consider frames that are in the steady state. Therefore, we skip the first $90\,\%$ of frames using skip = 0.9. Additionally, we specify the total number of frames to average over (time average) equally spaced in time over the last $90\,\%$ of the trajectory using the nav keyword, which is inherited from the BaseEvaluation class and is short for "number of averages". Due to the large number of particles, it is worth to use multiprocessing, to set a maximum distance until which the RDF is calculated, and to use a large number of bins using the njobs, rmax, and nbins keywords, respectively:

```
traj_int = amep.load.traj(
    "/path/to/interacting_ABPs",
    mode = "lammps"
)
rdf = amep.evaluate.RDF(
    traj_int,
    skip = 0.9,
    nav = 100,
    nbins = 20000,
    rmax = 300,
    njobs = 128
)
```

Before visualizing the results, we save them in HDF5 files. For that, AMEP offers two possibilities: One can store the result of either a single evaluate object (as done for the RDF) or multiple evaluate objects (as done for the MSD and the OACF) in one HDF5 file:

```
msd.save(
    "nonint-results.h5",
    database = True
)
oacf.save(
    "nonint-results.h5",
    database = True
)
rdf.save(
    "rdf.h5"
)
```

These can later be loaded by calling msd = amep.load.evaluation("*nonint-results.h5*", database = True).msd and rdf = amep.load.evaluation("*rdf.h5*") for example. Finally, the data and fits can be visualized with the Matplotlib wrappers provided by AMEP (Fig. 3.3):

```
fig, axs = amep.plot.new(
    (6.5,2), ncols = 3, wspace = 0.1
)
# plot msd
axs[0].plot(
```

```
    msd.times, msd.frames,
    "r-", label = "data"
)
axs[0].plot(
    msd.times, Dfit.generate(msd.times),
    "k--", label = "fit"
)
axs[0].set_xlabel("Time")
axs[0].set_ylabel("MSD")
axs[0].loglog()
axs[0].legend()

# plot oacf
axs[1].plot(
    oacf.times, oacf.frames,
    "r-", label = "data"
)
axs[1].plot(
    oacf.times, Tfit.generate(oacf.times),
    "k--", label = "fit"
)
axs[1].set_xlabel("Time")
axs[1].set_ylabel("OACF")
axs[1].semilogx()
axs[1].axhline(1/np.e, c = "k")
axs[1].axvline(1, c = "k")
axs[1].legend()

# plot rdf
axs[2].plot(rdf.r, rdf.avg, "r-")
axs[2].semilogx()
axs[2].set_xlabel("Distance")
axs[2].set_ylabel("RDF")

# plot boxes
amep.plot.draw_box(
    fig, [0, 0, 0.68, 1.01],
    edgecolor = "tab:blue", linestyle = "--",
    text = "Single ABP", c = "tab:blue"
)
amep.plot.draw_box(
    fig, [0.69, 0, 0.31, 1.01],
    edgecolor = "tab:orange", linestyle = "--",
    text = "Interacting ABPs", c = "tab:orange"
)
# save figure in file
fig.savefig("how_to_use_amep.pdf")
```

The whole workflow of this minimal example is marked with red arrows in the flowchart shown in Fig. 3.2 and its code is available at https://github.com/amepproject/amep/tree/main/examples.

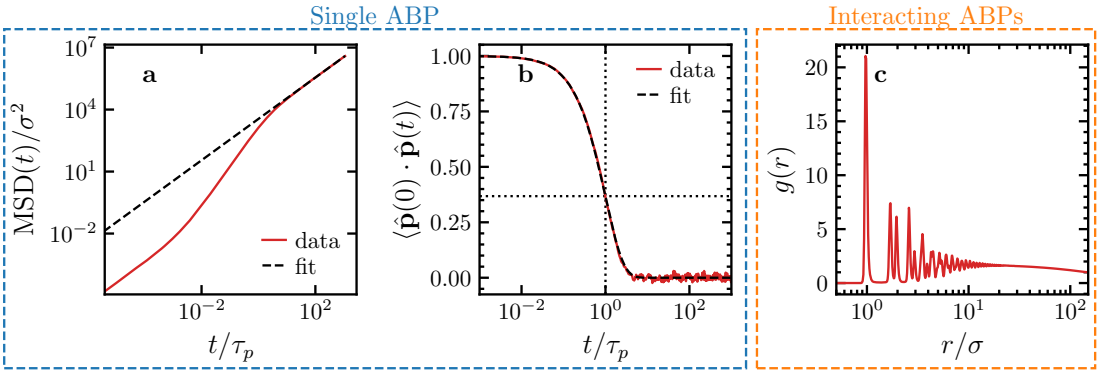

Fig. 3.3 How-to-use-AMEP example. **a** Mean-square displacement of a single overdamped ABP calculated with `amep.evaluate.MSD`. The black dashed line is a fit of Eq. (3.2) done with `amep.functions.Fit`. **b** Orientation autocorrelation function of a single overdamped ABP calculated with `amep.evaluate.OACF`. The black dashed line is a fit of $e^{-D_r t}$ done with `amep.functions.Fit` and the black dotted lines mark the point $(1, 1/e)$. The results in panels a and b are averaged over 4×10^3 particles. **c** Radial pair distribution function of $N = 10^5$ repulsively interacting overdamped ABPs calculated using `amep.evaluate.RDF` and averaged over time in the steady state. The plot has been created using the `amep.plot` module and the corresponding code is available at https://github.com/amepproject/amep/tree/main/examples.

3.3 Design

In the previous section, we introduced a short example of how to use AMEP. We will now give an overview of the design of the AMEP package. A more detailed description can be found in the online documentation available at https://amepproject.de.

3.3.1 Modules

AMEP contains a plethora of pre-implemented functions to analyze particle-based and continuum simulation data. In Tab. 3.1, the modules are listed with a short description and a few exemplary functions. The functions contained in these modules take NumPy arrays and native Python data types as input, and therefore, they can also be used without the data-handling framework provided by AMEP. In addition to the modules shown in Tab. 3.1, AMEP has a `plot` module to visualize simulation data and results as well as an `evaluate` module, which provides various evaluation methods that use a full trajectory as input data. The `plot` and the `evaluate` module will be described in more detail below.

3.3.2 Visualization

For visualizing simulation data and analysis results, AMEP provides the `plot` module, which is a wrapper for the Matplotlib library.[378] The `plot` module includes functions to plot particles and continuum fields (cf. Figs. 3.4 and 3.9), to create insets and colorbars (cf. Fig. 3.4), and to animate plots and simulation data. For example, a video of a trajectory `traj` can be created via `traj.animate("video.mp4")`. By varying the file extension, also other data formats can be used such as GIFs (Graphics Interchange Formats). Additionally, the

Tab. 3.1 Module overview. The shown AMEP modules take NumPy arrays and native Python data types as input. The description of each module is complemented with a few exemplary functions (italic text). AMEP additionally provides the modules `plot` and `evaluate` as described in Sec. 3.3. A detailed description of all modules and the contained functions can be found in the AMEP online documentation available at https://amepproject.de.

Module:	Description:
`cluster`	cluster identification and properties *identify clusters (particles)* *radius of gyration*
`continuum`	field data analysis and coarse-graining *identify clusters (fields)* *create field from particles*
`functions`	mathematical functions and fitting *Gaussian* *general fit class*
`order`	functions to characterize spatial order *local density* *k-atic bond order parameter*
`pbc`	handling of periodic boundary conditions *create periodic images* *fold coordinates back into the box*
`spatialcor`	spatial correlation functions *radial distribution function* *isotropic structure factor*
`statistics`	methods for statistical analysis *binder cumulant* *distribution (histograms) 1d, 2d*
`thermo`	thermodynamic observables *kinetic temperature* *kinetic energy*
`timecor`	time correlation functions *mean squared distance* *autocorrelation function*
`utils`	utility methods *averaging methods (running mean, ...)* *Fourier transform*

plot module provides useful functions to format the axis of a figure. All visualization functions are optimized to create figures and videos that can be directly used for a publication in various journals. Most figures within this thesis are created with AMEP.

3.3.3 Evaluate module

We already introduced the different modules of AMEP, which contain a plethora of functions relevant for the analysis of active matter simulation data. The evaluate module is a special module in the sense that it uses functions from all other modules to calculate certain observables for a whole trajectory. In our first example in Sec. 3.2, we already used the MSD, OACF, and RDF classes, which are part of the evaluate module. We will now

introduce the concept of these classes, which will be referred to as “evaluate classes” in the following.

While the functions of the modules discussed above take NumPy arrays as input data, evaluate classes take a whole trajectory as an input. One example is the amep.evaluate.RDF class used in Sec. 3.2. To initialize an object of an evaluate class, the trajectory as well as certain parameters are supplied. The evaluate classes offer the functionality to average over multiple frames automatically (the keyword nav, which is an abbreviation for “number of averages”, allows specifying the number of frames to average over) as well as to skip a certain amount of frames at the beginning of the trajectory (in percent) by specifying the skip keyword. The resulting data can be returned as NumPy arrays. Furthermore, one or more evaluate objects can be stored in HDF5 files using their .save("*filename.h5*") method and can be read again with amep.load.evaluation("*filename.h5*"). The evaluate classes are a crucial part in the user-focused design of AMEP and make it possible to achieve results within a few lines of code.

3.3.4 File format

Based on the Hierarchical Data Format version 5 (HDF5),[461,462] AMEP introduces a new file format `h5amep` to store simulation data and additional metadata. This format is used in the backend of AMEP. The HDF5 files are structured into groups and datasets. The `h5amep` format has the following groups, subgroups, and attributes:

```
h5amep root
\amep
\info
    \authors
    \software
\scripts
\params
\type
\particles or \fields
\frames
    \steps
    \times
    \[frame0]
        \coords
        \velocities
        \...
    \[frame1]
        \...
    \...
```

The group `amep` contains information about the AMEP version that has been used to create the `h5amep` file. The group `info` contains the saved information about authors (cf. Sec. 3.2) and software. The `scripts` group gives the possibility to save text files such as simulation scripts and log files that correspond to the simulation data. In the `params` group, AMEP stores parameters such as the simulation timestep for example. Additional simulation parameters can be added. The attribute `type` contains a flag about the type of data stored in the `h5amep` file. This can be either "*particle*" or "*field*". The groups

`particles` and `fields` contain user-defined information about the particles and the fields used in the simulation, respectively. Finally, the group `frames` contains multiple datasets and subgroups with the simulation data. The dataset `steps` stores a list of all the frame numbers (i.e., the number of timesteps for each frame) and the dataset `times` the corresponding (physical) time, while the individual frames of the simulation are stored in subgroups of `frames` named by their simulation step. Within an individual frame, the simulation data is stored, e.g., coordinates and velocities for particle-based simulations or density and concentrations for continuum simulations, as separate datasets.

3.3.5 Trajectories and frames

The `h5amep` file is connected to Python via the amep.load module with which the simulation data is imported to a ParticleTrajectory or FieldTrajectory object. Saved evaluation objects can also be imported with the amep.load module. Because a ParticleTrajectory or FieldTrajectory object works as a reader for the `h5amep` file, the simulation data (coordinates, velocities, density, concentration,...) is not stored in the main memory all the time but only the portion that is requested for the specific analysis. The simulation data can be accessed via BaseFrame or BaseField objects for particle-based and continuum data, respectively, which will be referred to as "frame" in the following. Technically, the ParticleTrajectory or FieldTrajectory object acts as a list of frames, i.e., frame = traj[0] returns the first frame of the trajectory traj. The data of one frame can be accessed through various methods. For example, the coordinates and velocities of particles can be accessed via frame.coords() and frame. velocities (). Other data can be accessed via the frame.data method, e.g., frame.data("*mass*") returns the mass of each particle and frame.data("*rho*") the density field of a continuum simulation. A list of all available keys can be accessed via frame.keys. All these methods return NumPy arrays for efficient calculations and simple integrity to other Python packages (see also Fig. 3.2).

3.4 Analyzing particle-based simulation data with AMEP

We will now use AMEP to analyze simulation data of large-scale simulations of ABPs. After introducing the simulation details, we demonstrate how to calculate certain observables using AMEP and briefly discuss the results. The code examples demonstrate the workflow of AMEP and serve as a guide for using AMEP. Further observables that are available in AMEP but which are not discussed in this section are exemplarily shown in Fig. 3.12.

3.4.1 Brownian dynamics simulations of active Brownian particles

As a first detailed example, we analyze particle-based simulation data obtained with the active Brownian particle (ABP) model as introduced in Subsec. 2.2.1 as Eqs. (2.2) and (2.3). The repulsive interaction is modeled by the Weeks-Chandler-Anderson (WCA) potential (Eq. (2.8)).[256] For the simulations here, we have chosen a persistence length $l_\mathrm{p} = 100\,\sigma$, repulsion strength $\epsilon/(k_\mathrm{B}T_\mathrm{b}) = 1.0$, and for simplicity, $\gamma_\mathrm{t} = \gamma_\mathrm{r}/\sigma^2$ unless otherwise stated (note that in experiments of active granulates, the Stokes-Einstein relation does not apply).[157] We define the Péclet number as $\mathrm{Pe} = v_0/\sqrt{2D_\mathrm{t}D_\mathrm{r}}$, which

quantifies the strength of self-propulsion relative to diffusive motion. Here, $D_\mathrm{t} = k_\mathrm{B}T_\mathrm{b}/\gamma_\mathrm{t}$ and $D_\mathrm{r} = k_\mathrm{B}T_\mathrm{b}/\gamma_\mathrm{r}$ are the translational and rotational diffusion coefficients, respectively. Note that all simulations are done in the overdamped regime, i.e., we choose a small mass $m/(\gamma_\mathrm{t}\tau_\mathrm{p}) = 5 \times 10^{-5}$. Since it has been found in previous works that the influence of the moment of inertia I on the simulation results is rather unimportant,[103] it is held constant at $I/(\gamma_\mathrm{r}\tau_\mathrm{p}) = 0.33$ unless otherwise stated. All simulations are done within a two-dimensional quadratic box of length L with periodic boundary conditions and up to $N = 1.28 \times 10^6$ particles with a time step of $\Delta t/\tau_\mathrm{p} = 10^{-5}$–$10^{-6}$ using LAMMPS.[255] We choose $\mathrm{Pe} = 70.7$ and a packing fraction of $\varphi = 0.5$ with $\varphi = N\pi\sigma^2/(4L^2)$ and start each simulation from uniformly distributed particle positions unless otherwise stated.

AMEP can load the common LAMMPS plain text format in which LAMMPS stores one snapshot of the simulation per text file named as `dump*.txt` for example, where the `*` is a placeholder for the current time step. These files are formatted as follows:

```
ITEM: TIMESTEP
20000
ITEM: NUMBER OF ATOMS
1280000
ITEM: BOX BOUNDS pp pp pp
0.0000000000000000e+00 1.5000000000000000e+03
0.0000000000000000e+00 1.5000000000000000e+03
-5.0000000000000000e-01 5.0000000000000000e-01
ITEM: ATOMS id type x y z fx fy mux muy radius mass
1 1 26.206 44.939 0 95.5607 9.87064 0.99913 0.04168 0.5 0.00005
2 1 45.187 24.985 0 -94.141 -33.726 -0.9414 -0.3373 0.5 0.00005
3 1 53.126 32.953 0 -86.024 12.4595 -0.9831 0.18303 0.5 0.00005
...
```

Here, `id` denotes a unique identifier for each particle, `type` denotes the particle type, `x,y,z` denote the position of each particle, `fx,fy` denote the forces acting on each particle, `mux,muy` are the components of the orientation vector $\hat{\mathbf{p}}$, `radius` denotes the radius $\sigma/2$ of each particle, and `mass` their mass m. Note that `z` is zero for all particles because the simulation is done in two spatial dimensions. An exemplary dataset is available at https://github.com/amepproject/amep/tree/main/examples. AMEP reads all data from each text file and converts it into the `h5amep` format. Each item from the `ATOMS` section in the LAMMPS text file can then be accessed with the `.data()` method of the corresponding `BaseFrame` object, e.g., the force in x direction of frame 5 can be returned as NumPy array by calling

```
import amep
traj = amep.load.traj(
    "/path/to/data",
    mode = "lammps"
)
fx = traj[5].data("fx")
```

For many standard quantities such as coordinates, forces, or velocities, AMEP provides further commands exemplarily shown below:[c]

[c] See online documentation at https://amepproject.de for further details.

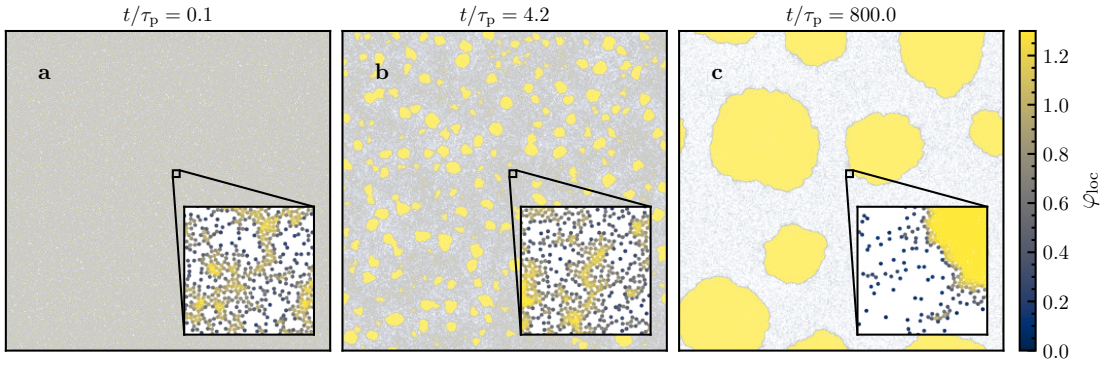

Fig. 3.4 Plotting snapshots with `amep.plot.particles`. a–c Snapshots of ABPs undergoing MIPS starting from a uniform distribution for three different times as given in the key. The particles are colored with respect to their local area fraction φ_loc as obtained from a Voronoi tesselation calculated using `amep.order.voronoi_density` (see Subsec. 3.4.3 for further details). The insets show the indicated extract of the simulation box and have been plotted using `amep.plot.add_inset`. Parameters: $m/(\gamma_\mathrm{t}\tau_\mathrm{p}) = 5 \times 10^{-5}$, $I/(\gamma_\mathrm{r}\tau_\mathrm{p}) = 0.33$, $N = 1.28 \times 10^6$, $\varphi = 0.5$, $\mathrm{Pe} = 70.7$.

```
coords = traj[5].coords()
forces = traj[5].forces()
mu = traj[5].data("mux", "muy")
```

3.4.2 Motility-induced phase separation

For large enough packing fraction φ and large enough Péclet number Pe, ABPs can phase separate into a dense and a dilute phase. This phenomenon is well-known as motility-induced phase separation (MIPS; cf. Sec. 2.3)[72,83,103,110,259,374,398–401,465] and can be understood as follows: If two ABPs collide, they can block each other due to their effective self-propulsion force. The collision can be resolved if the ABPs reorient their self-propulsion direction due to rotational diffusion and the self-propulsion direction of one ABP deviates from the other (cf. Fig. 2.11). Small clusters can form if more ABPs collide with the two ABPs blocking each other. Roughly, if now the mean time τ_c between collisions is smaller than the mean time τ_p a particle randomly reorients its self-propulsion direction, small clusters tend to grow, which finally results in a phase separation where an active gas coexists with a dense liquid.[83,86,99,204] This process is exemplarily visualized by the snapshots shown in Fig. 3.4, which have been created using the amep.plot.particles function. In the following, we will mainly focus on the analysis of the simulation visualized in Fig. 3.4.

3.4.3 Voronoi diagrams and local order

Whether a simulation undergoes MIPS can be quantified by calculating the distribution of the local density or local area fraction, which is unimodal in the uniform regime and becomes bimodal in the MIPS regime.[71,72,152,398] AMEP provides multiple functions

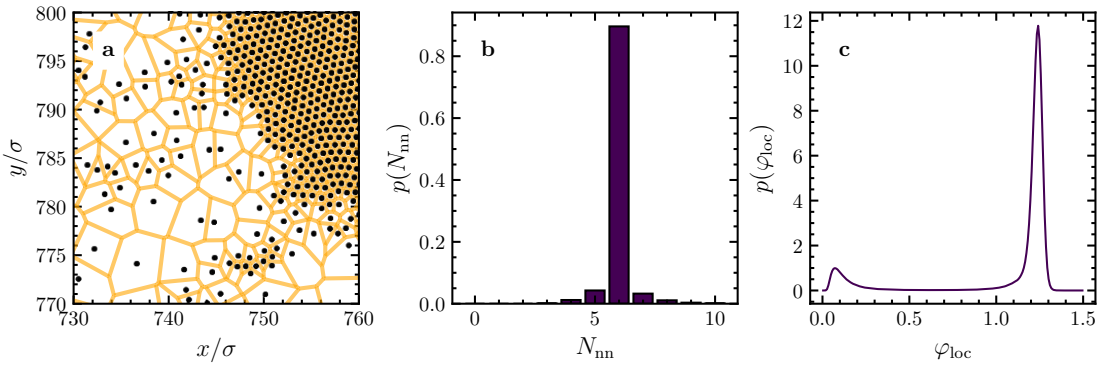

Fig. 3.5 Analyzing local order with the `amep.order` and `amep.evaluate` modules. **a** Same extract of the simulation box as shown in the inset of Fig. 3.4c now with the corresponding Voronoi diagram obtained from `amep.order.voronoi` and plotted with `amep.plot.voronoi`. The black circles denote the particle positions, the orange lines the border of each Voronoi cell. **b** Distribution of the number of next neighbors obtained from the Voronoi diagram using `amep.order.next_neighbors` and `amep.statistics.distribution`. **c** Distribution of the local area fraction obtained from the areas of the Voronoi cells using `amep.evaluate.LDdist`. The results in panels b and c are averaged over five independent ensembles as exemplary demonstrated in the code examples in Subsec. 3.4.3. Parameters are the same as in Fig. 3.4.

to calculate the local density or area fraction: amep.order.local_number_density, amep.order.local_mass_density, and amep.order.local_packing_fraction determine the local number density, mass density, and area/volume fraction, respectively, from averages over circles of radius R, which can be written as

$$\varphi_{\mathrm{loc}}(\mathbf{r}_i) = \sum_{j=1}^{N} \frac{\sigma_j^2 \mathrm{H}(R - |\mathbf{r}_i - \mathbf{r}_j|)}{4R^2} \tag{3.4}$$

in case of the local area fraction. Here, H is the Heaviside step function and σ_j is the diameter of particle j. Alternatively, amep.order.voronoi_density calculates the local mass density, number density, or area/volume fraction based on a Voronoi tesselation. Here, we will use the latter for calculating the distribution of (i) the local area fraction and (ii) the number of next neighbors.

The Voronoi diagram serves as a method for modeling the structures of materials across various disciplines, including crystallography, ecology, astronomy, epidemiology, geophysics, computer graphics, and more.[466–470] In essence, when given a set of points in the plane, the Voronoi diagram divides the plane based on the nearest neighbor rule, associating each point with the region of the plane closest to it. The mathematical definition extends to N-dimensions, often referred to as Voronoi tessellation.[471,472] For a set of finite points $P = \{p_1, p_2, \cdots, p_n\}$ in a subspace Λ in the Euclidean space, the Voronoi cell is formed through the division of the plane into regions, where each region encompasses all points that are closer to each p_i. Points equidistant from at least two points in set P are not part of the Voronoi cell. Instead, they constitute the Voronoi edges. The compilation of all Voronoi cells forms the Voronoi tessellation associated with Λ.

The Voronoi tesselation is included in the order module of AMEP as function amep.order.voronoi. It calculates the Voronoi diagram for a given set of particle coordinates using the scipy.spatial.Voronoi class of the SciPy package.[377] Here, we use the Voronoi tesselation to calculate the number of next neighbors and the local area fraction. Let us first calculate the Voronoi diagram of the last frame (traj[−1]) via

```
import amep
# load the simulation data
traj = amep.load.traj(
    "/path/to/data",
    mode = "lammps"
)
# calculate the Voronoi diagram
vor, ids = amep.order.voronoi(
    traj[-1].coords(),
    traj[-1].box,
    pbc = True
)
```

The obtained Voronoi diagram is demonstrated in Fig. 3.5a for the simulation snapshot shown in Fig. 3.4c. It can be easily visualized using amep.plot.voronoi. Next, we calculate the number of next neighbors from the Voronoi diagram and its distribution via

```
# number of next neighbors for each particle
nnn, _, _, _, _ = amep.order.next_neighbors(
    traj[-1].coords(),
    traj[-1].box,
    vor = vor,
    ids = ids,
    pbc = True
)
# distribution of the number of next neighbors
nndist, bins = amep.statistics.distribution(
    nnn
)
```

As we can see in Fig. 3.5b, the distribution of the number of next neighbors attains its highest point at $N_{\mathrm{nn}} = 6$. This observation indicates the existence of a hexagonal structure within the dense phase, as we will discuss in more detail below. Finally, we calculate the local area fraction using the Voronoi areas and evaluate its distribution:

```
# local area fraction of each particle
ld = amep.order.voronoi_density(
    traj[-1].coords(),
    traj[-1].box,
    radius = traj[-1].radius(),
    mode = "packing",
    vor = vor,
    ids = ids
)
# distribution of the local area fraction
lddist, bins = amep.statistics.distribution(ld)
```

If one would like to calculate the distribution of the local area fraction averaged over several frames of a trajectory, i.e., using a time average, one can simply create an amep.evaluate.LDdist object which is directly performing the time average and allows us to store the results in an HDF5 file. Additionally, multiple results can be stored in the same HDF5 file using AMEP's database feature: As an example, we calculate the distribution of the local area fraction for five independent simulation runs (ensembles) stored in directories `/path/to/data/do00`–`/path/to/data/do04` and store them together in one HDF5 file `ld.h5`:

```
import amep
# load all trajectories
trjs = [
    amep.load.traj(
        f"/path/to/data/do{i:02}",
        mode = "lammps"
    ) for i in range(5)
]
for i,traj in enumerate(trjs):
    # distribution of the local area fraction
    ld = amep.evaluate.LDdist(
        traj,
        nav = traj.nframes,
        use_voronoi = True,
        mode = "packing"
    )
    # set name under which the data
    # is stored in the HDF5 file
    ld.name = f"do{i:02}"

    # save all in file ld.h5
    ld.save("ld.h5", database = True)
```

Now, we can calculate the ensemble average:

```
# load the analysis results
lds = amep.load.evaluation(
    "ld.h5", database = True
)
# ensemble average
ensavg = 0.0
for i in range(5):
    ensavg += lds[f"do{i:02}"].avg/5
```

The ensemble-averaged result is shown in Fig. 3.5c. As expected, the distribution of the local area fraction shows two peaks indicating that the system is phase-separated into a dense and a dilute phase. Note that the high-density peak is located at $\varphi_{\mathrm{loc}} > 1.0$ due to the softness of the particles.

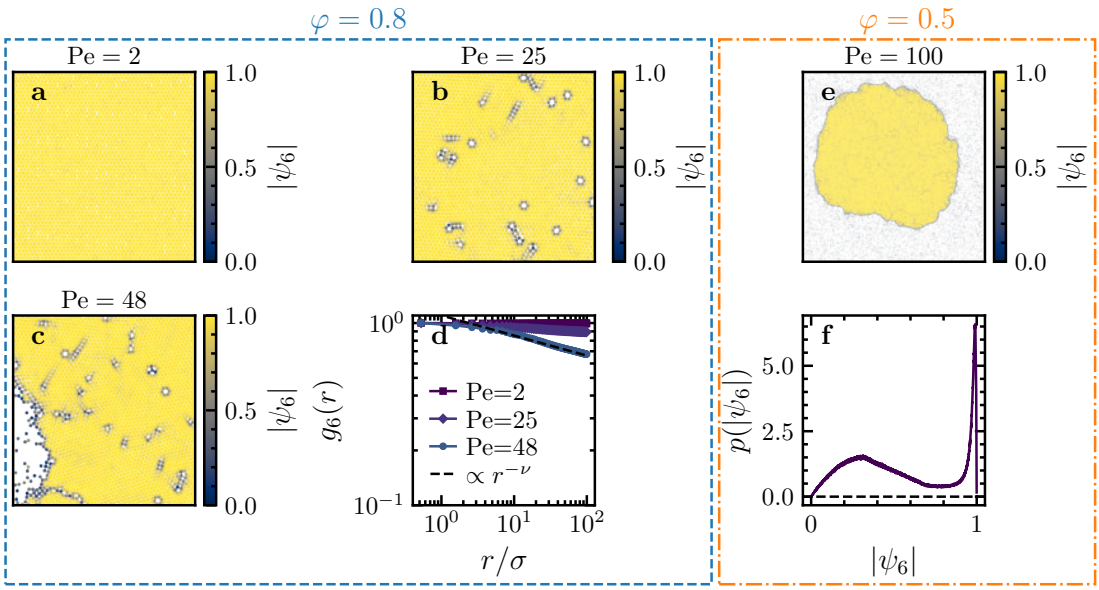

Fig. 3.6 Analyzing the hexagonal order using the `amep.order`, `amep.spatialcor`, and `amep.evaluate` modules. a–c Extracts from the simulation box of an ABP system at high area fraction $\varphi = 0.8$ for Pe $= 2, 25, 48$, respectively. The particles are colored with respect to their hexagonal order parameter as defined in Eq. (3.5) and calculated with `amep.order.psi_k`. Here, the simulations started from a hexagonal crystal as initial condition. **d** Spatial correlation function $g_6(r)$ as defined in Eq. (3.6) for the three snapshots shown in panels a–c averaged over three independent ensembles and over time in the steady state using `amep.evaluate.HexOrderCor`. The black dashed line shows an algebraic decay of the form $r^{-\nu}$ with exponent $\nu = 0.11$ as a guide for the eye. **e** Snapshot of one cluster of the simulation shown in Fig. 3.4c with Pe $= 70.7$ and $\varphi = 0.5$. Again, the particles are colored with respect to their hexagonal order parameter. **f** Distribution of the hexagonal order parameter corresponding to the snapshot shown in panel e calculated with `amep.evaluate.Psi6dist` and averaged over five independent ensembles. Parameters: $I/(\gamma_\mathrm{r}\tau_\mathrm{p}) = 5 \times 10^{-6}$, $N = 100\,000$, $\varphi = 0.8$, and $\epsilon/(k_\mathrm{B}T_\mathrm{b}) = 10$ (a–d), and (e–f) as in Fig. 3.4.

3.4.4 Hexagonal order

In the last paragraph, we saw that on average, each particle has six next neighbors, indicating that a hexagonal order dominates the local order of the particles. To quantify the local order in more detail, we calculate the hexagonal order parameter

$$\psi_6(\mathbf{r}_i) = \frac{1}{6}\sum_{j=1}^{6} \exp\{\mathrm{i}6\phi_{ij}\} \tag{3.5}$$

of each particle, where the sum goes over the six nearest neighbors of particle i and ϕ_{ij} is the angle between the connection line from $\mathbf{r}_i$ to $\mathbf{r}_j$ and the x-axis.[72,473,474] In two spatial dimensions, the particles within the dense phase typically show local hexagonal order while they are disordered in the dilute phase. Therefore, the distribution of ψ_6 can also be used to assess whether a system is phase separated similarly to the local area

fraction.[72,447,474,475] Calculating the distribution of the hexagonal order parameter can be easily done using AMEP's evaluate module:

```
import amep
# load the simulation data
traj = amep.load.traj(
    "/path/to/data",
    mode = "lammps"
)
# psi6 distribution (for all frames)
p6dist = amep.evaluate.Psi6dist(
    traj,
    nav = traj.nframes
)
# save results in HDF5 file
p6dist.save("p6dist.h5")

# plot the result of the last frame
fig, ax = amep.plot.new()
ax.plot(
    p6dist.psi6,
    p6dist.frames[-1,0]
)
fig.savefig("p6dist.png")
```

The result is demonstrated in Fig. 3.6f, where we have averaged over five independent ensembles. The broad peak at small values corresponds to the dilute phase while the sharp peak at $|\psi_6| = 1$ corresponds to the hexagonally packed dense phase as shown in Fig. 3.6e. It is also common to analyze the spatial range of the hexagonal order to check whether there exists a short-range or (quasi) long-range hexagonal order like in a crystal. To this end, one can calculate the spatial correlation function of the hexagonal order parameter

$$g_6(r) = \frac{\langle \psi_6^*(\mathbf{r}_i)\psi_6(\mathbf{r}_j)\rangle}{\langle |\psi_6(\mathbf{r}_i)|^2\rangle} \tag{3.6}$$

with $r = |\mathbf{r}_i - \mathbf{r}_j|$.[72,474] Here, we calculate $g_6(r)$ for ABP simulations with $\epsilon/(k_\mathrm{B}T_\mathrm{b}) = 10$, $N = 100\,000$ particles, and at $\varphi = 0.8$ starting from a hexagonal lattice instead of a uniform distribution (Fig. 3.6a–c) and average over multiple frames in the steady state:

```
import amep
# load simulation data
traj = amep.load.traj(
    "/path/to/data",
    mode = "lammps"
)
# calculate g6
g6 = amep.evaluate.HexOrderCor(
    traj,
    nav = traj.nframes,
    njobs = 16,
    rmax = 100.0,
    skip = 0.5
```

```
)
# save results in an HDF5 file
g6.save(
    "g6.h5"
)
# plot average
fig, ax = amep.plot.new()
ax.plot(
    g6.r,
    g6.avg
)
fig.savefig("g6.png")
```

Since this calculation is computationally expensive, we speed it up using parallelization by specifying the number of jobs that should run in parallel with the njobs keyword. Additionally, we give a maximum distance up to which the correlation function should be calculated, and we skip the first $50\,\%$ of the trajectory to ensure that only the second half of the trajectory, which is in the steady state, is used for the calculation. The result is shown in Fig. 3.6d together with the corresponding snapshots in Fig. 3.6a–c for three different Pe. In accordance to Ref. [72], we observe a constant g_6 at small Pe and an algebraic decay of the form $r^{-\nu}$ with exponent ν at higher Pe.

3.4.5 Structure factor and coarsening

To further probe the order of an active system, one can exploit the radial distribution function $g(r)$, which we have exemplarily calculated in Sec. 3.2 using amep.evaluate.RDF. From an experimental viewpoint, it is easier to obtain the structure factor $S(\mathbf{q}, t)$, which is defined as[303]

$$S(\mathbf{q}, t) = \frac{1}{N} \left\langle \sum_{i=1}^{N} \sum_{j=1}^{N} \exp\left\{ i\mathbf{q} \cdot [\mathbf{r}_i(t) - \mathbf{r}_j(t)] \right\} \right\rangle . \tag{3.7}$$

Here, $\mathbf{q}$ represents the wave vector, $\mathbf{r}_i(t)$ and $\mathbf{r}_j(t)$ denote the positions of particles i and j at time t, respectively, and N is the total number of particles. For isotropic systems, the structure factor only depends on the magnitude $q = |\mathbf{q}|$ of the wave vector. It gives information about the density response to an external perturbation of wave length $2\pi/q$ and can be probed experimentally via scattering experiments. Note that $S(\mathbf{q}, t)$ is directly related to $g(\mathbf{r}, t)$ via Fourier transform. However, in practice, it is often preferable to calculate $S(\mathbf{q}, t)$ directly to achieve good numerical results in the low q regime. Within AMEP, $S(\mathbf{q}, t)$ can be directly calculated with amep.evaluate.SF2d and the isotropic structure factor $S(q, t)$ with $q = |\mathbf{q}|$ (i.e., $S(\mathbf{q}, t)$ averaged over the direction of $\mathbf{q}$) with amep.evaluate.SFiso. Here, we use $S(q, t)$ to analyze the coarsening process of the clusters forming when the ABPs undergo MIPS. To this end, we deduce a characteristic length scale $L(t)$ based on the first moment of $S(q, t)$ given by[292,293,299,476,477]

$$L(t) = \frac{\int_{2\pi/L}^{q_{\text{cut}}} S(q, t) \mathrm{d}q}{\int_{2\pi/L}^{q_{\text{cut}}} q S(q, t) \mathrm{d}q}, \tag{3.8}$$

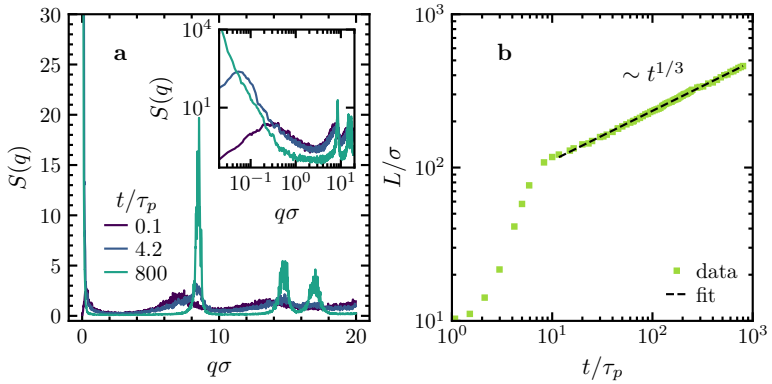

Fig. 3.7 Structure factor from `amep.evaluate.SFiso` and corresponding domain length from `amep.utils.domain_length`. **a** Isotropic structure factor obtained from the three simulation snapshots shown in Fig. 3.4 using `amep.evaluate.SFiso`. The data is smoothed using a running average over seven points with the `amep.utils.runningmean` function. The inset shows the same data but with logarithmic axes. **b** Length scale $L(t)$ over time derived from the first moment of the structure factor as defined in Eq. (3.8) using the `amep.utils.domain_length` function. The data has been averaged over five independent ensembles and the black dashed line is a power-law fit of the form $L(t) = L_0 t^{\alpha}$ done with `amep.functions.Fit` resulting in an exponent $\alpha = 0.324 \pm 0.001$.

where L is the length of the simulation box. We set the upper limit $q_{\text{cut}}\sigma = 0.3$, i.e., we only consider length scales larger than $2\pi/q_{\text{cut}} \approx 21\sigma$. Notably, under suitable conditions, overdamped ABPs undergoing MIPS exhibit an effective mapping onto a suitable equilibrium system at coarse-grained scales, as established in the literature.[374] This mapping explains why the coarsening dynamics follows the universal law $L(t) \sim t^{1/3}$ – a characteristic scaling behavior observed in equilibrium systems.

To visually elucidate this process, we present instances of $S(q,t)$ at distinct times $t/\tau_p = 0.1, 4.2, 800.0$ (Fig. 3.7a) corresponding to the snapshots shown in Fig. 3.4. These results can be obtained using the following code example:

```
import amep
import numpy as np
# load simulation data
traj = amep.load.traj(
    "/path/to/data",
    mode = "lammps"
)
# calculate S(q)
sf = amep.evaluate.SFiso(
    traj,
    nav = traj.nframes
)
# plot S(q) of the last frame
fig, axs = amep.plot.new()
axs.plot(sf.q, sf.frames[-1][0])
fig.savefig("sf.pdf")
```

We can now subsequently compute $L(t)$ by using the amep.utils.domain_length function and fit a power-law of the form $L(t) = L_0 t^{\alpha}$ to it using amep.functions.Fit:

```
# calculate domain length
L = np.zeros(len(sf.frames))
for i,frame in enumerate(sf.frames):
    length = amep.utils.domain_length(
        frame[0], sf.q, qmax = 0.3
    )
    L[i] = length

# fit growth exponent
def f(x, L0 = 1, alpha = 1):
    return L0*x**alpha
fit = amep.functions.Fit(f)
mask = sf.times > 10
fit.fit(sf.times[mask], L[mask])

# plot data and fit
fig, axs = amep.plot.new()
axs.plot(sf.times, L, label = "data")
axs.plot(
    sf.times[mask],
    fit.generate(sf.times[mask]),
    marker = "", ls = "--",
    label = "fit"
)
axs.legend()
fig.savefig("domain-length.pdf")
```

The result is illustrated in Fig. 3.7b and we obtain a growth exponent of $\alpha = 0.324 \pm 0.001$ in accordance with the literature.[103,291,293]

3.4.6 Cluster analysis

Finally, we analyze the clustering of ABPs when undergoing MIPS by using AMEP's cluster module. For particle-based simulation data, we define a cluster as a collection of particles in which each particle has an interparticle distance smaller than r_{max} to some other particle, where the cut-off distance r_{max} can be chosen by the user. Particle i and j with position coordinates $\mathbf{r}_i$ and $\mathbf{r}_j$, respectively, belong to the same cluster if $|\mathbf{r}_i - \mathbf{r}_j| \leq r_{\text{max}}$. To find the distance between different particle pairs and identify the neighboring particle pairs that satisfy this distance criterion, we use the KDTree algorithm (scipy.spatial.KDTree) from the SciPy library.[377,478] In the following, we will first show how to identify clusters using AMEP and afterward analyze the coarsening of the clusters as well as their radius of gyration and fractal dimension.

Let us consider the last frame of a simulation showing MIPS (Fig. 3.4c). The clusters can be identified using the amep.cluster.identify function:

```
import amep
import numpy as np
# load simulation data
```

```
traj = amep.load.traj(
    "/path/to/data",
    mode = "lammps"
)
# get the last frame
frame = traj[-1]

# cluster detection
clusters, idx = amep.cluster.identify(
    frame.coords(),
    frame.box,
    pbc = True,
    rmax = 1.122
)
```

It takes the coordinates of all particles (frame.coords()) and the boundaries of the simulation box (frame.box) as an input and returns a list (clusters) of all clusters, sorted in descending order of their size, with each list element containing the indices of the particles belonging to the respective cluster. It also returns the array idx which stores the cluster indices assigned to each particle. The optional argument pbc is used to consider periodic boundary conditions and the cut-off distance rmax is set to the cut-off distance of the WCA potential (i.e., the contact distance). The algorithm works not only with simulation data of particles of the same size but can also identify clusters comprising particles of different sizes, which requires different values of the cut-off distance r_{max} depending on the pair of particles. In the latter case, the user can provide the sizes of the particles (diameter) through the additional keyword sizes in amep.cluster.identify. In Fig. 3.8a, we show the same snapshot as in Fig. 3.4c, but with the particles of the eight largest clusters colored according to their cluster ids.

Based on the identified clusters, one can calculate various properties of the different clusters using the cluster module. One of them is the cluster size, defined as the number of particles within a cluster, the distribution of which often provides an insight into coexisting phases in a system.[50,53,117,118,479–482] We can calculate the cluster sizes and masses by using the amep.cluster.sizes and amep.cluster.masses functions:

```
sizes = amep.cluster.sizes(
    clusters
)
masses = amep.cluster.masses(
    clusters, frame.data("mass")
)
```

Based on sizes, we can now calculate the cluster size distribution $p(s) = N_s/\left(\sum_s N_s\right)$, where N_s is the number of clusters with size s. Since we are interested in the coarsening behavior of the large clusters, but their number is relatively small, it has been proven to be beneficial to analyze the weighted cluster size distribution

$$p_{\mathrm{w}}(s) = \frac{sN_s}{\sum_s sN_s}, \tag{3.9}$$

where each cluster is weighted with its size s.[483,484] Here, we use the amep.statistics.distribution function with logarithmic bins:

```
# weighted cluster size distribution
hist, bins = amep.statistics.distribution(
    sizes, logbins = True,
    nbins = 50, density = False
)
hist = hist*bins/np.sum(hist*bins)

# plot result
fig, axs = amep.plot.new()
axs.bar(
    bins, hist, width = 0.2*bins
)
axs.loglog()
fig.savefig("size-dist.pdf")
```

The result is shown in Fig. 3.8b and exhibits two distinct peaks at small and large cluster sizes suggesting that the system is phase separated into two distinct phases. Large clusters characterize the dense liquid-like phase whereas the dilute gas-like phase comprises smaller clusters.[53,483,484]

The cluster sizes can also be used to study the average growth rate of the clusters, which is a commonly used measure of the coarsening kinetics of phases in soft matter and biophysics.[110,146,291,293] Here, we use amep.evaluate.ClusterGrowth to calculate the weighted mean cluster size $\langle s \rangle_\mathrm{w}$ and the mean cluster size $\langle s \rangle$ defined as

$$\langle s \rangle_\mathrm{w} = \sum_s s p_\mathrm{w}(s) = \frac{\sum_s s^2 N_s}{\sum_s s N_s} \tag{3.10}$$

$$\langle s \rangle = \sum_s s p(s) = \frac{\sum_s s N_s}{\sum_s N_s} \tag{3.11}$$

over time (Fig. 3.8c). Similar to the domain length $L(t)$ obtained from the structure factor above, we will deduce a growth exponent from the growing mean cluster sizes. Note that for $L(t)$, we only considered $q\sigma < q_\mathrm{max}\sigma = 0.3$, i.e., length scales larger than $l_\mathrm{min} = 2\pi/q_\mathrm{max} \approx 21\sigma$, which resulted in a growth exponent of $\alpha \approx 1/3$ (where $L(t) \propto t^\alpha$). Since the cluster size measures the number of particles within a cluster, which is proportional to the area of the cluster, we can define a cluster length as $l/\sigma = \sqrt{\langle s \rangle}$ that is expected to also scale as $l \propto t^{1/3}$. However, this holds true only if we either disregard very small clusters that do not grow over time or assign greater importance to larger clusters by calculating the weighted mean cluster size. Therefore, additionally to the weighted mean cluster size, we also compute the mean cluster size considering all the clusters (i.e., having at least two particles) and only the large clusters with at least 400 particles (in accordance to $l_\mathrm{min} \approx 21\sigma$ used for the calculation of $L(t)$).

```
# mean cluster size (>2)
mean_2 = amep.evaluate.ClusterGrowth(
    traj,
    mode = "mean",
```

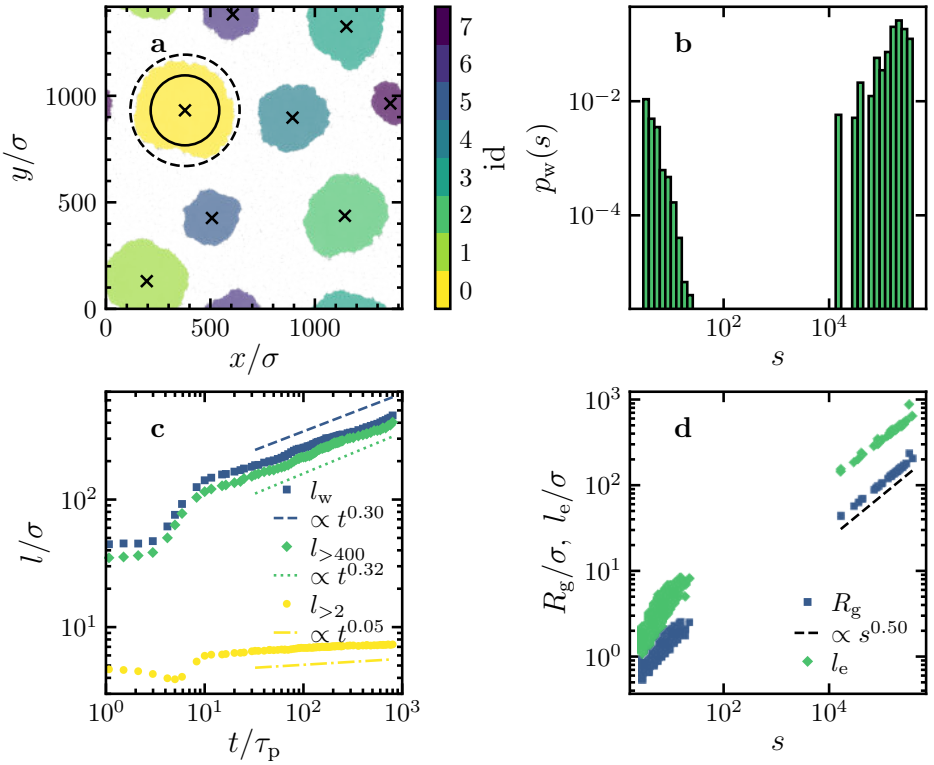

Fig. 3.8 Cluster analysis for particle-based simulation data with the `amep.cluster` and the `amep.evaluate` modules. a Same snapshot as in Fig. 3.4c showing the eight largest clusters identified with the `amep.cluster.identify` function and colored with respect to their cluster index. The centers of mass of the clusters calculated with `amep.cluster.center_of_mass` are marked with black crosses. The black solid and dashed circles have radii equal to the radius of gyration and half the linear extension of the largest cluster (yellow) as obtained from Eqs. (3.12) and (3.13) using `amep.cluster.radius_of_gyration` and `amep.cluster.linear_extension`, respectively. **b** Weighted cluster size distribution as defined in Eq. (3.9) corresponding to the snapshot in panel a as obtained from `amep.evaluate.ClusterSizeDist` averaged over five independent ensembles. **c** Cluster length $l/\sigma = \sqrt{\langle s \rangle}$ calculated from the weighted mean cluster size $\langle s \rangle_w$ (Eq. (3.10)) and mean cluster sizes $\langle s \rangle_{>400}$ and $\langle s \rangle_{>2}$ (Eq. (3.11)) averaged over all clusters larger than 400 and 2 particles, respectively, calculated using `amep.evaluate.ClusterGrowth` as function of time. The data has been averaged over five independent ensembles. The dashed, dotted, and dash-dotted lines are fits to $l(t) = l(0)t^\beta$ done with `amep.functions.Fit`. **d** Radius of gyration R_g and linear extension l_e as function of the cluster size s for the simulation shown in panel a. A fit to $R_g(s) \propto s^{1/d_f}$ results in a fractal dimension of $d_f = 1.99 \pm 0.03$.

```
    min_size = 2
)
# mean cluster size (>400)
mean_400 = amep.evaluate.ClusterGrowth(
    traj,
    mode = "mean",
    min_size = 400
)
# weighted mean cluster size
weighted_mean = amep.evaluate.ClusterGrowth(
    traj,
    mode = "weighted mean"
)
```

We now use amep.functions.Fit to obtain the growth exponent from $l(t) \propto t^{\beta}$ (here, exemplarily done for the weighted mean in the logarithmic domain):

```
# define fit function
def f(l, beta = 1.0, l0 = 1.0):
    return np.log(l0) + beta*l

# create fit object
fit = amep.functions.Fit(f)

# fit function to data at large times
# in logarithmic domain
mask = weighted_mean.times > 3e1
fit.fit(
    np.log(weighted_mean.times[mask]),
    np.log(weighted_mean.frames[mask])/2
)
print(fit.results)

# plot data and fit
fig, axs = amep.plot.new()
axs.plot(
    weighted_mean.times,
    np.sqrt(weighted_mean.frames)
)
axs.plot(
    weighted_mean.times[mask],
    np.exp(fit.generate(
        np.log(weighted_mean.times[mask])
    ))
)
axs.loglog()
fig.savefig("cluster-growth.pdf")
```

```
{'beta': (0.297, 0.004), 'l0': (64.6, 1.1)}
```

The results are demonstrated in Fig. 3.8c. Consistent with the established $\propto t^{1/3}$ growth of the characteristic domain length $L(t)$ of such ABP clusters,[293] we obtain an exponent

$\beta \approx 1/3$ for the cluster length calculated from the weighted mean and the mean over all clusters that are larger than 400 particles (Fig. 3.8c). For the mean over all clusters larger than two particles, the growth rate is significantly smaller because very small clusters do not grow.

To demonstrate the versatility of the cluster module, we present two additional calculable quantities using AMEP: the radius of gyration R_g and the linear extension l_e of the clusters. For a cluster composed of s particles of masses $m_i, i = 1, 2, \ldots, s$, located at fixed distances d_i from the cluster's center of mass, the radius of gyration is defined as[479,485]

$$R_g = \sqrt{\frac{\sum_{i=1}^{s} m_i d_i^2}{\sum_{i=1}^{s} m_i}}. \tag{3.12}$$

The linear extension (also known as the end-to-end length) of a cluster is defined as the maximal distance between two particles in the cluster, i.e,

$$l_e = \max_{\{i,j\}} |\mathbf{r}_i - \mathbf{r}_j| , \tag{3.13}$$

with $\mathbf{r}_i$ denoting the position vector of the i-th particle and $i, j = 1, 2, \ldots, s$.[479,486] The mean linear extension along with the mean size of the largest cluster is commonly used as an order parameter to characterize isotropic percolation phase transitions in different systems.[479,486,487] On the other hand, the dependence of the radius of gyration on the cluster size s (or mass) allows us to understand the (possibly fractal)[488] geometry of the clusters and calculate their fractal dimension d_f according to the relation $R_g \propto s^{1/d_f}$.[479,488–495] With AMEP, we can calculate such cluster properties easily by using its `cluster` module (here exemplarily done for the largest cluster):

```
# ids of particles in largest cluster
ids = clusters[0]

# center of mass
com = amep.cluster.center_of_mass(
    frame.coords()[ids],
    frame.box,
    frame.data("mass")[ids],
    pbc = True
)
# geometric center
gmc = amep.cluster.geometric_center(
    frame.coords()[ids],
    frame.box,
    pbc = True
)
# radius of gyration
rg = amep.cluster.radius_of_gyration(
    frame.coords()[ids],
    frame.box,
    frame.data("mass")[ids],
    pbc = True
)
```

```
# linear extension
le = amep.cluster.linear_extension(
    frame.coords()[ids],
    frame.box,
    frame.data("mass")[ids],
    pbc = True
)
```

To handle periodic boundary conditions, AMEP uses the method proposed in Ref. [496]. The radius of gyration and the linear extension of the largest cluster are visualized in Fig. 3.8a. Additionally, we plotted R_g and l_e as function of the cluster size s in Fig. 3.8d to obtain the fractal dimension using amep.functions.Fit to fit the function $R_g(s) \propto s^{1/d_f}$. We obtain $d_f = 1.99 \pm 0.03$, i.e, essentially the same as the spatial dimension of the system, which is expected here since the clusters are compact.

3.5 Analyzing continuum simulation data with AMEP

Let us now discuss some examples on how to analyze continuum simulation data with AMEP. To this end, we will use numerical solutions of the active model B+ (AMB+), which is a corresponding continuum model for active Brownian particles.

3.5.1 Numerical solutions of the active model B+

Here, we use the AMB+ as introduced in Subsec. 2.2.2 as Eqs. (2.15) and (2.16). It describes a system of active Brownian particles featuring a generic self-propulsion mechanism and models the time evolution of the scalar field ϕ. Here, we set the free parameters of the model to $a = -0.25$, $b = 0.25$, $K = 1.0$, $\zeta = 1.0$, $\lambda = -0.5$, $k_BT = 0.2$, and $M = 1.0$ corresponding to a parameter regime showing phase separation.[300] We start from a uniform initial condition with $\phi_0 = -0.4$ disturbed with weak fluctuations. To solve Eq. (2.15) numerically, we used an in-house finite-volume solver written in C++ using a grid of 256×256 grid points with a grid spacing of $\Delta x = \Delta y = 1.0$ and time step $\Delta t = 0.001$. All simulations run for 10^8 time steps. To load the resulting data with AMEP, the data has to be stored in a certain data format as discussed in Subsec. 3.5.5 and as exemplified in the exemplary dataset which can be downloaded from https://github.com/amepproject/amep/tree/main/examples.

3.5.2 Motility-induced phase separation

Similar to the particle-based simulations of ABPs, the AMB+ also undergoes MIPS in a certain parameter regime.[300] Whether the system is phase separated can again be determined by evaluating the local density distribution. In case of continuum data, one can simply calculate the distribution of the density at each grid point, as done by the amep.evaluate.LDdist class:

```
import amep
# load the data
traj = amep.load.traj(
```

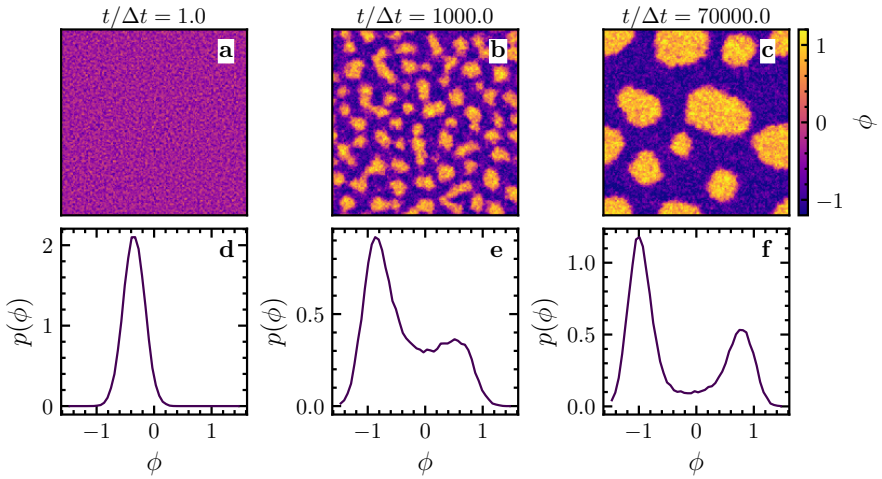

Fig. 3.9 Plotting snapshots with `amep.plot.field` and density distributions using `amep.evaluate.LDdist`. a–c Snapshots of numerical solutions of the active model B+ as given in Eqs. (2.15) and (2.16) plotted with `amep.plot.field` at three different times given in the key. **d–f** Corresponding density distributions calculated with `amep.evaluate.LDdist`.

```
    "/path/to/data",
    mode = "field"
)
# local density distribution of each frame
lddist = amep.evaluate.LDdist(
    traj,
    nav = traj.nframes,
    xmin = -1.5,
    xmax = 1.5,
    ftype = "phi"
)
# save results in HDF5 file
lddist.save("lddist.h5")

# plot for the last frame
fig, axs = amep.plot.new()
axs.plot(lddist.ld, lddist.frames[-1,0])
axs.set_xlabel(r"$\phi$")
axs.set_ylabel(r"$p(\phi)$")
fig.savefig("lddist.pdf")
```

The results are demonstrated in Fig. 3.9 at different times together with the corresponding snapshots. While the distribution is unimodal at the beginning of the simulations (which start with a uniform distribution), it becomes bimodal at long times showing that the system phase separates into a dense and a dilute phase by forming dense clusters that coexist with a surrounding gas-like phase.

3.5.3 Coarsening processes

Let us now analyze the coarsening behavior of the clusters based on the isotropic structure factor. For a continuum field, the (two-dimensional) structure factor can directly be calculated from the numerical Fourier transform of the scalar field ϕ as[299,303,497]

$$S(\mathbf{q},t) = \langle \phi(\mathbf{q},t)\phi(-\mathbf{q},t)\rangle = \left\langle |\phi(\mathbf{q},t)|^2 \right\rangle \tag{3.14}$$

using the amep.continuum.sf2d function. Here, $\phi(\mathbf{q},t)$ is the spatial Fourier transform of $\phi(\mathbf{r},t)$. To obtain the isotropic structure factor, the resulting two-dimensional structure factor must be averaged over the direction of $\mathbf{q}$, i.e., (using polar coordinates)

$$S(q,t) = \frac{1}{2\pi}\int_0^{2\pi} \mathrm{d}\varphi\, S((q\cos(\varphi), q\sin(\varphi)), t) \tag{3.15}$$

which can be done in AMEP with the amep.utils.sq_from_sf2d function:

```
import amep
import numpy as np
# load data
traj = amep.load.traj(
    "/path/to/data",
    mode = "field"
)
# get last frame
frame = traj[-1]

# 2d structure factor
sf2d, qx, qy = amep.continuum.sf2d(
    frame.data("phi"),
    *frame.grid
)
# isotropic structure factor
sfiso, q = amep.utils.sq_from_sf2d(
    sf2d, qx, qy
)
```

AMEP's evaluate module allows to calculate the isotropic structure factor directly from the traj object and also performs a time average:

```
# isotropic structure factor
# for all frames (time average)
sf = amep.evaluate.SFiso(
    traj,
    nav = traj.nframes,
    ftype = "phi"
)
```

Here, we can specify which field of the given trajectory should be used via ftype. From the structure factor, we can then again calculate the domain length as defined in Eq. (3.8) via

```
# domain length over time
L = np.zeros(traj.nframes)
```

```
for i,f in enumerate(sf.frames):
    L[i] = amep.utils.domain_length(
        f[0], f[1]
    )
```

Note that we do not specify qmax here because we integrate over all q up to its largest possible value $q_{\text{max}} = \pi/\Delta x$ given by the grid spacing Δx. The results are demonstrated in Fig. 3.10, which shows three exemplary curves of the structure factor at three different times and the domain length over time. From the domain length, we extract the growth exponent by fitting a power law to the domain length at long times in the logarithmic domain:

```
# define fit function
def f(t, L0 = 1.0, alpha = 1.0):
    return np.log(L0) + alpha*t
# create fit object
fit = amep.functions.Fit(f)

# fit at large times
mask = traj.times > 1e1
fit.fit(
    np.log(traj.times[mask]),
    np.log(L[mask])
)
print(fit.results)
```

```
{'L0': (4.168, 0.085), 'alpha': (0.2702, 0.0029)}
```

Interestingly, for our continuum simulations of the AMB+, we obtain $\alpha \approx 0.27$, which is smaller than the value $\alpha \approx 1/3$ as obtained in our particle-based simulations. Such subdiffusive scaling has been obtained in previous studies of active field theories as well and is typically expected to be an intermediate scaling regime that leads to a $t^{1/3}$ scaling at longer times.[292,293,299]

3.5.4 Cluster analysis

Next, we will analyze the clusters forming at late times in more detail by performing a similar cluster analysis as done in Subsec. 3.4.6. For the continuum data, a cluster is defined as a connected region of similar and higher density than the surroundings. AMEP provides two algorithms to detect clusters in continuum data (i.e., discretized density fields). The standard algorithm is dividing up pixels according to their values relative to a threshold value, i.e., for a scalar continuum field ϕ, a zero is assigned to all pixels with $\phi \leq a_{\text{thres}}(\phi_{\text{max}} - \phi_{\text{min}})$ and a one to all pixels with $\phi > a_{\text{thres}}(\phi_{\text{max}} - \phi_{\text{min}})$. Here, $a_{\text{thres}} \in [0, 1]$ denotes the relative threshold and ϕ_{min}, ϕ_{max} are the minimum and maximum values of the continuum field. On the resulting two-valued image, all connected regions are then labeled as a cluster using skimage.measure.label.[379,498,499] Within AMEP, this algorithm is called "*threshold*". An alternative way for cluster detection is the watershed algorithm.[500] It is more stable against slowly varying background fields but needs more fine-tuning of parameters to work. Therefore, the watershed algorithm is

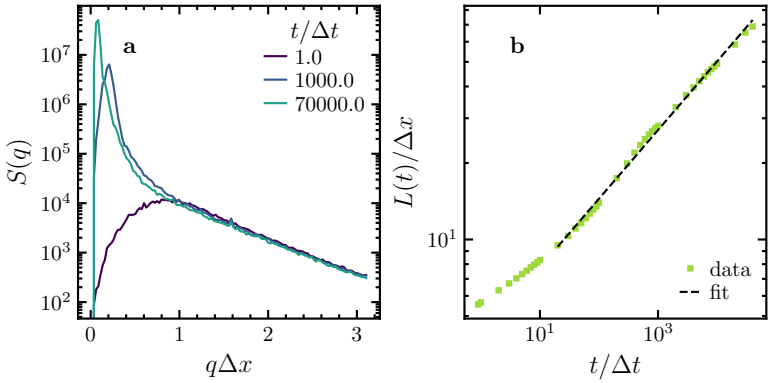

Fig. 3.10 Structure factor from `amep.evaluate.SFiso` and corresponding domain length from `amep.utils.domain_length` for continuum simulation data. a Isotropic structure factor obtained from the three simulation snapshots of the AMB+ shown in Fig. 3.9 calculated with `amep.evaluate.SFiso`. Note that the upper limit for the wave vector q is given by the resolution of the discretized grid, i.e., $q_{\text{max}} = \pi/\Delta x$. **b** Length scale $L(t)$ as obtained from Eq. (3.8) using the `amep.utils.domain_length` function. The data has been averaged over five independent ensembles and the black dashed line is a power-law fit of the form $L(t) = L_0 t^{\alpha}$ done with `amep.functions.Fit` and resulting in a growth exponent of $\alpha = 0.270 \pm 0.003$.

not the first choice for detecting clusters over time, i.e., for multiple frames of a trajectory, because the parameters may need to be adjusted for each frame individually. In AMEP, the skimage.segmentation.watershed function is used for the *"watershed"* cluster detection.[379]

Clusters within a continuum field can be identified with AMEP using the amep.continuum .identify_clusters function. In the following example, we detect the clusters in the last frame of a continuum simulation using the *"threshold"* method:

```
import amep
# load data
traj = amep.load.traj(
    "path/to/data",
    mode = "field"
)
# get the last frame
frame = traj[-1]

# identify clusters
ids, labels =\
amep.continuum.identify_clusters(
    frame.data("phi"),
    pbc = True,
    threshold = 0.1,
    method = "threshold"
)
```

Here, frame.data(*"phi"*) returns an array of values of field *"phi"* at each point of the underlying discretized grid, the pbc keyword can be set to True to apply periodic boundary conditions, and threshold specifies the relative threshold a_{thres}. The keyword method chooses

between the "*threshold*" or "*watershed*" method. The amep.continuum.identify_clusters function assigns a unique identifier to each detected cluster returned as NumPy array (ids in the example above), and it returns an array of the same shape as the underlying discretized grid denoting which grid point belongs to which cluster (labels in the example above). The result is examplarily visualized in Fig. 3.11a.

As a next step, the amep.continuum.cluster_properties function can be used to calculate certain properties of the detected clusters such as their sizes, masses, centers, or radii of gyration:

```
s, gmc, com, rg, le, gt, it =\
amep.continuum.cluster_properties(
    frame.data("phi"),
    *frame.grid,
    ids,
    labels,
    pbc = True
)
```

Here, s, gmc, com, rg, le, gt, it denote the size, geometric center, center of mass, radius of gyration, linear extension, gyration tensor, and inertia tensor of each cluster, respectively. The size of cluster i within a field ϕ is defined as the integral over its area A_i, i.e., $s_i = \int_{A_i} \mathrm{d}^2 r\, \phi(\mathbf{r})$. All other cluster properties are calculated with the same methods as used for the particle-based simulation data by treating each grid point (i, j) as a particle at position $\mathbf{r}_{ij}$ with "mass" $\phi(\mathbf{r}_{ij})$. The radius of gyration and the linear extension of the largest cluster are visualized in Fig. 3.11a.

Similarly to the cluster analysis for particle-based data, we can now calculate the weighted cluster-size distribution, the growth exponents, and the fractal dimension of the clusters exploiting AMEP's evaluate module. Let us first calculate the weighted cluster-size distribution as defined in Eq. (3.9):

```
# weighted cluster size distribution
cd = amep.evaluate.ClusterSizeDist(
    traj,
    nav = traj.nframes,
    ftype = "phi",
    method = "threshold",
    threshold = 0.1,
    use_density = False,
    nbins = 50,
    logbins = True,
    xmin = 1e0,
    xmax = 1e4
)
```

Here, the keyword use_density allows specifying whether the integrated density s_i as defined above (use_density = True) or area A_i (use_density = False) should be used as size of cluster i. Furthermore, we have used the "*threshold*" method and logarithmic bins and the result is shown in Fig. 3.11b. Next, we analyze the cluster growth by calculating the average cluster size over time using the weighted mean and mean as defined in Eqs. (3.10) and (3.11), respectively:

```
# mean cluster sizes
mean = amep.evaluate.ClusterGrowth(
    traj,
    ftype = "phi",
    method = "threshold",
    mode = "mean",
    threshold = 0.1,
    use_density = False
)
# mean cluster size over all clusters
# with size larger than 20
mean_20 = amep.evaluate.ClusterGrowth(
    traj,
    ftype = "phi",
    method = "threshold",
    mode = "mean",
    threshold = 0.1,
    use_density = False,
    min_size = 20
)
# weighted mean cluster size
weighted_mean = amep.evaluate.ClusterGrowth(
    traj,
    ftype = "phi",
    method = "threshold",
    mode = "weighted mean",
    threshold = 0.1,
    use_density = False
)
```

Again, we define the cluster length as $l = \sqrt{\langle s \rangle}$ and use amep.functions.Fit to obtain the growth exponent from $l(t) \propto t^{\beta}$ as already demonstrated in Subsec. 3.4.6. Consistently with the growth exponent $\alpha \approx 0.27$ obtained from the domain length $L(t)$ (see Subsec. 3.5.3), we obtain $\beta \approx 0.26$ (Fig. 3.11c). Additionally, we plotted the radius of gyration R_g as function of the cluster size s in Fig. 3.11d to obtain the fractal dimension using amep.functions.Fit to fit the function $R_g(s) \propto s^{1/d_f}$. We obtain $d_f = 1.99 \pm 0.01$, i.e, the same as the spatial dimension of the system, which is expected here since the clusters are compact.

3.5.5 Continuum data format

Continuum simulation data as analyzed within this thesis has to be stored in a specific format such that it can be loaded with AMEP. In the following, we briefly introduce the basic format requirements. In AMEP, field data is internally stored using the `h5amep` file format, similar to the particle-based simulation data. Converting field data to an AMEP dataset is done by use of a reader class (amep.reader.ContinuumReader). This data reader expects the following format: The standard file structure for field data is inspired by the LAMMPS dump file format, i.e., all relevant data is stored in one base directory which contains (i) a file named `grid.txt` and (ii) multiple files named `field_<index>.txt`. The former is of the form

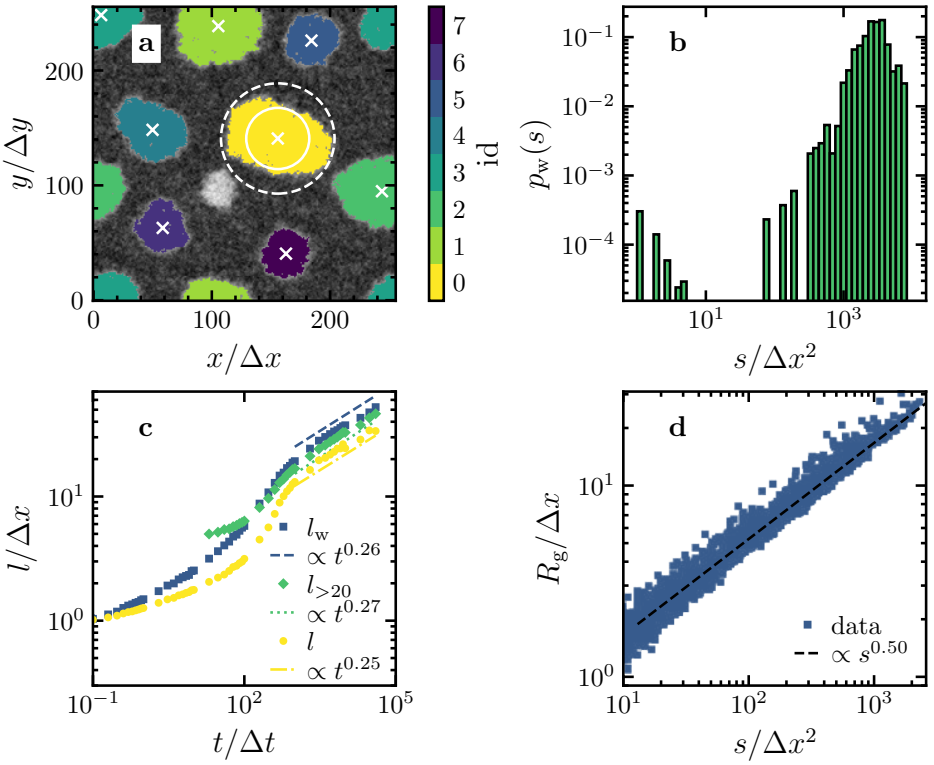

Fig. 3.11 Cluster analysis for continuum simulation data with the `amep.continuum` and the `amep.evaluate` modules. **a** Same snapshot as in Fig. 3.9c showing the eight largest clusters identified with the `amep.continuum.identify_clusters` function and colored with respect to their cluster index. The centers of mass of the clusters calculated with `amep.continuum.cluster_properties` are marked with white crosses. The white solid and dashed circles have radii equal to the radius of gyration and half the linear extension of the largest cluster (yellow) as obtained from Eqs. (3.12) and (3.13), respectively, using `amep.continuum.cluster_properties`. **b** Weighted cluster size distribution as defined in Eq. (3.9) corresponding to the snapshot in panel a as obtained from `amep.evaluate.ClusterSizeDist` averaged over five independent ensembles. **c** Cluster length $l = \sqrt{\langle s \rangle}$ obtained from the weighted mean cluster size $\langle s \rangle_\mathrm{w}$ (Eq. (3.10)) and mean cluster sizes $\langle s \rangle$ (Eq. (3.11)) and $\langle s \rangle_{>20}$ averaged over all clusters and over all clusters larger than an area of $20\,\Delta x \Delta y$, respectively, calculated using `amep.evaluate.ClusterGrowth` as function of time. The data has been averaged over five independent ensembles. The dashed, dotted, and dash-dotted lines are fits to $l(t) = l(0)t^\beta$ done with `amep.functions.Fit`. **d** Radius of gyration R_g as function of the cluster size s for five independent simulations as exemplarily shown in panel a. A fit to $R_\mathrm{g}(s) \propto s^{1/d_\mathrm{f}}$ results in a fractal dimension of $d_\mathrm{f} = 1.99 \pm 0.01$.

```
BOX:
<X_min> <X_max>
<Y_min> <Y_max>
<Z_min> <Z_max>
SHAPE:
<nx> <ny> <nz>
COORDINATES: X Y Z
<X_0> <Y_0> <Z_0>
<X_1> <Y_0> <Z_0>
...
<X_N> <Y_0> <Z_0>
<X_0> <Y_1> <Z_0>
<X_1> <Y_1> <Z_0>
...
```

and contains all information about the simulation box and the underlying discrete grid. The values in the `BOX` category define the borders of the simulation box, which is assumed to be rectangular, the `SHAPE` category contains the shape of the grid, and `COORDINATES` contains the coordinates of all grid points. If the data is based on an evenly spaced rectangular grid and the grid points are given in rising order, the `SHAPE` category tells AMEP in what kind of multidimensional array the data should be cast for representation. The files named `field_<index>.txt` contain all data that varies in time. The index should rise in time and could be chosen as the number of timesteps for example. The data files should be of the following form:

```
TIMESTEP:
<Simulation timestep>
TIME:
<Physical time>
DATA: <name 0> <name 1> <name 2> <name 3>
<field 0 0> <field 1 0> <field 2 0> <field 3 0>
<field 0 1> <field 1 1> <field 2 1> <field 3 1>
<field 0 2> <field 1 2> <field 2 2> <field 3 2>
...
```

Here, the names describe the scalar field written to the column beneath, e.g., density. The columns are then filled by the values of the respective field at each grid point in the same order as in `grid.txt`. The columns can be separated by spaces, tabs, commas, semicolons, colons, or a vertical bar. The `TIMESTEP` category contains the number of timesteps corresponding to the contained data and the `TIME` category the corresponding (physical) time. If we have data of this type in the directory `/path/to/data`, it can be loaded with AMEP via

```
field_trajectory = amep.load.traj(
    "/path/to/data",
    mode = "field",
    delimiter = " ",
    dumps = "field_*.txt",
    reload = True
)
```

The `mode` keyword tells AMEP to expect field data, `delimiter` specifies the delimiter used for the columns in the data files, `dumps` takes a regular expression that matches the name

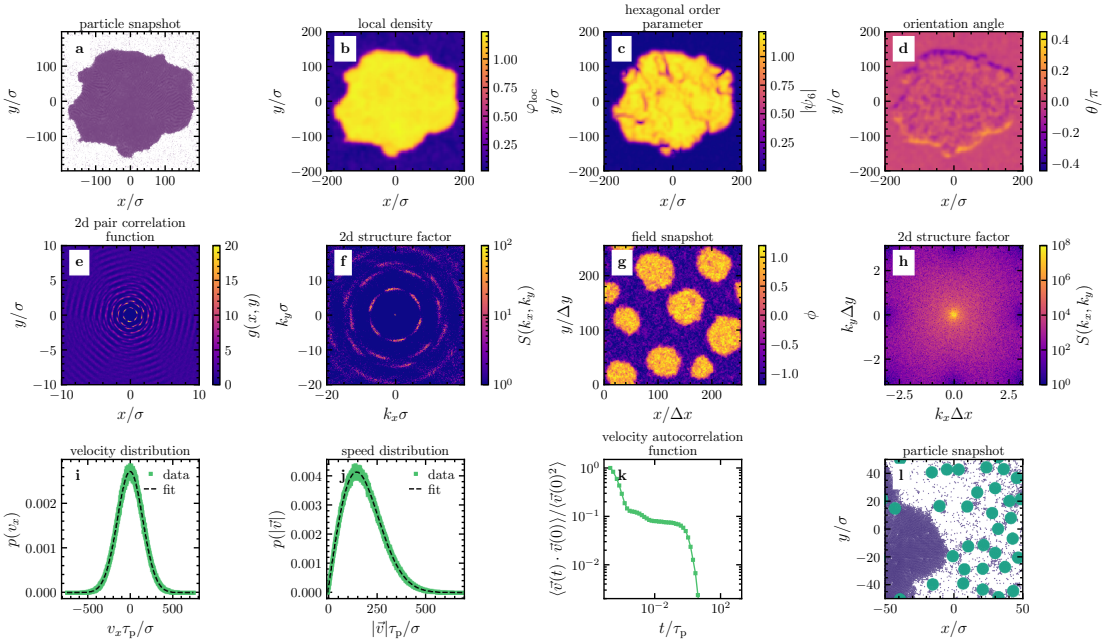

Fig. 3.12 Further observables calculated with AMEP. a Snapshot of MIPS plotted with `amep.plot.particles`. **b–d** Corresponding coarse-grained local density φ_{loc}, hexagonal order parameter ψ_6 (Eq. (3.5)), and orientation angle θ, respectively, calculated with `amep.continuum.gkde`. **e** Two-dimensional pair correlation function of the snapshot shown in panel a calculated with `amep.evaluate.PCF2d`. **f** Two-dimensional structure factor of the snapshot shown in panel a calculated with `amep.evaluate.SF2d`. **g** Snapshot of MIPS in the active model B+ plotted with `amep.plot.field`. **h** Two-dimensional structure factor of the field shown in panel g calculated with `amep.evaluate.SF2d`. **i,j** Distribution of the velocity v_x in x direction and the magnitude $|\mathbf{v}|$ from a particle-based simulation in two spatial dimensions calculated with `amep.evaluate.VelDist`. The black dashed lines are fits obtained with `amep.functions.NormalizedGaussian` and `amep.functions.MaxwellBoltzmann`, respectively. **k** Velocity autocorrelation function calculated with `amep.evaluate.VACF`. **l** Snapshot of a simulation with particles of different sizes plotted with `amep.plot.particles`.

format of the variable data files, and the keyword reload tells AMEP whether to look for an existing `h5amep` file and use it if it exists or to create a new one from the raw data. This should be used when your base data has changed between analysis runs. An exemplary dataset can be downloaded from https://github.com/amepproject/amep/tree/main/examples.

3.6 Conclusion

AMEP is a powerful Python library for analyzing simulation data of active matter systems. It provides a unified framework for handling both particle-based and continuum simulation data and combines it with an easy-to-learn Python API. With AMEP, one can quickly analyze and plot simulation results and develop new analysis methods utilizing AMEP's features and its seamless integrability to powerful scientific Python libraries through NumPy arrays. While its collection of analysis methods is primarily targeted at the active matter community, AMEP's general design allows applying AMEP to almost any particle-based or continuum simulation data as obtained from classical molecular dynamics and Brownian dynamics simulations, or any kind of numerical solutions of partial differential equations.

We have exemplarily shown the potential of AMEP by analyzing particle-based systems of more than 10^6 particles and continuum simulations with up to 10^5 grid points as typically used in active matter research. AMEP enables the analysis of a broader class of simulation data compared to most other analysis libraries. Such simulation data comprises "dry" particle-based models such as the active Brownian particle model and its various relatives, "wet" models that explicitly model surrounding fluids including particles that are coupled to flow fields, and continuum models such as the active model B+, the Keller-Segel model, or the Cahn-Hilliard model. Applied to such models, AMEP can provide essential insights, e.g., into phase separation, pattern formation, and critical phenomena in active matter systems. In addition to the presented observables, many more observables will be included in the future, for instance, entropy production using the method introduced in Ref. [431], finite-size scaling analysis, and cluster tracking.

4 Defining Temperature in Active Systems

When we measure the temperature of a room, different types of thermometers show the same temperature. This universality applies in thermodynamic equilibrium. In particular, the different phenomena which are exploited by different types of thermometers are evidently linked by a global thermodynamic temperature. In contrast, in active systems, which are intrinsically out of equilibrium, this universality of temperature does not apply. Therefore, we now pose the general question of how to define temperature in active systems. To provide essential insights into this fundamental question, we systematically apply different possibilities to define temperature to active systems. One possibility is examplarily outlined in Fig. 4.1. In this chapter, we show that different temperatures typically lead to different values by using BD simulations and theory for inertial ABPs. However, we find that there are parameter regimes even far from equilibrium in which several definitions lead to very similar temperature values. In particular, we show that the kinetic temperature and the configurational temperature form one class of temperatures while temperatures exploiting the virial theorem, the Stokes-Einstein relation, or a harmonic confinement form a second class of temperatures whose values strongly differ from those of the first temperature class. We find that the two classes are linked by the particle mass as a scaling parameter. Finally, we discuss the advantages and disadvantages of the different possibilities to define temperature for measuring the temperature of active systems. The content of this chapter is taken from my publication "How to define temperature in active systems?" published in *The Journal of Chemical Physics* (2024) under the CC BY 4.0 license,[501] and the majority of this chapter is taken verbatim from it. For this publication, I wrote the original draft with input from all co-authors, performed all simulations, and created all final figures.

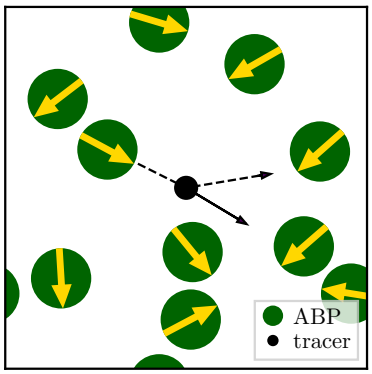

Fig. 4.1 Using a passive tracer particle (black) as a thermometer for the temperature of active particles (green), which collide with the tracer particle (black arrows). Its velocity distribution could provide a measure for the temperature of the active particles. The yellow arrows denote their self-propulsion direction.

4.1 Introduction

"Temperature is a physical quantity that expresses quantitatively the attribute of hotness or coldness. Temperature is measured with a thermometer."[502] This is the temperature definition reported in the leading encyclopedia of our times.[503] Clearly, this notion of

temperature is rather imprecise. Indeed, our sensation of hotness and coldness not only depends on temperature but also on the heat conductivity of the material we are touching. As an example, this can be experienced by touching a cold piece of wood and recognizing that it feels hotter than a piece of metal at the same temperature.[172]

There are many different ways to define temperature more precisely, and before we are taught thermodynamics, it may come as a surprise that in everyday life, different types of thermometers all essentially lead to the same result across a broad variety of environmental conditions. In particular, we may wonder why the reading of a liquid thermometer measuring the extension of a liquid agrees with the reading of an infrared thermometer that measures thermal radiation and even with that of a vapor-pressure thermometer that measures temperature through the vapor pressure of a liquid (exploiting the Clausius-Clapeyron equation). When learning statistical mechanics, we are in a position to understand that the universality of temperature and the link between different phenomena which are exploited by different types of thermometers exclusively hold true in thermodynamic equilibrium. In fact, the thermodynamic temperature can be linked to different observables in equilibrium systems.[170,176] This leads to different equivalent possibilities to define temperature which exploit the equipartition theorem,[504,505] the virial theorem,[506] or fluctuation-dissipation relations for example.[169,507–509] Alternatively, tracer particles can be used as a thermometer such that their properties can be linked to the thermodynamic temperature of the system in which the tracer particles are immersed.[177]

In principle, these and other definitions of temperature can all be generalized to non-equilibrium systems. In particular, classical irreversible thermodynamics grounds on the local-equilibrium hypothesis assuming that thermodynamic concepts like temperature may still be applied locally in non-equilibrium states.[510] However, when we are no longer near equilibrium and the local equilibrium hypothesis is invalid, the reading of a thermometer may (and typically will) depend on the details of the system under consideration (and may even be time-dependent).[123,511] Such a situation is generally expected for systems where the relaxation times of certain degrees of freedom are long or if large persistent fluxes are present in the system, in particular, also for the large class of active matter systems containing self-propelled particles.[123,170,172,264,440]

For such systems, we may wonder if it is sensible to define and speak of temperature at all. First, when touching a piece of glass or when putting our finger into a non-equilibrium liquid containing swimming bacteria, there is of course still a perception of hotness or coldness, and accordingly, it is tempting to introduce a measure to quantify our experience. Second, it may be instructive to explore when and by how much the different possibilities to define temperature, which we may use to quantify our experience, may deviate from each other. In particular, we may wonder if there are subsets in parameter space for which the reading of different thermometers would coincide. One might expect that different temperatures in active systems lead to strongly different temperature values for a system far from equilibrium, which can be quantified by measuring the total entropy production for example.[264,268,512]

In this chapter, we comparatively explore different possibilities to define temperature for inertial active Brownian particles such as used in Refs. [103, 106, 123, 125, 142, 165, 406, 513–518]. As expected, we find that different temperatures lead to results that depend on the details of the considered non-equilibrium system, and in general, that all obtained

temperature values deviate from each other. However, perhaps surprisingly, we identify parameter regimes where different temperatures provide consistent results even far from equilibrium. This applies in particular to regimes in which the active particles are heavy or in which their rotational diffusion is fast, and it has been previously found that within these regimes, an active system behaves as an effective equilibrium system.[140,142,158] Indeed, we find that within this regime, also the considered temperatures lead to similar temperature values independently of the values of all other dimensionless parameters that control the dynamics of the active particles. Interestingly, we find that the different temperatures which we have compared can be sorted in two classes: The first one shows a strong mass dependence (and scales linearly with the mass in a wide parameter regime) and the second one is almost mass independent. We show that these two classes can approximately be matched by rescaling with the particle mass. This finding has important consequences for the calculation of temperature in active systems, as we shall see.

4.2 Possibilities to define temperature

Let us first discuss the different possibilities under consideration to define temperature. In general, we can distinguish three different approaches to define temperature: First, one can define temperature based on the fluctuations of the particle velocity, which is a very common approach in the field of granular particles.[519–522] Second, it is possible to define temperature based on fluctuations in particle positions.[518] The third approach takes inspiration from glassy systems and exploits fluctuation-dissipation relations.[523–525] In the following, we briefly introduce the different possibilities to define temperature as used in this work and summarize some known analytical results. The considered temperatures are summarized in Tab. 4.1.

Before introducing the different possibilities to define temperature, let us recap some general concepts known from equilibrium physics. In particular, let us consider an equilibrium system of N particles in three spatial dimensions and let $\mathbf{\Gamma} = (\Gamma_1, ..., \Gamma_{6N}) = (p_1, ..., p_{3N}, q_1, ..., q_{3N})$ be the phase-space vector representing the spatial coordinates q_i and the conjugate momenta p_i. Furthermore, let the system be described by the Hamiltonian $\mathcal{H}(\mathbf{\Gamma}) = \sum_i p_i^2/(2m) + V(\{q_j\})$, where m denotes the mass of the particles and V the potential energy of the system. Based on the standard thermodynamic relation $1/T = \mathrm{d}S(E)/\mathrm{d}E$ with entropy $S(E)$ and energy E, one can show that the thermodynamic temperature can be calculated as[176]

$$k_\mathrm{B}T = \frac{\langle \boldsymbol{\nabla}\mathcal{H} \cdot \mathbf{B}(\mathbf{\Gamma})\rangle}{\langle \boldsymbol{\nabla} \cdot \mathbf{B}(\mathbf{\Gamma})\rangle}, \tag{4.1}$$

where $\mathbf{B}(\mathbf{\Gamma})$ is an arbitrary vector field with $0 < |\langle \boldsymbol{\nabla}\mathcal{H} \cdot \mathbf{B}(\mathbf{\Gamma})\rangle|, |\langle \boldsymbol{\nabla} \cdot \mathbf{B}(\mathbf{\Gamma})\rangle| < \infty$ and $\boldsymbol{\nabla}$ is the gradient operator in the $3N$-dimensional space. Furthermore, $\langle \boldsymbol{\nabla}\mathcal{H} \cdot \mathbf{B}(\mathbf{\Gamma})\rangle$ must grow slower than e^N in the thermodynamic limit.[176] Note that for $\mathbf{B}(\mathbf{\Gamma}) = (0, ..., \Gamma_i, ..., 0)$, we obtain the generalized equipartition theorem $k_\mathrm{B}T = \langle \Gamma_i \partial\mathcal{H}/\partial\Gamma_i\rangle$. If $\Gamma_i = p_i$, we recover the equipartition theorem $k_\mathrm{B}T = \langle p_i^2/m\rangle$,[505] which we will exploit for some temperature definitions below. In turn, if Γ_i is a coordinate q_i, we obtain the Clausius virial theorem $k_\mathrm{B}T = -\langle q_i F_i\rangle$.[506] From the general expression in Eq. (4.1), we can directly

derive different temperatures such as the kinetic temperature and the configurational temperature as shown below.

Tab. 4.1 Temperature definitions. Summary of different possibilities to define temperature for a system of (inertial) ABPs in d spatial dimensions.

Symbol	Name	Definition	References	Comments
Velocity-based definitions				
T_{kin}	kinetic	$\frac{1}{2Nd}\sum_{i=1}^{N} m\left\langle (\mathbf{v}_i - \langle\mathbf{v}\rangle)^2 \right\rangle$	[103, 123, 162–168]	Eq. (4.3)
T_{kin4}	fourth-moment kinetic	$\frac{1}{2}m\sqrt{\frac{4}{Nd(d+2)}\sum_{i=1}^{N}\left\langle (\mathbf{v}_i - \langle\mathbf{v}\rangle)^4 \right\rangle}$		Eq. (4.6)
T_{MB}	Maxwell-Boltzmann	$\sqrt{\frac{m_{\text{T}}}{2\pi k_{\text{B}} T_{\text{MB}}}}\exp\left\{-\frac{m_{\text{T}} v_i^2}{2k_{\text{B}}T_{\text{MB}}}\right\},\ i = x, y, z$	[516]	Eq. (4.9)
Position-based definitions				
T_{vir}	virial	$\gamma_{\text{t}}\lim_{t\to\infty}\partial_t \text{MSD}(t) - \frac{1}{2Nd}\sum_{i=1}^{N}\left\langle \sum_{j<i}\mathbf{r}_{ij}\cdot\mathbf{F}_{ij} + \gamma_{\text{t}} v_0 \mathbf{r}_i\cdot\hat{\mathbf{p}}_i \right\rangle$		Eq. (4.11)
T_{osc}	oscillator	$k\left\langle x^2\right\rangle$	[165]	Eq. (4.12)
T_{conf}	configurational	$\frac{\left\langle (\boldsymbol{\nabla} U_{\text{tot}})^2 \right\rangle}{\langle \nabla^2 U_{\text{tot}}\rangle}$	[174, 406]	Eq. (4.14)
Dynamics-based definitions				
T_{Ein}	Einstein	$\gamma_{\text{t}} D_{\text{eff}}$		Eq. (4.15)
T_{eff}	effective	$\lim_{t\gg 1}\frac{\text{MSD}(t)}{2d\chi(t)}$	[123, 125, 526]	Eq. (4.18)

4.2.1 Velocity-based definitions

Velocity fluctuations can be used to define temperature either based on the velocities of the active particles themselves or based on the velocity distribution of tracer particles that are suspended in a bath of active particles. Here, we consider the following possibilities to define temperature based on velocities:

(1) **Kinetic temperature:** Starting from Eq. (4.1), we can derive the kinetic temperature by choosing $\mathbf{B}(\mathbf{\Gamma}) = (0, ..., 0, p_1, ..., p_{3N})$, which yields[527,528]

$$k_\mathrm{B}T = \left\langle \frac{1}{3N} \sum_{i=1}^{3N} \frac{p_i^2}{m} \right\rangle, \tag{4.2}$$

where $p_i = mv_i$ is the momentum. When we consider the average translational kinetic energy $E_\mathrm{kin} = \frac{1}{2}\sum_{i=1}^{N} m_i \left(\mathbf{v}_i - \langle \mathbf{v} \rangle\right) \cdot \left(\mathbf{v}_i - \langle \mathbf{v} \rangle\right)$ (subtracting any possible drift velocity $\langle \mathbf{v} \rangle$), we can write the kinetic temperature as

$$k_\mathrm{B}T_\mathrm{kin} \coloneqq \frac{1}{Nd} \sum_{i=1}^{N} m \left\langle \left(\mathbf{v}_i - \langle \mathbf{v} \rangle\right) \cdot \left(\mathbf{v}_i - \langle \mathbf{v} \rangle\right) \right\rangle, \tag{4.3}$$

where d is the spatial dimension. The kinetic temperature is commonly used in the field of granular particles[173,529–536] and complex plasmas,[537,538] and it is equal to the thermodynamic temperature in equilibrium systems where $\langle \mathbf{v} \rangle = 0$ and Eq. (4.3) coincides with Eq. (4.2).[504] It has also been frequently used as a well-defined temperature definition in active systems.[103,123,162–168] Note that the kinetic temperature is proportional to the mass of the particles. This has an important implication for the kinetic temperature of (inertial) active particles: Free non-interacting active particles move with their self-propulsion speed v_0 in the steady state independently of their mass. Therefore, their kinetic temperature strongly depends on their mass as demonstrated in Fig. 4.2.

For the kinetic temperature in active systems, some analytical results are known. For example, the kinetic temperature of free non-interacting ABPs ($u = 0$ in Eq. (2.2)) and similarly of active Ornstein-Uhlenbeck particles (AOUPs; see Appx. A) can be written as[158]

$$k_\mathrm{B}T_\mathrm{kin} = k_\mathrm{B}T_\mathrm{b} + mv_0^2\alpha, \tag{4.4}$$

where m is the mass of the particles and the dimensionless coefficient α is given by

$$\alpha = \frac{\tau_\mathrm{p}\gamma_\mathrm{t}/m}{1 + \tau_\mathrm{p}\gamma_\mathrm{t}/m}. \tag{4.5}$$

The first term in Eq. (4.4) is the bath temperature that determines the strength of the Brownian noise. The second term has a pure non-equilibrium origin and disappears in equilibrium. Note that Eq. (4.4) can be obtained based on the AOUP model as defined in Eq. (2.11) leading to similar results as for ABPs (cf. Subsec. 2.2.1). Further analytical results are shown in Appx. A.

The previous definition of kinetic temperature is based on the second moment of the velocity distribution. Similarly, one can use higher moments to define a variant

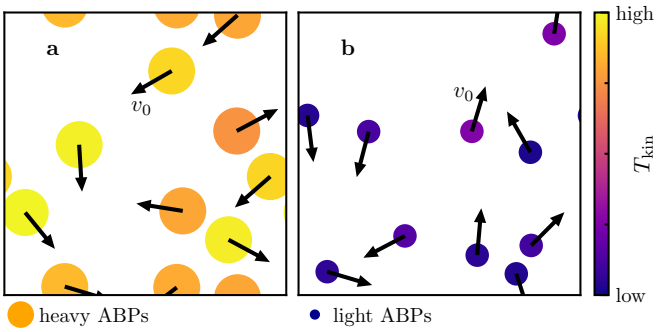

Fig. 4.2 Kinetic temperature. Schematic visualization of the kinetic temperature of active particles moving with a self-propulsion speed v_0. **a** Heavy active particles feature a large kinetic temperature and **b** light active particles have a low kinetic temperature. The color denotes the kinetic temperature, the black arrows the velocity of the particles.

of the kinetic temperature. Exemplarily, we introduce a temperature based on the fourth moment. In particular, we obtain

$$k_{\mathrm{B}}T_{\mathrm{kin4}} \coloneqq \frac{1}{2}m\sqrt{\frac{4}{Nd(d+2)}\sum_{i=1}^{N}\left\langle(\mathbf{v}_i - \langle\mathbf{v}\rangle)^4\right\rangle}, \tag{4.6}$$

where $d = 1, 2, 3$ is the spatial dimension. This temperature is again equal to the bath temperature in equilibrium, i.e., for $v_0 = 0$ in Eq. (2.2). Note that $T_{\mathrm{kin}} = T_{\mathrm{kin4}}$ if the velocity distribution $\mathcal{P}(v_i),\ i = x, y, z$ is Gaussian, i.e., if $\mathcal{P}(|\mathbf{v}|)$ follows the Maxwell-Boltzmann distribution.

(2) **Maxwell-Boltzmann temperature:** For free non-interacting particles of mass m in a classical equilibrium gas at temperature T, the Maxwell-Boltzmann distribution reads[539,540]

$$\mathcal{P}(v_x, v_y, v_z) = \left(\frac{m}{2\pi k_{\mathrm{B}}T}\right)^{3/2}\exp\left\{-\frac{m(v_x^2 + v_y^2 + v_z^2)}{2k_{\mathrm{B}}T}\right\}, \tag{4.7}$$

i.e., each velocity component $v_i,\ i = x, y, z$ is Gaussian distributed:

$$\mathcal{P}(v_i) = \sqrt{\frac{m}{2\pi k_{\mathrm{B}}T}}\exp\left\{-\frac{mv_i^2}{2k_{\mathrm{B}}T}\right\}. \tag{4.8}$$

Within an equilibrium system, the Maxwell-Boltzmann distribution can be exploited to determine the temperature of the system by measuring the velocity distribution of the particles. However, since the velocity of active particles is generally not Maxwell-Boltzmann distributed, this procedure is not directly applicable to active systems. In turn, one could use passive tracer particles as a thermometer (Fig. 4.3). While passive particles immersed in an active bath can be out of equilibrium, there are some parameter regimes, in which their velocity distribution approximately has a Maxwell-Boltzmann shape.[541,542] Therefore, their velocity distribution provides

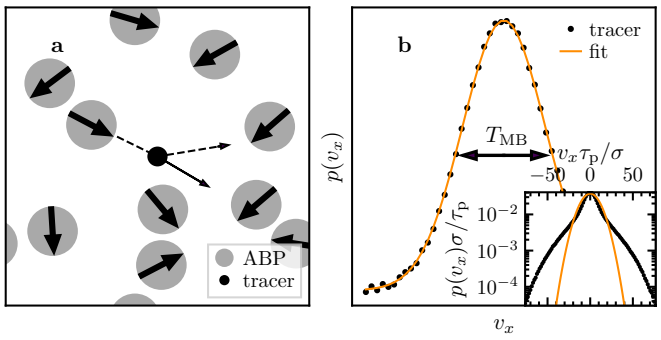

Fig. 4.3 Maxwell-Boltzmann temperature. a A passive tracer particle (black) that interacts with the surrounding active particles (gray) is used as a thermometer for the active particles. **b** Velocity distribution (black dots) of passive tracer particles in a bath of active particles. The Maxwell-Boltzmann temperature T_{MB} is obtained from the variance of a Gaussian (yellow line) fitted to the tracer velocity distribution. The inset shows the velocity distribution for the passive particles in a mixture of overdamped ABPs ($m/(\gamma_{\mathrm{t}}\tau_{\mathrm{p}}) = 5 \times 10^{-5}$) and inertial PBPs ($m/(\gamma_{\mathrm{t}}\tau_{\mathrm{p}}) = 5 \times 10^{-2}$) at Pe $= 100$, $\varphi_{\mathrm{tot}} = 0.5$, and $x_{\mathrm{a}} = 0.9$, where x_{a} denotes the fraction of active particles. In this parameter regime, the velocity distribution is clearly non-Gaussian, and therefore, the Maxwell-Boltzmann temperature cannot be sensibly calculated. The data has been taken from Ref. [542].

an approximate measure for the temperature of the active particles. We name this the Maxwell-Boltzmann temperature T_{MB} (Fig. 4.3b), which is defined via

$$\mathcal{P}(v_i) = \sqrt{\frac{m_{\mathrm{T}}}{2\pi k_{\mathrm{B}} T_{\mathrm{MB}}}} \exp\left\{-\frac{m_{\mathrm{T}} v_i^2}{2k_{\mathrm{B}} T_{\mathrm{MB}}}\right\}, \; i = x, y, z \tag{4.9}$$

where m_{T} denotes the mass of the tracer particle. Note that the Maxwell-Boltzmann temperature depends on the tracer mass and on the interactions between the active particles and the tracer. In fact, the tracer should follow the slow dynamics of the active system, which is only guaranteed if the tracer is sufficiently heavy.[516] In addition, the tracer has to be small enough to not affect the structure of the active system. Note that there are parameter regimes in which the velocity distribution is not Gaussian anymore,[542] and therefore, the Maxwell-Boltzmann temperature cannot be calculated (see inset in Fig. 4.3b). Hence, we do not show the Maxwell-Boltzmann temperature in the numerical results below.

4.2.2 Position-based definitions

We now introduce different possibilities to define temperature based on the positions of active particles and tracers.

(3) **Virial temperature:** The virial theorem connects the average kinetic energy of a system to its average potential energy by $\sum_{i=1}^{N} m \langle \mathbf{v}_i \cdot \mathbf{v}_i \rangle = -\frac{1}{2} \sum_{i=1}^{N} \langle \mathbf{r}_i \cdot \mathbf{F}_i \rangle$ and was first introduced by R. Clausius in 1870.[506] Here, $\mathbf{F}_i$ denotes the total force acting on the i-th particle. In equilibrium, the average virial $\langle \mathcal{V} \rangle = -\frac{1}{2} \sum_{i=1}^{N} \langle \mathbf{r}_i \cdot \mathbf{F}_i \rangle$ can be connected to the thermodynamic temperature T of the system by applying the

equipartition theorem as already done for the definition of the kinetic temperature. This leads to the virial temperature defined as

$$k_\mathrm{B}T_\mathrm{vir} \coloneqq \frac{2}{Nd}\langle \mathcal{V} \rangle, \tag{4.10}$$

where d denotes the spatial dimension of the system and N is again the number of active particles.[543] For inertial ABPs (Eqs. (2.2) and (2.3)) in the steady state, the virial temperature can be written as (see Appx. A for details)

$$k_\mathrm{B}T_\mathrm{vir}^\mathrm{ABP} = \gamma_\mathrm{t} \lim_{t\to\infty} \partial_t \mathrm{MSD}(t) - \frac{1}{2Nd}\sum_{i=1}^{N}\left\langle \sum_{j<i} \mathbf{r}_{ij}\cdot\mathbf{F}_{ij} + \gamma_\mathrm{t} v_0 \mathbf{r}_i \cdot \hat{\mathbf{p}}_i \right\rangle \tag{4.11}$$

with the mean-square displacement $\mathrm{MSD}(t) = \langle \mathbf{r}_i(t)^2 \rangle$ (assuming $\mathbf{r}_i(0) = 0$), interaction force $\mathbf{F}_{ij}$, and spatial dimension d. Hence, the virial temperature does only require information about the positions and the forces but not about the velocities of the particles. Therefore, it is also applicable to simulations in the overdamped limit. Note that for free ABPs, the first term is equal to $\gamma_\mathrm{t} D_\mathrm{eff}$, where D_eff is their effective diffusion coefficient, which we obtain from their long-time MSD. All other contributions are directly calculated from the particle trajectories by averaging over time in the steady state.

(4) **Oscillator temperature:** Let us now consider a particle that is confined in an external potential with a minimum at $\mathbf{r} = 0$. In equilibrium, the position fluctuations $\langle \mathbf{r}^2 \rangle$ are directly related to the thermodynamic temperature (see Appx. A). For simplicity, let us consider a harmonic confinement, i.e., $U_\mathrm{ext}(\mathbf{r}) = k\mathbf{r}^2/2$, which leads to an additional force $\mathbf{F}_{\mathrm{ext},i} = -\boldsymbol{\nabla}_{\mathbf{r}_i} U_\mathrm{ext}(\mathbf{r}_i)$ that is added on the right-hand side of Eq. (2.2).[154,171,544–546] For non-interacting particles in equilibrium, i.e., $v_0 = 0$ and $u = 0$ in Eq. (2.2), one can show that $\langle r_i^2 \rangle = k_\mathrm{B}T/k$ with $i = x, y, z$. It is tempting to generalize this equilibrium result to define an oscillator temperature. Therefore, assuming that the system is isotropic, we define the oscillator temperature as[171,547]

$$k_\mathrm{B}T_\mathrm{osc} \coloneqq k\left\langle r_i^2 \right\rangle,\ i = x, y, z. \tag{4.12}$$

There are two possibilities to measure the oscillator temperature: First, one can place the active particles themselves in the harmonic potential (Fig. 4.4a). Second, one can use a passive tracer particle trapped in a harmonic potential and interacting with surrounding non-trapped active particles (Fig. 4.4b). In terms of a general temperature definition, the tracer-based scenario has the drawback that the obtained temperature values depend on the mass of the tracer and its size, and defining a suitable tracer-based thermometer is only possible when choosing sufficiently small and heavy tracers.[165,516] Furthermore, it has been shown that the position distribution of the tracer becomes non-Gaussian for certain k.[548] Also in the former scenario, the strength k of the harmonic potential has to be adjusted to the self-propulsion speed of the active particles such that they can still reach most positions inside the harmonic potential but cannot leave it across the periodic boundaries of the simulation box (see below). We remark that the dependence on the potential

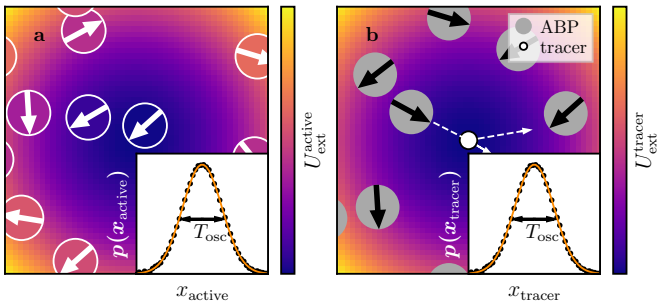

Fig. 4.4 Oscillator temperature. a Schematic illustration of active particles in a harmonic potential $U_{\text{ext}}^{\text{active}}(r) = kr^2/2,\ r = \sqrt{x^2+y^2}$ of strength k. The inset shows an exemplary distribution of the particle positions in x direction $p(x_{\text{active}})$ from which T_{osc} can be determined from the variance of a Gaussian that is fitted to the data. **b** Schematic visualization of a passive tracer particle trapped in a harmonic potential $U_{\text{ext}}^{\text{tracer}}(r) = kr^2/2,\ r = \sqrt{x^2+y^2}$ of strength k and subject to a bath of non-trapped active particles, which can collide with the tracer particle (white arrows).[165] The inset shows an exemplary distribution of the tracer position in x direction $p(x_{\text{tracer}})$ from which T_{osc} can be determined analogously as in panel a.

strength makes the use of this temperature questionable. Additionally, the use of the oscillator temperature causes problems when we consider interacting particles that repel each other and fill up the trapping potential from the center towards higher and higher potential values, as we shall see in more detail below. For simplicity, we only calculate T_{osc} without using immersed tracer particles.

For non-interacting ABPs (and AOUPs), the oscillator temperature has been calculated analytically and reads[158]

$$k_{\text{B}}T_{\text{osc}} = k_{\text{B}}T_{\text{b}} + \frac{1+\tau_{\text{p}}\gamma_{\text{t}}/m}{1+\tau_{\text{p}}\gamma_{\text{t}}/m+\tau_{\text{p}}^2 k/m} v_0^2 \tau_{\text{p}}\gamma_{\text{t}} \tag{4.13}$$

This expression is obtained from the AOUP model and coincides with the results for ABPs. It reflects the dependence of T_{osc} on the strength k of the harmonic potential and shows that it also depends on the ratio $\tau_{\text{p}}\gamma_{\text{t}}/m$.

(5) **Configurational temperature:** The configurational temperature provides another possibility to define temperature independently of the particle momenta. It can be derived from Eq. (4.1) by choosing $\mathbf{B}(\mathbf{\Gamma}) = -\boldsymbol{\nabla}U_{\text{tot}}(\{\mathbf{r}_i\})$, where $U_{\text{tot}}(\{\mathbf{r}_i\})$ denotes the total potential energy of the systems. This yields[527,528]

$$k_{\text{B}}T_{\text{conf}} = \frac{\langle \boldsymbol{\nabla}U_{\text{tot}} \cdot \boldsymbol{\nabla}U_{\text{tot}} \rangle}{\langle \nabla^2 U_{\text{tot}} \rangle}. \tag{4.14}$$

Here, $\boldsymbol{\nabla}$ is again the gradient operator in the $3N$-dimensional space. Recently, Saw et al. used the configurational temperature to measure the temperature of an active system.[174,406] In the special scenario of non-interacting particles in an external harmonic potential $U_{\text{ext}}(\mathbf{r}) = k\mathbf{r}^2/2$, we get $U_{\text{tot}} = U_{\text{ext}}$ and $T_{\text{conf}} = T_{\text{osc}}$.

As shown in Fig. 4.5, the configurational temperature measures how far a particle can ramp up the interaction potential. It is large if the forces ($\boldsymbol{\nabla}U_{\text{tot}}$) are large

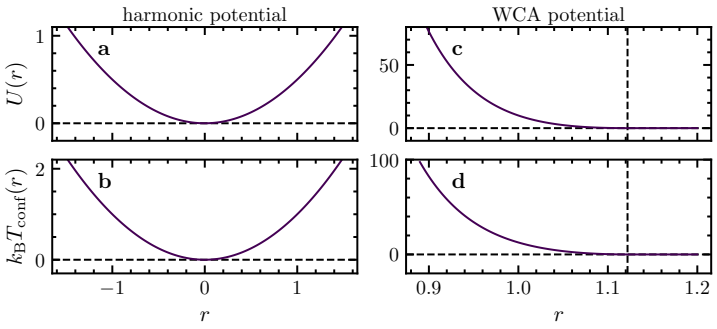

Fig. 4.5 Configurational temperature. a,**b** Exemplary harmonic potential $U(r) = 0.5kr^2$ and the corresponding contributions to the configurational temperature as defined in Eq. (4.14) as function of the distance r from the potential minimum, respectively. **c** Exemplary Weeks-Chandler-Anderson (WCA) potential as defined in Eq. (2.8) and as used for the simulations in this chapter. **d** Corresponding contributions to the configurational temperature as defined in Eq. (4.14) as function of the inter-particle distance r.

and if the curvature of the potential ($\nabla^2 U_{\text{tot}}$) is small. Therefore, contributions to T_{conf} from particles residing near the minimum of the external potential and near the equilibrium distance for interacting particles are small, i.e., if all particles are placed in the potential minimum, $T_{\text{conf}} = 0$ (Fig. 4.5b).

4.2.3 Dynamics-based definitions

All previous possibilities to define temperature directly exploit either the velocities or the positions of the particles. However, one can also exploit dynamical properties of an active system to measure its temperature. In particular, we present two approaches, one based on the Einstein relation and one following Cugliandolo and Kurchan based on linear response theory.[125,523]

(6) **Einstein temperature:** Let us again consider free non-interacting PBPs, i.e., $u = 0$ in Eq. (2.1). Then, the translational diffusion coefficient D_{t} is connected to the bath temperature via the Einstein relation: $D_{\text{t}} = k_{\text{B}} T_{\text{b}} / \gamma_{\text{t}}$.[549] We can now define a temperature for active particles based on their effective long-time diffusion coefficient D_{eff}, which can be calculated from the mean-square displacement (MSD) of the active particles (Fig. 4.6), by exploiting the Einstein relation. In particular, we define the Einstein temperature T_{Ein} as

$$k_{\text{B}} T_{\text{Ein}} \coloneqq \gamma_{\text{t}} D_{\text{eff}}. \tag{4.15}$$

If the active particles interact with each other, i.e., $u \neq 0$ in Eq. (2.2), γ_{t} has to be replaced by an effective drag coefficient γ_{eff} that is calculated from the response of a tracer particle to a constant force $\mathbf{F} = F\hat{\mathbf{e}}_x$ (exemplarily in x-direction with unit vector $\hat{\mathbf{e}}_x$) in the presence of the considered active system, i.e.,

$$\gamma_{\text{eff}} = F / \lim_{t\to\infty} \langle v_x(t) \rangle \,. \tag{4.16}$$

Note that for sufficiently low density, we have $\gamma_{\text{eff}} \approx \gamma_{\text{t}}$.

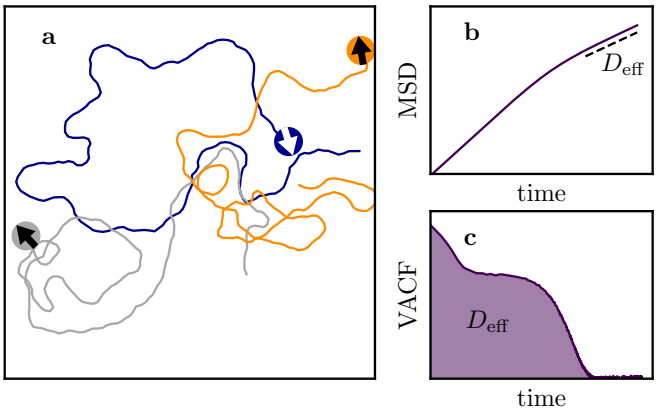

Fig. 4.6 Einstein temperature. a Exemplary trajectories of free non-interacting ABPs. Arrows denote the self-propulsion directions. **b** Mean-square displaced (MSD) of the active particles in double-logarithmic representation and long-time effective diffusion coefficient D_{eff} yielding the Einstein temperature as defined in Eq. (4.15). **c** Alternative calculation of the long-time diffusion coefficient D_{eff} from the integral of the velocity auto-correlation function (VACF) of the active particles.

For free non-interacting inertial ABPs, the effective diffusion coefficient has been calculated analytically and reads[133,157,550]

$$D_{\text{eff}}^{\text{ABP}} = D_{\text{t}} + \frac{v_0^2 \tau_{\text{p}}}{2} e^{S_{\text{R}}} S_{\text{R}}^{1-S_{\text{R}}} \Gamma(S_{\text{R}}, 0, S_{\text{R}}), \tag{4.17}$$

where $D_{\text{t}} = k_{\text{B}} T_{\text{b}} / \gamma_{\text{t}}$ denotes the translational diffusion coefficient, $S_{\text{R}} = \frac{I}{\tau_{\text{p}} \gamma_{\text{r}}}$, and $\Gamma(a, b, c) = \int_b^c \mathrm{d}q\, q^{a-1} e^{-q}$. Here, I denotes the moment of inertia of the active particles. In the overdamped limit $S_{\text{R}} \to 0$, we obtain the following popular result for the active diffusion coefficient: $D_{\text{eff}} = D_{\text{t}} + v_0^2 \tau_{\text{p}} / 2$,[77,181,253] yielding $k_{\text{B}} T_{\text{Ein}} = k_{\text{B}} T_{\text{b}} + \gamma_{\text{t}} v_0^2 \tau_{\text{p}} / 2$.

(7) **Effective temperature:** Inspired from glassy systems[507,508] and following Refs. [123, 125, 437, 526], we now define the so-called effective temperature of an active system. This expression is inspired by linear response theory and is defined as the ratio between the MSD (Eq. (3.1)) and the susceptibility χ in the long-time limit, i.e.,

$$k_{\text{B}} T_{\text{eff}}(t) := \lim_{t \gg 1} \frac{\text{MSD}(t)}{2 d \chi(t)}, \tag{4.18}$$

where d is the number of spatial dimensions. To calculate the susceptibility, one can use the Malliavin weights sampling (MWS), as used in Refs. [123, 125], or approaches that are based on the simulation of a perturbed and an unperturbed system with the same noise realizations (Fig. 4.7).[264,551,552] Here, will we use the latter approach to numerically determine T_{eff} (see Appx. A for details). Note that the calculation of the effective temperature requires to average over many independent ensembles, which is computationally expensive. In particular, we average over 100 independent simulation runs for each data point and over time in the diffusive

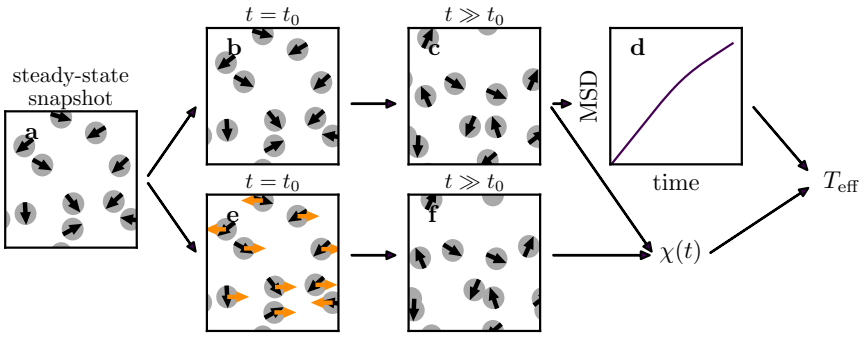

Fig. 4.7 Effective temperature. Schematic visualization of the calculation of the effective temperature T_{eff} as defined in Eq. (4.18). Starting from a snapshot of the system of active particles in the steady state (panel **a**), a copy of the system is created and perturbed by a small perturbing force at a fixed time $t = t_0$ (orange arrows in panel **e**). The original system (panel **b**) and the perturbed system are then simulated with the same noise realizations up to a time $t \gg t_0$ (panels **c** and **f**). From the unperturbed system, the mean-square displacement (MSD, panel **d**) is calculated and from the comparison of both systems, the susceptibility $\chi(t)$ is obtained. Finally, this leads to T_{eff} following Eq. (4.18).

long-time regime of the MSD. Due to the high computational costs, we calculated the effective temperature exemplarily for some parameter regimes, and we only consider data points with reasonably good statistics, i.e., data points with a standard deviation that is at least smaller than the value itself.

4.3 Simulation Results

To systematically compare the introduced possibilities to define temperature, we perform Brownian dynamics (BD) simulations of systems of $N = 2 \times 10^4$ inertial ABPs as described by Eqs. (2.2) and (2.3). The interaction between the ABPs is modeled by the Weeks-Chandler-Anderson (WCA) potential as defined in Eq. (2.8). We fix the interaction strength to $\epsilon/(k_{\text{B}}T_{\text{b}}) = 10$ or to $\epsilon = 0$ for non-interacting particles. For simplicity, we choose $\gamma_{\text{t}} = \gamma_{\text{r}}/\sigma^2$, where σ is the particle diameter. As free parameters, we vary the dimensionless mass $M = m/(\gamma_{\text{t}}\tau_{\text{p}}) = \tau_{\text{m}}/\tau_{\text{p}}$ (and accordingly, the moment of inertia I), the Péclet number $\text{Pe} = v_0/\sqrt{2D_{\text{r}}D_{\text{t}}}$, and the area fraction $\varphi = N\pi\sigma^2/(4A)$, where $A = L^2$ is the area of the two-dimensional quadratic simulation box of box length L. Here, $D_{\text{t}} = k_{\text{B}}T_{\text{b}}/\gamma_{\text{t}}$ is the translational diffusion coefficient and $\tau_{\text{m}} = m/\gamma_{\text{t}}$ is the inertial timescale. The Langevin equations (Eqs. (2.2) and (2.3)) are solved numerically with LAMMPS[255] using a time step $\Delta t/\tau_{\text{p}} = 10^{-5}$ and periodic boundary conditions. We run the simulations first for a time of $200\,\tau_{\text{p}}$ to reach a steady state and afterward for a time of $800\,\tau_{\text{p}}$ for computing time averages of observables in the steady state. For simulations in a harmonic confinement, we have chosen $k \propto 2\gamma_{\text{t}}v_0/L$ such that the resulting external force due to the harmonic confinement fulfills $|\mathbf{F}_{\text{ext}}(L/2)| = \gamma_{\text{t}}v_0$. This ensures that the active particles are able to reach each position in the harmonic potential but cannot leave it across the periodic boundaries of the simulation box. In the following, we present our

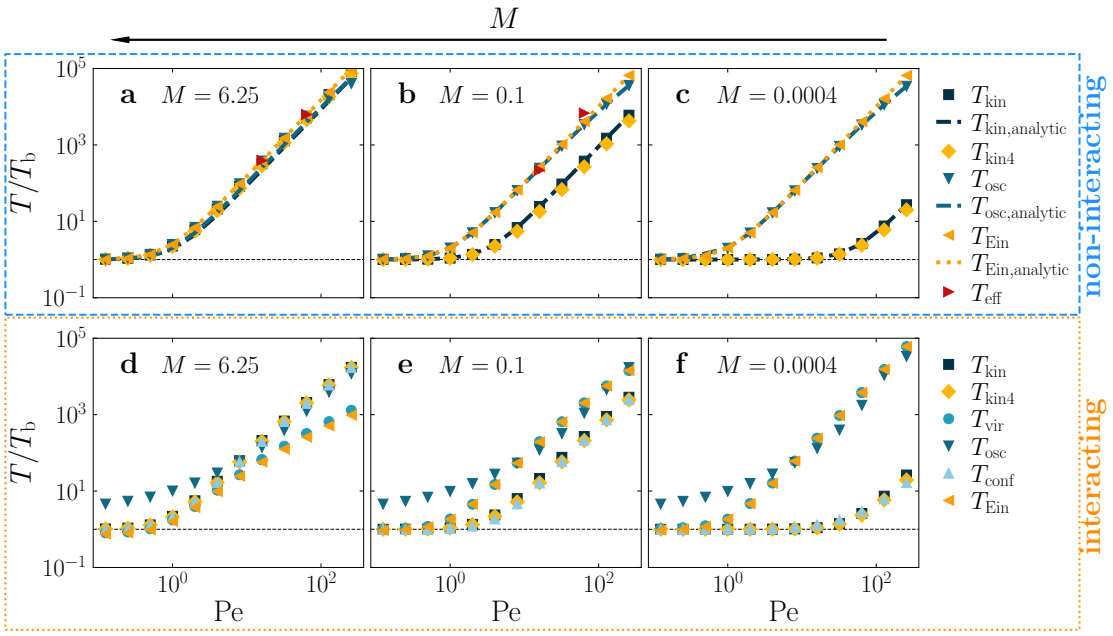

Fig. 4.8 Péclet number dependence. Temperature as function of Péclet number Pe for three different masses $M = m/(\gamma_t \tau_p)$ as given in the key. **a–c** Results for non-interacting ABPs and **d–f** for interacting ABPs at total packing fraction of $\varphi_{tot} = 0.025$. For the non-interacting case, analytical expressions are shown for the kinetic temperature (Eqs. (4.4) and (4.5); $T_{kin,analytic}$), for the oscillator temperature (Eq. (4.13); $T_{osc,analytic}$), and for the Einstein temperature (Eqs. (4.15) and (4.17); $T_{Ein,analytic}$).

main results. In particular, we show how the obtained temperature values depend on the Péclet number and the mass of the active particles.

4.3.1 Péclet dependence

Let us first discuss the Pe dependence of the considered temperatures. For simplicity, we only consider parameter regimes in which the system does not phase separate[72] and study two scenarios: non-interacting ABPs and interacting ABPs at total area fraction $\varphi_{tot} = 0.025$. To scan all regimes from the near-equilibrium case to the strongly active regime, we vary Pe from $\mathrm{Pe} = 0.125$ to $\mathrm{Pe} = 256$. To also explore different regimes from the strongly inertial regime to the overdamped regime, we determine the temperatures for three different masses $M \in \{0.0004, 0.1, 6.25\}$. The results are shown in Fig. 4.8 together with the corresponding analytical expressions for non-interacting ABPs as discussed above. These expressions perfectly match with the numerical results obtained from the BD simulations (Fig. 4.8a–c). As expected, all temperatures increase with increasing Pe. For very low Pe, the system essentially behaves as an equilibrium system and all temperatures coincide (except for the oscillator temperature for interacting ABPs as we discuss below).

Non-interacting active particles: Let us now first focus on the non-interacting case. Here, for large mass M (Fig. 4.8a), all temperatures lead to the same value and the curves

collapse to one master curve. In this case, the persistence time τ_p is small compared to the inertial time τ_m, which leads to a vanishing entropy production rate such that the system approaches an effective equilibrium state.[140,142,158] When decreasing the mass, i.e., $\tau_\mathrm{m}/\tau_\mathrm{p} \ll 1$, different temperatures generally lead to different values (Fig. 4.8b,c). Notably, the two kinetic temperatures T_kin and T_kin4 lead to very similar temperature values suggesting that the velocity distributions are approximately Gaussian. Remarkably, also T_osc and T_Ein lead to very similar temperature values even for very large Pe, where they significantly differ from T_kin and T_kin4. In fact, we find $T_\mathrm{osc} \geq T_\mathrm{kin}$ in accordance with previous literature.[171] Note that T_osc and T_kin might coincide after renormalizing the forces as demonstrated in Ref. [141]. The difference to the kinetic temperatures further increases when decreasing the mass of the active particles (Fig. 4.8b,c). This indicates that velocity-based definitions strongly depend on the dimensionless particle mass M while T_osc and T_Ein do not. The effective temperature T_eff is similar to T_osc and T_Ein (Fig. 4.8a,b). Note that we show only a few data points for T_eff because its computation is numerically rather costly.

Interacting active particles: If we now consider interactions between the active particles, we qualitatively obtain the same results. Again, all temperature values obtained with the different possibilities to define temperature except the oscillator temperature coincide for large masses and lead to the bath temperature at small Pe (Fig. 4.8d). However, the oscillator temperature T_osc saturates at a temperature larger than the bath temperature. This is because (i) the confining potential pushes the particles together such that the particles may form a dense cluster around the minimum of the confining potential and (ii) not all particles can be placed in the potential minimum in the initial state of the simulation. The latter adds some additional potential energy to the particles. As a consequence, particles at the border of the cluster have a large potential energy and lead to a large contribution to the position fluctuations $\langle r^2 \rangle$. Hence, the oscillator temperature can reach values higher than the bath temperature even for passive particles and is therefore considered as unsuitable to measure temperature. At large Pe, another deviation is visible: The Einstein temperature T_Ein and the virial temperature T_vir lead to smaller temperature values at large Pe compared to the other temperature values especially in the case of large particle mass (Fig. 4.8d). This is because collisions slow down the particles and lead to a smaller diffusion coefficient. This effect is stronger at large Pe due to a higher collision rate, and it is also stronger for heavier active particles because they need a comparatively long time to reach their self-propulsion speed v_0 after each collision. However, similar to the non-interacting scenario, the Einstein temperature T_Ein and the oscillator temperature T_osc almost coincide at intermediate and small masses and for large Pe (Fig. 4.8d–f). This is because they both effectively measure position fluctuations, and therefore, they approximately coincide. Note that T_Ein, T_vir, and T_osc do not coincide with the other temperatures because they have a weaker mass dependence as we will discuss further below. Remarkably, the configurational temperature T_conf coincides with T_kin and T_kin4 for all parameters (Fig. 4.8d–f). It measures how far an active particle can ramp up the interaction potential, and therefore, it is directly related to the kinetic energy of the particles that is converted into potential energy during collisions for example. Hence, T_conf leads to very similar temperature values as T_kin and T_kin4.

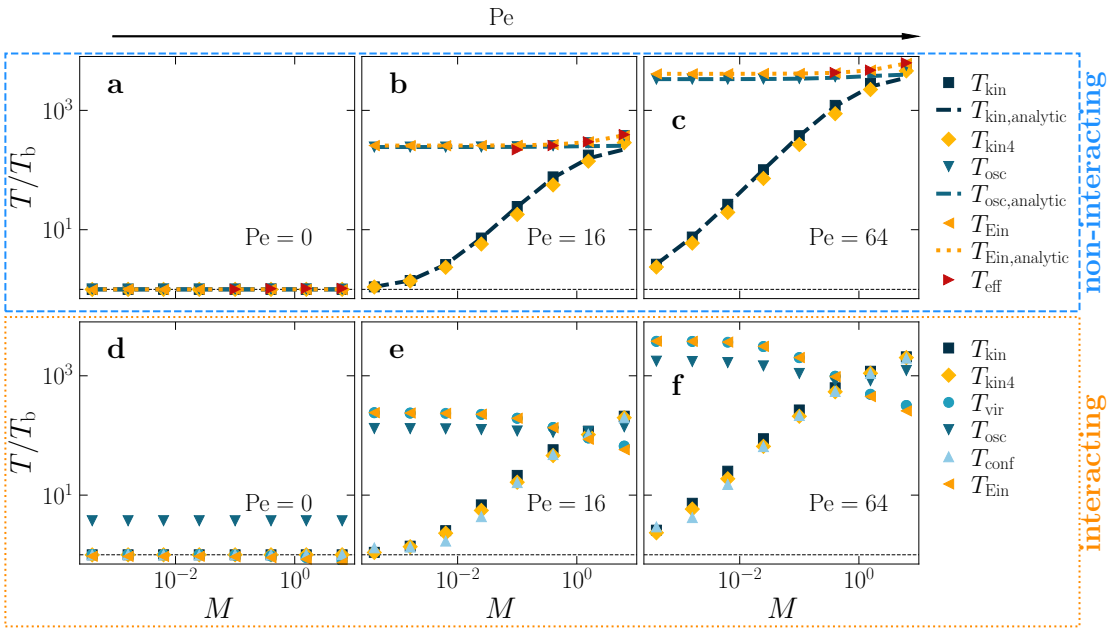

Fig. 4.9 Mass dependence. Temperature as a function of the particle mass $M = m/(\gamma_\mathrm{t}\tau_\mathrm{p})$ for three different values of Pe as given in the key. **a–c** Results for non-interacting ABPs and **d–f** for interacting ABPs at total packing fraction of $\varphi_\mathrm{tot} = 0.025$. For the non-interacting case, analytical expressions are shown for the kinetic temperature (Eqs. (4.4) and (4.5); $T_\mathrm{kin,analytic}$), for the oscillator temperature (Eq. (4.13); $T_\mathrm{osc,analytic}$), and for the Einstein temperature (Eqs. (4.15) and (4.17); $T_\mathrm{Ein,analytic}$).

4.3.2 Mass dependence

To obtain further insights into the parameter dependencies of the different temperatures, we now analyze the mass dependence in more detail. We vary $M = m/(\gamma_\mathrm{t}\tau_\mathrm{p})$ from 0.0004 to 6.25 for Pe $\in \{0, 16, 64\}$. The results are shown in Fig. 4.9 again together with the analytical results for non-interacting ABPs. For the latter, the numerical results perfectly coincide with analytical expressions discussed above (Fig. 4.9a–c). As expected from equilibrium thermodynamics, all temperatures lead to the same temperature values, namely the bath temperature T_b, for Pe $= 0$. For Pe > 0, the different temperatures again lead to different temperature values and exhibit an important mass dependence: While the oscillator temperature T_osc does not depend on M and the Einstein temperature T_Ein, the effective temperature T_eff, and the virial temperature T_vir only show a weak mass dependence, both kinetic temperatures T_kin and T_kin4 as well as the configurational temperature T_conf feature a strong mass dependence (Fig. 4.9). In the absence of interactions, this is because the particles move with their self-propulsion speed $\langle|\mathbf{v}|\rangle \approx v_0$, and accordingly, we have $T_\mathrm{kin} \approx mv_0^2/2 \propto m$ for large Pe. Thus, for $m \to 0$ (i.e, $M \to 0$), the active contribution to T_kin vanishes and we have $T_\mathrm{kin} \approx T_\mathrm{b}$. In turn, T_Ein, T_eff, T_vir, and T_osc only slightly depend on M (Fig. 4.9b,c): Their calculation is based on position fluctuations which depend only weakly on M in some parameter regimes if the particles (on average) move with their self-propulsion speed v_0. The observed trends are robust and still apply in the presence of interactions (Fig. 4.9d–f).

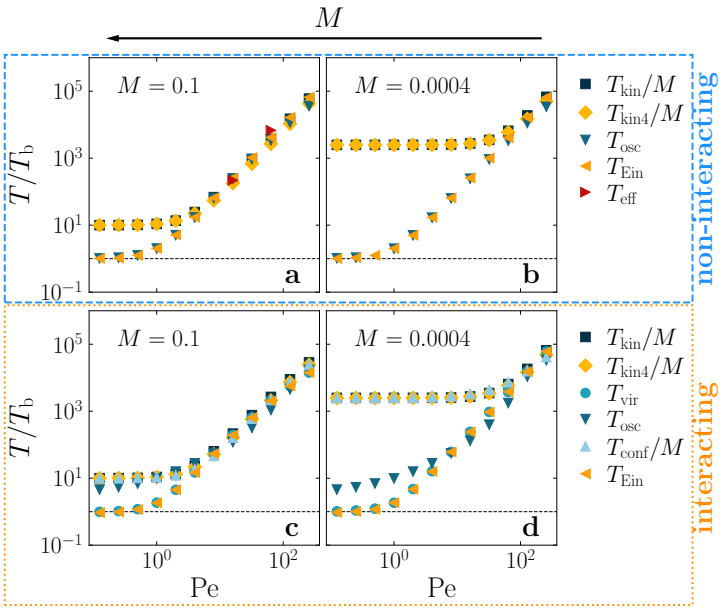

Fig. 4.10 Péclet number dependence of rescaled temperatures. Temperature as a function of Pe for two different masses $M = m/(\gamma_t \tau_p)$ as given in the key. All temperatures with a strong mass dependence are rescaled with M. **a**,**b** Results for non-interacting ABPs, i.e., $u = 0$ in Eq. (2.2). **c**,**d** Results for interacting ABPs at total packing fraction $\varphi_{tot} = 0.025$.

Mass scaling: From Fig. 4.9, we see that some temperature definitions strongly depend on the mass of the active particles. Inspired by the proportionality to m of the kinetic temperatures for large Pe, where $\langle \mathbf{v} \rangle \approx v_0$ (Eqs. (4.3) and (4.6)), we divide all temperatures that show a strong mass dependence (T_{kin}, T_{kin4}, and T_{conf}) by $M = m/(\gamma_t \tau_p)$ (Figs. 4.10 and 4.11). From the Pe-dependence, we see that now all definitions lead to similar temperatures at large Pe for both non-interacting and interacting ABPs (Fig. 4.10). Note that the regime in which the (rescaled) temperatures coincide is larger if the active particles are heavier. This is reflected by the analytical expressions discussed above, which show that for low or moderate Pe, the kinetic temperature is not simply proportional to m but has a more complicated mass dependence encoded in the factor α for example (cf. Eq. (4.5)). This becomes visible in Fig. 4.11, which reflects that the different temperatures do of course not fully match even if rescaled with M.

4.3.3 Effect of the packing fraction

Finally, we exemplarily analyzed the effect of the total packing fraction on the values of the kinetic temperatures T_{kin} and T_{kin4}, the configurational temperature T_{conf}, and the Einstein temperature T_{Ein}. We have chosen the total packing fraction as $\varphi_{tot} \in \{0.025, 0.05, 0.1, 0.2\}$ such that the system is still uniform and does not undergo MIPS[72,124,165] and fixed an intermediate mass of $M = 0.1$. As shown in Fig. 4.12, increasing the packing fraction decreases the temperature values but the overall Pe dependence is the same. This is because increasing the total packing fraction leads to an increased collision rate. The collisions tend to slow down the active particles and hinder the particles to reach their

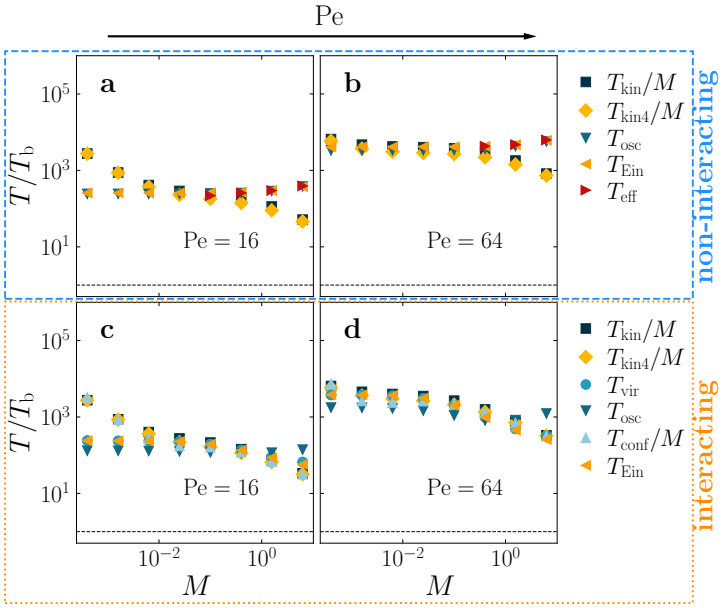

Fig. 4.11 Mass dependence of rescaled temperatures. Temperature as a function of the dimensionless particle mass $M = m/(\gamma_t \tau_p)$ for two different Pe as given in the key. All temperatures with a strong mass dependence are rescaled with M. **a**,**b** Results for non-interacting ABPs, i.e., $u = 0$ in Eq. (2.2). **c**,**d** Results for interacting ABPs at total packing fraction $\varphi_{tot} = 0.025$.

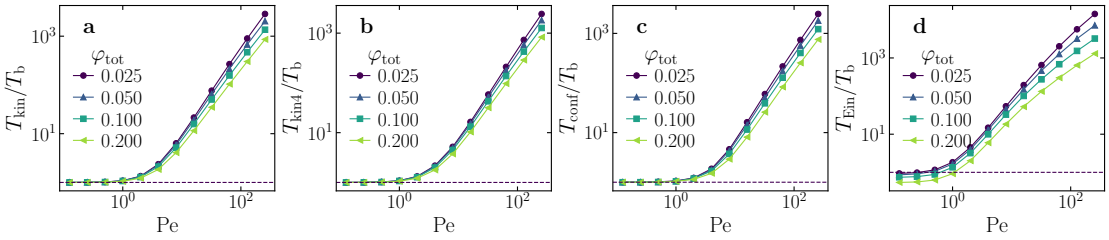

Fig. 4.12 Effect of the packing fraction. Temperature values for a fixed mass $M = 0.1$ as function of the Péclet number Pe and at different total packing fractions φ_{tot} (indicated in the keys) for **a** the kinetic temperature T_{kin}, **b** the fourth-moment kinetic temperature T_{kin4}, **c** the configurational temperature T_{conf}, and **d** the Einstein temperature T_{Ein}. The black dashed line denotes the bath temperature T_b.

self-propulsion speed v_0. Hence, increasing the packing fraction opposes the effect of activity on the average speed of the particles and reduces the values of the considered temperatures. Close to equilibrium, all temperatures are equal to the bath temperature for all packing fractions except for the Einstein temperature (Fig. 4.12d). Here, we have used the same drag coefficient γ_t for all packing fractions to calculate T_{Ein}. However, increasing φ_{tot} reduces the MSD, and hence, also T_{Ein}. In particular, the resulting diffusion coefficient becomes smaller for larger packing fraction. Hence, also T_{Ein} decreases with increasing φ_{tot}. This also happens close to equilibrium and leads to an Einstein temperature slightly smaller than the bath temperature. One could compensate for this effect by calculating the effective drag coefficient as shown in Eq. (4.16).

4.4 Conclusions

Our analytical and numerical results show that different possibilities to define temperature typically lead to different temperature values. However, close to equilibrium, all temperatures coincide. In active systems, one can approach (effective) equilibrium states in two ways: First, in the limit Pe $\to 0$, activity vanishes and the system forms an equilibrium system made of passive Brownian particles, for which all temperatures coincide with the bath temperature. Second, in the limit $M \to \infty$, the persistence time τ_p becomes small compared to the inertial time $\tau_\mathrm{m} = m/\gamma_\mathrm{t}$. Then, the motion of the active particles is dominated by (rotational) diffusion, and the system reaches an effective equilibrium state at a larger temperature than the bath temperature. This is also indicated by a vanishing entropy production rate in the limit $1/M = \tau_\mathrm{p}/\tau_\mathrm{m} \to 0$.[140,264]

It is now tempting to distinguish between "good" and "bad" temperature definitions: A "good" temperature definition should provide consistent temperature values that are independent of details of the thermometer and the confining potential. Therefore, we conclude that the oscillator temperature and any tracer-based temperature definition generally can be considered as a comparatively "bad" definition of temperature in active systems. This is because the oscillator temperature strongly depends on the potential strength k and bears the risk of not agreeing with the bath temperature in the equilibrium limit for interacting particles because it does not appropriately account for interaction forces compared to the virial temperature for example. In turn, any tracer-based definition requires heavy and small tracer particles such that they (i) follow the slow dynamics of the active system and (ii) do not affect its structure.[165,516] Furthermore, some temperatures are computationally demanding such as the effective temperature. In contrast, all other temperatures can be considered as comparatively "good" in the sense that they do not suffer from these drawbacks. While their values of course depend on details of the considered system (dimensionless parameters such as the reduced mass, Péclet number, and packing fraction), we found that several temperatures approximately coincide even far from equilibrium. Concretely, the kinetic temperature T_kin, the fourth-moment-based kinetic temperature T_kin4, and the configurational temperature T_conf constitute a class of temperatures that all assume very similar temperature values over a wide parameter range. Notably, the virial temperature T_vir, the Einstein temperature T_Ein, the oscillator temperature T_osc, and the effective temperature T_eff form a second class of temperatures whose values approximately coincide with each other but which strongly differ from those of the first class. Beyond that, we found that the two different classes of temperatures can be matched in the far-from equilibrium regime where the system is dominated by activity (large Pe, small mass) by rescaling temperatures with the particle mass.

Overall, regarding the question of "How to define temperature in active systems?", we note that our numerical results reflect the general expectation that far from equilibrium, different temperatures lead to different temperature values. This is because the particle positions and velocities are non-trivially coupled in active systems, and in general, they often follow different non-Boltzmann distributions. This implies that it is impossible to uniquely quantify fluctuations in active systems based on a single temperature parameter. However, beyond this generic fact, we found that certain possibilities to define temperature are advantageous over others in the sense that they are (i) easy to calculate from numerical

(or experimental) data, (ii) do not depend on properties of the used “thermometer” such as tracer size and mass or a confining potential, and (iii) mutually lead to similar temperature values over a wide parameter regime. In particular, the kinetic temperatures T_{kin}, T_{kin4} and the configurational temperature T_{conf} have these advantages.

The results of this chapter serve as a starting point towards a systematic classification and unification of different possibilities to define temperature in active systems. They invite further studies to generalize the suggested temperature definitions and to fundamentally explain and exploit the identified temperature classes that lead to similar temperature values. Of course, alternatively, for non-homogeneous systems, one can choose to give up the definition of a global temperature altogether in far-from-equilibrium systems and to define a local temperature instead, which can be done by calculating the presented temperature definitions in a subdomain of the considered system.

5 Active Refrigerators

Now, we explore the kinetic temperature in systems of inertial ABPs that undergo MIPS. Based on the observation that inertial ABPs show different kinetic temperatures in the dense and the dilute phase when undergoing MIPS (see Sec. 2.3 for details), we now pose the question how we can use this effect to create a refrigerator for active particles, i.e., to cool active particles in a predefined spatial region. In this chapter, we present the refrigerator's operational principle, which is illustrated in Fig. 5.1. It exploits the peculiar but so-far unknown shape of the phase diagram of inertial ABPs to initiate MIPS in the targeted cooling domain only. This allows us to reduce the kinetic temperature of the active particles by up to two orders of magnitude below the environmental temperature. The main content of this chapter is taken from my publication "Active Refrigerators Powered by Inertia" published in the *Physical Review Letters* (2022) and reprinted with permissions from Ref. [165], © 2022 by the American Physical Society, and the majority of this chapter is taken verbatim from it. In this publication, I have performed all simulations, analyzed all simulation data, wrote the initial draft, and created all figures.

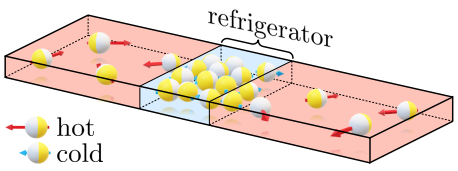

Fig. 5.1 Sketch of an active refrigerator. The active particles undergo MIPS in the cooling domain (blue) leading to a smaller kinetic temperature compared to the environment (red).

5.1 Introduction

Many processes in nature allow to readily heat up an isolated system. Examples include the release of heat in chemical reactions occurring, e.g., when burning wood or gas, inelastic collisions occurring within resistors when exposed to electric currents, and mass-energy conversion processes in nuclear power plants and helium-burning stars. Following the second law of thermodynamics, none of these processes can be reverted, making us believe that it is impossible to cool down an isolated physical system. Accordingly, cooling down a target domain such as the inside of a refrigerator or atoms in a magneto-optical trap requires that the relevant domain is in contact with an external bath to which heat can be transferred via conduction, convection, radiation, or evaporation. Accordingly, developing sophisticated techniques to transfer heat from a target system to the environment has been a great challenge of twenties century physics.[504,553–556]

For active systems,[4,21,27,28,65,83,557,558] which consist of self-propelled particles and are intrinsically out of equilibrium, the second law does not apply to the active particles but only to the overall system, as we discuss further below. Therefore, in this chapter,

we ask if it is possible to cool down a system of active Brownian particles (ABPs)[21,249] *in a certain target region* (refrigerator, Fig. 5.2a) in terms of their kinetic temperature without requiring a mechanism to transfer energy to particles in the (spatially separated) environment.

To achieve this, we exploit the previous finding that ABPs can spontaneously phase separate into a dense and a dilute phase via MIPS, as explained in Sec. 2.3.[72,83,110,259,293] While MIPS behaves similarly to an equilibrium phase transition at large scales in the overdamped limit,[110,111,559,560] in the presence of inertia, as relevant for, e.g., activated dusty plasmas[561,562] or vibrating granular particles,[121,154,156,157,229,290,563–566] the coexisting phases feature different temperatures, which is, in contrast to clustering in granular gases caused by inelastic collisions,[567–571] a consequence of self propulsion and elastic collisions.[103,123] However, this finding alone is not sufficient to design an active refrigerator, because it leads to a dense and cold phase which occurs as randomly distributed clusters which move, merge, and coarsen, and ultimately lead to a uniform temperature profile when averaging over many realizations or a long time (Fig. 5.3a).

Thus, to create an active refrigerator, we need to meet the challenge of finding a mechanism allowing us to initiate MIPS in the targeted cooling domain only and to localize the dense phase in that region. To achieve this, one naive approach could be to implement a nonuniform motility[572,573] (e.g., through controlling the laser intensity in light-fueled swimmers)[237,574–576] such that particles in the targeted cooling domain show a (large) Péclet number beyond the critical value for the MIPS phase transition, whereas particles in the environment feature a (small) sub-critical Péclet number (Fig. 5.2b, regime (I)). However, this does not work because Pe and density essentially behave inversely to each other[83,293] such that locally increasing Pe decreases the density in the same spatial region and does not result in a significant temperature difference (Fig. 5.3b). Remarkably, however, the opposite strategy turns out to work in a carefully selected portion of the phase diagram (Fig. 5.2b, regime (II)): We find that reducing Pe in the targeted cooling domain by less than 5 % as compared to the environment reduces the kinetic temperature of the ABPs by two orders of magnitude. This surprising finding exploits a remarkable difference between the phase diagram of inertial ABPs and the well-known phase diagram of overdamped ABPs: While MIPS occurs in overdamped ABPs when both Pe and the density are sufficiently large, in underdamped ABPs, it occurs at sufficiently large density and intermediate Pe. Thus, when choosing values of Pe within this intermediate regime in the targeted cooling domain and higher values in the environment, the density further increases in the former region bringing the system deeper into the MIPS regime and further away from it outside. That is, inertia is required twice: First, to induce the two-temperature coexistence and second, to create the required shape of the phase diagram.

The resulting active refrigerator exemplifies a fundamentally new way to locally cool down a physical system. Like ordinary refrigerators, it can be used to cool down other objects. However, as opposed to ordinary cooling devices, active refrigerators use a self-organized cooling domain such that no isolating walls are required to separate the cooling domain from its environment. As a consequence, active refrigerators can in principle also be used as a device to absorb particles from the environment and to store them for a long time, as we shall see.

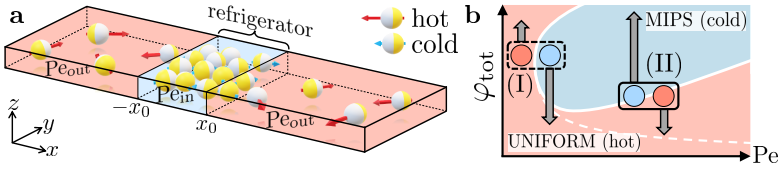

Fig. 5.2 Active refrigerator and schematic phase diagram. a Schematic of the active refrigerator, which exploits the peculiar shape of the phase diagram schematically shown in panel **b**. The blue region represents phase coexistence (MIPS), the white solid line the newly discovered transition line for inertial ABPs in comparison with the well-known transition line for overdamped ABPs (dashed line). Boxes and arrows refer to relevant parameter regimes discussed in the text.

5.2 Results

We consider Brownian dynamics simulations of the inertial ABP model in two spatial dimensions as introduced in Subsec. 2.2.1. In the following, we first briefly discuss simulation details and the refrigerator setup. Then, we present an exemplary realization of the refrigerator, and we explore the MIPS phase diagram to identify suitable parameter regimes for its design. Based on the phase diagram, we develop a design rule and explore the underlying mechanism in detail. Afterwards, we show how the operational principle of the refrigerator depends on system parameters such as the system size, the size of the targeted cooling domain, the Péclet number, and the mass of the active particles. Finally, we demonstrate the use of an active refrigerator to trap and cool passive tracer particles.

5.2.1 Simulation details

All simulations are performed with LAMMPS[255] using the ABP model with inertia (Eqs. (2.2) and (2.3)). Note that the ABP model does not explicitly describe the self-propulsion mechanism, the underlying energy source, or how energy is dissipated into the bath.[77,249] We develop a thermodynamically consistent picture in Sec. 5.3. Here, we fix $m/(\gamma_{\mathrm{t}}\tau_{\mathrm{p}}) = 5\times10^{-2}$, $\epsilon/(k_{\mathrm{B}}T_{\mathrm{b}}) = 10$, and $\sigma/\sqrt{D_{\mathrm{t}}/D_{\mathrm{r}}} = 1$ with the persistence time $\tau_{\mathrm{p}} = 1/D_{\mathrm{r}}$. We use the moment of inertia of a rigid sphere, i.e., $I = m\sigma^2/10$, leading to $I/(\gamma_{\mathrm{r}}\tau_{\mathrm{p}}) = 5\times10^{-3}$. For simplicity, we choose $\gamma_{\mathrm{t}} = \gamma_{\mathrm{r}}/\sigma^2$ (note that in experiments of active granulates, the Stokes-Einstein relation does not apply)[157] and vary Pe and the total area fraction $\varphi_{\mathrm{tot}} = N\pi\sigma^2/(4A)$, where $A = L_xL_y$, $L_y/L_x = 0.05$, denotes the area of the simulation box. The Langevin equations are solved for up to $N = 10^5$ particles using periodic boundary conditions and a time step $\Delta t/\tau_{\mathrm{p}} = 10^{-5}$.

The refrigerator setup is illustrated in Fig. 5.2a: The simulation area is divided into two regions, in which the particles have different Péclet numbers $\mathrm{Pe}(x_i) = v_0(x_i)/\sqrt{2D_{\mathrm{r}}D_{\mathrm{t}}}$, i.e., the self-propulsion speed of each particle depends on its position according to

$$v_0(x_i) = \begin{cases} v_{0,\mathrm{in}}, & -x_0 < x_i < x_0 \\ v_{0,\mathrm{out}}, & \text{else} \end{cases}, \tag{5.1}$$

with $x_0 \ll L_x$. Note that our results are robust with respect to changes of x_0, N, m, $v_{0,\mathrm{in}}$, and $v_{0,\mathrm{out}}$ and in particular apply to values of $m/(\gamma_{\mathrm{t}}\tau_{\mathrm{p}})$ used in previous works (Figs.

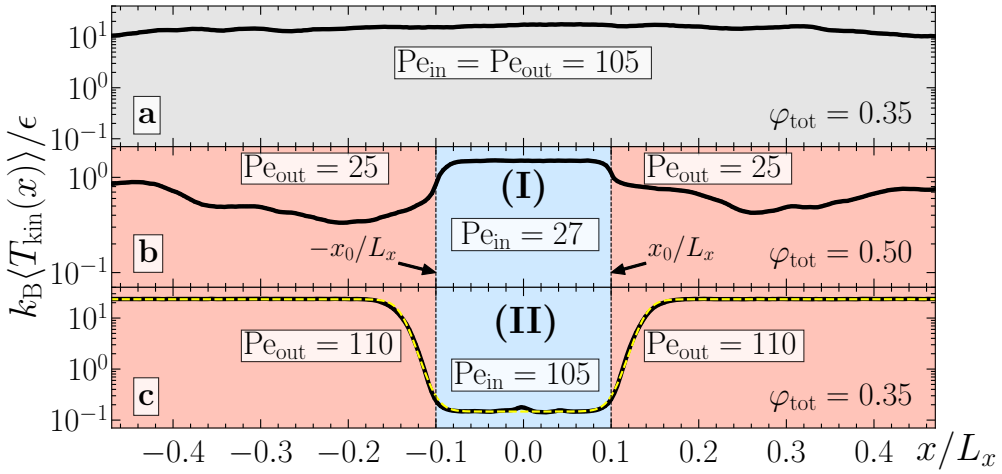

Fig. 5.3 Kinetic temperature profiles. Kinetic temperature profiles $k_{\mathrm{B}}T_{\mathrm{kin}}(x) = m\langle|\mathbf{v}|^2\rangle_y/2$ in the steady state averaged over the y coordinate and 20 realizations with $N = 16\,000$ particles for **a** uniform Pe and **b–c** nonuniform Pe and parameters shown in the key. The yellow dashed line is a fit of $f(x) = a(2 - \tanh(b(x + c)) + \tanh(b(x - c)))/2 + d$, where a, b, c, and d are free fit parameters.

5.8–5.11).[103,123,124,138,152,577] Initially, all particles are uniformly distributed in the whole simulation area.

5.2.2 Cooling active particles in a certain spatial region

The goal is now to find $\mathrm{Pe_{in}}$ and $\mathrm{Pe_{out}}$ such that (i) MIPS occurs in the targeted cooling domain only and (ii) the resulting dense phase stays in that region. Notice first, that when choosing $\mathrm{Pe_{in}} = \mathrm{Pe_{out}}$, in each individual realization, we find different kinetic temperatures in coexisting phases, but the ensemble-averaged (or time-averaged) kinetic temperature profile is uniform (Fig. 5.3a). If we choose $\varphi_{\mathrm{tot}} = 0.5$ and $\mathrm{Pe_{in}} > \mathrm{Pe_{out}}$ (regime (I) in Fig. 5.2b) to trigger MIPS in the target domain only, however, we obtain only a weak temperature difference, which even goes in the wrong direction (Fig. 5.3b). Here, the particle density compensates the difference in Pe because the residential time of a particle in a small volume element scales inversely to its speed. This effect is indicated by the gray arrows in Fig. 5.2b. Note that the arrow length depends on the density of both phases and thus, is not obvious. More generally, when choosing other combinations $\mathrm{Pe_{in}} > \mathrm{Pe_{out}}$ and density in the left part of the phase diagram (Fig. 5.2b, regime (I)), we do not observe any relevant cooling in the target domain. Remarkably, however, if we choose a comparatively low area fraction of $\varphi_{\mathrm{tot}} = 0.35$ and $\mathrm{Pe_{in}} = 105 < \mathrm{Pe_{out}} = 110$ (regime (II) in Fig. 5.2b), we observe that the system undergoes MIPS exclusively in the target domain and the dense phase remains in that region (see also Fig. B1 in Appx. B). This results in a striking cooling effect by more than two orders of magnitude in the cooling domain from $k_{\mathrm{B}}\langle T_{\mathrm{kin}}^{(\mathrm{out})}\rangle/\epsilon \approx 23.4$ to $k_{\mathrm{B}}\langle T_{\mathrm{kin}}^{(\mathrm{in})}\rangle/\epsilon \approx 0.147$ (Fig. 5.3c), which is further enhanced when choosing larger Pe differences and complemented by a significantly lower entropy production rate in the cooling domain and an inward flow of kinetic energy as discussed further below.

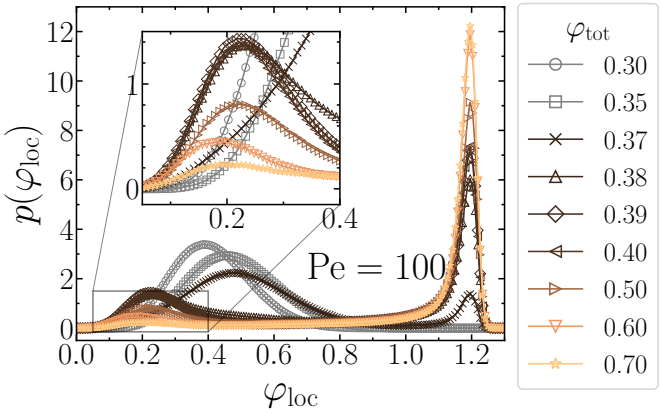

Fig. 5.4 Local area fraction. Distribution of the local area fraction φ_{loc} (Eq. (3.4)) for different total area fractions φ_{tot} (values are shown in the key). Gray curves correspond to a uniform state, colored curves to a phase-separated (MIPS) state. Parameters: $N = 20\,000$, $m/(\gamma_{\mathrm{t}}\tau_{\mathrm{p}}) = 5 \times 10^{-2}$, $I/(\gamma_{\mathrm{r}}\tau_{\mathrm{p}}) = 5 \times 10^{-3}$, $\epsilon/(k_{\mathrm{B}}T_{\mathrm{b}}) = 10$, $\sigma/\sqrt{D_{\mathrm{t}}/D_{\mathrm{r}}} = 1$, Pe $= 100$.

5.2.3 Phase diagram of inertial active Brownian particles

To understand the possible parameter choices for constructing active refrigerators in detail, we now explore the phase diagram of inertial ABPs in the Pe-φ_{tot}-plane, which has remained unknown to date. The key control parameters of the system are ϵ, Pe, and φ_{tot} for fixed m and I. We additionally fix ϵ and vary Pe and φ_{tot}. To determine the phase diagram, we used a quadratic simulation area with periodic boundary conditions and $N = 20\,000$ particles. We scanned the parameter ranges $\varphi_{\mathrm{tot}} \in [0.1, 0.9]$ in steps of 0.01 in the vicinity of to the transition line and in steps of 0.1 otherwise, and Pe $\in [0, 300]$ in steps of 2 for Pe < 60 and in steps of 20 for Pe ≥ 60. We averaged over 3–10 realizations for each parameter combination resulting in about 4 770 simulations in total. The phase transition line between the uniform and the coexistence (MIPS) regime was obtained based on the distribution of the local area fraction $p(\varphi_{\mathrm{loc}})$, which is unimodal in the uniform regime and bimodal in the coexistence regime.[71,72,152] We calculated $p(\varphi_{\mathrm{loc}})$ based on averages over circles of radius 5σ and 3–10 realizations using Eq. (3.4). The results are exemplarily shown in Fig. 5.4 for Pe $= 100$. Interestingly, the resulting transition line shown in Fig. 5.5 does not follow the well-known relation Pe $\propto 1/\varphi_{\mathrm{tot}}$, which was found in the overdamped regime.[99,259] In striking contrast, we find that Pe $\propto \varphi_{\mathrm{tot}}$ in the large Pe regime (green part of the transition line in Fig. 5.5). This relation serves as a crucial ingredient to construct an active refrigerator. Intuitively, it can be understood to occur as a direct consequence of inertial effects: The particles bounce back when they collide with each other, and the rebound is much stronger for large Pe than for moderate Pe. Therefore, to slow down locally, more collisions are necessary. Hence, a larger area fraction is required at larger Pe to initiate MIPS.

5.2.4 Design rule for active refrigerators

Based on the transition line, we can formulate the following strategy to realize an active refrigerator: First, we want to initiate MIPS in the target domain. This can be achieved

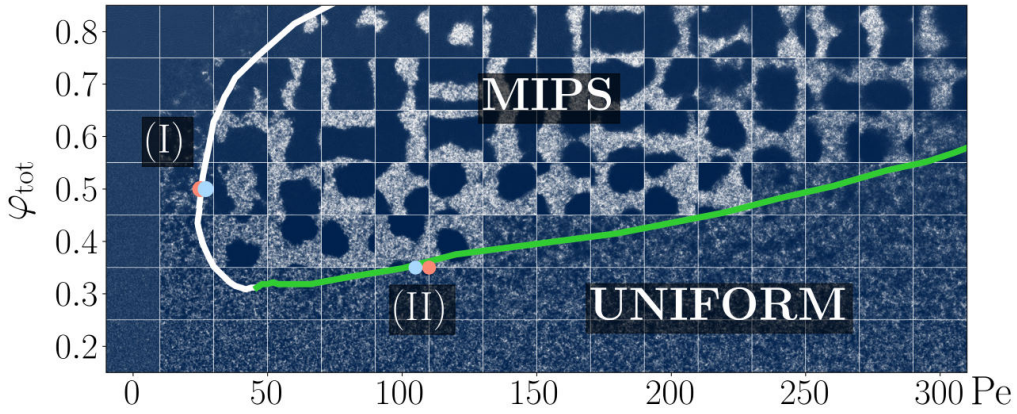

Fig. 5.5 Phase diagram. Phase diagram of $N = 20\,000$ inertial ABPs (background images are steady-state snapshots) showing parameter regimes in which the system undergoes MIPS and in which it stays uniform. The solid line shows the transition line obtained from the analysis of the local packing fraction (cf. Subsec. 5.2.3). In the vicinity of its green part, parameters can be chosen to construct active refrigerators.

by choosing $(\mathrm{Pe}_{\mathrm{in}}, \varphi_{\mathrm{in}})$ inside the MIPS region of the phase diagram for the target domain. Second, we do not want the system to undergo MIPS outside the target domain. Hence, we choose $(\mathrm{Pe}_{\mathrm{out}}, \varphi_{\mathrm{out}})$ outside the coexistence region. Third, we want the particle flux which emerges as a consequence of choosing two different Pe to bring the system deeper into the coexistence regime within the target domain but further away from it outside. Clearly, based on the obtained detailed knowledge of the phase transition line, the first two criteria can be easily met by fixing a suitable area fraction $\varphi_{\mathrm{in}} = \varphi_{\mathrm{out}} = \varphi_{\mathrm{tot}}$ and choosing two Péclet numbers on both sides of the transition line. However, the third criterion can only be met by choosing parameter combinations in the vicinity of the green marked part of the transition line in Fig. 5.5 (regime (II)). To see this, we will next discuss the particle current which emerges when choosing two different Pe.

5.2.5 Mechanism: Supportive and counteracting feedback

Let us first recall that the mean speed of an ABP decreases with increasing φ_{tot} and increases with increasing Pe. To show this relation explicitly, we exemplarily evaluated the dependence of the mean speed $\langle|\mathbf{v}|\rangle$ on the total area fraction φ_{tot} for $\mathrm{Pe} \in \{10, 20, 30, 40\}$ (Fig. 5.6). When we have no MIPS (small Pe) at low enough area fractions, a linear dependence similar to the overdamped regime is observed,[83,292,293] which breaks down at large area fractions. For higher Pe and especially in the MIPS regime, the linear dependence also breaks down as already found for overdamped ABPs,[292] but $\langle|\mathbf{v}|\rangle$ is still decreasing with increasing φ_{tot}. Consequently, when we have two regions with different Pe, a lower density will emerge in the high-Pe region and a larger one in the low-Pe region. Therefore, the gray arrows in Fig. 5.2b always point to lower φ_{tot} at the high-Pe point and vice versa.

In regime (I) and more generally, in the vicinity of the white part of the transition line in Fig. 5.5, we need to choose $\mathrm{Pe}_{\mathrm{in}} > \mathrm{Pe}_{\mathrm{critical}} > \mathrm{Pe}_{\mathrm{out}}$ to initiate MIPS in the target domain only. Consequently, the density initially decreases in that region (Fig. 5.7a).

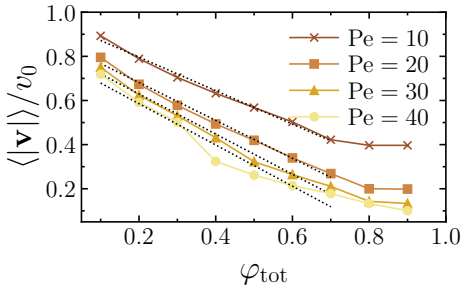

Fig. 5.6 Density-dependent mean speed. Density dependence of the mean speed (parameters as in Fig. 5.4) for different Pe (values are shown in the key). Black dotted lines are fits of $\langle|\mathbf{v}|\rangle/v_0 = a(1 - \varphi_{\mathrm{tot}}/\varphi^*)$ to the first seven data points. For Pe $= 10$ and Pe $= 20$, we obtain $a = 0.95 \pm 0.01$, $\varphi^* = 1.25 \pm 0.03$ and $a = 0.85 \pm 0.02$, $\varphi^* = 0.99 \pm 0.03$, respectively.

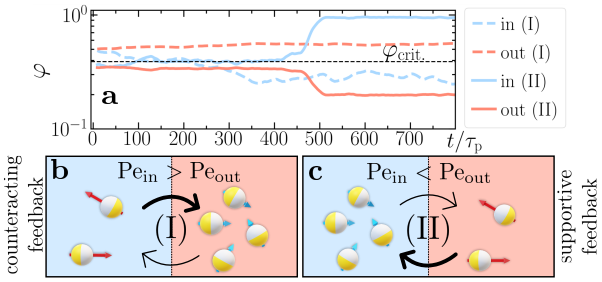

Fig. 5.7 Mechanism. a Area fraction φ calculated using Eq. (3.4) in inner and outer regions over time for regime (I) and (II) (parameters as in Fig. 5.3). The dashed horizontal line shows the critical area fraction $\varphi_{\mathrm{crit.}} \approx 0.39$ for Pe $= 27$. A **b** counteracting (**c** supportive) feedback loop decreases (increases) the particle density in the target region.

Interestingly, the area fraction in the target domain typically decreases to values below the transition line even for a relatively small Pe difference, which fully prevents MIPS in the target domain. This surprisingly strong decrease can be viewed as the result of a positive feedback loop: The decrease of the particle density in the target domain increases the mean speed of the particles in that region, which further decreases the particle density in the target domain. Thus, no cooling occurs within that region (but rather the opposite, see Fig. 5.3). In stark contrast, following the peculiar shape of the phase transition line at large Pe (Fig. 5.5), the initial particle flux points into the right direction and gives rise to the enormous cooling effect for only tiny differences in Pe. More specifically, when choosing $\mathrm{Pe_{in}} < \mathrm{Pe_{critical}} < \mathrm{Pe_{out}}$ (as in regime (II)), the particles are initially faster in the environment, which enhances the density inside the target domain where MIPS occurs and further slows down the particles, which further supports the particle flux from the environment.

5.2.6 Robustness

To see how robust this mechanism is, we now explore the influence of four system parameters on the temperature difference between the targeted cooling domain and its environment. These parameters are the refrigerator size x_0, the system size N, the Péclet number Pe, and the mass m of the active particles.

Role of the refrigerator size

The length x_0 defines the size of the targeted cooling domain (cf. Fig. 5.2a). The role of x_0 for our proposed cooling mechanism and the regimes (I) and (II) (see Fig. 5.2b) can be understood as follows:

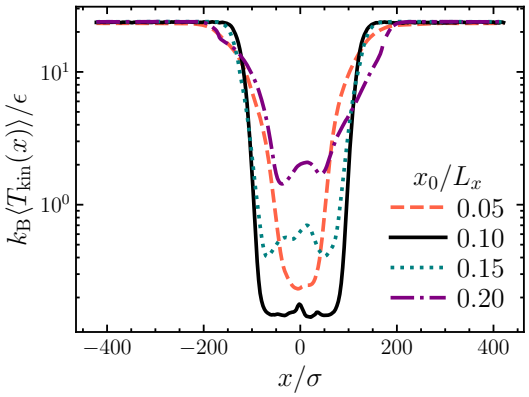

Fig. 5.8 Role of the refrigerator size. Time-averaged kinetic temperature profile in the steady state for different sizes x_0/L_x of the refrigerator domain (values are shown in the key) obtained from simulations with $N = 16\,000$ particles, $\mathrm{Pe}_{\mathrm{in}} = 105$, $\mathrm{Pe}_{\mathrm{out}} = 110$, and $\varphi_{\mathrm{tot}} = 0.35$ and averaged over 20 realizations. Further parameters: $m/(\gamma_t\tau_p) = 5 \times 10^{-2}$, $I/(\gamma_r\tau_p) = 5 \times 10^{-3}$, $\epsilon/(k_BT_b) = 10$, $\sigma/\sqrt{D_t/D_r} = 1$.

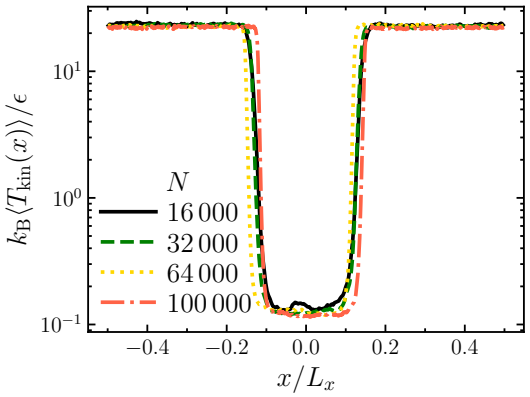

Fig. 5.9 Role of the system size. Time-averaged kinetic temperature profile in the steady state for $\mathrm{Pe}_{\mathrm{in}} = 105$ and $\mathrm{Pe}_{\mathrm{out}} = 110$ (regime (II) in Fig. 5.2b) and different system sizes, i.e., number of particles N (values are shown in the key). The ratios $L_y/L_x = 0.05$, $x_0/L_x = 0.1$ and the total area fraction $\varphi_{\mathrm{tot}} = 0.35$ are kept constant. Further parameters as in Fig. 5.8.

Regime (I): Due to the counteracting feedback loop, the density inside the refrigerator region decreases below φ_{tot} and prevents the particles from undergoing MIPS. Simultaneously, the density outside the refrigerator region increases. The steady-state density in the environment of the refrigerator region strongly depends on the value of x_0: For x_0 comparable to the system size L_x, the number of particles which can leave the refrigerator region due to the counteracting feedback loop is large and vice versa. Thus, the steady-state density outside the active refrigerator increases with increasing x_0. Due to the linear dependence of the mean speed on the area fraction, the kinetic temperature outside the refrigerator decreases with increasing x_0 and causes a (weak) cooling of the environment.

Regime (II): Here, the cooling is triggered by MIPS inside the targeted cooling domain. For x_0 small compared to L_x, the dense cluster fills the whole target domain. Thus, particles are cooled in the whole cooling domain (black solid line in Fig. 5.8). However, if $x_0/L_x \lesssim 0.05$, the dense cluster might occupy a spatial region larger than the refrigerator domain. Furthermore, the localization is less effective in this case such that the dense phase moves around the refrigerator domain (and eventually leaves it partially). As a consequence, the ensemble-averaged kinetic temperature inside the refrigerator is slightly larger as shown with the dashed orange line in Fig. 5.8. For $x_0/L_x \gtrsim 0.15$, the dense cluster might not fill the whole domain anymore and it will be placed at a random position inside the domain, which finally decreases the cooling effect when taking the ensemble average (see, e.g., dash-dotted purple line in Fig. 5.8). In the limit of very large x_0, i.e., $x_0/L_x \to 1$, the dense cluster is placed at a random position inside the cooling

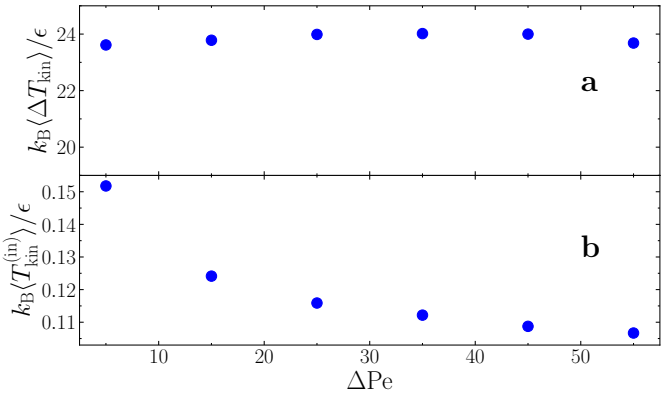

Fig. 5.10 Role of the Péclet number. a Temperature difference $\Delta T_{\text{kin}} = T_{\text{kin}}^{(\text{out})} - T_{\text{kin}}^{(\text{in})}$ between the refrigerator domain and its environment and **b** temperature in the refrigerator domain over $\Delta\text{Pe} = \text{Pe}_{\text{out}} - \text{Pe}_{\text{in}}$. All results are averaged over time in the steady state and over three realizations. Parameters: $N = 16\,000$, $\varphi_{\text{tot}} = 0.35$, $\text{Pe}_{\text{in}} \in \{55, 65, 75, 85, 95, 105\}$, $\text{Pe}_{\text{out}} = 110$, $m/(\gamma_{\text{t}}\tau_{\text{p}}) = 5 \times 10^{-2}$, $I/(\gamma_{\text{r}}\tau_{\text{p}}) = 5 \times 10^{-3}$, $\epsilon/(k_{\text{B}}T_{\text{b}}) = 10$, $\sigma/\sqrt{D_{\text{t}}/D_{\text{r}}} = 1$, $x_0/L_x = 0.1$.

domain causing the ensemble-averaged temperature profile to be approximately uniform (Fig. 5.3a).

Robustness against changes of the system size

To ensure that our results are not affected by finite-size effects, we performed additional simulations with $N = 32\,000$, $64\,000$, and $100\,000$ particles by keeping the total area fraction and the ratio x_0/L_x constant. As we show in Fig. 5.9, we obtain the same results for all studied system sizes resulting in a well-defined refrigerator domain with a temperature difference of about two orders of magnitude. Thus, our setup is robust against changes of the system size and our observations are not affected by finite-size effects.

Role of the Péclet number

As long as the requirements of regime (II) (see Fig. 5.2b) are met, the cooling effect is robust against variations of the choice of Péclet numbers. As we show in Fig. 5.10a, the (kinetic) temperature difference between the refrigerator domain and its environment is approximately invariant under variations of $\Delta\text{Pe} = \text{Pe}_{\text{out}} - \text{Pe}_{\text{in}}$ with $\text{Pe}_{\text{out}} = 110$ fixed and Pe_{in} varied. Remarkably, increasing ΔPe decreases the (kinetic) temperature in the refrigerator domain close to the lower limit of $k_{\text{B}}T_{\text{kin}}/\epsilon = 0.1$, which is given by the strength of the translational noise, as shown in Fig. 5.10b. Thus, the active refrigerator can be realized for very small differences in Péclet numbers but is still stable and even more efficient when the difference in Pe is increased. As a side remark, notice that even for choices of ΔPe (and x_0) which result in a left gray arrow in Fig. 5.2b (regime (II)) which is long enough to cross the upper transition line, we observe a significant cooling effect.

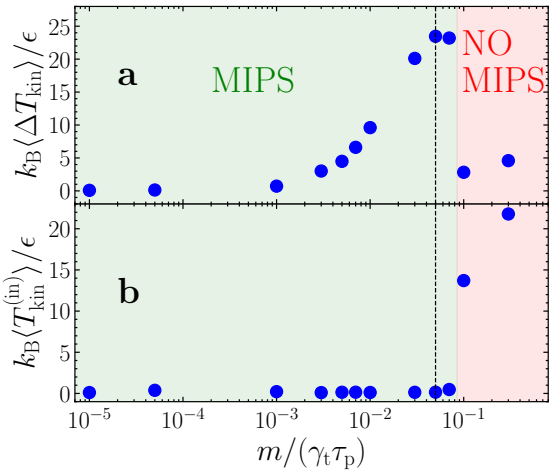

Fig. 5.11 Role of inertia. a Temperature difference $\Delta T_{\text{kin}} = T_{\text{kin}}^{(\text{out})} - T_{\text{kin}}^{(\text{in})}$ between the refrigerator domain and its environment and **b** temperature in the refrigerator domain over the mass m of the particles (averaged over time in the steady state and over three realizations). MIPS occurs in the green region while it is not possible in the red region (see also Ref. [103] for a detailed discussion about the breakdown of MIPS at large inertia). The vertical dashed line indicates the value $m/(\gamma_t\tau_p) = 5 \times 10^{-2}$ which we used throughout this chapter. Parameters: $N = 16\,000$, $\varphi_{\text{tot}} = 0.35$, $\text{Pe}_{\text{in}} = 105$, $\text{Pe}_{\text{out}} = 110$, $I/(\gamma_r\tau_p) = 1/10 \times m/(\gamma_t\tau_p)$, $\epsilon/(k_B T_b) = 10$, $\sigma/\sqrt{D_t/D_r} = 1$.

Role of Inertia

Up to this point, we fixed the value of the mass $m/(\gamma_t\tau_p) = 5 \times 10^{-2}$. However, our results are valid even in a broader range of inertia as demonstrated in Fig. 5.11: While for $m/(\gamma_t\tau_p) \gtrsim 0.09$ MIPS breaks down (see Ref. [103] for a detailed discussion of the break down at large inertia), the temperature difference between the refrigerator domain and its environment decreases with decreasing inertia and finally vanishes when we are close to the overdamped regime at $m/(\gamma_t\tau_p) = 10^{-5}$. Although a temperature difference exists within the red region caused by the different Péclet numbers and different steady-state densities in the refrigerator domain and its environment, MIPS enhances the cooling effect significantly. Thus, both activity and inertia are crucial for the construction of an active refrigerator, and a local maximum of the temperature difference can be observed for values of m close to the breakdown of MIPS.

5.2.7 Absorbing, trapping, and cooling tracers with active refrigerators

One unique feature of the proposed refrigerators is that they cool down colloidal particles in a certain region in space without requiring any isolating walls separating the cooling domain from the environment. Since the kinetic temperature differences are much larger than the temperature differences in the underlying bath, active refrigerators can also be used to absorb sufficiently large substances from the environment and to trap them for times longer than $100\,\tau_p$ (Fig. 5.12). To demonstrate this, we have performed simulations of inertial ABPs (parameters as in Fig. 5.3c) and additional passive tracer particles (modeled as passive Brownian particles with the same size σ and mass m as the

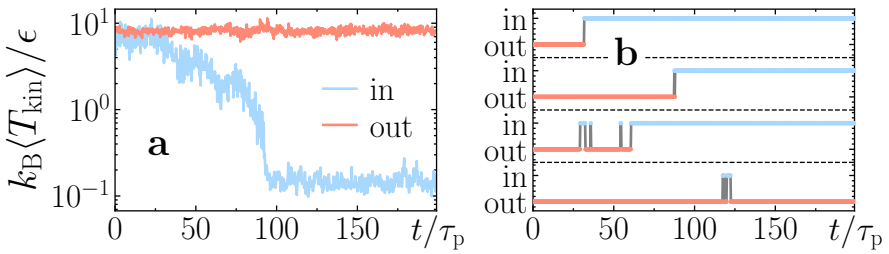

Fig. 5.12 Absorbing, trapping, and cooling tracers with active refrigerators. a Kinetic temperature of passive tracers inside and outside the cooling domain. **b** Position (inside or outside the cooling domain) of four exemplary passive tracers over time (parameters as in Fig. 5.3c but with $\mathrm{Pe}_{\mathrm{in}} = \mathrm{Pe}_{\mathrm{out}} = 0$ for passive tracers and $N_{\mathrm{passive}}/N = 0.02$).

ABPs, see Eq. (2.1)), which may represent, e.g., certain toxic substances and are randomly distributed outside the cooling domain. Remarkably, the active refrigerator systematically absorbs tracers from the environment and cools them by two orders of magnitude below the kinetic temperature of tracers outside the refrigerator domain (Fig. 5.12a). Note that it can take a long time before a tracer enters the cooling domain, but once it is deep inside this region it stays there for a very long time, as indicated by the exemplary trajectories in Fig. 5.12b and Fig. B2 in Appx. B.

5.3 Discussion

The active particles considered here are intrinsically out of equilibrium, and hence, the second law of thermodynamics only applies to the overall system (particle plus fluid/substrate) but not to the particle subsystem alone. However, the finding of a persistent temperature gradient for the active particles does of course not contradict thermodynamics: Heat always flows from hot to cold within the bath (solvent/gas) which surrounds the active particles. This heat flow persists in the steady state and is maintained by the (external) energy source driving the system. Therefore, from a microscopic viewpoint, cooling down the active particles locally without transferring heat to an external (spatially separated) bath means that heat is transported from the active particles to the surrounding solvent. The latter has a comparatively large number of degrees of freedom and would heat up only very little (or very slowly) while the active particles cool down by orders of magnitude. In the following, we discuss the energy flow within the surrounding bath and the flow of kinetic energy within the particle subsystem in detail. The discussion is further complemented with the analysis of the entropy production rate and the demonstration of a possible thermometer for active particles.

5.3.1 Energy flow

Let us imagine light-powered Janus colloids in a liquid[21] or a complex plasma,[561,562] where inertia is important. Clearly, in steady state, when neglecting temperature changes of the particle material, essentially all the energy which is absorbed by the active particles from the external light source is ultimately transferred to the bath. That is, for a uniform

Pe (defocused laser), the particles act as identical heat sources for the bath. When realizing active refrigerators with a slightly nonuniform Pe ($\mathrm{Pe}_{\mathrm{out}} \gtrsim \mathrm{Pe}_{\mathrm{in}}$), we obtain a significantly enhanced particle density within the refrigerator region and hence, a comparatively hot solvent. Thus, T_{b} is large in regions where T_{kin} is low, leading to a persistent bath-energy-flow from hot to cold (see below). Note that changes in T_{b} are small compared to changes in T_{kin} since the bath has many degrees of freedom. Hence, in our simulations, we keep T_{b} constant (as typical for ABP models).[21] This argument is of course not restricted to light-powered swimmers but essentially applies also to, e.g., chemically powered swimmers when considering the fuel as an external energy source. In the following, we discuss the flow of kinetic energy at the level of the active particles and the energy flow within the bath (liquid/gas) that surrounds the particles in more detail. As we will see, completely consistent with the basic thermodynamic fact, energy naturally flows from hot to cold regions both at the level of the active particles and within the bath. This energy flow persists in steady state and is maintained by the driving (e.g., due to a laser).

Bath temperature and bath energy flow

We now use a minimal model for the bath temperature T_{b}, which explicitly shows that the energy persistently flows from hot to cold within the bath in the steady state. We begin with the heat equation

$$\frac{\partial T_{\mathrm{b}}}{\partial t} = \alpha \nabla^2 T_{\mathrm{b}} + g(\mathbf{r}, t) \tag{5.2}$$

with bath temperature field $T_{\mathrm{b}}(\mathbf{r}, t)$, thermal diffusivity α, and heat source or sink $g(\mathbf{r}, t)$.[578–581] Here, for simplicity, we assume that heat diffusion dominates over heat advection and neglect the latter. Describing each ABP as a point-like heat source in 3D (which is confined to a 2D interface/substrate) for simplicity with strength proportional to its self-propulsion speed v_0 (reasonable for laser-powered Janus particles for example),[575] we can write $g(\mathbf{r}) = g_0 \sum_{i=1}^{N} v_{0,i} \delta(\mathbf{r} - \mathbf{r}_i)$ with self-propulsion speed $v_{0,i}$ of the i-th particle and a suitable constant g_0. Here, we assume that all the energy which is absorbed by an active particle from the (external) energy source is ultimately transferred to the bath if we neglect temperature changes of the particle material. The corresponding solution of Eq. (5.2) in the steady state ($\partial_t T_{\mathrm{b}} = 0$) can be written in terms of a Green's function as[79,582]

$$T_{\mathrm{b}}(\mathbf{r}) = \frac{g_0}{4\pi\alpha} \sum_{i=1}^{N} \frac{v_{0,i}}{|\mathbf{r} - \mathbf{r}_i|}. \tag{5.3}$$

Based on this minimal model, we estimate the steady-state temperature field of the bath by inserting the coordinates of the active particles into Eq. (5.3) and averaging over 20 snapshots in the steady state. In Fig. 5.13 we show that for a uniform Pe or a small Pe difference, regions of high ABP density feature a higher bath temperature (yellow) than regions of low ABP density (blue, see Fig. 5.13a). Consequently, we observe an energy flow from the dense region to the dilute region within the bath (Fig. 5.13b), which is related to the temperature field by Fourier's law.[578–580,583,584] That is, in Fig. 5.13b, we have an energy current pointing to the left for $x < 0$ (where $-\partial_x T_{\mathrm{b}} < 0$) and an energy current pointing to the right for $x > 0$ (where $-\partial_x T_{\mathrm{b}} > 0$). The direction of the bath-energy-flow

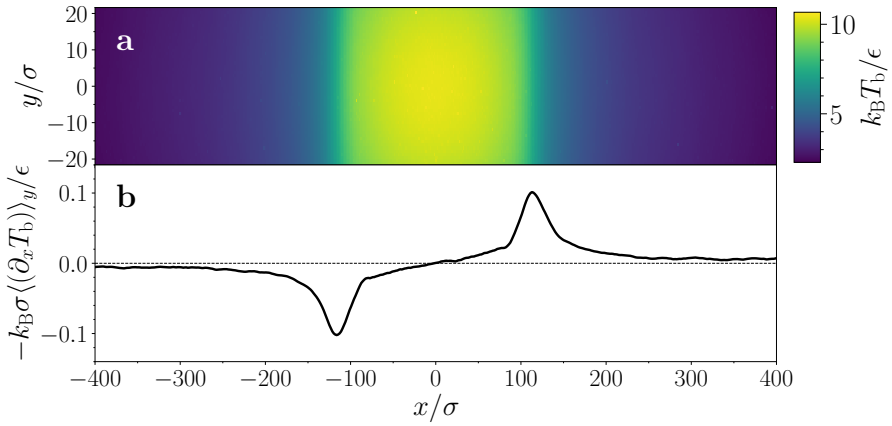

Fig. 5.13 Bath temperature field at small Pe difference. a Estimated steady-state bath temperature field and **b** its negative gradient in x direction averaged over the y coordinate for a small Pe difference $\mathrm{Pe}_{\mathrm{out}} - \mathrm{Pe}_{\mathrm{in}} = 5$. The color denotes the reduced temperature from dark blue (cold) to yellow (hot). Parameters: $\mathrm{Pe}_{\mathrm{in}} = 105$, $\mathrm{Pe}_{\mathrm{out}} = 110$, $\alpha\tau_{\mathrm{p}}/\sigma^2 = 1.0$, $g_0/(T_{\mathrm{b}}\sigma^2) = 10^{-4}$.

can also be spatially reverted: For a large Pe difference ($\mathrm{Pe}_{\mathrm{out}} \gg \mathrm{Pe}_{\mathrm{in}}$), the bath heats up stronger outside the refrigerator region because the light absorption grows faster than the particle density inside, which cannot exceed close packing. Then, heat flows into the refrigerator region within the bath but still from hot to cold (Fig. 5.14).

While we have discussed the minimal model for a finite number of particles so far, in the thermodynamic limit, one needs to take into account that heat would be absorbed by boundaries or would ultimately be radiated off the system, which we need to take into account to obtain a converged temperature field. A minimal way to achieve convergence is to introduce a loss term $-k_{\mathrm{d}}T_{\mathrm{b}}$ with some suitable loss coefficient k_{d}. For convenience, we also introduce the spatially dependent self-propulsion speed $v_0(\mathbf{r})$ and the steady-state particle density $\rho(\mathbf{r})$. Then, the heat source reads $g(\mathbf{r}) = g_0 v_0(\mathbf{r})\rho(\mathbf{r})$ and the steady-state heat equation reads

$$0 = \alpha\nabla^2 T_{\mathrm{b}} + g(\mathbf{r}) - k_{\mathrm{d}}T_{\mathrm{b}}. \tag{5.4}$$

It's solution can again be written in terms of a Green's function as[585]

$$T_{\mathrm{b}}(\mathbf{r}) = \frac{g_0}{4\pi\alpha}\int \mathrm{d}^3 r'\, v_0(\mathbf{r}')\rho(\mathbf{r}')\frac{\exp\left\{-\sqrt{\frac{k_{\mathrm{d}}}{\alpha}}|\mathbf{r}-\mathbf{r}'|\right\}}{|\mathbf{r}-\mathbf{r}'|}. \tag{5.5}$$

This shows that the bath temperature is high in regions where the product $v_0(\mathbf{r}')\rho(\mathbf{r}')$ is large. That is, for a small Pe difference, T_{b} is large in regions of high particle density and hence, according to Fourier's law, heat is flowing away from such regions within the bath (Fig. 5.13). In contrast, heat will flow from the dilute to the dense region within the bath for $\mathrm{Pe}_{\mathrm{out}} \gg \mathrm{Pe}_{\mathrm{in}}$ (Fig. 5.14).

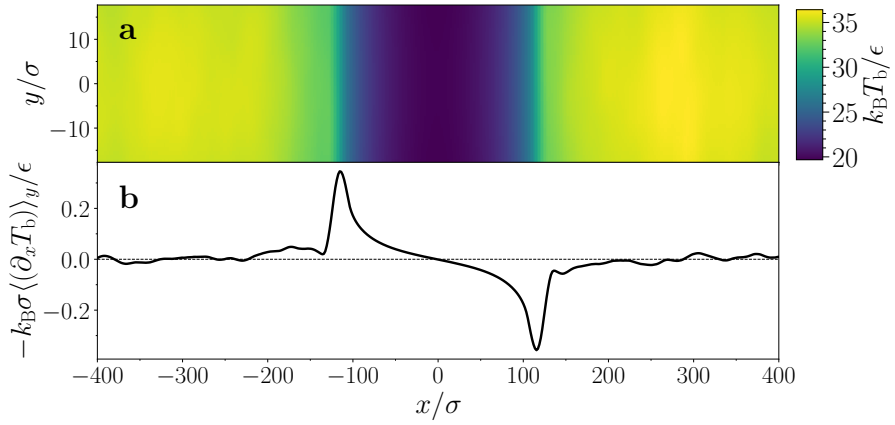

Fig. 5.14 Bath temperature field at large Pe difference. a Estimated steady-state bath temperature field and **b** its negative gradient in x direction averaged over the y coordinate for a large Pe difference $\mathrm{Pe}_{\mathrm{out}} - \mathrm{Pe}_{\mathrm{in}} = 360$. The color denotes the reduced temperature from dark blue (cold) to yellow (hot). Parameters: $\mathrm{Pe}_{\mathrm{in}} = 40$, $\mathrm{Pe}_{\mathrm{out}} = 400$, $\alpha\tau_{\mathrm{p}}/\sigma^2 = 1.0$, $g_0/(T_{\mathrm{b}}\sigma^2) = 10^{-4}$.

Kinetic temperature gradient and energy flow of the active particles

Next, let us discuss the flow of kinetic energy at the level of the active particles. We calculate the current density of the kinetic energy at the boundary of the dense phase, which can be defined by

$$\mathbf{J}_{\mathrm{kin}}(\mathbf{r}) = \frac{1}{2} m \langle \mathbf{v}(\mathbf{r}) \rangle^2 \rho_{\mathrm{loc}}(\mathbf{r}) \langle \mathbf{v}(\mathbf{r}) \rangle, \tag{5.6}$$

where $\rho_{\mathrm{loc}}(\mathbf{r})$ denotes the (local) particle number density and $\mathbf{v}(\mathbf{r})$ the velocity of the ABPs (averaged over a small area of size $\Delta x \Delta y$ with $\Delta x = \Delta y = 5\sigma$). The result is demonstrated in Fig. 5.15a: As expected, an inward flow of kinetic energy is observed at the boundary of the dense phase, which is mainly caused by a local alignment of the effective self-propulsion force as demonstrated by the coarse-grained polarization field $\langle \hat{\mathbf{p}} \rangle$ shown in Fig. 5.15b. This kind of alignment has already been observed for overdamped ABPs in a motility gradient.[586,587]

Furthermore, Fourier's law can be used to relate the current density of the kinetic energy to a (kinetic) temperature gradient:

$$\mathbf{J}_{\mathrm{Fourier}} = -\kappa \boldsymbol{\nabla} T_{\mathrm{kin}}, \tag{5.7}$$

where κ denotes an effective thermal conductivity.[583] The temperature gradient must be compensated by a particle current in the steady state in the presence of a density gradient[530,588] and the condition

$$-\kappa \boldsymbol{\nabla} T_{\mathrm{kin}} - \mu \boldsymbol{\nabla} \rho = 0 \tag{5.8}$$

with a positive transport coefficient μ and particle density ρ must hold. In particular, the (kinetic) temperature and density gradients are opposite at the border of the refrigerator domain and Eq. (5.8) is fulfilled in our simulations once we set $\mu/\kappa \approx 23$ (see Fig. 5.16).

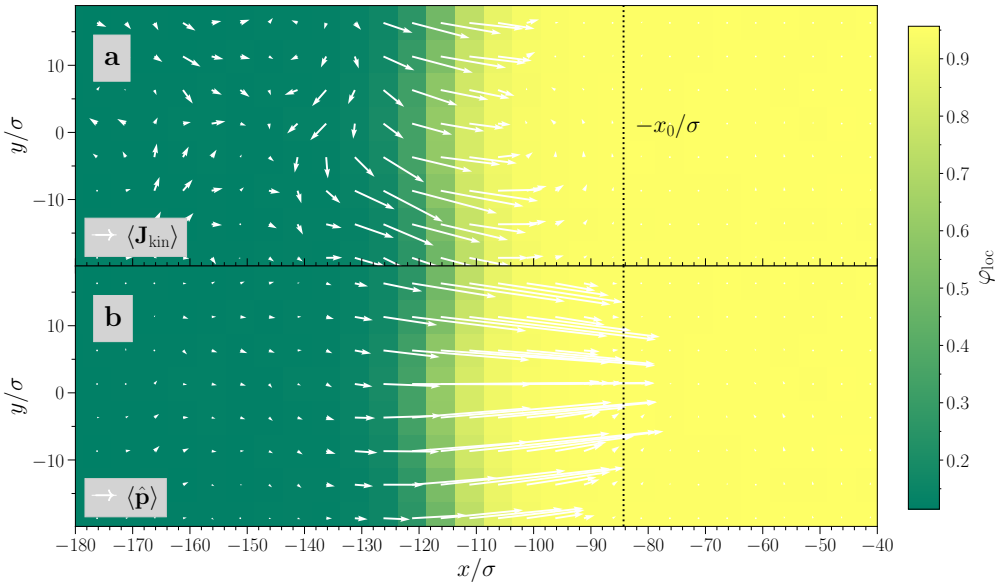

Fig. 5.15 Kinetic energy flow and polarization field. a Flow of kinetic energy (see Eq. (5.6)). The white arrows denote the direction of the flow, their length correspond to the strength in arbitrary units. **b** Polarization field. The white arrows denote the direction, their length denotes the strength of the polarization in arbitrary units. The background colors show the local area fraction, the vertical black dotted line denotes the border of the refrigerator domain at $-x_0$. All data are averaged over time in the steady state and over 20 realizations. Parameters: $N = 16\,000$, $\varphi_{\mathrm{tot}} = 0.35$, $\mathrm{Pe}_{\mathrm{in}} = 105$, $\mathrm{Pe}_{\mathrm{out}} = 110$, $m/(\gamma_{\mathrm{t}}\tau_{\mathrm{p}}) = 5 \times 10^{-2}$, $I/(\gamma_{\mathrm{r}}\tau_{\mathrm{p}}) = 5 \times 10^{-3}$, $\epsilon/(k_{\mathrm{B}}T_{\mathrm{b}}) = 10$, $\sigma/\sqrt{D_{\mathrm{t}}/D_{\mathrm{r}}} = 1$, $x_0/L_x = 0.1$.

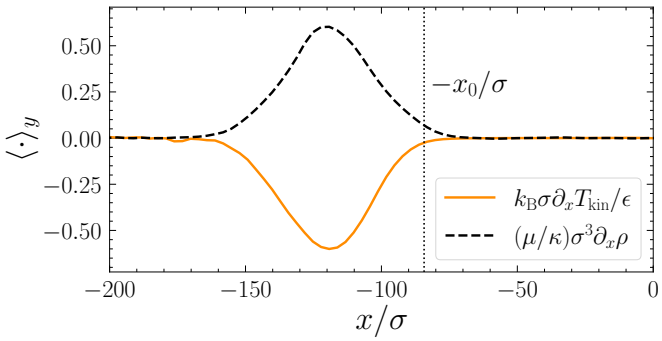

Fig. 5.16 Kinetic temperature and particle density gradients. Gradient of the kinetic temperature T_{kin} and the particle density ρ at the border of the cooling domain in the steady state (averaged over the y direction and over 20 realizations). The gradient of the particle density is scaled with a factor $\mu/\kappa \approx 23$, and the vertical black dotted line denotes the border of the refrigerator domain at $-x_0$ (parameters as in Fig. 5.15).

5.3.2 Entropy production

The entropy production rate measures how strongly detailed balance is broken and thus, how far the state of a system deviates from an equilibrium state.[23,24,194,264,589] Therefore, entropy production is required to observe a temperature difference between coexisting phases in a steady state (however, the opposite is not true).[103,431] Therefore, we now explore the entropy production rate of the active particles inside and outside the targeted cooling domain. The entropy production rate for inertial ABPs can be calculated as follows: Let Γ denote one trajectory of the system, i.e., the set of positions, velocities, and orientation angles for all particles over a time interval $[0, t]$. Furthermore, we denote the corresponding time-reversed trajectory by $\tilde{\Gamma}$. The entropy production is defined by[25]

$$\Delta s = \ln \left[\frac{p(\Gamma)}{p(\tilde{\Gamma})} \right], \tag{5.9}$$

where $p(\Gamma)$ denotes the probability density of the trajectory Γ, which is given by the Onsager-Machlup functional.[590] For inertial ABPs, we obtain

$$p(\Gamma) \propto \exp\left\{ -\frac{\gamma_\mathrm{t}}{4k_\mathrm{B}T_\mathrm{b}} \sum_{i=1}^{N} \int_0^t \mathrm{d}\tau \left[\frac{m}{\gamma_\mathrm{t}} \dot{\mathbf{v}}_i + \mathbf{v}_i - v_0 \mathbf{p}_i - \frac{1}{\gamma_\mathrm{t}} \mathbf{F}_{\mathrm{int},i} \right]^2 \right\}, \tag{5.10}$$

where $\mathbf{F}_{\mathrm{int},i} = \sum_{j=1, j\neq i}^{N} \nabla_{\mathbf{r}_i} u(r_{ij})$ denotes the interaction force due to the WCA potential with $r_{ij} = |\mathbf{r}_i - \mathbf{r}_j|$ (see Eq. (2.8)). Following Refs. [25, 432, 438, 591–593], positions, velocities, orientations, and forces transform under time reversal as $\mathbf{r}(t) = \mathbf{r}(-t)$, $\mathbf{v}(t) = -\mathbf{v}(-t)$, $\mathbf{p}(t) = \mathbf{p}(-t)$, and $\mathbf{F}_\mathrm{int}(t) = \mathbf{F}_\mathrm{int}(-t)$, respectively. Therefore, we finally obtain the total entropy production

$$\Delta s = \frac{1}{D_\mathrm{t}} \sum_{i=1}^{N} \int_0^t \mathrm{d}\tau \left[v_0 \mathbf{p}_i \cdot \mathbf{v}_i + \frac{1}{\gamma_\mathrm{t}} \mathbf{v}_i \cdot \mathbf{F}_{\mathrm{int},i} - \frac{m}{\gamma_\mathrm{t}} \mathbf{v}_i \cdot \dot{\mathbf{v}}_i \right], \tag{5.11}$$

with $D_\mathrm{t} = k_\mathrm{B}T_\mathrm{b}/\gamma_\mathrm{t}$. Since the last term obeys $2\mathbf{v}_i \cdot \dot{\mathbf{v}}_i = \partial_t \mathbf{v}_i^2$ and the mean kinetic energy $\langle m\mathbf{v}^2/2 \rangle$ is constant in the steady state, this term vanishes. Thus, we finally have two contributions: one from the self propulsion and one from pair interactions. Hence, the mean entropy production rate is given by

$$\langle \Delta \dot{s} \rangle = \frac{1}{N D_\mathrm{t}} \sum_{i=1}^{N} \left[v_0 \mathbf{p}_i \cdot \mathbf{v}_i + \frac{1}{\gamma_\mathrm{t}} \mathbf{v}_i \cdot \mathbf{F}_{\mathrm{int},i} \right]. \tag{5.12}$$

Its time evolution is shown in Fig. 5.17a: Once the steady state is reached, the entropy production rate in the refrigerator domain is about two orders of magnitude smaller than in the environment. The distribution of the entropy production rate is narrow and centered around a small positive value for particles inside the refrigerator and broad for particles in the environment (Fig. 5.17b). The two contributions are demonstrated in Fig. 5.17c confirming our observations.

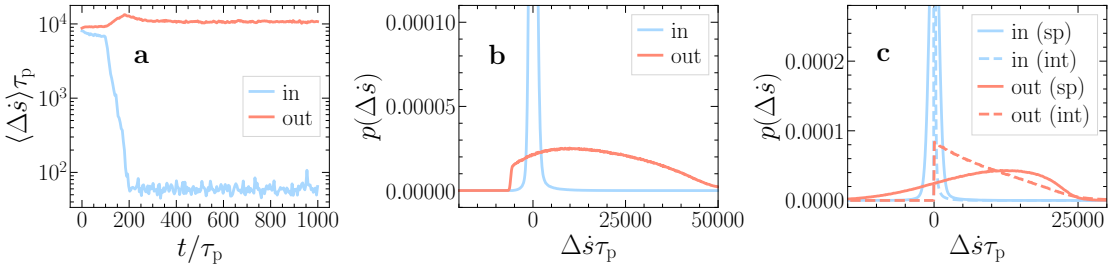

Fig. 5.17 Entropy production rate. **a** Mean entropy production rate inside and outside the refrigerator domain over time. Time-averaged probability density **b** of the entropy production rate and **c** of the entropy production rate separated in the self-propulsion (sp) contribution and the interaction (int) contribution. Parameters: $N = 64\,000$, $\varphi_{\text{tot}} = 0.35$, $\text{Pe}_{\text{in}} = 105$, $\text{Pe}_{\text{out}} = 110$, $m/(\gamma_t \tau_p) = 5 \times 10^{-2}$, $I/(\gamma_r \tau_p) = 5 \times 10^{-3}$, $\epsilon/(k_B T_b) = 10$, $\sigma/\sqrt{D_t/D_r} = 1$, $x_0/L_x = 0.1$.

5.3.3 Thermometer for Active Particles

Thus far, we defined the temperature of the active particles in terms of their (translational) kinetic energy. In equilibrium, this kinetic temperature is equal to the thermodynamic temperature as long as the Hamiltonian of the system is quadratic in the momentum coordinates (equipartition theorem).[504] Note that a temperature based on fluctuation-dissipation relations (FDRs) can only be defined by generalizing the equilibrium FDR, which is violated in active systems.[106,123,125,170,516,518,594] However, as an alternative temperature measure, one can construct a "thermometer" that measures an effective temperature of the active-particle subsystem and follows the idea of the oscillator temperature introduced in Subsec. 4.2.2: We assign a temperature to the active particles based on passive tracer particles trapped in a harmonic potential $U_{\text{harm.}}(\mathbf{r}) = k\mathbf{r}^2/2$ of strength k. These tracer particles are modeled as passive Brownian particles following Eq. (2.1) with mass m_p and diameter σ_{tracer}. We choose the effective diameter for the interaction between the ABPs and the passive tracers as $\tilde{\sigma} = (\sigma + \sigma_{\text{tracer}})/2$. As we will see, the temperature measured by this thermometer behaves analogously to the kinetic temperature. Compared to a standard thermometer, which would measure the temperature of the surrounding bath, the tracer-based thermometer exclusively measures the temperature of the active particle subsystem. In particular, the tracer particles could be made semi-permeable experimentally as in Refs. [595, 596], so that they essentially interact only with the active particles. The distribution of tracer displacements Δx along the x-axis is expected to be Gaussian and is found to be Gaussian in our simulations (similar results are obtained for the displacements Δy along the y axis). Its variance $\langle (\Delta x - \langle \Delta x \rangle)^2 \rangle$ is used to estimate an effective temperature

$$k_B T_{\text{AP}}(k) = k \left\langle (\Delta x - \langle \Delta x \rangle)^2 \right\rangle , \tag{5.13}$$

of the active particles similar to the oscillator temperature defined in Eq. (4.12), which generally depends on the strength k of the harmonic potential.[545,597–599] Obtaining a consistent measurable value for T_{AP} is however not completely straight forward as already discussed in Chap. 4: First, the tracer particles should be small because in the dense phase, large tracers would be trapped by surrounding active particles. Second, the

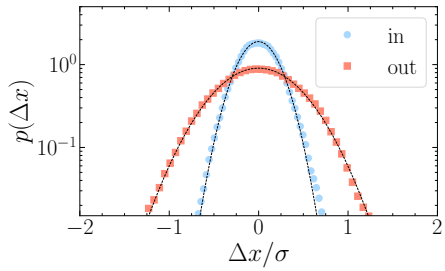

Fig. 5.18 Passive tracer displacement distribution. Displacement distribution of passive tracers with mass $m_\mathrm{p}/(\gamma_\mathrm{t}\tau_\mathrm{p}) = 1.0$ and radius $R/\sigma = 0.005$ trapped in a harmonic potential of strength $k\sigma^2/\epsilon = 60$ inside and outside the cooling domain averaged over 40 realizations. Black dashed lines are Gaussian fits yielding $k_\mathrm{B}T_\mathrm{AP}^\mathrm{(in)}/\epsilon \approx 2.65$ and $k_\mathrm{B}T_\mathrm{AP}^\mathrm{(out)}/\epsilon \approx 11.03$. Parameters: $N = 16\,000$, $\varphi_\mathrm{tot} = 0.35$, $\mathrm{Pe}_\mathrm{in} = 105$, $\mathrm{Pe}_\mathrm{out} = 110$, $m/(\gamma_\mathrm{t}\tau_\mathrm{p}) = 5 \times 10^{-2}$, $I/(\gamma_\mathrm{r}\tau_\mathrm{p}) = 5 \times 10^{-3}$, $\epsilon/(k_\mathrm{B}T_\mathrm{b}) = 10$, $\sigma/\sqrt{D_\mathrm{t}/D_\mathrm{r}} = 1$, $x_0/L_x = 0.1$.

tracer particles should also be sufficiently heavy such that they do not slow down too much between subsequent collisions. Third, k has to be large because especially a tracer particle in the dense phase should only move within the cage of the surrounding active particles. Accordingly, we use tracer particles with mass $m_\mathrm{p}/(\gamma_\mathrm{t}\tau_\mathrm{p}) = 1.0$ and diameter $\sigma_\mathrm{tracer} = 0.01\sigma$ and place one tracer in the middle of the cooling domain and one in the dilute phase. For an exemplary value $k\sigma^2/\epsilon = 60$ we obtain a low effective temperature $k_\mathrm{B}T_\mathrm{AP}^\mathrm{(in)}/\epsilon \approx 2.65$ inside the cooling domain and a high temperature $k_\mathrm{B}T_\mathrm{AP}^\mathrm{(out)}/\epsilon \approx 11.03$ outside the cooling domain (see Fig. 5.18). Importantly, a lower temperature is measured inside the cooling domain for all values of k. This is consistent with our findings based on the kinetic temperature.

5.4 Conclusion

In this chapter, we have proposed a mechanism for a refrigerator to cool active particles in a targeted cooling domain. This mechanism requires inertia not only to create a temperature difference across coexisting phases but also to induce the peculiar shape of the MIPS phase transition line, which we exploit to localize the cooling domain in a predefined region of space. As their key feature, the proposed refrigerators create a self-organized cooling domain, in which active particles feature a much lower kinetic temperature compared to their environment. As they do not require any isolating walls to separate the cooling domain from its environment, the proposed refrigerators prove a route towards possible future applications, e.g., to trap and absorb large (toxic) molecules or viruses. Overall, we found that the active-particle subsystem alone does not behave as one might expect from the laws of thermodynamics but makes the bath pay the thermodynamic bill for a self-organized cooling domain which does not decay. This could be further explored within microscopic theories[167,600] as well as experiments with self-propelled particles which feature significant inertia and elastic collisions such as activated micro-particles in a plasma,[561,562] mesoscopic propellers such as vibrated granular particles,[121,154,156,157,229,290,563–565] drones,[37,566,601] and mini-robots,[602] and dense animal collections.[186,603]

6 Coexisting Temperatures in Mixtures of Active and Passive Brownian Particles

In the previous chapter, we have shown that temperature differences in inertial ABPs can be used to design refrigerators for active particles. As a key ingredient, these refrigerators require that the ABPs are sufficiently heavy. However, for most experimental realizations of active particles such as bacteria, algae, or synthetic Janus colloids, inertial effects are negligible, i.e., they move in the overdamped limit, and therefore, these systems alone would not feature different temperatures in coexisting phases. Hence, we now ask if such temperature differences can be realized in systems that contain overdamped active particles. In particular, we consider mixtures of overdamped active and inertial passive Brownian particles and show that when they phase separate into a dense and a dilute phase, the passive particles have different kinetic temperatures in both phases. Surprisingly, we find that the dense phase (liquid) cannot only be colder but also hotter than the dilute phase (gas). The main content of this chapter is taken from my publication "Motility-Induced Coexistence of a Hot Liquid and a Cold Gas" published in *Nature Communications* (2024) under the CC BY 4.0 license,[542] and the majority of this chapter is taken verbatim from it. For this publication, I helped with the supervision of a related bachelor thesis, performed all final simulations, analyzed all final simulation data, wrote the initial draft, and created all figures.

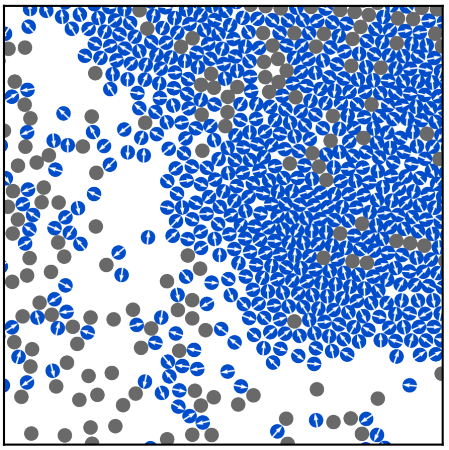

Fig. 6.1 Boundary of a dense cluster in a system of overdamped ABPs (blue) and inertial PBPs (gray) as studied in Chap. 6. The white arrows denote the self-propulsion direction of the ABPs.

6.1 Introduction

We are all used to the experience that a gas is often hotter than a liquid of the same material. For example, to evaporate water from a pot in our kitchens, we need to increase its temperature. Then, at some point, vapor molecules rapidly escape from the liquid and distribute in the surrounding air. This experience that vapor emerges when increasing the temperature of a liquid has played a key role throughout human history: It was an essential ingredient, e.g., for the development of the steam engine,[604] and it is key to technological

applications like distillation techniques[605,606] or physical vapor deposition[607,608] as well as to natural spectacles such as geysers.[609] The central exception from the experience that gases are hotter than liquids of the same material occurs when two phases, e.g., a gas and a liquid, coexist at the same time. Then they share the same temperature. This is guaranteed by the fundamental laws of statistical mechanics and thermodynamics for all equilibrium systems, and it also applies to some non-equilibrium systems.[103,110,111,559,560] Intuitively, this is plausible since any type of temperature gradient seems to evoke an energy flow evening out an initial temperature gradient.

Despite this, very recently, it was found that at phase coexistence in certain active systems consisting of active particles which consume energy from their environment to propel themselves,[21,22,27] the dilute (gas-like) phase is hotter by up to one or two orders of magnitude compared to the dense (liquid-like) phase in terms of the kinetic temperature.[103,123,165] While this complies with our intuition that gases are often hotter than liquids, it is in stark contrast to the situation in equilibrium systems and the expectation that any temperature difference should evoke an energy flux that balances it out. By now, such a temperature difference across coexisting phases has been shown to occur for a variety of temperature definitions that all coincide in equilibrium. It has been observed, e.g., for the kinetic temperature,[103] the effective temperature[123] as well as for tracer-based temperature definitions[165,598] in systems undergoing motility-induced phase separation (MIPS)[53,72,83,92,109–111,119,124,129,152,259,292,443,559,610], i.e., in systems of particles that self-organize into a dilute (gas) and a coexisting dense (liquid) phase (see Sec. 2.3 for details). The mechanism underlying the emergence of a temperature difference across coexisting phases hinges on the consumption of energy at the level of the active particles when undergoing frequent collisions within the dense phase. This mechanism crucially requires inertia,[103,123,165] whereas overdamped active particles show the same kinetic temperature in coexisting phases (see also Sec. 2.3). The requirement of inertia restricts the observation of different coexisting temperatures to a special class of active systems and precludes its experimental observation in generic microswimmer experiments.

In this chapter, we explore the possibility to achieve a kinetic temperature difference across coexisting phases in mixtures of two components that on their own would not lead to a temperature difference: an ordinary equilibrium system made of inertial passive Brownian tracer particles such as granular particles or colloidal plasmas and overdamped active Brownian particles like bacteria or synthetic microswimmers. Our exploration leads to the following central insights: First, we show that when the mixture undergoes MIPS, the passive particles in the dense and the dilute phase indeed can have different kinetic temperatures (and different Maxwell-Boltzmann temperatures, which are defined based on the width of the velocity distribution; cf. Eq. (4.9)). This demonstrates that kinetic temperature differences in coexisting phases can occur in a broader class of systems than what was anticipated so far. Second, we find that not only the gas can be hotter —but, counterintuitively— also the dense phase can be hotter than the dilute phase. This appears particularly surprising since the current understanding of the mechanism leading to different temperatures across coexisting phases in pure active systems hinges on the idea that frequent directional changes due to collisions lead to a local loss of kinetic energy (similarly as inelastic collisions do in granular systems).[530–535,567–571,611,612] Such collisions are

more frequent in dense regions suggesting that the dense phase is always colder than the dilute one, which coincides with all previous observations.[103,123,165,530–535,567–571,611,613] We find that this mechanism also applies to the passive tracers of the active-passive mixtures studied here in a certain parameter regime in which the tracers are trapped within dense clusters by surrounding active particles leading to low tracer temperatures in dense regions analogously as in the single-species case of inertial active particles. However, surprisingly, we find that this effect can also be reverted in mixtures of active and passive particles. This is because for strong self-propulsion, the active particles persistently push passive ones forward even within the dense phase, which can overcompensate the slowing of the latter ones due to (isotropic) collisions with other particles. Hence, the passive particles can achieve a higher (kinetic) temperature in the dense phase than in the surrounding gas, where correlated active-passive motions occur less frequently and last shorter. Our results pave the route towards the usage of microswimmers such as bacteria,[4,52,184,614,615] algae,[616,617] or Janus particles and other synthetic microswimmers[21,53,181,185,618] for controlling the kinetic temperature profile and hence, the dynamics of fluids and other passive materials.

6.2 Results

The active and passive particles in the mixtures considered here are modeled with the ABP and the PBP model as introduced in Subsec. 2.2.1, and the Langevin equations are solved numerically using BD simulations. In the following, we first discuss the simulation setup in more detail before we present the main results. Following the latter, we investigate the underlying mechanism in detail. Finally, we explore the non-equilibrium state diagram and the influence of particle sizes and inertia on the observed temperature differences.

6.2.1 Simulation details

Now, we study a mixture of active and passive Brownian particles, which are represented by the ABP and the PBP model as introduced in Eqs. (2.2) and (2.3) as well as Eq. (2.1), respectively. Similar to the previous chapter, the particles are represented by (slightly soft) spheres that interact via the WCA potential as defined in Eq. (2.8). The dynamics of the active particles is made overdamped by choosing a very small mass m_a and a small moment of inertia $I = m_\mathrm{a}\sigma_\mathrm{a}^2/10$ (corresponding to a rigid sphere), where σ_a denotes the diameter of the active particles. That is, we explicitly account for inertia for the active particles to have access to a well-defined instantaneous particle velocity, but we choose a very small mass to stay in the overdamped regime. Notice that using overdamped Langevin equations instead ($m_\mathrm{a} = 0$) essentially yields the same results (Fig. C1, Appx. C). The passive particles feature a comparatively large mass m_p and their velocity $\mathbf{v}_j$ evolves according to Eq. (2.1), where $j = N_\mathrm{a} + 1, N_\mathrm{a} + 2, ..., N_\mathrm{a} + N_\mathrm{p}$ denotes the index of the passive particles. N_a denotes the number of active particles and N_p denotes the number of passive particles. For simplicity, we consider active and passive particles with the same size and drag coefficients γ_t but different material density,[619] i.e., we choose $\sigma_\mathrm{a} = \sigma_\mathrm{p}$, where σ_p denotes the diameter of the passive particles (unless otherwise indicated). However, note that the key effects which we discuss in the following are similar for particles with

significantly different sizes and drag coefficients, as we shall see. For these simulations, the effective diameter for the interaction between the active and passive particles is chosen as $\sigma_{\mathrm{ap}} = (\sigma_{\mathrm{a}} + \sigma_{\mathrm{p}})/2$.

In all simulations, we fix $m_{\mathrm{a}}/(\gamma_{\mathrm{t}}\tau_{\mathrm{p}}) = 5 \times 10^{-5}$, $I/(\gamma_{\mathrm{r}}\tau_{\mathrm{p}}) = 5 \times 10^{-6}$ to recover overdamped dynamics for the active particles.[103] For the passive particles, we fix $m_{\mathrm{p}}/(\gamma_{\mathrm{t}}\tau_{\mathrm{p}}) = 5 \times 10^{-2}$ (unless otherwise indicated) with the persistence time $\tau_{\mathrm{p}} = 1/D_{\mathrm{r}}$. Furthermore, we set $\epsilon = 10\, k_{\mathrm{B}}T_{\mathrm{b}}$ and $\sigma_{\mathrm{a}} = \sigma_{\mathrm{p}} = \sigma = \sqrt{D_{\mathrm{t}}/D_{\mathrm{r}}}$ (unless otherwise indicated), and we use systems with $N = N_{\mathrm{a}} + N_{\mathrm{p}}$ particles. Again, we choose $\gamma_{\mathrm{t}} = \gamma_{\mathrm{r}}/\sigma^2$ and vary the Péclet number Pe and the fraction $x_{\mathrm{a}} = N_{\mathrm{a}}/(N_{\mathrm{a}} + N_{\mathrm{p}})$ of the active particles. The total area fraction $\varphi_{\mathrm{tot}} = (N_{\mathrm{a}} + N_{\mathrm{p}})\pi\sigma^2/(4A)$ is set to $\varphi_{\mathrm{tot}} = 0.5$, where A denotes the area of the simulation box. The Langevin equations (Eqs. (2.2), (2.3), and (2.1)) are solved numerically in a quadratic box with periodic boundary conditions, with initially uniformly distributed particle positions, and with a time step $\Delta t = 10^{-6}\,\tau_{\mathrm{p}}$ using LAMMPS[255] first for a time of $100\,\tau_{\mathrm{p}}$ to reach a steady state and afterward for a time of $900\,\tau_{\mathrm{p}}$ for computing time averages of observables in the steady state.

As a key observable, we calculate the kinetic temperature as defined in Eq. (4.3) for passive particles in the dense and the dilute phase separately. We distinguish between passive particles in the dense and the gas phase by identifying the largest cluster in the system using the criterion that two particles belong to the same cluster if their distance to each other is smaller than the cutoff distance $r_{\mathrm{c}} = 2^{1/6}\sigma$ of the WCA potential (see also Subsec. 3.4.6). Then, all particles in the largest cluster are considered as the dense phase and all other particles as the gas phase (Fig. C2, Appx. C). Finally, the kinetic temperature of the passive particles in the dense and the gas phase is obtained by averaging over all passive particles in the dense phase and all passive particles in the gas phase, respectively.

6.2.2 Coexistence of a hot gas and a cold liquid

Let us first consider an initially uniform distribution of an overdamped mixture of active and passive particles.[450,619,620] In our simulations with Péclet number $\mathrm{Pe} = 100$, an area fraction of $\varphi_{\mathrm{tot}} = 0.5$, and a fraction of $x_{\mathrm{a}} = 0.6$ active particles, we observe that the active and passive particles aggregate and form persistent clusters despite the fact that they interact purely repulsively. These clusters are motility induced[53,72,83,111,124,129,152,292,443,559,610] and continuously grow (coarsen), ultimately leading to a phase separated state comprising a dense liquid-like region that coexists with a dilute gas phase (Fig. 6.2a–d), which is in agreement with previous studies.[450,619] As for systems of active overdamped particles alone,[103] we find that the active and passive particles in both phases have the same kinetic temperature (shown in Fig. 6.2d for the passive particles). Here, following Refs. [103, 163–165], we define the temperature of the particles based on their kinetic energy as shown in Subsec. 4.2.1 (Eq. (4.3)), which is well-defined also in non-equilibrium systems.[170] Note that the phenomena which we report occur similarly if using other temperature definitions such as the Maxwell-Boltzmann temperature defined in Eq. (4.9), as further discussed below. Let us now explore if the situation found for the overdamped mixture changes when replacing the overdamped tracers with (heavier) underdamped ones (Fig. 6.2e–h). Then, at the level of the structures that emerge, not much changes in our simulations: We still observe the formation of small clusters, which is followed by coarsening, ultimately

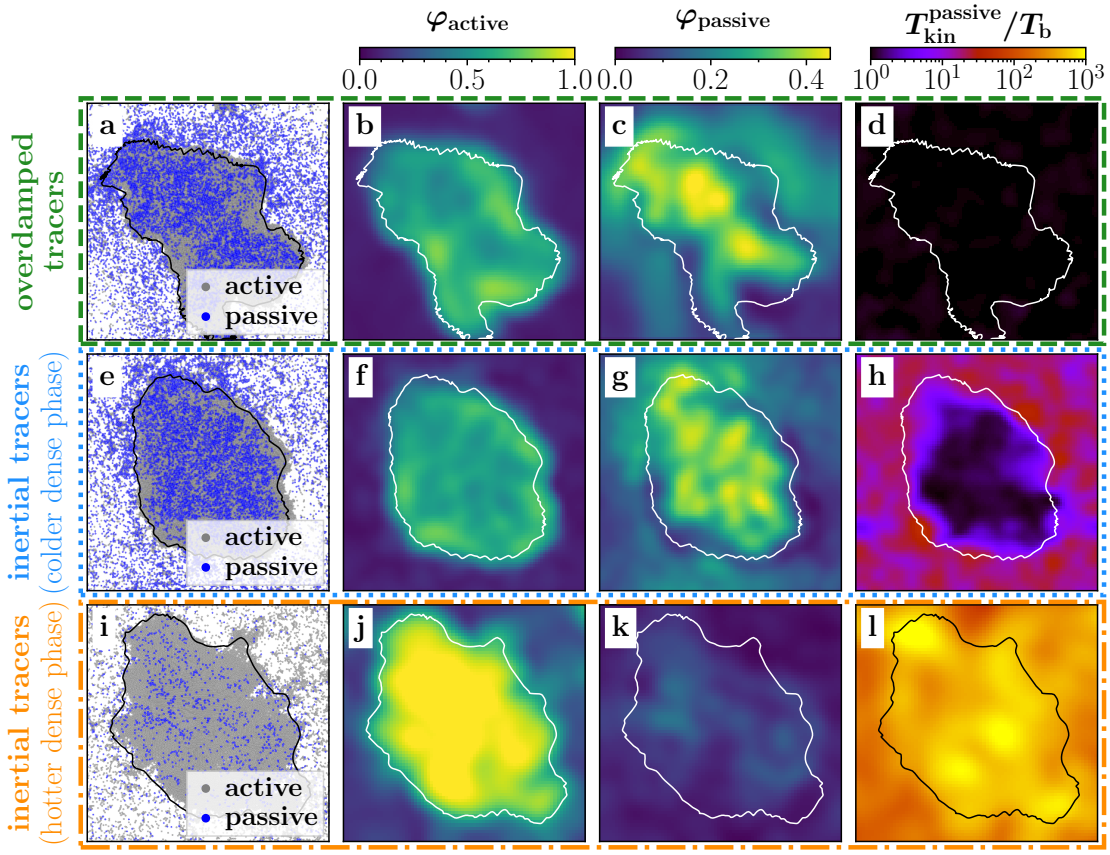

Fig. 6.2 Kinetic temperature and area fraction at coexistence. From left to right we show a snapshot of the particle positions in the steady state (**a**, **e**, and **i**), the local area fraction of active (**b**, **f**, and **j**) and passive (**c**, **g**, and **k**) particles, and the coarse-grained kinetic temperature field of the passive tracer particles (**d**, **h**, and **l**) averaged over time in the steady state, respectively. Panels i–l are slightly zoomed in and the black and white solid lines are guides to the eye denoting the border of the dense phase. Parameters: $x_{\text{a}} = 0.6$, Pe $= 100$, $m_{\text{p}}/(\gamma_{\text{t}}\tau_{\text{p}}) = 5 \times 10^{-5}$ (**a–d**); $x_{\text{a}} = 0.6$, Pe $= 100$, $m_{\text{p}}/(\gamma_{\text{t}}\tau_{\text{p}}) = 5 \times 10^{-2}$ (**e–h**); $x_{\text{a}} = 0.9$, Pe $= 400$, $m_{\text{p}}/(\gamma_{\text{t}}\tau_{\text{p}}) = 5 \times 10^{-2}$ (**i–l**); $N_{\text{a}} + N_{\text{p}} = 20\,000$, $\varphi_{\text{tot}} = 0.5$.

leading to complete phase separation. However, when exploring the kinetic temperature of the passive particles within the steady state, we find that, remarkably, the passive particles in the dense phase are colder than in the dilute phase. The temperature ratio of the two phases is highly significant and is approximately 2.5 (Fig. 6.2h). While this temperature difference is similar to what has previously been seen in underdamped active particles[103,123,165] and driven granular particles,[530–535,567–571,611,613] its emergence in the present setup is surprising since it is well known that neither the overdamped active particles[103] nor the underdamped tracers alone[504,621] would result in a kinetic temperature difference across coexisting phases. Accordingly, the temperature difference must arise from the interactions of the two species. To understand this in detail, it first might be tempting to start from the common understanding of kinetic temperature differences in granular systems or purely active systems made of inertial ABPs such as Janus colloids

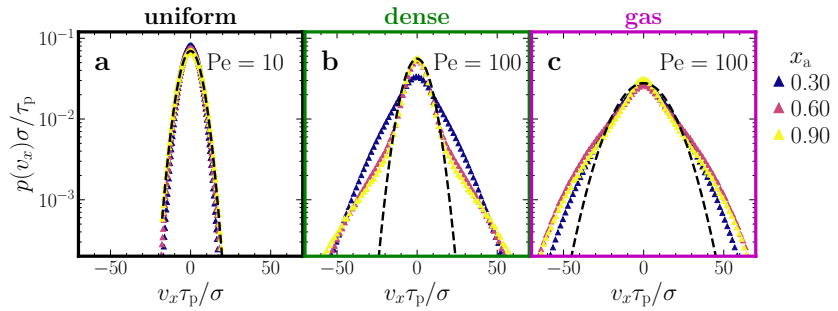

Fig. 6.3 Velocity distribution. Distribution of the x component of the velocities of the passive particles **a** in the uniform state at Pe $= 10$ and in the MIPS state at Pe $= 100$ **b** in the dense phase and **c** in the gas phase for different values of x_a as given in the key. The black dashed lines are Gaussian fits showing that the distributions are clearly non-Gaussian in the MIPS state. Parameters: $m_a/(\gamma_t\tau_p) = 5 \times 10^{-5}$, $m_p/(\gamma_t\tau_p) = 5 \times 10^{-2}$, $\varphi_{tot} = 0.5$, $N_a + N_p = 20\,000$.

in a plasma,[562] microflyers,[157] or beetles at interfaces,[603] which relates the emergence of a temperature difference to an enhanced energy dissipation in the dense phase at the level of the particles. The latter could occur due to inelastic collisions as for granular particles[531] or due to multiple collisions between which drag forces transfer energy from the particles to the surrounding liquid as for active particles (cf. Sec. 2.3).[103,165] However, in the present case of a mixture, collisions between active and passive particles have a different effect in the dense and in the dilute phase. In the dense phase, the motion of the passive particles is constricted by the surrounding clustered ABPs (see, e.g., Fig. 6.2e), which accumulate mostly at the border of the clusters, similarly as in completely overdamped mixtures,[450,619] and which cause an effective attraction between the passive tracers by pushing them together (see also Subsec. 6.3.3).[52,203,622] Therefore, the passive particles cannot move much in the dense phase and have a lower kinetic energy there compared to the dilute phase. This is also visible in the velocity distribution of the passive particles, which narrows for increasing x_a in the dense phase (Fig. 6.3). In contrast, in the dilute phase, when active particles collide with passive particles, they can persistently push passive particles forward and accelerate them such that their kinetic energy increases above the energy they would have due to the surrounding heat bath. Such a correlated active-passive dynamics heats up the passive particles in the dilute phase and leads to a broader velocity distribution at intermediate Pe such as Pe $= 100$ (see below).

6.2.3 Hot liquid-like droplets in a cold gas

Since the observed temperature differences are activity induced, one might expect that the temperature gradient further increases when enhancing the self-propulsion speed of the active particles, i.e., when increasing Pe. Surprisingly, however, in many cases, the opposite is true. For example, for fractions $x_a = 0.3$, 0.6, or 0.9 of ABPs, we find that the kinetic temperature difference is largest for some intermediate Pe and then decreases essentially monotonously with increasing Pe (Fig. 6.4) before it even reverts and we obtain dense liquid-like droplets that are hotter than the surrounding gas. As time evolves, these droplets grow (coarsening) leading to larger and larger clusters, ultimately resulting

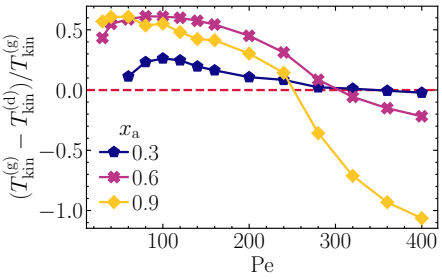

Fig. 6.4 Kinetic temperature difference. Normalized kinetic temperature difference $(T_{\rm kin}^{(g)} - T_{\rm kin}^{(d)})/T_{\rm kin}^{(g)}$ with mean kinetic temperatures of passive tracers $T_{\rm kin}^{(g)}$ and $T_{\rm kin}^{(d)}$ in the gas and the dense phase, respectively, as a function of Pe for three different values of x_a as denoted in the key. Parameters: $m_{\rm a}/(\gamma_{\rm t}\tau_{\rm p}) = 5 \times 10^{-5}$, $m_{\rm p}/(\gamma_{\rm t}\tau_{\rm p}) = 5 \times 10^{-2}$, $\varphi_{\rm tot} = 0.5$, $N_{\rm a} + N_{\rm p} = 20\,000$.

in a single hot and dense cluster that persists over time. Exemplarily, we show typical snapshots for the case Pe $= 400$, $x_{\rm a} = 0.9$ in Fig. 6.2i–l (see also Fig. C3, Appx. C). In panel l, one can clearly see that the liquid in the center of the figure is hotter than the surrounding gas. Such a coexistence of a hot liquid-like droplet and a cold gas —in terms of the kinetic temperature— is in stark contrast to what has been found for underdamped active particles[103,123,165] and for driven granular particles.[530–535] Note that for very large liquid-like droplets containing significantly more than about 10^4 particles, it may happen that not the entire droplets are hot but only a certain layer at their boundaries. The emergence of a hot dense droplet also contrasts with the intuitive picture given above that hinges on the idea that active particles can efficiently push forward and accelerate passive particles only in low density regions. Therefore, the key question that guides our explorations in the following is: What is the mechanism allowing for a coexistence of hot liquid-like droplets and a colder gas?

6.2.4 Mechanism: Correlated active-passive dynamics heats tracers in the dense phase

We now explore the mechanism underlying our previous observations that in mixtures of overdamped ABPs and inertial PBPs dense liquid-like droplets are persistently hotter than the surrounding gas at large Pe. To this end, we first analyze the velocity distribution of the PBPs in the uniform regime at $x_{\rm a} = 0.2$ and in the phase-separated regime at $x_{\rm a} = 0.8$, which broadens as Pe increases (Fig. 6.5a–c). Strikingly, if and only if the ABPs are sufficiently fast (Pe $\gtrsim 200$), the velocity distribution broadens more in the dense phase than in the dilute phase (Fig. 6.5b–d). This means that increasing the speed of the ABPs (i.e., increasing Pe) has a much stronger effect on the speed of the PBPs in the dense regime (where collisions are more frequent) than in the dilute regime, which ultimately leads to hot liquid-like droplets. What remains open at this stage is why the velocity distribution broadens faster for passive particles in the dense regime than in the dilute regime (only) if the Péclet number is large.

To answer this question, we now explore the power balance of the passive particles in the dense and the dilute phase. As we will see, this power balance points us to correlations between active and passive particles which lead to hot liquid-like droplets at large Pe. To

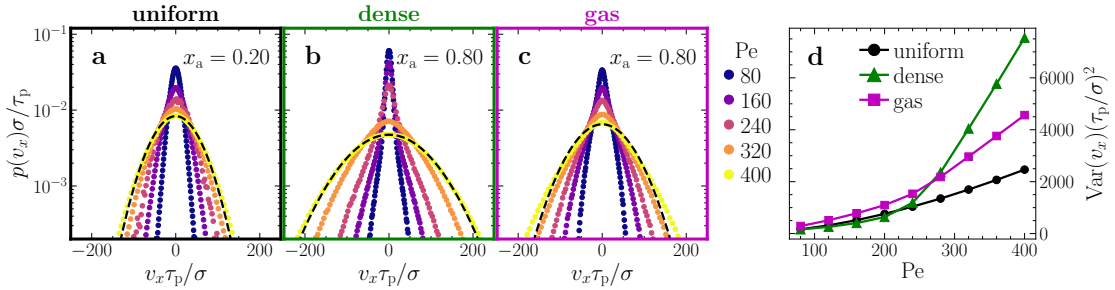

Fig. 6.5 Velocity distribution of passive tracers. Distribution of the x component v_x of the passive particles' velocities **a** in the uniform state at $x_a = 0.2$ and **b**,**c** in the phase-separated state at $x_a = 0.8$ for passive particles in the dense and the gas phase, respectively, averaged over time in the steady state. Different Pe values are given in the key (parameters as in Fig. 6.4). The black dashed lines are Gaussian fits. **d** Variance of v_x as function of Pe for the three cases shown in panels **a**–**c** averaged over 5 independent ensembles in the steady state.

obtain a power balance equation for the PBPs, we first multiply Eq. (2.1) by $\mathbf{v}_j$ and take the ensemble average. With $k_B T_{kin} = m_p \langle \mathbf{v}_j^2 \rangle / 2$, this leads to

$$\frac{2\gamma_t}{m_p} k_B T_{kin} = \frac{2\gamma_t}{m_p} k_B T_b + \langle \mathbf{v}_j \cdot \mathbf{F}_{int,j} \rangle \tag{6.1}$$

in the steady state, where $\mathbf{F}_{int,j} = -\sum_{\substack{n=1 \\ n \neq j}}^{N} \boldsymbol{\nabla}_{\mathbf{r}_j} u(r_{jn})$ is the total interaction force on particle j and $r_{jn} = |\mathbf{r}_j - \mathbf{r}_n|$. If we now compare the power balance for particles in the dense and in the gas phase, we can express the kinetic temperature difference as (we omit the index j from now on)

$$k_B \left(T_{kin}^{gas} - T_{kin}^{dense} \right) = \frac{m_p}{2\gamma_t} \left[\langle \mathbf{v} \cdot \mathbf{F}_{int} \rangle_{gas} - \langle \mathbf{v} \cdot \mathbf{F}_{int} \rangle_{dense} \right], \tag{6.2}$$

where $\langle \cdot \rangle_{dense}$ and $\langle \cdot \rangle_{gas}$ denote the average over all particles in the dense and the gas phase, respectively. This central equation leads to two important conclusions: First, the kinetic temperature difference between the dense and the gas phase is proportional to m_p/γ_t, which vanishes if the PBPs are overdamped in accordance with our simulations (see Fig. 6.2d and Subsec. 6.2.6). Interestingly, the same proportionality has also been observed for a single-component system consisting of inertial ABPs, where it has been observed that the dense phase is always colder than the gas phase.[103] Second, the temperature difference depends on the interaction between the particles given by the term $\langle \mathbf{v} \cdot \mathbf{F}_{int} \rangle$, which measures how strongly interactions push the PBPs forward in their direction of motion. From the probability distribution of the individual values $\mathbf{v} \cdot \mathbf{F}_{int}$ that contribute to the mean (Fig. 6.6a,e), we obtain significant differences between the dense and the gas phase at large values of $\mathbf{v} \cdot \mathbf{F}_{int}$, which determine the sign of the temperature difference: At intermediate Pe, e.g., Pe $= 80$ (Fig. 6.6a), large values of $\mathbf{v} \cdot \mathbf{F}_{int}$ are more frequent in the gas phase than in the dense phase (see also Fig. 6.6d). That is, events in which the interaction force and the velocity of the PBPs are aligned and large (e.g., if an ABP is pushing a PBP forward)[623] are more frequent in the gas phase than in the dense phase, in which the particles have significantly less space to move and accelerate. In contrast,

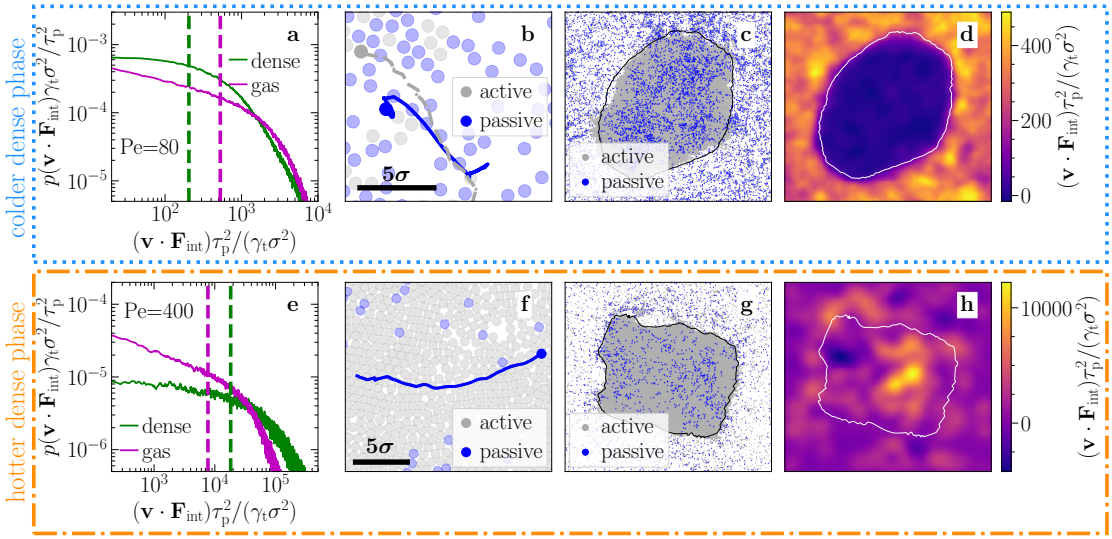

Fig. 6.6 Correlated particle dynamics. a,e Distribution of $\mathbf{v}\cdot\mathbf{F}_{\rm int}$ for the passive tracers (PBPs) averaged over time in the steady state. The dashed vertical lines mark the corresponding mean values. **b** Exemplary trajectories of an active and a passive particle in the dilute phase (gray dashed and blue solid line, respectively), where the active particle pushes the passive particle forward such that $\mathbf{v}$ and $\mathbf{F}_{\rm int}$ are aligned and $\mathbf{v}\cdot\mathbf{F}_{\rm int}$ is large. **f** Exemplary trajectory of a passive particle in a liquid-like droplet pushed forward as a result of correlated dynamics of the active particles. **c,g** Snapshots of the corresponding simulations in the steady state. **d,h** Corresponding coarse-grained values of $\mathbf{v}\cdot\mathbf{F}_{\rm int}$. The black and white solid lines in panels c,d,g, and h indicate the border of the dense phase. Parameters: Pe $= 80$ and $x_{\rm a} = 0.7$ (a,c, and d), Pe $= 100$ and $x_{\rm a} = 0.6$ (b), Pe $= 400$ and $x_{\rm a} = 0.9$ (e–h); other parameters as in Fig. 6.4.

at large Pe, such events are more frequent in the dense phase finally leading to the coexistence of hot liquid-like droplets with a colder gas (Fig. 6.6e,h). Intuitively, this is because at very large Pe, ABPs can (collectively) push PBPs forward over relatively long periods of time even in the dense phase without being stopped by collisions with other particles due to the strong effective self-propulsion force. These correlated particle dynamics are exemplarily shown in Fig. 6.6b,f and schematically visualized in Fig. 6.7. The correlated dynamics of active and passive particles also lead to a long ballistic regime in the mean-square displacement of the passive particles at intermediate times (similar as for a completely overdamped mixture)[450] before the dynamics of the passive particles becomes diffusive again (Fig. C5f, Appx. C). The corresponding long-time diffusion coefficient increases with Pe and $x_{\rm a}$ (Fig. C5c,g, Appx. C). Finally, we can ask why the temperature difference between the hot liquid-like droplets and the cold gas is larger at large fraction $x_{\rm a}$ of active particles. This is because at large $x_{\rm a}$, the active particles accumulate in the dense phase and induce stronger collective motions in that place when they are many (see also Fig. C6, Appx. C). Conversely, the fraction of active particles in the surrounding gas does not depend much on $x_{\rm a}$, and hence, the collision rate in the gas does not increase with $x_{\rm a}$.

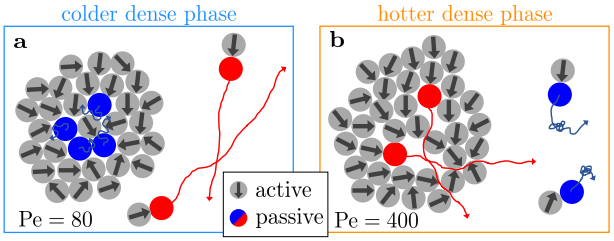

Fig. 6.7 Schematic illustration of the mechanism. a At low Pe, passive particles are trapped in the dense phase and have no space to speed up. Long correlated trajectories where active particles push passive ones forward occur only in the dilute phase. Thus, passive particles are faster in the dilute phase. **b** At large Pe (fast self-propulsion), long correlated trajectories where active particles push passive ones forward occur even in the dense phase (and are supported by collective motion of the active particles). The more frequent collisions in combination with the collective motion of the ABPs in the dense phase lead to faster PBPs in liquid-like droplets compared to the surrounding gas.

6.2.5 Non-equilibrium state diagram

The coexistence of hot liquid-like droplets and a cold gas requires sufficiently fast self propulsion of the ABPs, i.e., large Pe. For this reason, we now examine the parameter dependence more systematically. Therefore, we explore the non-equilibrium state diagram by varying Pe $\in [0, 400]$ and $x_\mathrm{a} \in [0.0, 1.0]$ at a constant area fraction $\varphi_\mathrm{tot} = 0.5$. The transition line between the uniform and the MIPS regime is obtained by analyzing the local area fraction calculated from averages over circles of radius $R = 5\sigma$ (see Eq. (3.4)). Its distribution is unimodal in the uniform regime and bimodal in the coexistence regime allowing to distinguish between the uniform and the MIPS regime (Fig. C4, Appx. C).[71,72,152,398] We distinguish between the passive particles in the dense and the dilute phase in the steady state and calculate their mean kinetic temperature (see Subsec. 6.2.1 and Fig. C2, Appx. C, for details). The system phase separates for large enough fraction of active particles x_a and large enough Pe (Fig. 6.8). At small Pe, the transition line approximately follows the transition line of a purely overdamped mixture, which reads $x_\mathrm{a}^{(\mathrm{critical})} \propto 1/(\varphi_\mathrm{tot}\mathrm{Pe})$.[619] However, at large Pe, the partially underdamped system requires a larger fraction of active particles to undergo MIPS than the purely overdamped system, which can be understood as a consequence of inertial effects: At large Pe, the PBPs are typically fast when they collide with an ABP. Due to their inertia, the PBPs slow down only gradually and sometimes even push aggregated ABPs apart, which can destroy small aggregations. This effect is particularly pronounced for large Pe and opposes the onset of MIPS. Hence, compared to a completely overdamped system, a larger fraction of active particles is required to initiate MIPS at large Pe.

The different kinetic temperatures in the dense and the dilute phase are indicated by the colors in Fig. 6.8. It can be seen that the temperature difference between the dense and the dilute phase strongly depends on both x_a and Pe: In accordance to the mechanism which we have discussed in Subsec. 6.2.4, we find that for intermediate Pe, the dense phase shows a lower kinetic temperature than the dilute phase with a maximum temperature difference around $(\mathrm{Pe}, x_\mathrm{a}) \approx (80, 0.7)$ (red circle in Fig. 6.8). For large Pe and large x_a, the kinetic temperature difference changes its sign, indicated by the squares

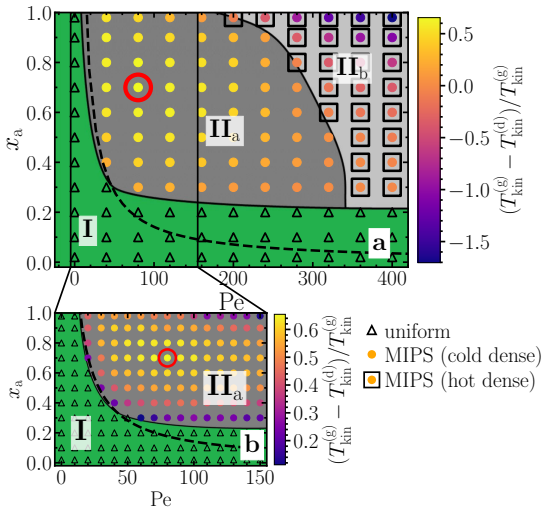

Fig. 6.8 Non-equilibrium state diagram for 2×10^4 particles. a (I) uniform state, ($\mathrm{II_a}$) hot gas and cold liquid coexistence, and ($\mathrm{II_b}$) cold gas and hot liquid-like droplets coexistence. The colors denote the (normalized) kinetic temperature difference of the passive particles in the dense and the gas phase. The black dashed line denotes the transition line as obtained in Ref. [619] for a purely overdamped mixture. Panel **b** shows a zoomed version of panel **a** and the red circle denotes the maximum temperature difference in regime $\mathrm{II_a}$. All data is averaged over a time interval $\Delta t = 900\,\tau_\mathrm{p}$ in the steady state (parameters as in Fig. 6.4).

in Fig. 6.8a, i.e., hot liquid-like droplets coexist with a cold gas. The latter occurs at lower Pe for increasing x_a because the overall energy transfer from the active to the passive particles is larger for large x_a only in the dense phase, where the active particles increasingly accumulate as x_a increases (see also Figs. C5 and C6, Appx. C). This can also be seen from the parameter dependence of the kinetic temperature of the passive particles (Fig. C7, Appx. C): The kinetic temperature increases with increasing x_a (and increasing Pe) in the dense phase but shows a maximum at intermediate x_a in the gas phase, where the fraction of active particles hardly increases when increasing x_a beyond a certain point.

6.2.6 Role of inertia

Inertia of the PBPs is a key ingredient to observe coexisting temperatures. This can be seen in Fig. 6.9 and from Eq. (6.2): The temperature difference is proportional to the ratio $m_\mathrm{p}/\gamma_\mathrm{t}$. Thus, in the overdamped limit $m_\mathrm{p}/\gamma_\mathrm{t} \to 0$, the temperature difference vanishes (Fig. 6.2d) because the PBPs react instantaneously to acting forces. Thus, their motion, and hence, also their kinetic temperature, is dominated by diffusion.[103] In contrast, sufficiently heavy (inertial) PBPs can store the energy gained during collisions with active particles as kinetic energy such that their kinetic temperature is not determined by diffusion alone, which is fully consistent with our simulation data and previous literature.[103,123,165,530–535] Increasing inertia does also lead to a significant violation of the equipartition theorem both in the dense and the gas phase (see Subsec. 6.3.2), which indicates that the system is increasingly far away from equilibrium when increasing inertia of the PBPs.

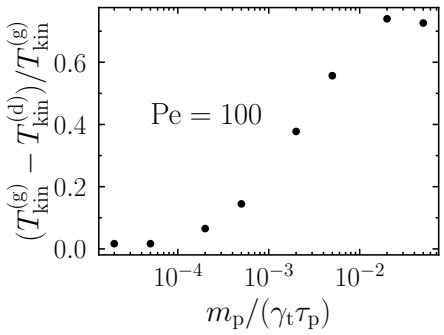

Fig. 6.9 Effect of inertia. Normalized difference of the kinetic temperature of the passive particles in the dense and in the gas phase as function of their mass m_{p}. Parameters: $x_{\mathrm{a}} = 0.6$, Pe $= 100$, $m_{\mathrm{a}}/(\gamma_{\mathrm{t}}\tau_{\mathrm{p}}) = 5 \times 10^{-5}$ (other parameters as in Fig. 6.4).

6.2.7 Role of the particle size

For simplicity, we have considered active and passive particles with the same size and the same drag coefficients so far but with significantly different material density. Now, we show that persistent temperature differences also occur when the passive particles are significantly larger than the active ones. We have varied the size ratio $s = \sigma_{\mathrm{p}}/\sigma_{\mathrm{a}} \in \{1, 2, 3, 4, 6, 8, 10\}$ keeping σ_{a} as well as m_{p}, m_{a}, and φ_{tot} fixed. The fraction x_{a} is chosen such that the area fraction of active particles is approximately 0.5 for small size ratios. For large size ratios, we kept $x_{\mathrm{a}} = 0.99$ fixed to ensure that enough passive particles are inside the system. For the drag coefficient of the passive particles, we now choose $\tilde{\gamma}_{\mathrm{t}} = \sigma_{\mathrm{p}}\gamma_{\mathrm{t}}/\sigma_{\mathrm{a}}$. Our results are exemplarily shown in Fig. 6.10 for Pe $= 100$. Here, we observe a persistent kinetic temperature difference between the passive particles in the dense and the gas phase even for significantly different particle sizes (Fig. 6.10h). This temperature difference is also visible in the velocity distributions, which are broader in the gas phase compared to the dense phase (Fig. 6.10e,f). Hence, the observation of a cold dense phase that coexists with a hotter surrounding gas persists even for large size ratios. The opposite case, i.e., hot liquid-like droplets coexisting with a colder gas, is also robust and leads to a temperature difference of $T_{\mathrm{kin}}^{(\mathrm{dense})} - T_{\mathrm{kin}}^{(\mathrm{gas})} \approx 196.0\, T_{\mathrm{b}}$ for $\sigma_{\mathrm{p}}/\sigma_{\mathrm{a}} = 10$ at Pe $= 400$, $x_{\mathrm{a}} = 0.99$, and $\varphi_{\mathrm{tot}} = 0.70$ for example. Notice however, that very large PBPs tend to accumulate in the dilute phase especially at large Pe making it challenging to calculate a precise value of the temperature difference. Interestingly, this is in contrast to purely overdamped mixtures, where large size ratios support the formation of large passive-particle clusters.[52,203]

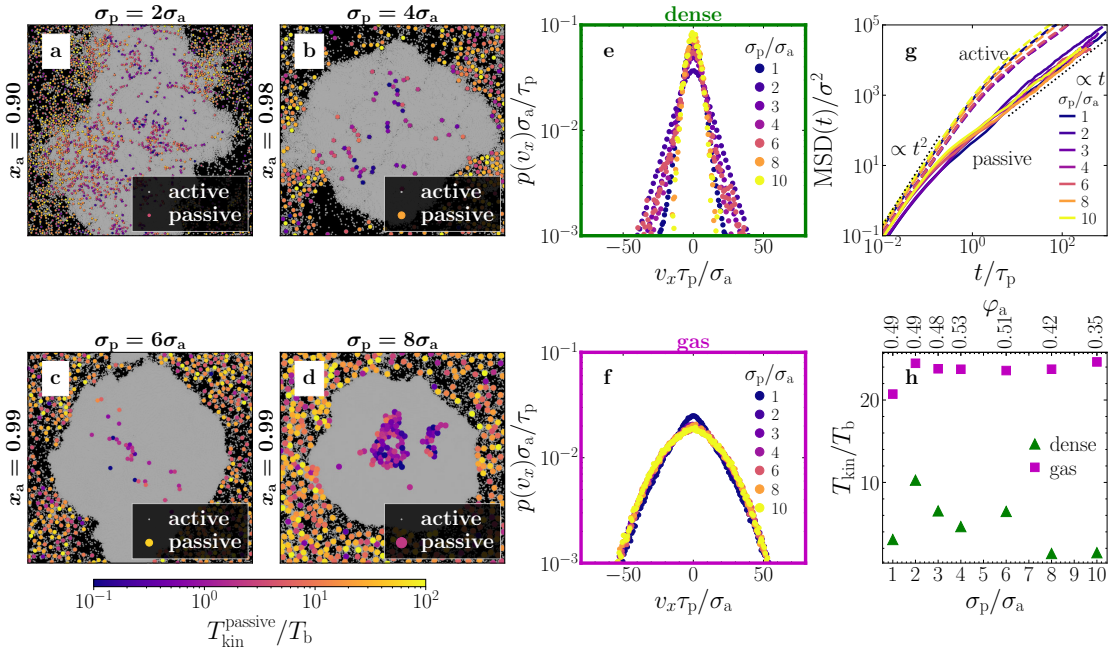

Fig. 6.10 Effect of the particle size. a–d Simulation snapshots with four different sizes of the passive particles as given in the panel titles. The passive particles are colored with respect to their kinetic temperature (Eq. (4.3)). **e,f** Velocity distribution of the passive particles in the dense and the gas phase, respectively, for different size ratios as indicated in the key. **g** Mean-square displacement of the active (dashed lines) and passive (solid lines) particles. **h** Corresponding kinetic temperatures of passive particles in the dense and the gas phase. Parameters: $\mathrm{Pe} = 100$, $\tilde{\gamma}_t = \sigma_p\gamma_t/\sigma_a$, $\varphi_{tot} = 0.7$, $N_a + N_p = 2 \times 10^4$ for $\sigma_p/\sigma_a = 1, 2, 3, 4$ and $N_a + N_p = 5 \times 10^4$ for $\sigma_p/\sigma_a = 6, 8, 10$ (other parameters as in Fig. 6.4).

6.3 Discussion

The results presented above show that a kinetic temperature difference across coexisting phases can occur even in equilibrium systems (inertial PBPs) when adding overdamped self-propelled particles (ABPs). They represent a striking non-equilibrium phenomenon for collective behavior in active systems and answer the fundamental question if a non-equilibrium gas can be colder than a coexisting liquid. The temperature difference between the coexisting phases is maintained by the implicit energy source that drives the active particles. As a consequence, the system is intrinsically out of equilibrium. In equilibrium, the equipartition theorem would imply that the kinetic temperature of the active and passive particles are the same. Here, the emergence of a persisting temperature difference is directly related to the violation of the equipartition theorem, which we discuss in Subsec. 6.3.2. To measure the temperature difference, we have used the kinetic temperature as defined in Eq. (4.3). However, this definition is sensitive to collective movements of the particles, which are present especially in the dense phase. Since a suitable temperature definition should measure the fluctuations only as already discussed in Chap. 4, we discuss the effects of this sensitivity on our results in the following subsection. In particular, we show that our results are qualitatively the same even for other

temperature definitions that are not sensitive to collective movements. In the scenario of a cold liquid coexisting with a hot gas, passive particles are trapped by surrounding active ones. To discuss this effect in more detail, we calculate the effective force at the interface between the dense and the dilute phase in Subsec. 6.3.3.

6.3.1 How representative is the kinetic temperature?

So far, following Refs. [103, 163–165], we have used the kinetic energy of the particles to define a kinetic temperature as a measure for the temperature (cf. Eq. (4.3)). The kinetic temperature has frequently been used for granular systems[173,529–536] and is also well-defined in non-equilibrium systems.[170] In equilibrium, the kinetic temperature is equal to the thermodynamic temperature.[504] In the binary mixtures of active and passive particles studied in the present chapter, the kinetic temperature of the PBPs, which measures the velocity fluctuations, has two contributions: one from the thermal Brownian motion and one originating from collisions with surrounding active and passive particles. From the previously discussed results, we know that the latter causes the kinetic temperature difference between PBPs in the dense and the gas phase. Additionally, we analyzed the velocity distribution of the PBPs in the dense and the gas phase. Its variance exhibits the same behavior as the kinetic temperature (Fig. 6.5d). Remarkably, the velocity distributions are approximately Gaussian for sufficiently large Pe (Fig. 6.5a–c). We exploit this to calculate the Maxwell-Boltzmann temperature T_{MB} as defined in Eq. (4.9). For the data shown in Fig. 6.5b,c at $\mathrm{Pe} = 400$ we obtain $T_{\mathrm{MB}}/T_{\mathrm{b}} = 3.6 \times 10^2$ (liquid-like droplets) and $T_{\mathrm{MB}}/T_{\mathrm{b}} = 1.9 \times 10^2$ (gas). This shows that mixtures of inertial PBPs and overdamped ABPs can lead to self-organized hot liquid-like droplets that coexist with a colder gas also in terms of the Maxwell-Boltzmann temperature.

A sensible measure for the temperature of the particles should measure their independent motion. Since both the kinetic temperature and the Maxwell-Boltzmann temperature are sensitive to local collective motion patterns of the particles, we now explore if spatial velocity correlations of the passive tracer particles are crucial for the emergence of a temperature difference. For that we calculate the spatial velocity correlation function[577]

$$C_v(r) = \frac{\langle \mathbf{v}(r) \cdot \mathbf{v}(0) \rangle}{\langle \mathbf{v}(0)^2 \rangle}. \tag{6.3}$$

As shown in Fig. 6.11b, velocity correlations are indeed present between the PBPs in the dense phase over a significant spatial range indicating that collective motion might strongly influence the kinetic temperatures. In fact, we find that the mean distance between the PBPs in the dense phase calculated from a Voronoi tessellation (cf. Subsec. 3.4.3) is given by approximately $4.6\,\sigma$ for the case shown in Fig. 6.11a–c and therefore, much smaller than the length scale of the velocity correlations (Fig. 6.11b). To exclude that such collective motions are required to achieve a coexistence of a hot liquid and a cold gas, we have performed simulations with a very low fraction of passive particles such that their typical distances to each other are significantly longer than the velocity correlations within the dense phase. Concretely, we did a simulation with 10^5 particles and $x_{\mathrm{a}} = 0.996$ at $\mathrm{Pe} = 400$, which again shows MIPS and a significant temperature difference between the passive particles in the dense droplets and the surrounding gas (Fig. 6.11d–f and Tab. 6.1). In contrast to the previous scenario shown in Fig. 6.11a–c, the correlations

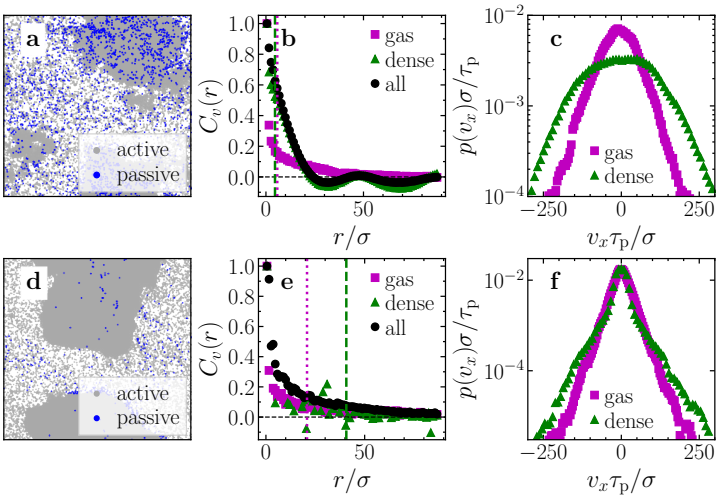

Fig. 6.11 Spatial velocity correlations. a–c Snapshot in the steady state, spatial velocity correlation function of passive particles (Eq. (6.3)), and velocity distribution of passive particles in the dense and the gas phase, respectively, for a simulation of $N = 20\,000$ particles at $x_\mathrm{a} = 0.90$. The dashed and dotted lines in panel b denote the mean distance $\bar{d}$ between passive particles obtained from a Voronoi tessellation in the dense phase ($\bar{d} \approx 4.6\,\sigma$) and in the gas phase ($\bar{d} \approx 5.8\,\sigma$), respectively. **d–f** Same as a–c but for a simulation of $N = 100\,000$ particles at $x_\mathrm{a} = 0.996$. The mean distance between the passive particles denoted by the dashed and dotted line in panel e is $\bar{d} \approx 41\,\sigma$ (liquid) and $\bar{d} \approx 21\,\sigma$ (gas), respectively. All data has been averaged over time in the steady state. Simulation parameters: $\mathrm{Pe} = 400$ (other parameters as in Fig. 6.4).

between the PBPs are now significantly reduced, and the mean distance between the PBPs in the dense phase is approximately $41\,\sigma$, i.e., larger than the length scale of the velocity correlations (Fig. 6.11e). Hence, in this parameter regime, the temperature calculation is not much influenced by local collective motion of the PBPs, but remarkably, the PBPs in the dense phase still have a higher temperature than the PBPs in the gas phase. This is shown in Fig. 6.11f and in Tab. 6.1. Hence, the coexistence of hot liquid-like droplets with a colder gas should also occur when using other (fluctuation-based) temperature definitions that are not sensitive to collective movements of the passive particles.

To explicitly see this, we additionally calculate a relative kinetic temperature by using the relative velocity of each particle to the mean velocity of particles in the vicinity

$$k_\mathrm{B} T_\mathrm{kin,\,rel} = \frac{m_\mathrm{p}}{2} \left\langle \left(\mathbf{v} - \langle \mathbf{v} \rangle_R \right)^2 \right\rangle , \tag{6.4}$$

where $\langle \mathbf{v} \rangle_R$ denotes the mean velocity of all particles in a circle of radius $R = 5\sigma$ around the tagged particle. As shown exemplarily in Tab. 6.1, the temperature difference is also visible for the relative kinetic temperature, and thus, it is not only a consequence of the observed collective motion but rather a pure effect of the particle interactions. As a result, the key phenomenon —the coexistence of hot liquid-like droplets and a cold gas— is robust with respect to the choice of the definition of the particle temperature.

Tab. 6.1 Temperature definitions. Exemplary temperature values of the passive particles in the dense and the gas phase obtained from the different temperature definitions. The values for **A** and **B** correspond to the two simulations shown in Fig. 6.11a–c and d–f, respectively. For the latter, the velocity distribution is not Gaussian, and therefore, T_{MB} cannot be determined.

		$T_{\mathrm{kin}}/T_{\mathrm{b}}$	$T_{\mathrm{kin,\,rel}}/T_{\mathrm{b}}$	$T_{\mathrm{MB}}/T_{\mathrm{b}}$
A (Fig. 6.11a–c)	dense	4.4×10^2	2.8×10^2	4.3×10^2
	gas	2.2×10^2	2.2×10^2	1.7×10^2
B (Fig. 6.11d–f)	dense	6.6×10^1	6.2×10^1	-
	gas	5.0×10^1	4.9×10^1	-

6.3.2 Violation of the equipartition theorem

The different persisting temperatures are accompanied by a violation of the equipartition theorem, which holds for classical systems in equilibrium (cf. Sec. 4.2). It states that each degree of freedom (which is quadratic in the (momentum) coordinates) contributes on average with $k_{\mathrm{B}}T/2$ to the total energy of the system.[504,505] This would imply that the kinetic temperature of the active and passive particles are the same, which is in fact the case for a completely overdamped system (Fig. 6.12). In contrast, increasing inertia leads to a significant violation of the equipartition theorem both in the dense and the gas phase, as shown in Fig. 6.12. This indicates that the system is increasingly far away from equilibrium when increasing inertia of the PBPs. Irrespective of this, the equipartition theorem applies for small Pe, where the dynamics of the system is dominated by thermal diffusion and the system is near equilibrium (Figs. C8 and C9a,b, Appx. C). However, the ratio $T_{\mathrm{kin}}^{\mathrm{passive}}/T_{\mathrm{kin}}^{\mathrm{active}}$ of the kinetic temperature of the passive and active particles increases significantly with increasing Pe both in the uniform regime and in the coexistence regime (Figs. C8 and C9a,b, Appx. C). Note that the ratio $T_{\mathrm{kin}}^{\mathrm{passive}}/T_{\mathrm{kin}}^{\mathrm{active}}$ is largest at large x_{a} (and large Pe) in the dense phase (Figs. C8 and C9a,c, Appx. C), whereas in the dilute phase, it reaches its maximum at intermediate (small Pe) or small (large Pe) x_{a} (Fig. C9d, Appx. C), which is in line with our analysis leading to the transition between the scenarios hot-liquid–cold-gas and hot-gas–cold-liquid.

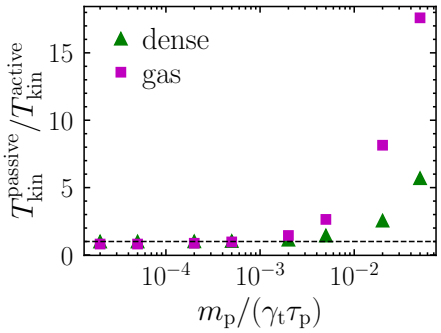

Fig. 6.12 Mass dependence of the violation of the equipartition theorem. Ratio between the kinetic temperature of the active and the passive particles in the dense phase (triangles) and the gas phase (squares) as function of the mass m_{p} of the passive particles. Parameters: Pe $= 100$, $x_{\mathrm{a}} = 0.6$, and $m_{\mathrm{a}}/(\gamma_{\mathrm{t}}\tau_{\mathrm{p}}) = 5 \times 10^{-5}$ (other parameters as in Fig. 6.4).

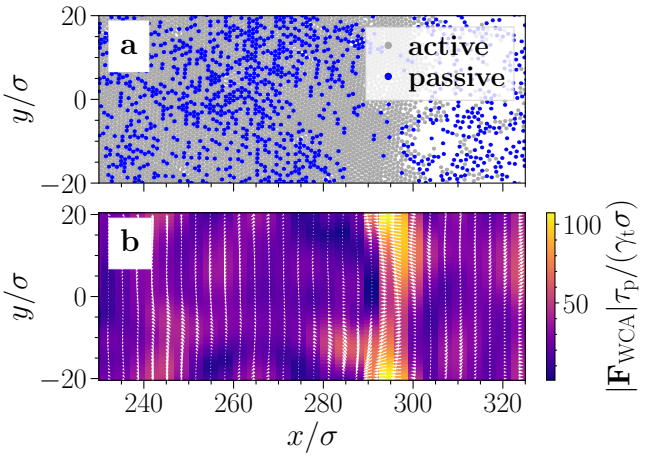

Fig. 6.13 Effective force on passive particles. a Snapshot of the binary mixture in a thin rectangular box showing MIPS. The box shape ensures that the border of the dense phase is approximately stationary allowing for long-time averages. Here, we show an extract from the simulation showing one interface and a part of the dense and the dilute phase in its vicinity. **b** Corresponding coarse-grained force field of the interaction force from the WCA potential acting on the passive particles. The color and arrow length represent its strength, the orientation of the white arrows its direction. A strong effective force is pushing passive particles towards the dense phase (yellow region). Parameters: Pe $= 100$, $x_{\mathrm{a}} = 0.6$, $L_x = 784\sigma$, $L_y = 40\sigma$ (other parameters as in Fig. 6.4).

6.3.3 Effective forces on passive particles

At low and intermediate Pe, we have shown that the PBPs are colder in the dense phase compared to the dilute phase in terms of their kinetic temperature. As described in Subsec. 6.2.2, the mechanism of this phenomenon is based on a trapping of inertial PBPs within the dense phase. In contrast, in the dilute phase, ABPs can push the PBPs forward and persistently speed them up. One key ingredient of this mechanism is that the PBPs remain trapped and are densely packed within the dense phase. To explore this in more detail, we have calculated the effective force acting on the PBPs depending on their position. To this end we made a simulation in a slit geometry in which the border of the dense phase is approximately stationary and does not move much, which allows us to perform a long-time average. In particular, we use a simulation box of length $L_x = 784\,\sigma$ and $L_y = 40\,\sigma$. We calculate the interaction force acting on each passive particle and coarse-grain the forces by using Gaussian-kernel density estimation using the amep.continuum.gkde function provided by AMEP with Gaussians of width $5.0\,\sigma$ (bandwidth=5.0). As shown in Fig. 6.13b, the effective force always points to the dense phase at its border, i.e., the passive particles are pushed inside the dense phase. This effective force finally ensures that the passive particles remain densely packed within the dense phase.

6.4 Conclusion

Mixing overdamped active Brownian particles and inertial passive Brownian particles leads to a persistent kinetic temperature difference between the dense and the dilute phase when the system undergoes motility-induced phase separation. This temperature difference emerges despite the fact that each of the two components on their own would show a uniform temperature profile. Counterintuitively, the dilute gas-like phase is not always hotter than the dense liquid-like phase but at large Péclet numbers and fractions of active particles, hot liquid-like droplets can coexist with a cold gas. This temperature reversal results from the competition of two effects: The trapping of passive particles in the dense cluster provokes a cold liquid whereas the emergence of persistent correlated active-passive particle trajectories in the dense phase primarily heats up the liquid. While the latter effect has not been known in the literature so far, we have shown that it can even overcome the previously discussed trapping effect such that active particles collectively push and heat up passive ones primarily within the dense phase. This leads to the coexistence of a cold gas and hot liquid-like droplets and shows that a non-equilibrium gas can be colder than a coexisting liquid. The observed phenomenon is robust with respect to the choice of definition of particle temperature and particle-size effects at least up to a size ratio of 10. For even larger size ratios, it can happen that all inertial passive particles remain in the gas phase, and hence, no temperature difference can be observed. Besides their conceptual relevance, our results open a route to create a persistent temperature profile in systems like dusty plasmas or passive granulates by inserting overdamped active particles like bacteria, algae, or synthetic colloidal microswimmers.

7 Writing into Water

Up to this point, we have discussed self-assembly phenomena of particles in purely active systems and in mixtures of active and passive particles leading to particle clusters that have significantly different kinetic temperatures compared to the particles in their environment. This self-assembly is driven by motility-induced phase separation, a prime example for non-equilibrium phase separation in active systems. Self-assembly of particles can also be achieved in purely passive systems such as colloidal particles dispersed in a liquid medium. Here, hydrodynamic effects can lead to collective particle movements, hydrodynamic interactions, and assembly of particles. In this chapter, we address the question of whether we can use self-assembly phenomena in colloidal systems to "write" lines, letters, and complex patterns into a liquid medium.

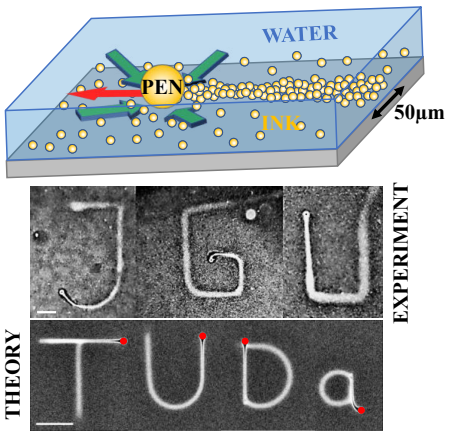

Fig. 7.1 Illustration of the experimental setup (top) and two exemplary writing results from experiments (mid) and simulations (bottom).

As an ancient communication technique, writing is typically based on solid surfaces on which letters are engraved or on which ink is deposited. However, to write into a liquid medium, fundamentally different approaches are required. In this chapter, we demonstrate a new technique to write lines, letters, and complex patterns in water by assembling lines of colloidal particles. The written lines are fully reconfigurable and do not require any fixation onto a substrate. The corresponding experiments are based on an ion-exchange resin bead (pen) that rolls on a substrate across a layer of sedimented colloidal particles (ink). The pen produces a hydrodynamic flow that collects ink particles along its trajectory, as illustrated in Fig. 7.1. With sophisticated pen-steering techniques, we can draw and write with durable, high-contrast lines. We developed a minimal model to theoretically predict the ink assembly along the trajectory of the pen. Based on numerical simulations, the model predicts the observed parameter dependence for writing lines in a liquid medium and exposes the key ingredients required for writing letters into water: long-ranged (hydrodynamic) attractions between the pen and the ink particles, low diffusivity, and programmable steering of the pen.

The main content of this chapter is taken from my joint publication with Nadir Möller "Writing into Water" published in *Small* (2023) with permission from John Wiley & Sons, Inc. (Ref. [624], © 2023 The Authors. Small published by Wiley-VCH GmbH.), and the majority of this chapter is taken verbatim from it. The study has been performed in collaboration with Nadir Möller and co-workers from the group of Prof. Thomas Palberg

at Johannes Gutenberg-Universität Mainz. They did all the experimental work. In turn, I performed all simulations, analyzed all simulation data, and created all figures that include data from simulations. In the following, the main focus is on the theoretical model and numerical simulations. The experiments are explained in detail in the PhD thesis of Nadir Möller in Ref. [625].

7.1 Introduction

Traditional writing techniques comprise carving and engraving as well as printing and writing with ink. Earliest human drawings date back around $30\,000$ years, possibly even much longer.[626] As visible language, writing appeared in the Middle East between $3\,400$ and $2\,600$ before the Common Era.[627,628] These techniques continue to coexist as means of storing and transporting information, nowadays accompanied by various multimedia techniques for displaying.[629] In addition, various novel techniques extend and complement these traditional techniques, including (electron) lithography, optical tweezers, direct printing, or force microscopic manipulation.[630–637] Remarkably, the size of glyphs and letters covers the range from a few hundred meters[638] down to the atomic scale[639] and even below.[640] In the more classical approaches, one creates a local, line-shaped variation of the material density in or on an extended substrate acting as background: A line is carved out or some ink is deposited. A solid substrate stabilizes the density variation by strong inter-molecular forces, keeping it in shape. The same principle has been applied to write on surfaces submerged in a fluid. For instance, scanning probe lithography was used to carve or deposit lines within or onto self-assembled monolayers submerged in fluids containing suitable chemicals.[641,642] In addition, sophisticated micron-sized structures have been printed using two-photon polymerization.[643,644] UV-polymerization and crosslinking was also used to write on a solid surface within a liquid starting from a dispersion of reactive chemicals to manufacture patterns with superb thermoresponsive mechanical properties.[645] There are now even commercial scuba diver slates available for under-water writing on a substrate. Importantly, however, all these approaches still rely on a substrate (i) for fixing the written structures and (ii) for providing mechanical support. In contrast, writing into a fluid requires a mechanism that does not depend on such localization measures. The mechanism must also be intrinsically robust against rapid line dispersion, which would cause short lifetimes of any drawn lines. In fact, even in a quiescent (convection-free) fluid, the moving pen would transfer kinetic energy to the fluid, provoking line dispersion by locally created eddies. While such local eddies are rather unimportant when the pen is much smaller than the written letters, as, e.g., in skywriting,[646] the creation of fine, durable, and freely-floating lines remains challenging. In fact, to write fully reconfigurable lines into a liquid at the microscale, an approach fundamentally different from underwater ink deposition or line carving and a new type of micro-pen are required. To develop such an approach, we exploit the following ideas.

Incidentally, a mobile fluid offers an alternative way of writing lines by particle transport towards a prescribed pattern. Imagine to start from a homogeneous density of ink particles in a quiescent fluid and to use a pen which attracts the ink particles towards itself and/or its trajectory. If the resulting accretion process is sufficiently efficient and fast as compared to the subsequent dispersion of the ink particles, an increase of ink density may result

past the pen and a line is written. As key ingredients, this approach requires a sufficient range of the particle-transporting attraction, a slow line dispersion, and a suitable way of pen steering.

To meet the first requirement, directed transport of colloidal particles by chemical, thermal, or light-intensity gradients can be exploited. A key example are phoretic effects, where, in general, the imposed gradient leads to a difference in chemical potential along a particle surface and drives a slip flow of the adjacent fluid along the surface, which, in turn, evokes directed motion of the particle.[647–651] By using a large chemical-loaded "beacon" falling under gravity, Banerjee et al. created a colloidal over-density evolving along the trajectory within a few minutes.[652] Here, colloidal motion relied on the local strength and direction of the gradient of electrolyte concentration. While these pioneering experiments demonstrate the possibility of writing freely buoyant lines within a fluid, they lack the option of deliberate pen steering.

In this chapter, we demonstrate a generic method for writing lines and letterings into a liquid rather than onto a solid. This method uses an ion-exchange resin bead (IEX) as fully steerable micro-pen and exploits the presence of a solid substrate only for line assembly but not for fixing the ink. Instead, lines are written near a substrate but are not attached to it yielding freely floating long-lived lines which can be reconfigured and allow us to recycle the ink for writing new lines before optionally fixing them to the substrate.[645,653,654] To achieve this, we exploit an effective way to transport colloids along extended surfaces: The IEX (pen) evokes a so-called diffusio-osmotic (DO) flow.[647,655,656] Such a flow emerges because the ion-exchange process induces a nonuniform concentration profile which causes a stress (force) on the solvent within the interfacial layer of the substrate resulting in a solvent flow towards the IEX.[657] This flow then advects colloidal tracers towards the IEX, which can be viewed as an effective attraction between the IEX and the tracers.[658] In the past, DO flows have been successfully employed with fixed sources,[657–663] self-propelling sources,[664,665] and combinations of sources and sinks[666] to create centrally symmetric or asymmetric assemblies of tracer particles at the source. Here, we exploit this mechanism to dynamically assemble a line of tracer particles (ink) in the wake of a moving IEX. Once assembled, those tracers will disperse only very slowly by thermal diffusion in the eddy-free fluid. Moreover, the ongoing pen-induced DO flows focus ink particles towards the center of the written lines supporting their durability and sharpness.

Our results exemplify a generic pathway for writing and drawing fine, free-floating but durable lines in a liquid medium. Our approach is modular and allows combinations of different inks, drives, steering, and, optionally, fixation techniques. This could be used in the future for structuring liquids with deliberate line-based patterns, decorate and thus visualize chemical tracers, or create desired initial states for future colloid experiments.

7.2 Experimental results

The following experimental results have been obtained from Nadir Möller and co-workers in the group of Prof. Thomas Palberg at Johannes Gutenberg-Universität Mainz. We discuss the experimental results here to put our numerical results in perspective and to compare them to experimental data. For completeness, experimental details are summarized in Appx. D. The experimental methods are explained in detail in Nadir Möller's dissertation.[625]

7.2.1 Experimental setup and writing of straight lines

The experimental approach is sketched in Fig. 7.2a: Samples are placed on a programmable, motorized stage, allowing for tilting by ϑ and rotation around the optical axis (OA) by β, and are observed at moderate magnification ($10\times$ or $20\times$) using an inverted microscope. A dilute suspension of weakly charged, micro-sized silica spheres (Si832, tracers, T), is left to settle under gravity in a slit cell of $500\,\mu\text{m}$ height onto a charged glass substrate. To this dilute homogeneous monolayer, we add a larger bead of cationic ion-exchange resin (C-IEX45, IEX). It exchanges residual cations ($c \approx 10^{-8}\,\text{mol}\,\text{L}^{-1}$) for protons, and thus, it acts as mobile proton source (see also Tab. D1 in Appx. D for details about the used tracers and IEXs).[657] The high proton mobility quickly establishes a large-scale pH-field.[667] Tilting the substrate in x-direction by an angle ϑ causes the IEX to roll straight across the substrate with a velocity $v_{\text{IEX}} = (gV\Delta\rho/\gamma)\sin\vartheta$ (red arrow in Fig. 7.2a and Fig. D10, Appx. D).[625,668] Here, g is the gravitational acceleration, and V, $\Delta\rho$, and γ are the volume, density mismatch, and the drag coefficient of the IEX. Tracers also roll, but at negligibly small velocities. The rolling IEX (pen) remains embedded in its self-generated, co-moving pH-field,[667] and the corresponding DO flow along the substrate points towards the low pH region (green arrows). It accretes tracers towards the pen,[647,648,664] from where they are expelled to the back leaving a trail of enhanced ink-particle density. In principle, the same mechanism could be exploited to co-assemble other small objects, e.g, initiator, (macro-)monomers, and cross-linker molecules, which could later be used to fix line centers containing high tracer density by ultraviolet (UV) curing. Note that in all figures regarding experiments, the substrate is tilted such that IEX and tracers move from right to left.

Samples are studied either in dark field (Fig. 7.2b, see also Fig. D10, Appx. D) or bright field (Fig. 7.2c). In the stationary state depicted in Fig. 7.2c, the line drawn at $v_{\text{IEX}} = 7.7\,\mu\text{m}\,\text{s}^{-1}$ first narrows and then broadens again. We identify a line focus (red arrow) separating an initial formation zone of length $l_{\text{f}} = v_{\text{IEX}}t_{\text{f}}$ (where $t_{\text{f}} \approx 60$–$70\,\text{s}$ denotes the time elapsing between the passage of the IEX and the line focus) from a subsequent decay zone. To quantify the underlying mechanisms, we show the co-moving, height averaged pH-field recorded in bright field using 3-channel photometry in Fig. 7.2d.[667,669] The arrows denote the local pH-gradient directions. We observe a stationary, elliptically distorted, and rather diffuse pH distribution. From this, we calculate the pH variation at the substrate height following Möller et al. (Fig. 7.2e).[667] Note that at this height, the gradients driving the DO flow are much more pronounced. Figure 7.2f shows the resulting trajectories of individual tracers relative to the IEX. Tracers in the line of the IEX motion approach from the front and leave at the back. Tracers to the sides show

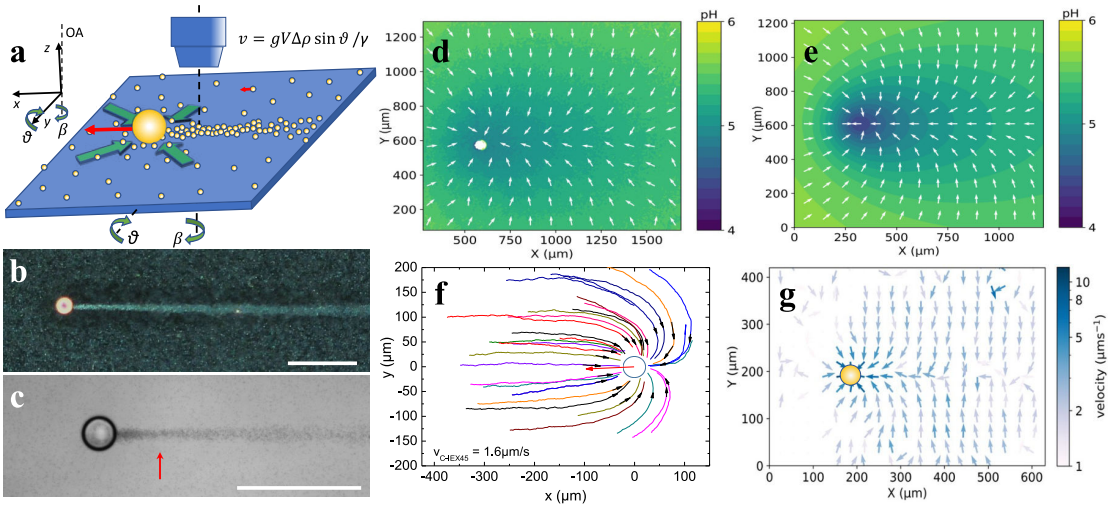

Fig. 7.2 Writing of straight lines. a Sketch of the experimental situation. The sample is placed on a stage allowing for tilting by ϑ and rotation around the optical axis (OA) by β. The IEX (large sphere) rolls under gravity (large red arrow) through settled tracer particles (small spheres), rolling at much smaller speed (short red arrow). Tracers are swept towards the IEX by the co-moving solvent flow field (green arrows) and are assembled in the back of the IEX into a line of positive density contrast, which is left behind and disperses slowly by diffusion. **b** Dark field image of C-IEX45 rolling on an inclined glass substrate ($\vartheta = 3.1°$, substrate ζ-potential $\zeta_S = -105\,\mathrm{mV}$, $v_{IEX} = 7.7\,\mu\mathrm{m\,s^{-1}}$) in a suspension of Si832 at $c = 0.1\,\mathrm{wt\%}$ (tracer ζ-potential $\zeta_T = -68\,\mathrm{mV}$). Scale bar: $200\,\mu\mathrm{m}$. **c** The same but in bright field b/w and at $c = 0.02\,\mathrm{wt\%}$. The red arrow denotes the location of the line focus. **d** Height averaged pH field in lab coordinates as determined by 3-channel micro-photometry for the experiment shown in panel b. The pH-values are color coded as indicated in the key. Arrows denote the local gradient direction. **e** Ground pH-field as derived from panel d. **f** Map of tracer approach trajectories in IEX-relative coordinates for C-IEX45 rolling at $v_{IEX} = 1.6\,\mu\mathrm{m\,s^{-1}}$. The red arrow denotes the rolling direction. **g** Tracer velocity field in lab coordinates as determined from Particle Image Velocimetry for the situation in panel c. Local velocities are color coded according to the key.

bent trajectories as they are swept towards the IEX. We depict the instantaneous lateral solvent flow field in Fig. 7.2g in lab coordinates and with color-coded flow strength. Note the striking similarity with Fig. 7.2e. Solvent flows towards the IEX but moreover also towards and along the lateral pH-minimum extending in the wake of the IEX. Due to its incompressibility, the solvent has to flow upward at the IEX.[657]

To explore the influence of the IEX speed on line writing, we varied the tilt angle ϑ to change v_{IEX} (Fig. D10b–d, Appx. D). To good approximation, the IEX speed increases linearly with $\sin\vartheta$ (Fig. D10a, Appx. D). For IEX speeds in the range of $1.5\,\mu\mathrm{m\,s^{-1}} < v_{IEX} < 11\,\mu\mathrm{m\,s^{-1}}$, straight single lines of long extension are obtained, with maximum contrast observed for $6\,\mu\mathrm{m\,s^{-1}} < v_{IEX} < 10\,\mu\mathrm{m\,s^{-1}}$. At lower v_{IEX}, tracers become trapped in asymmetric assemblies close to the IEX. At larger v_{IEX}, lines get rather faint and occasionally a short-lived line split is observed, with the two lines merging by diffusion (Fig. D10b–d, Appx. D).

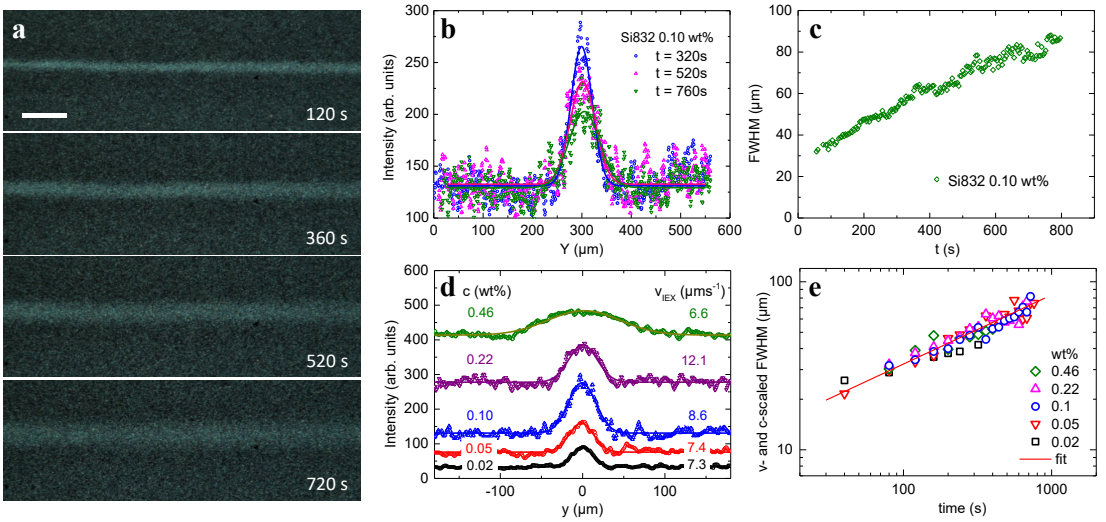

Fig. 7.3 Line evolution past the formation zone. **a** Dark field images of a line written by C-IEX45 in $0.1\,\mathrm{wt}\%$ Si832 for different times after IEX passage, as indicated. Scale bar: $100\,\mu\mathrm{m}$. **b** Line profiles (symbols) in lab coordinates for three selected times as indicated in the key. The solid lines are fits of Gaussians with an offset corresponding to the background scattering intensity. **c** Full Width at Half Maximum (FWHM) as determined from fits to line profiles taken at different times t after IEX passage. Data are taken after the passage of the line focus. The increase in linewidth slows with time. **d** Line profiles in IEX-relative coordinates obtained at different tracer concentrations and IEX speeds as indicated in the keys. These averages over 50 individual line profiles sampled over $100\,\mu\mathrm{m}$ along the lines were recorded at $t = 80\,\mathrm{s}$. All profiles are well described by fits of a Gaussian with an offset corresponding to the background scattering intensity. **e** Scaling analysis: We separately determined the c-dependence and the v-dependence of the FWHM and scaled the obtained fit results to $c = 0.1\,\mathrm{wt}\%$ and $v_{\mathrm{IEX}} = 8\,\mu\mathrm{m\,s}^{-1}$. Data arrange on a straight line in this double logarithmic plot. From the fit of a linear function, we obtain $\mathrm{FWHM} \propto t^{\lambda}$ with $\lambda = 0.48 \pm 0.04$, which is very close to the theoretically expected value of $\lambda = 0.5$.

7.2.2 Line stability

For writing complex patterns, lines should be durable. The line in Fig. 7.3a was written in Si832 at $c = 0.1\,\mathrm{wt}\%$ for increasing times after IEX passage, which defines $t = 0$. Figure 7.3b shows the line profiles fitted by Gaussians, from which we derive the linewidth in terms of the Full Width at Half Maximum (FWHM). The FWHM increases slowly and at continually slowing pace with increasing time. Notably, even after some ten minutes, the linewidth has increased from $40\,\mu\mathrm{m}$ to merely $90\,\mu\mathrm{m}$ (Fig. 7.3). The relative height of the maximum has decreased correspondingly by some $50\,\%$, and the line remains clearly visible (Fig. 7.3a). We further studied the linewidth evolution for different tracer concentrations c and IEX speeds v_{IEX}. The linewidth increases with the tracer concentration and decreases with the IEX speed. The double logarithmic plot of Fig. 7.3e shows the time-dependent FWHM scaled to $v_{\mathrm{IEX}} = 8\,\mu\mathrm{m\,s}^{-1}$ and $c = 0.1\mathrm{wt}\%$. Data arrange on a single straight line of slope 0.48. A systematic analysis suggests an overall scaling of the line width as $\mathrm{FWHM} \propto v_{\mathrm{IEX}}^{-1} c^{1/2} t^{1/2}$ (Fig. D1, Appx. D). This scaling is compatible with accretion at constant solvent flux and purely diffusive line dispersion.

7.3 Results from theory and simulations

The line formation results as the net effect of the pH-driven DO flow and typically involves Péclet numbers of Pe $\approx$ 10–30. Thus, the line formation is dominated by tracer advection caused by the DO flow. The Reynold numbers, however, are small (Re $\approx 10^{-4}$), i.e., the flow is dominated by viscous forces and thus, laminar. Furthermore, the ratio of the tracer mass and drag coefficients is small ($m_\mathrm{T}/\gamma_\mathrm{T} \approx 10^{-7}$ s), and therefore, the motion of the tracers is overdamped. Based on these conditions, we now develop a minimal model that effectively describes the motion of the tracer (ink) particles in the pH-field of the IEX.

7.3.1 Effective attraction

Overall, the DO flow induced by the IEX leads to a directed motion of the tracers towards the moving IEX, whereas the IEX does not significantly respond to the tracers. Thus, the effective interaction between the IEX and each tracer can be described as an effective non-reciprocal attraction exerted by the IEX on the tracers leading to a center of mass motion of the tracers.[658] We extracted the form of these effective interactions from experimentally measured velocities obtained from video-tracking. We fitted the tracer velocity field behind the IEX by using different functional forms (Fig. 7.4). The fit was done on the logarithmic scale using the nonlinear least-squares method. The goodness of each fit is measured by the normalized mean-squared distance of the fit values f_i to the data values d_i on the logarithmic scale (mean-squared logarithmic error, MSLE):

$$\mathrm{MSLE} = \sum_i \frac{[\ln(d_i) - \ln(f_i)]^2}{\ln(d_i)}. \tag{7.1}$$

We found that the tracer velocity field at a distance r behind the IEX can be fitted by the following form:

$$|\mathbf{v}(r)| = \frac{c_1}{r^\alpha + c_2}. \tag{7.2}$$

Unlike the other shown fits (dashed-dotted and dotted lines in Fig. 7.4) it also captures the plateau for $r \to 0$ and leads to a reasonable extrapolation capturing the expected power-law decay for $r \to \infty$. Finally, it yields a non-reciprocal attractive effective force of strength $F_\mathrm{a}(r) = \gamma_\mathrm{T}|\mathbf{v}(r)|$ reaching out some hundreds of microns (Fig. 7.4 and inset in Fig. 7.5a). Here, γ_T denotes the Stokes drag coefficient of the tracers. The parameters c_1, c_2, and α are obtained from the nonlinear least-squares fit and are given in the caption of Fig. 7.5.

7.3.2 Particle model

Based on the effective force, we formulate a minimal (particle-based) model for the tracer dynamics at prescribed motion of the IEX. Within this model, the tracers are considered as overdamped Brownian particles with radius a_T, which experience a non-reciprocal effective force $\mathbf{F}_\mathrm{eff}(t, \mathbf{r})$ due to the IEX as obtained from Eq. (7.2) (see also inset of

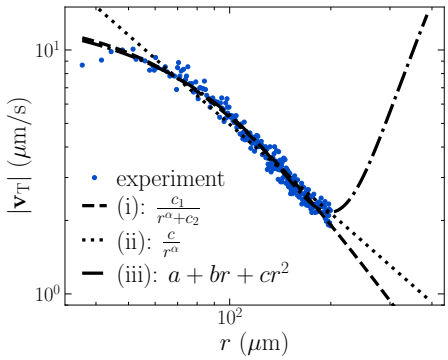

Fig. 7.4 Fit comparison. Nonlinear least-squares fits of the velocity field behind the IEX as used to extract a functional form of the effective interaction between IEX and tracers. The data is fitted on the logarithmic scale. The three shown fit functions (i)-(iii) have mean-squared logarithmic errors of MSLE $= 0.94, 1.55, 0.81$, respectively (see Eq. (7.1)). Since fit (iii) results in an unphysical behavior at large distances and the simpler two-parameter fit (ii) has a significantly larger error, we finally used fit (i) which captures both the plateau at small r and the power-law decay at large r.

Fig. 7.5a) and are subject to thermal diffusion. The position of the i-th tracer particle evolves in time according to

$$\dot{\mathbf{r}}_i(t) = \frac{1}{\gamma_\mathrm{T}}\left[\mathbf{F}_\mathrm{eff}(t,\mathbf{r}) - \sum_{\substack{j=1\\ j\neq i}}^{N} \boldsymbol{\nabla}_{\mathbf{r}_i} u(|\mathbf{r}_i - \mathbf{r}_j|)\right] + \sqrt{2D}\boldsymbol{\xi}_i(t), \tag{7.3}$$

where $D = k_\mathrm{B}T_\mathrm{b}/\gamma_\mathrm{T}$ is the diffusion coefficient with bath temperature T_b and $\boldsymbol{\xi}_i(t)$ denotes Gaussian white noise with zero mean and unit variance. The optionally considered (repulsive) pair interaction $u(r)$ between the tracer particles is modeled by a Weeks-Chandler-Anderson (WCA) potential as defined in Eq. (2.8).[256] For simplicity, we assume that the total effective force $\mathbf{F}_\mathrm{eff}(t,\mathbf{r})$ is radially symmetric. Clearly, this is a simplification of the overall DO-flow pattern (Fig. 7.2g and Fig. D4, Appx. D), but, as we shall see, sufficient to capture the essentials of line writing. Motivated by the experimental observations (Fig. 7.2), we further neglect the very slow collective tracer motion under gravity and any diffusio-phoretic motion of tracers originating from DO flows along the surfaces of the mobile tracers due to the concentration gradient.[647] Finally, the total effective force is given as a sum of a short-ranged repulsion and a long-ranged attractive force $\mathbf{F}_\mathrm{a}$ (Eq. (7.2)). The former accounts for steric repulsion between tracers and IEX. The latter accounts for the net effect of the hydrodynamic flow that is created by the IEX. Following Eq. (7.2), the attractive part can be written as

$$\mathbf{F}_\mathrm{a}(t,\mathbf{r}) = -\frac{\gamma_\mathrm{T} c_1}{(|\mathbf{R}(t)|^\alpha + c_2)}\frac{\mathbf{R}}{|\mathbf{R}|}, \tag{7.4}$$

where $\mathbf{R}(t) = \mathbf{r} - \mathbf{r}_\mathrm{IEX}(t)$ denotes the distance from the IEX located at $\mathbf{r}_\mathrm{IEX}(t)$ and moving deterministically at constant speed v_IEX. The constants c_1 and c_2 and the exponent α are determined from the fit to the velocity measurements (Figs. 7.4 and 7.5). The uncertainties in c_1 and c_2 are rather large due to the interference of upward advection

Tab. 7.1 Simulation parameters. Default parameters used for the BD simulations and the numerical solution of the continuum model if not stated explicitly.

Parameter:	Description:	Value:
a_{IEX}	IEX radius	$22.5\,\mu\mathrm{m}$
a_{T}	tracer radius	$0.412\,\mu\mathrm{m}$
γ_{T}	tracer drag coefficient	$7.854 \times 10^{-9}\,\mathrm{kg\,s^{-1}}$
v_{IEX}	IEX speed	$8.0\,\mu\mathrm{m\,s^{-1}}$
D	tracer diffusion coefficient	$0.5\,\mu\mathrm{m^2\,s^{-1}}$
φ	tracer packing fraction	0.152
T_{b}	bath temperature	$298\,\mathrm{K}$

with lateral attraction for $|\mathbf{R}(t)| < 60\,\mu\mathrm{m}$. We compensate for the neglected asymmetry of the flow field and the large uncertainties by introducing an ad hoc factor 2 using $c_1 \approx 3.6 \times 10^4\,\mu\mathrm{m^3\,s^{-1}}$. This leads to the formation of straight, narrow, and durable lines of increased tracer density (Fig. 7.5b) and results in a quantitative match of experimental observations and model predictions over an extended parameter range (Fig. 7.7).

The Langevin equations for the tracer dynamics (Eq. (7.3)) are solved numerically with a deterministically moving IEX at prescribed velocity with and without considering direct tracer-tracer interactions $u(r)$ to check the effect of the latter on the line formation. The simulations are performed in two spatial dimensions on an area $A = L_x L_y$ with periodic boundary conditions and area fraction $\varphi = N\pi a_{\mathrm{T}}^2/A$ using LAMMPS.[254,255] The repulsive part of the effective IEX-tracer interaction is modeled by a shifted Yukawa-like potential of the form

$$u_{\mathrm{Yuk}}(|\mathbf{R}|) = \begin{cases} \epsilon_{\mathrm{Yuk}} \frac{e^{-(|\mathbf{R}|-\Delta r)/\sigma_{\mathrm{Yuk}}}}{|\mathbf{R}|-\Delta r}, & |\mathbf{R}| > \Delta r \\ \infty, & \text{else} \end{cases} \tag{7.5}$$

with strength $\epsilon_{\mathrm{Yuk}} = 10 k_{\mathrm{B}} T_{\mathrm{b}} \sigma_{\mathrm{Yuk}}$, range $\sigma_{\mathrm{Yuk}} = 1\,\mu\mathrm{m}$, and shift $\Delta r = a_{\mathrm{IEX}}$.[670] The time steps are $\Delta t = 10^{-4}\,\mathrm{s}$ for non-interacting tracer particles and $\Delta t = 10^{-5}\,\mathrm{s}$ for repulsively interacting tracer particles. All other simulation parameters are summarized in Tab. 7.1.

7.3.3 Continuum model

To access larger length and time scales, we additionally formulate an equivalent continuum model, which describes the probability density $p(t, X, Y)$ of the (point-like) tracer particles in presence of the moving IEX. We formulate the corresponding Smoluchowski equation, which describes the time evolution of the probability density for finding a tracer particle at a point (t, X, Y) in space and time, where X and Y denote the coordinates in the laboratory frame.[302] For simplicity, we neglect any direct tracer-tracer interactions here and set $u(r) = 0$ in Eq. (7.3). We only account for the net effect of the flow field and for the volume exclusion between the IEX and the tracers using the total effective force

$$\mathbf{F}_{\mathrm{eff}}(t, \mathbf{r}) = \mathbf{F}_{\mathrm{a}}(t, \mathbf{r}) \tanh\left(\sqrt{(X - v_{\mathrm{IEX}} t)^2 + Y^2} - a_{\mathrm{IEX}}\right), \tag{7.6}$$

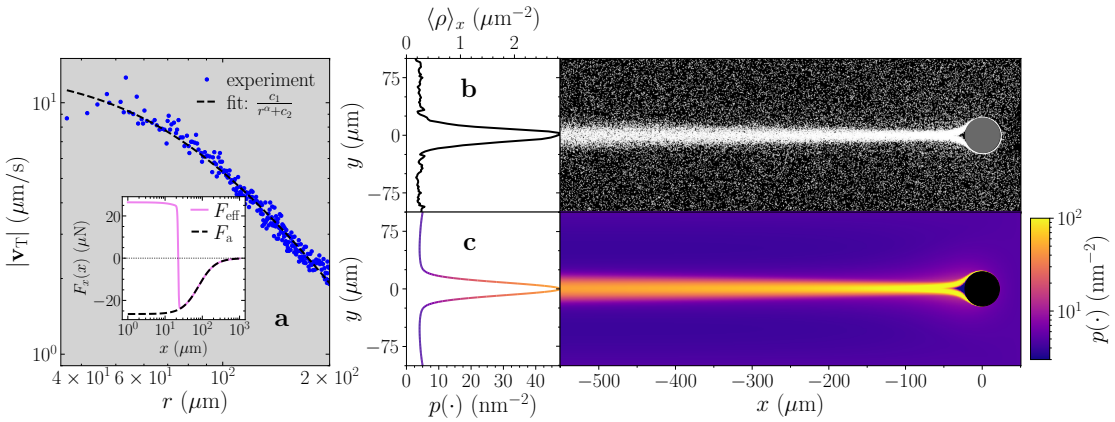

Fig. 7.5 Modeling of line writing. a Tracer approach speed averaged over an angular region of 30° behind the IEX rolling at $v_{\mathrm{IEX}} = 1.6\,\mu\mathrm{m\,s^{-1}}$ (blue) in dependence on the radial distance r to the IEX center. The black dashed line is a nonlinear least-squares fit of Eq. (7.2) returning $c_1 = (7.2 \pm 2.3) \times 10^4\,\mu\mathrm{m^3\,s^{-1}}$, $c_2 = (5.3 \pm 1.9) \times 10^3\,\mu\mathrm{m^2}$, and $\alpha = 1.96 \pm 0.06$. Inset: x-component of effective forces as used in the continuum model. The attractive part F_{a} corresponds to the fit in the main panel (black dashed curve), the full effective force F_{eff} (solid pink curve) additionally accounts for volume exclusion interactions between the IEX and the tracers (see Eq. (7.6)). **b**,**c** Exemplary results from theoretical modeling based on the effective force shown in panel a in IEX-relative coordinates. Parameters were chosen to correspond closely to those of the experiments: $2a_{\mathrm{IEX}} = 45\,\mu\mathrm{m}$, $D = 0.5\,\mu\mathrm{m^2\,s^{-1}}$, $\gamma_{\mathrm{T}} = 7.85 \times 10^{-9}\,\mathrm{kg\,s^{-1}}$, $v_{\mathrm{IEX}} = 8.0\,\mu\mathrm{m\,s^{-1}}$ (b) and $v_{\mathrm{IEX}} = 8.6\,\mu\mathrm{m\,s^{-1}}$ (c) (see also Tab. 7.1). **b** Snapshot taken at $t = 100\,\mathrm{s}$ from a BD simulation starting from $N = 112\,200$ uniformly distributed point-like tracers. The line profile (left) is averaged over the interval $x \in [-550\,\mu\mathrm{m}, -500\,\mu\mathrm{m}]$. **c** Numerical solution of Eq. (7.8) with initially uniform probability density $p_0 = 5 \times 10^{-6}\,\mu\mathrm{m^2}$ after $t = 2000\,\mathrm{s}$. The probability density $p(\cdot) = p(2000\,\mathrm{s}, x, y)$ (right) and the line profile at $x = -550\,\mu\mathrm{m}$ (left) are color-coded as indicated in the key.

with $\mathbf{r} = (X, Y)$ and IEX-radius a_{IEX} (see inset of Fig. 7.5a). We assume that the IEX moves along the x-axis at a constant speed $v_{\mathrm{IEX}} > 0$. We transformed the corresponding Smoluchowski equation for the probability density $p(t, X, Y)$ (we omit the arguments for clarity)

$$\frac{\partial p}{\partial t} = -\frac{1}{\gamma_{\mathrm{T}}} \boldsymbol{\nabla} \cdot (\mathbf{F}_{\mathrm{eff}} p) + D \nabla^2 p \tag{7.7}$$

into the coordinate frame of the IEX by applying the Galilei transformation $x := X - v_{\mathrm{IEX}} t$, $y := Y$. The transformed equation reads

$$\frac{\partial \tilde{p}}{\partial t} = -\frac{1}{\gamma_{\mathrm{T}}} \boldsymbol{\nabla} \cdot (\mathbf{F}_{\mathrm{eff}} \tilde{p}) + v_{\mathrm{IEX}} \frac{\partial \tilde{p}}{\partial x} + D \left(\frac{\partial^2 \tilde{p}}{\partial x^2} + \frac{\partial^2 \tilde{p}}{\partial y^2} \right), \tag{7.8}$$

where now $\tilde{p} = p(t, x, y)$. We omit the tilde throughout this work. Again, $D = k_{\mathrm{B}} T_{\mathrm{b}} / \gamma_{\mathrm{T}}$ denotes the tracer diffusion coefficient.

We solve Eq. (7.8) numerically in two spatial dimensions on a rectangular area of size $(Lx, Ly) = (1000\,\mu\mathrm{m}, 200\,\mu\mathrm{m})$ with $x \in [-950\,\mu\mathrm{m}, 50\,\mu\mathrm{m}]$ and $y \in [-100\,\mu\mathrm{m}, 100\,\mu\mathrm{m}]$. The initial condition is given by a uniform distribution $p(0, x, y) = 1/(LxLy)$. We use Dirichlet boundary conditions at the right, top, and bottom boundary with $p(t, 50\,\mu\mathrm{m}, y) =$

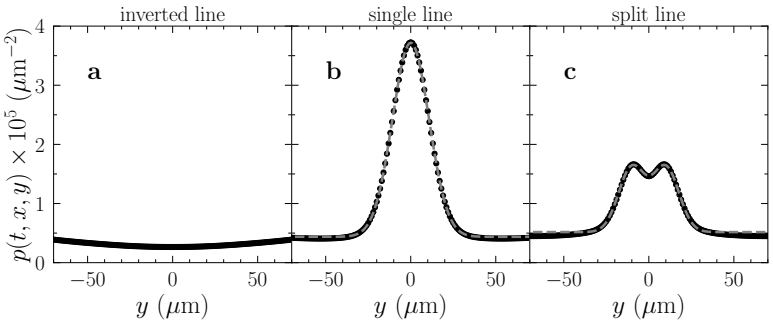

Fig. 7.6 Analysis of line shapes. Exemplary line profiles obtained in the continuum model (Eq. (7.8)) at $t = 2000\,\mathrm{s}$ and $x = -950\,\mu\mathrm{m}$ with $D = 0.5\,\mu\mathrm{m}^2\,\mathrm{s}^{-1}$. The dashed lines denote the corresponding fits of single or double Gaussians. **a** $v_{\mathrm{IEX}} = 3.63\,\mu\mathrm{m\,s}^{-1}$ (inverted line), **b** $v_{\mathrm{IEX}} = 8.6\,\mu\mathrm{m\,s}^{-1}$ (single line), and **c** $v_{\mathrm{IEX}} = 16.4\,\mu\mathrm{m\,s}^{-1}$ (split line). Note the pronounced differences in line amplitudes. All other parameters are given in Tab. 7.1.

$p(t, x, \pm 100\,\mu\mathrm{m}) = 1/(LxLy)$ and no-flux boundary conditions at the left boundary, i.e., $\partial_x p(t, x, y)|_{x=-950\,\mu\mathrm{m}} = 0$. Finally, the Smoluchowski equation is solved with the NDSolve method from Mathematica[671] by using the method of lines,[672,673] finite element discretization,[674] and the parameters displayed in Tab. 7.1. As shown in Fig. 7.5c, our continuum model also leads to the formation of a straight and narrow line of increased probability density. Note from the profile in Fig. 7.5c that the lines are embedded within a region of marginally reduced tracer density reflecting the extension of the accretion zone. As in the experiments, this depleted accretion region serves to enhance the contrast of the main line. Our observations demonstrate that the main ingredients of line formation are simple and generic: Writing into water requires a quick, medium-range ink-transport towards the moving pen caused by an effective hydrodynamic attraction of ink particles towards the IEX and a slow, diffusive line decay. Thus, we term this novel type of writing a line of increased density in water hydrodynamic writing (HDW).

7.3.4 State diagram

Using the continuum model (Eq. (7.8)), we systematically varied the IEX speed v_{IEX} (equivalent to changing the tilt angle ϑ in the experiment) and the tracer diffusion constant D (equivalent to changing the tracer particle size or the bath temperature). To discriminate between different line types, we fitted a Gaussian or a sum of two Gaussians to the line profiles of the probability density taken in the stationary state after $t = 2000\,\mathrm{s}$ at distance $x = -950\,\mu\mathrm{m}$ behind the IEX (Fig. 7.6). We observed three different line types: single line, split line, and inverted line (Fig. 7.7a). Consequently, the state diagram in the v_{IEX}-D-plane shows three distinct regions (Fig. 7.7b).

Pronounced single lines are obtained at intermediate velocities (color-coded region with state points I and II in Fig. 7.7b). We define a line sharpness $p_{\max}/\sqrt{\mathrm{Var}(y)}$, where $p_{\max}$ denotes the maximum of the fitted Gaussian line profile and $\sqrt{\mathrm{Var}(y)}$ denotes its standard deviation. Line sharpness, and thus, contrast, is largest at small D. With increasing diffusivity, sharpness decreases and lines get continuously broader and fainter. Towards larger velocities, the line formation length expands and results in a split line (III). The

simulated profile at $x = -950\,\mu\text{m}$ now shows two maxima, which eventually merge at larger distances x by diffusive broadening. The regime of split line formation is thus located in the lower right corner of the state diagram (low D, large v_{IEX}).

Interestingly, the model further reveals a third line type at low velocities. Due to the low IEX velocity, a substantial amount of attracted tracers is trapped and no line of positive density contrast is written. Instead, in the steady state, a stationary cloud of tracers forms in the vicinity of the IEX due to a balance between trapping and diffusion, which is also observed in the experiments (example IV in Fig. 7.7c). Accretion of tracers from the IEX surroundings leads to a broad shallow minimum in the line profile, i.e., the line contrast is inverted (Fig. 7.6a and example IV in Fig. 7.7a). The width of the minimum mirrors the y-extension of the range of attraction. Note that such a shallow depletion zone is also present at larger IEX velocities in the single-line regime (HDW), but as in the experiments, it is masked by a much more pronounced HDW line and increases the line contrast (Fig. 7.6b and Fig. D10c, Appx. D).

Overall, also lines written in the model vary considerably in quality but not all appear to be useful for actual writing. In practice, all inverted lines written at low v_{IEX} remain too faint. Additionally, for increasing velocities, the flux of incoming tracers is reduced and becomes too small for providing a large density contrast for the inverted line profile. Within all regimes, high diffusivities lead to a significant decrease of the line sharpness resulting again in lines unsuitable for actual writing. However, our model clearly predicts that single narrow lines of large density contrast are obtained for low diffusivity and intermediate IEX speed, exactly as observed in the experiments (cf. orange/yellow region in Fig. 7.7b as compared to Fig. 7.2b,c and Fig. D10b–d, Appx. D).

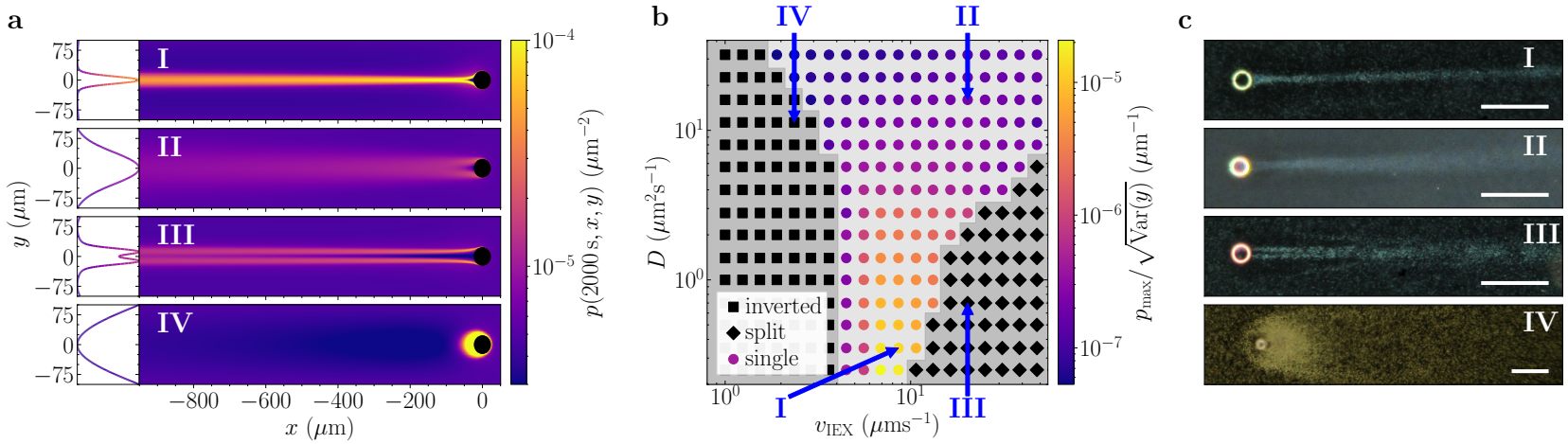

Fig. 7.7 State diagram. a Snapshots (right) and line profiles at $x = -950\,\mu\mathrm{m}$ (left) obtained from the numerical solution of Eq. (7.8) in the stationary state at $t = 2\,000\,\mathrm{s}$. The representative examples are denoted by Roman numerals: narrow single line (I), broad single line (II), split line (III), and inverted line (IV). Colors encode the probability density $p(2\,000\,\mathrm{s}, x, y)$ as given in the key. **b** State diagram in the v_{IEX}-D-plane (other parameters as before, see also Tab. 7.1). Symbols denote the three principal line types as discriminated by the line profiles at $x = -950\,\mu\mathrm{m}$: inverted line (squares), split line (diamonds), and single line (color-filled circles). The state points corresponding to the examples shown in panel a are marked by blue arrows and Roman numerals. For single lines, colors encode the line sharpness $p_{\max}/\sqrt{\mathrm{Var}(y)}$, where $p_{\max}$ denotes the maximum of the fitted Gaussian line profile and $\sqrt{\mathrm{Var}(y)}$ denotes its standard deviation. **c** Representative experimental examples observed in the three regions of the state diagram: narrow single line written with $0.10\,\mathrm{wt}\%$ Si832 at $v_{\mathrm{IEX}} = 9.2\,\mu\mathrm{m\,s^{-1}}$ (I), broad single line written with $0.24\,\mathrm{wt}\%$ Si444 at $v_{\mathrm{IEX}} = 8.2\,\mu\mathrm{m\,s^{-1}}$ (II), split line written with $0.10\,\mathrm{wt}\%$ Si832 at $v_{\mathrm{IEX}} = 12.0\,\mu\mathrm{m\,s^{-1}}$ (III), and a line in the region of inverted lines shown in panel b, here written with $0.10\,\mathrm{wt}\%$ Si2.1 at very low $v_{\mathrm{IEX}} \approx 0.2\,\mu\mathrm{m\,s^{-1}}$ (IV). Scale bars: $250\,\mu\mathrm{m}$.

7.4 Discussion

Having explored the experimental and theoretical aspects of line writing by assembling colloidal particles on the trajectory of an IEX, we now discuss specific challenges, graphical applications, and some further details of the theoretical model. Again, all experimental results have been obtained by Nadir Möller and co-workers.

7.4.1 Graphical applications

Let us first discuss the question whether the presented approach can be used for actual writing. In the experiments, we again use weakly charged tracers and moderate writing velocities, which is essential for proceeding beyond straight lines by combining line writing with steering. We controlled the line orientation by using a manually programmable, motorized stage, allowing for sequences of changes in tilt direction β and angle ϑ. In the BD simulations, we simply prescribed IEX speeds and trajectories. Figure 7.8 shows representative examples, in which we successfully produced some simple patterns and symbols (Fig. 7.8a–f), drew complex patterns with multiple line crossings (Fig. 7.8g) or wrote text (Fig. 7.8h,i). Let us now discuss some practical issues encountered during their production. Downscaling is addressed for the example of a pattern with rectangular turns in Fig. 7.8a–c. The right angles and straight intervals start washing out when the length of straights approaches three to two times the line thickness. Another issue is line-shifting. In the simulation run of Fig. 7.8d, we compare the written line to the prescribed sinusoidal IEX trajectory. Due to the relatively long-ranged tracer attraction (Fig. 7.5a) and the continuing DO flows towards the back of the IEX (Fig. 7.2g), the written line is dragged along in the overall propulsion direction. This results in a shift of the final line as compared to the prescribed IEX trajectory. The intended sinusoidal shape, however, is fully retained. This is different for the case of line crossing. For instance, in the simulation run of Fig. 7.8e, the initial upward stroke of the lower-case Greek letter φ is bent to the left (see also Fig. 7.9). In addition, the freshly written line shows a local enhancement of line thickness (blob) also shifting in the propagation direction of the IEX. By contrast to blobbing by transient sticking of the IEX to the substrate (Fig. D12, Appx. D), blobbing upon line crossing is systematic. However, while it is kept at bay by high writing velocities ($v_{\mathrm{IEX}} \geq 10\,\mu\mathrm{m\,s^{-1}}$s), line bending is not. The inset of Fig. 7.8e shows a line crossing experiment at large v_{IEX}. Here, the duration of tracer attraction from the crossed high-density region is reduced, but the DO flows are retained, and the line is still bent. In principle, line crossing can be avoided using multiple pens on merely touching trajectories (Fig. 7.8f). Where it could not be avoided, we performed a stepwise adjustment of the stage tilting sequence to compensate for the observed and anticipated deviations from the desired line path (Fig. D11, Appx. D). With some experience, even complex patterns with multiple line crossings under desired angles, negligible line-bending, and little blobbing can be reproducibly drawn (Fig. 7.8g). Note that the base of the “house” shown in Fig. 7.8g is merely $500\,\mu\mathrm{m}$ and the height is about $850\,\mu\mathrm{m}$, i.e., the house´s size is on the order of a single letter in this text. The figure was drawn within about five minutes at an IEX speed of approximately $15\,\mu\mathrm{m\,s^{-1}}$. It retained its characteristic shape for more than 15 minutes. Writing of individual letters is less difficult. Picking up a

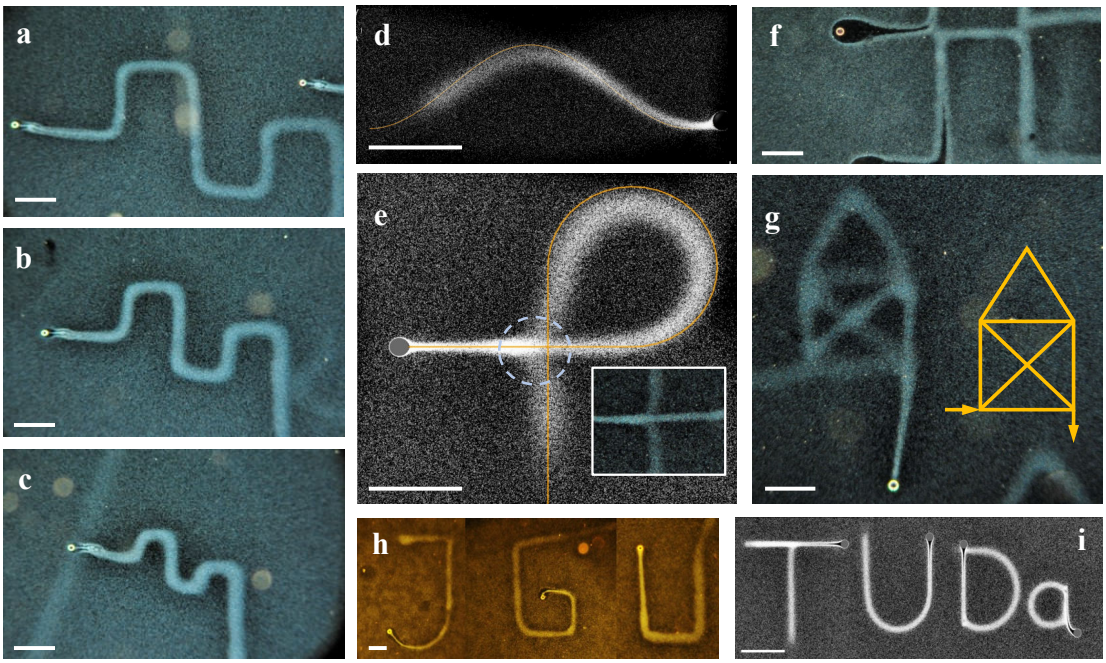

Fig. 7.8 Examples of writing and drawing. Experiments have been done with C-IEX45 in Si832 and BD simulations with parameters as given in Tab. 7.1. All scale bars: $250\,\mu\mathrm{m}$. **a–c** Successive downscaling of pattern size. The length of the horizontals is $500\,\mu\mathrm{m}$ (a), $350\,\mu\mathrm{m}$ (b), and $175\,\mu\mathrm{m}$ (c). **d** Sinusoidal line written in the BD simulation with parameters close to typical experimental ones (Tab. 7.1). Note the slight, leftward shift of the written line with respect to the IEX trajectory (solid yellow line). **e** Lower case Greek letter φ with loop and line crossing. Note the bending of the crossed line and the formation of a region of enhanced density along the freshly written line (dashed circle). Inset: Writing at high IEX speed of $v_{\mathrm{IEX}} = 10\,\mu\mathrm{m\,s^{-1}}$ reduces blobbing but retains line bending. **f** Avoiding blob formation upon line crossing by mere line touching. **g** One-line drawing of a complex pattern with rectangular and $45°$ angles as well as multiple line crossings. The inset shows the intended result ("Das Haus vom Nikolaus"). **h** Initials of the Johannes Gutenberg University, Mainz, written with C-IEX45 in $0.2\,\mathrm{wt\%}$ Si832. **i** Initials of the Technical University of Darmstadt written in a BD simulation with $v_{\mathrm{IEX}} = 12\,\mu\mathrm{m\,s^{-1}}$.

certain tradition,[634,635,637,639,640,645] we display the affiliation initials of the experimental and theoretical group in Fig. 7.8h and i, respectively.

7.4.2 Fine tuning

So far, we concentrated on writing of and with durable, narrow lines of enhanced tracer density (positive contrast). This was facilitated by rolling C-IEX45 at speeds of $v_{\mathrm{IEX}} = 6\text{–}10\,\mu\mathrm{m\,s^{-1}}$ through weakly charged Si832 ($\zeta_{\mathrm{T}} = -68\,\mathrm{mV}$) at $0.1\text{–}0.15\,\mathrm{wt\%}$ on native substrates ($\zeta_{\mathrm{S}} = -105\,\mathrm{mV}$). One may, however, wish to fine-tune the graphical appearance of the written lines. To this end, we exploit the modularity of our approach allowing tests of alternative inks, pens, and pen-drives. These additional and complementary experiments are described in detail in Appx. D. In short, tracers of larger or smaller size can be used to alter the line graininess and contrast (Fig. D5). Replacing weakly charged tracers by highly charged tracers introduces additional diffusio-phoretic tracer motion.

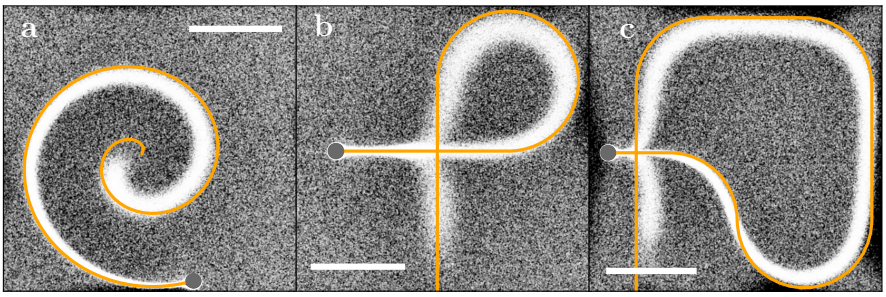

Fig. 7.9 Exemplary patterns drawn in the BD simulation. Scale bar: $250\,\mu\mathrm{m}$. **a** Spiral. **b** Clockwise loop with line crossing. **c** The same as in panel b but crossing starting after an additional left turn. Note the blob just past the crossing and the slight deformation of the already drawn line. Simulation parameters are given in Tab. 7.1.

This alters the shape of the formation zone but leaves the decay zone unaffected (Fig. D6). The driving pH gradient can be manipulated by using different pen types. Removing the pH gradient using chemically inert pens produces poor lines, while doubling the pH gradient using a pair of IEX yields thicker lines with weakly charged tracers and split lines with highly charged tracers (Figs. D7 and D3). Replacing the anionic by a cationic IEX switches the sign of the pH gradient. Tracers are then repelled and the IEX carves a tracer free line into the background (negative contrast, Fig. D8). Finally, we also tested different pen-driving mechanisms such as modular microswimmers self-assembling on horizontal substrates. These microswimmers propel autonomously and steer by more or less random rearrangements of the assembled tracers. Lacking a directed steering, microswimmers write curved lines of otherwise good quality (Fig. D9).

7.4.3 Accuracy of writing patterns

In the simulations, we prescribe IEX trajectories within the simulation box. Written lines follow these quite accurately, as illustrated in Fig. 7.9. Two small, unavoidable deviations are, however, obvious: First, tracers assembled in the line past the IEX are drawn towards the IEX at its actual position. This originates from the long-ranged nature of the attraction. It leads to an inward offset in the written spiral as compared to the prescribed trajectory (Fig. 7.9a), a right shift in the line crossing event shown in Fig. 7.9b, and a “short-cutting” of turns with small radius of curvature (Fig. 7.9c). In principle, all these effects can be compensated for by appropriate anticipation and fine-tuning of the prescribed trajectory. The second effect is a local increase in line strength and density upon line crossing events (Fig. 7.9b and c). This local effect occurs because the IEX acts on the already enhanced density in the immediate environment. Depending on the IEX speed, the corresponding short over-dense region (blob) is shifted in the direction of the effective attraction. The blob occurs past the crossing point. This effect cannot be cured but gets less pronounced for larger velocities.

The line shifts due to attraction are even more pronounced in experiments and increase with increasing substrate charge leading to more pronounced DO flows towards the IEX (cf. the solvent flow trajectories shown in Fig. D4). Blob formation is also present but can be minimized for writing with high IEX velocities $v_{\mathrm{IEX}} \geq 10\,\mu\mathrm{m\,s}^{-1}$. Yet another

effect becomes prominent in experiments attempting to draw complex figures. This is highlighted by yellow encircling in Fig. D11. If the pen moves on an already drawn line, its velocity is altered. If it moves against the former propagation direction, it is slowed. This shortens the written line as compared to the programmed trajectory. Moving in the opposite direction, its velocity is increased, and the written line becomes more extended than programmed. Lines are also lengthened if they approach an already written line from an angle. Likewise, lines written such as to pass in the immediate vicinity of an already finished line partly get shifted towards the latter. Together, this tends to wreck figures with many line crossings. However, such effects can be accommodated by variation of the programmed stage tilting sequence. Going from Fig. D11a–d, we successively adapted the programmed trajectory to make the drawn figure approach the desired one (inset in Fig. D11d). While somewhat tedious, this step-by-step procedure is nevertheless successful. In the future, it will be improved by replacing the manual programming by some learning package based on image processing feedback.

Apart from blob formation upon line-crossing, occasionally, we observe an additional type of blob formation. It is caused by a transient sticking of the IEX to the substrate. This process of blob formation is followed in a series of images in Fig. D12. The blob is mainly formed by the trail catching up with the now-stuck IEX and further tracer accretion at the fixed IEX. Note that during sticking, the tracers slowly overtake the IEX. After detachment, the IEX velocity initially is slower than the final velocity. This is attributed to IEX friction with the locally enhanced tracer density but may further be related to altered DO flows. By contrast to blobbing upon line crossing, this type is not systematic. It therefore may be an issue already in straight line writing. Blobbing by transient sticking is most prominent for low-charge substrates and elevated tracer concentrations. It is also more frequent at lower velocities. Blob formation events are uncorrelated, and the resulting line appears to be blotted (Fig. D12d). A regular blobbing pattern might be introduced for decorative purposes by transiently trapping the IEX by an optical tweezer for example.

7.4.4 Reaching the stationary state

Let us now discuss how long it takes to reach a steady-state line in our continuum model. In the numerical calculations, the IEX is fixed at $x = 0$ in a homogeneous background of tracer particles at $t = 0$ moving at constant speed v_{IEX} (cf. Galilei transform in Subsec. 7.3.3). In Fig. 7.10, we show the temporal evolution of the line amplitude in terms of the central probability density $p(t, x, 0)$ on the path of the IEX at certain distances behind the IEX. In Fig. 7.10a–c, we fixed the diffusion coefficient $D = 0.5\,\mu\mathrm{m}^2\,\mathrm{s}^{-1}$ and varied the IEX speed v_{IEX}. We obtain two types of curves reaching a stationary state within the investigated time span of $2\,000\,\mathrm{s}$. At large v_{IEX}, a stationary state for p is reached within 100–$400\,\mathrm{s}$ with a trivial dependence on x. The line amplitude plateaus well above the homogeneous background. This corresponds to the single-line formation regime of Fig. 7.7. At small v_{IEX}, a stationary state for p is reached later after some 500–$700\,\mathrm{s}$. Notably, the line amplitude reaches a plateau below the homogeneous background. This corresponds to the inverted line formation regime of Fig. 7.7. Interestingly, in both types of stationary state, the plateau amplitude decreases with increasing v_{IEX}. We attribute this to the smaller number of attracted and/or trapped tracer particles (Fig. D1, Appx. D). For speeds v_{IEX} in the transition region between inverted and single lines, the time to reach a stationary state

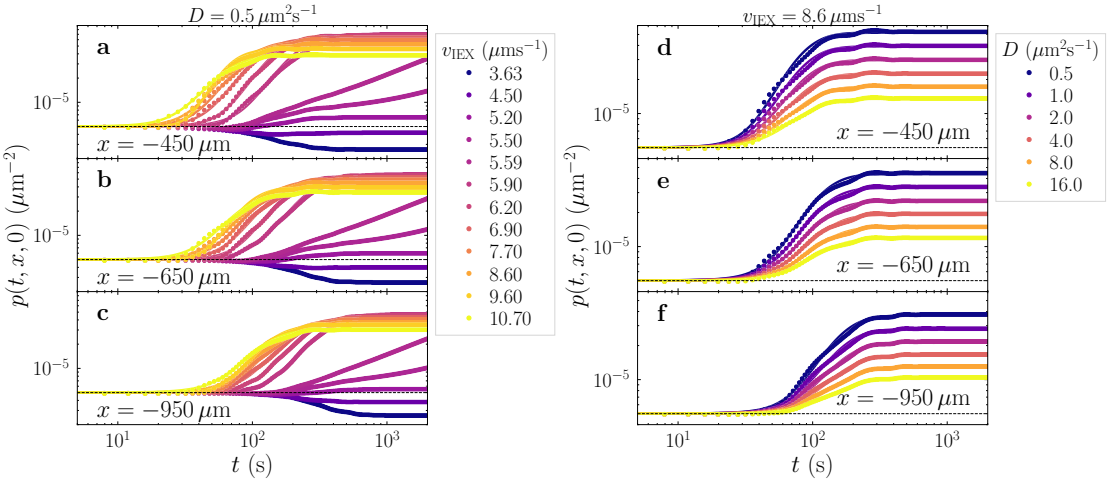

Fig. 7.10 Time evolution of the line amplitude. Central probability density $p(t < 2\,000\,\mathrm{s}, x, 0)$ at different distances x from the IEX (values are given in the panels) as obtained from the numerical solution of Eq. (7.8). The solid lines are fits of Eq. (7.9) to the data. **a–c** Data obtained for fixed diffusion constant $D = 0.5\,\mu\mathrm{m}^2\,\mathrm{s}^{-1}$ and different IEX speeds v_{IEX} (color-coded according to the key). **d–f** Data obtained for fixed IEX speed $v_{\mathrm{IEX}} = 8.6\,\mu\mathrm{m}\,\mathrm{s}^{-1}$ and different diffusion coefficients D (color-coded according to the key). Other parameters as given in Tab. 7.1.

significantly increases because the IEX traps a large amount of tracer particles, which can later escape the trapping region if the number of trapped tracers is large enough. In Fig. 7.10d–f, we fixed the IEX speed to $v_{\mathrm{IEX}} = 8.6\,\mu\mathrm{m}\,\mathrm{s}^{-1}$ and varied the diffusion coefficient. The chosen x are located past the line focus. The plateau amplitude decreases for increasing D.

To further study the line amplitude relaxation, we fitted the Gompertz equation

$$p(t) = p_0 \exp\left\{-\exp\left[-\frac{t-\Delta t}{\tau}\right]\right\} + p_{\mathrm{offset}} \tag{7.9}$$

with stationary central amplitude p_0, time delay Δt, amplitude relaxation time τ, and background amplitude p_{offset}.[675] The fit results are shown in Fig. 7.11. The amplitude relaxation time linearly decreases with the distance x to the IEX (Fig. 7.11a). For a typical distance of $500\,\mu\mathrm{m}$ past the IEX, corresponding approximately to the dimension of a single letter, the stationary state is reached with an amplitude relaxation time of $\tau \approx 30\,\mathrm{s}$. Furthermore, the stationary central amplitude shows a power-law dependence on the distance x (Fig. 7.11b) caused by diffusion processes. The time delay Δt of the amplitude relaxation increases linearly with x with a slope equal to the IEX speed (Fig. 7.11c). The time to reach the stationary state hardly changes with varying D and only shows a weak logarithmic dependence (Fig. 7.11d). However, it decreases with increasing IEX speed (Fig. 7.11f). The stationary central amplitude decreases with both the diffusion coefficient and the IEX speed (Fig. 7.11e and g).

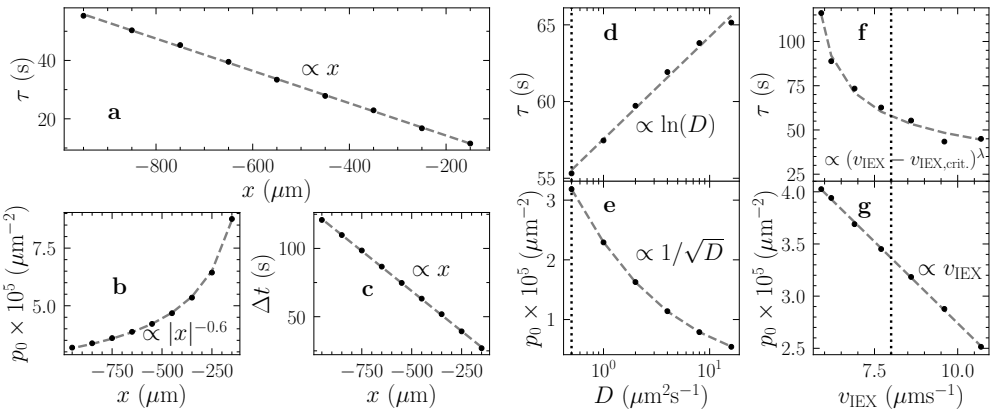

Fig. 7.11 Fit parameters. Analysis of the time evolution of the line amplitude as obtained from the fits shown in Fig. 7.10. Black dots correspond to the respective fit parameters, grey dashed lines to fits as given in the key. **a** Amplitude relaxation time τ, **b** stationary central amplitude p_0, and **c** time delay Δt over distance x to the IEX for $D = 0.5\,\mu\mathrm{m}^2\,\mathrm{s}^{-1}$ and $v_{\mathrm{IEX}} = 8.6\,\mu\mathrm{m\,s}^{-1}$. **d** Amplitude relaxation time τ and **e** stationary central amplitude p_0 as function of the diffusion coefficient for fixed $v_{\mathrm{IEX}} = 8.6\,\mu\mathrm{m\,s}^{-1}$ at $x = -950\,\mu\mathrm{m}$. **f** Amplitude relaxation time τ and **g** stationary central amplitude p_0 as function of v_{IEX} for fixed $D = 0.5\,\mu\mathrm{m}^2\,\mathrm{s}^{-1}$ at $x = -950\,\mu\mathrm{m}$. The critical IEX velocity $v_{\mathrm{IEX,crit.}}$ denotes the transition point from inverted to single lines. Vertical dotted lines denote typical values as used in the experiments.

7.4.5 Line formation zone and trail formation at early times

Let us now take a closer look at the line-formation zone close to the IEX. At very small distances to the IEX, a split line is observed in the model that merges to a single Gaussian-shaped line at intermediate distances (Fig. 7.12a-c). Past the merging distance, the line first narrows further but eventually broadens as the tracer attraction vanishes and diffusion begins to dominate the tracer motion. The location of this line focus, which separates the line formation zone from the decay zone, defines the line formation length l_{f}. The latter can be accurately determined via the x-dependent standard deviation $\sqrt{\mathrm{Var}(y)}$ of Gaussians fitted to the line profiles observed at different IEX speeds (Fig. 7.12). The distance at which the line shows a minimum standard deviation is identified as the line formation length (dashed lines in Fig. 7.12d). The line formation length increases with increasing v_{IEX}. For $v_{\mathrm{IEX}} = 8.6\,\mu\mathrm{m\,s}^{-1}$, we find $l_{\mathrm{f}} = 90\,\mu\mathrm{m}$ in good agreement with the experimental observations.

Since our minimal model is solely based on the long-range tracer transport towards the IEX and restricted to two dimensions, it is of course not capable to reproduce the detailed tracer motion close to the IEX within the formation zone. In Fig. 7.13, we show the trail formation in the BD simulation with point-like tracer particles at early times. Due to the constriction of the tracer motion to two spatial dimensions, a small layer of tracer particles accumulates at the front and sides of the IEX. Interestingly however, the trail formation behind the IEX is qualitatively similar to the experimental observations. Accumulation at the front is not seen in the experiments because tracer particles can either be swept further underneath the IEX sphere or escape this region by moving along the third spatial dimension due to strong upward solvent flows in the vicinity of the IEX.

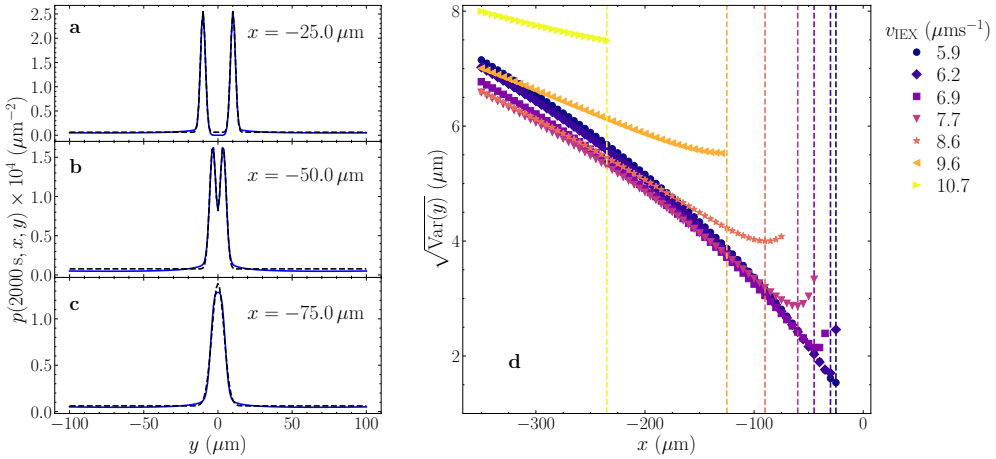

Fig. 7.12 Determination of the line formation length. a–c Line profiles for $v_{\text{IEX}} = 8.6\,\mu\text{m s}^{-1}$ and $D = 0.5\,\mu\text{m}^2\,\text{s}^{-1}$ and **d** line width for $D = 0.5\,\mu\text{m}^2\,\text{s}^{-1}$ and different v_{IEX} obtained from the numerical solution of Eq. (7.8) as a function of the distance past the IEX. The dashed black lines in panels a–c are fits to one Gaussian and a sum of two Gaussians, respectively. In panel d, we show the standard deviation $\sqrt{\text{Var}(y)}$ of the Gaussians fitted to the line profiles for different speeds v_{IEX} of the IEX (values are given in the key). A minimum coincides with the location of the line focus, whose position we denote as the line formation length l_{f} (dashed vertical lines). For x closer to 0, the line is not a single Gaussian anymore but rather a split line. Therefore, the curves stop at certain x.

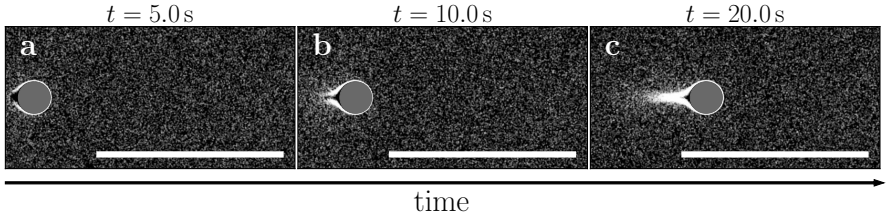

Fig. 7.13 Short-time trail formation. Onset of writing for non-interacting tracer particles of radius $a_{\text{T}} = 0.416\,\mu\text{m}$ and diffusion coefficient $D = 0.5\,\mu\text{m}^2\,\text{s}^{-1}$ at three different (early) times (**a–c**) ordered from left to right (values are given in the panels). The IEX moves at a speed $v_{\text{IEX}} = 8.0\,\mu\text{m s}^{-1}$ and the area fraction of tracer particles is $\varphi = 0.152$. Other parameters as given in Tab. 7.1. Scale bar: $250\,\mu\text{m}$.

7.4.6 Density dependence of the line shape

Thus far, we neglected interactions (volume exclusion) between the tracer particles. Considering repulsive tracer-tracer interaction $u(r)$ modeled by the Weeks-Chandler-Anderson (WCA) potential as defined in Eq. (2.8) with strength $\epsilon = 10\,k_{\text{B}}T_{\text{b}}$ and effective particle diameter $\sigma = 2a_{\text{T}}$ grants interesting insights into the limits and capabilities of our minimal model.

We studied the line shape for interacting tracer particles at different tracer area fractions $\varphi \in \{0.030, 0.076, 0.152, 0.304\}$ which correspond to tracer concentrations of $0.02\,\text{wt}\%$, $0.05\,\text{wt}\%$, $0.10\,\text{wt}\%$, and $0.20\,\text{wt}\%$ in the experiments, respectively. Figure 7.14 shows simulation snapshots after $t = 110\,\text{s}$ for the different tracer concentrations as well as

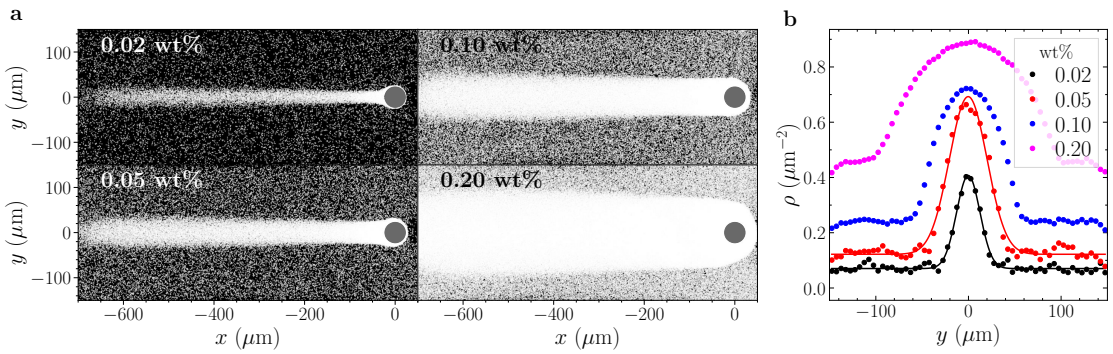

Fig. 7.14 Density dependence of line profiles in BD simulations with repulsively interacting tracer particles. The tracer particles have a radius $a_T = 0.416\,\mu m$ and diffusion coefficient $D = 0.5\,\mu m^2\,s^{-1}$. The IEX moves at a speed $v_{IEX} = 8.0\,\mu m\,s^{-1}$. **a** Simulation snapshots after $t = 110\,s$ taken at different tracer concentrations (i.e., different area fractions) as indicated by the key. **b** Corresponding line profiles obtained from averages over regions of $50\,\mu m$ extension at a distance of $x = -500\,\mu m$ past the IEX. Solid lines are Gaussian fits, describing the data well at low tracer concentrations (i.e., area fractions). Other parameters are given in Tab. 7.1.

the density profiles at $x = 500\,\mu m$. For higher concentrations, the line width increases. Remarkably, and in contrast to the experimental results (Fig. 7.3d), the line shows a Gaussian shape only at small tracer concentrations. At high concentrations, the shape features a broader, non-Gaussian peak caused by the restriction of the tracer motion to the 2D plane. This contrasts with the model calculations using point-like tracers, which can accumulate to arbitrarily large densities, and to the experiments, where particles may escape to higher elevations. We anticipate that flattening should become observable in experiments using tracers of large density mismatch, which stay settled and cannot escape to the third dimension.

The effects of tracer-tracer interactions have interesting implications on the difference between the experimental and our theoretical results: First, the use of point-like tracers in the numerical calculations strengthens the trapping effect because more tracers can be trapped in the vicinity of the IEX as compared to the experiments, in which the tracers have a finite size. Trapping is readily visualized in the present experiments particularly at low IEX velocities (example IV in Fig. 7.7c). However, there, the trapped particles are either sheared off the assembly at its sides, creating a short, diffusively dispersing double line feature, or they are expelled at the back of the assembly, thus filling any underlying depletion zone. As a result, no well-defined density variation (line) emerges, neither under- nor over-density. At larger velocities of $v_{IEX} \approx 8$–$10\,\mu m\,s^{-1}$, and in particular, for native substrates of large ζ-potential, the DO flow may be sufficiently strong to create a noticeable underdensity (Fig. D3a). However, only a small number of attracted tracers becomes trapped at large velocities. Rather, they are immediately expelled to the back. Thus, we observe a shallow depletion zone to both sides of a strong HDW-line, which extends way beyond the HDW-line focus. The shallow underdensity serves to enhance the optical contrast.

7.5 Conclusion

The present approach of writing by assembly features several advantages over other approaches. As ink is available all along the trajectory, writing by assembly eliminates the necessity of a large (potentially eddy-creating) reservoir required in deposition-approaches as well as any re-filling issues. Working with small pens in a viscous fluid at low Reynolds numbers for the pen motion ($\mathrm{Re}_{\mathrm{pen}} \approx 10^{-4}$–$10^{-3}$) avoids eddy-creation, leaves the fluid practically undisturbed, and allows writing of narrow lines of a few tens of μm thickness, which compares well with the line widths reached in microprinting. With this approach, ink was collected from a region of a few pen diameters in width at Péclet numbers on the order of $\mathrm{Pe}_{\mathrm{ink}} \approx 5$–$50$. This was large enough for a quick build-up of significant density modulations. Chosen pen-speeds of $v_{\mathrm{pen}} > 1.5\,\mu\mathrm{m\,s}^{-1}$ were large enough to avoid binding of the assembled micro-sized tracers to the pen, and thus, lead to line formation by tracer expulsion. At the same time, $\mathrm{Pe}_{\mathrm{ink}}$ was small enough to avoid excessive direct transfer of kinetic energy to the ink particles. (This so-called dynamical friction may spoil the formation of highly visible lines, e.g., in the wake of a large star crossing a background of small stars in a globular cluster.)[676,677] As a result, line dispersion occurred by diffusion only.

With our minimal model, we reproduced the essential experimental observations qualitatively and quantitatively within particle-based and continuum simulations. Exploiting the latter, we created a state diagram that exhibits the parameter dependencies and the three line types (single line, inverted line, split line) that we also found in experiments. Our minimal model shows that the key ingredients for writing lines into a liquid by assembling (colloidal) particles (ink) in the trail of an IEX (pen) are long-ranged (hydrodynamic) attractions between the pen and the ink particles, low diffusivity, and programmable steering of the pen.

Overall, we demonstrated a facile and inexpensive approach to write on the micron scale within a liquid medium. A variety of further technical extensions awaits realization. Parallel writing of finely structured, large-scale density patterns becomes possible with several pens. Interruptions between words as well as dashed lines could be facilitated using photo-switchable chemical sources. Guided motion of the pen can further be realized by mechanical guiding,[678] optical[576] or magnetic forces,[679] and chemical fields.[680] Exploiting steering by chemical gradients would allow visualizing faint chemical traces left by other objects. Additionally, steering pH sources with optical tweezers in 3D buoyant ink dispersions would open access to freely suspended 3D patterns of arbitrary shape. Beyond global erasing by sonication, typo correction and line reconfiguration may be implemented by rewriting with or without prior heating with an IR laser (Fig. D13, Appx. D). Conversely, one could co-assemble suitable chemicals for line fixing like a mixture of photo-initiators, monomers, and cross-linker molecules. The important objective of further downscaling into the few-μm-range appears to be feasible for fluorescent tracers imaged by fluorescence microscopy and assembled by thermophoresis at a micron-sized heat source steered by laser tweezers. Adaptive learning and supervised machine learning could be used to program trajectories leading to the analogue of handwriting. Already these few examples of possible future developments highlight an interesting point on the technical side: namely the versatility of our generic approach of combining ink assembly

via long-ranged attractions with purely diffusive decay and programmable steering of the pen. It comprises a high degree of modularity, allows for the exchange of the constituents (pen, ink, drive) as to one's requirements, and is open for the combination with further modules. Thus, we anticipate that our results and conclusions are valid for a broad class of systems and may open routes to many future enterprises including the structuring of fluids, the visualization of chemical traces, the assembling of functional objects like actuators or drug carriers, information storage, and numerous artistic applications. Finally, our results could also be used to prepare desired initial states for future colloid experiments, e.g., on collective diffusion. Drawing fine lines, durable patterns, and individual letters into water was only the first step.

8 Conclusions

In this thesis, we have explored the influence of inertia on collective behavior in active systems that are intrinsically out of equilibrium. Within these systems, the universality of temperature does not apply. In particular, they can phase separate into a hot dense and a cold dilute phase if the active particles are inertial. Based on Brownian dynamics simulations of inertial active Brownian particles, we were able to develop a systematic understanding of the role of inertia for the temperature of coexisting phases. We investigated their phase diagram with focus on motility-induced phase separation (MIPS), which allowed us to control the kinetic temperature difference between the dense and dilute phase. Additionally, we explored temperatures of coexisting phases in mixtures of overdamped active and inertial passive Brownian particles. Such systems are highly relevant for experiments with biological or synthetic microswimmers. Our numerical investigation required a variety of tools for analyzing the huge amount of simulation data. Therefore, we additionally developed the efficient analysis tool AMEP (Active Matter Evaluation Package). We finally applied this tool to simulations of a minimal model for colloidal self-assembly, which can be applied as a novel technique for writing lines and letters into water. These simulations agree very well with experimental results and provide fundamental insights into the key ingredients for writing lines into water. In the following, we briefly summarize our main findings in the same order as we discussed them in the previous chapters. In addition, we outline perspectives for future research.

8.1 Summary

In Chap. 3, we introduced the Active Matter Evaluation Package (AMEP), a Python library which has been developed as part of this thesis and which provides all observables used to analyze the simulation data. With AMEP, we provide a unified framework for analyzing both particle-based and continuum simulation data. It allows us to quickly calculate key observables that give us insights into structural and dynamical properties of the investigated systems. AMEP is the first Python library that is specifically designed for the analysis of active matter systems. Therefore, it denotes an important contribution to the active matter community. It is available as open-source software and has been downloaded more than 2 000 times to date. It provides an easy-to-learn API and an efficient HDF5-based backend to handle simulation data and analysis results. Hence, AMEP is perfectly suited for analyzing large-scale simulations that can provide essential insights into phase separation, pattern formation, and critical phenomena in active matter systems. Due to its growing collection of observables, which are especially relevant for the analysis of active matter systems, AMEP has the potential to become a key tool for researchers in the field of active matter and soft matter physics in general.

We exploited the developed tools provided by AMEP to systematically test different possibilities to define temperature in active systems. Our analytical and numerical results, which we presented in Chap. 4, show that different possibilities to define temperature typically lead to different values, but close to equilibrium, all values coincide. We have demonstrated that such an equilibrium state can be reached in the limit of vanishing Péclet number, where activity vanishes and the system forms an equilibrium system made of PBPs. In this system, all possibilities to define temperature coincide with the bath temperature. Moreover, we have shown that an effective equilibrium state can be reached in the limit of large ratio between particle mass and persistence time, where the latter becomes small compared to the inertial time. Within this limit, the motion of the active particles is dominated by rotational diffusion, and the system reaches an effective equilibrium state at a temperature that is larger than the bath temperature. Remarkably, we identified two classes of temperatures: The kinetic temperature and the configurational temperature both lead to very similar values exhibiting the same parameter dependence over a wide parameter regime. Hence, they constitute a first class. The effective temperature follows the values of this class but only in a limited parameter regime. The virial temperature, the Einstein temperature, and the oscillator temperature are also similar to each other and have the same parameter dependence. They form a second class of temperatures whose values strongly differ from those of the first class. Notably, we found that far from equilibrium at large Péclet number and small mass, the two classes are related to each other by the particle mass as a scaling parameter. These insights allowed us to identify temperatures that are advantageous over others in the sense that they are independent of details of a tracer used as a thermometer or of a confining potential and mutually lead to similar temperature values over wide parameter regimes. We conclude that the kinetic temperature and the configurational temperature have these advantages. Moreover, our findings provide a first starting point towards a unified non-equilibrium theory for the concept of temperature in active systems.

Based on the kinetic temperature, we proposed a mechanism to cool active particles in a targeted cooling domain, which is presented in Chap. 5. It exploits MIPS in inertial active Brownian particles and allows us to design a “refrigerator” for active particles. We performed intensive Brownian dynamics simulations to obtain the MIPS phase transition line by varying the Péclet number and the area fraction. In contrast to overdamped active Brownian particles, where the phase transition line is inversely proportional to the packing fraction at large Péclet number, we found that it is proportional to the packing fraction for inertial active Brownian particles. This form is purely induced by inertia and a key ingredient for the proposed refrigerator. We have shown that its design requires inertia to induce a temperature difference across the dense and the dilute phase and to induce the particular shape of the phase transition line. Such a refrigerator creates a self-organized cooling domain, in which the active particles undergo MIPS. Accordingly, they form a dense cluster inside the cooling domain. We have shown that this cluster features a kinetic temperature that is up to two orders of magnitude smaller than the kinetic temperature of active particles in its environment. Notably, these refrigerators do not require any isolating walls to separate the cooling domain from its environment. Hence, the active-particle subsystem alone does not behave as we might expect from the laws of thermodynamics.

In particular, the bath pays the thermodynamic bill for a self-organized cooling domain that does not decay.

The investigated temperature differences in Chap. 5 are only visible if the active particles are inertial. However, many experimental active systems consist of biological or synthetic microswimmers that are overdamped and would not feature different temperatures in coexisting phases. Hence, we investigated mixtures of overdamped active and inertial passive Brownian particles in Chap. 6 to show that such temperature differences can be observed in a broader class of systems especially relevant for experimental realizations. Indeed, we found a persistent kinetic temperature difference between passive particles in the dense and the dilute phase when the mixture undergoes MIPS. This temperature difference emerges although both the overdamped active and the inertial passive Brownian particles on their own would not show different temperatures in coexisting phases. Remarkably, we found parameter regimes in which the dilute phase is not always hotter than the dense phase but also vice versa. In this scenario, hot liquid-like droplets coexist with a cold gas. This remarkable non-equilibrium phenomenon is robust with respect to the choice of temperature definition and the particle size. We demonstrated that the observed temperature difference between the dense and the dilute phase can be controlled by the self-propulsion speed of the active particles, the mass of the passive particles, and the fraction of active particles in the mixture.

Finally, in Chap. 7, we applied our developed simulation and analysis tools to model a new writing technique that allows us to write letters into water. This technique is based on an ion-exchange resin bead which rolls through passive colloids suspended in a water solution. The resin bead creates a pH gradient, which induces osmotic flows that attract suspended colloids in its vicinity. Accordingly, colloids are assembled in the trail of the resin bead and form long-lasting lines that only broaden over time by diffusion. We developed a minimal model which we solved numerically using particle-based and continuum simulations. We demonstrated that this model qualitatively and quantitatively reproduces the essential experimental observations. Based on continuum simulations, we reported a state diagram that shows different line types. These results provide fundamental insights to fine-tune the writing process. More generally, they carve out the key ingredients for writing lines into a liquid by assembling colloidal particles in the trail of an ion-exchange resin bead: First, we need long-ranged (hydrodynamic) attractions between the resin bead and the colloids. Second, a low diffusivity and a programmable steering technique for the resin bead are required.

Our simulation studies provide a systematic understanding of the influence of inertia on the emergence of coexisting temperatures in active systems. We carved out suitable possibilities to define temperature in active systems, we studied the emergence of different temperatures in coexisting phases in different active systems that contain active or passive inertial particles, and we developed the powerful analysis tool AMEP. Our results pave the way for many future applications and interesting ongoing research. Therefore, they also raise various unanswered questions and challenges, which we will summarize in the following.

8.2 Future perspectives

Our systematic study of different possibilities to define temperature serves as a starting point towards a systematic classification and unification of different methods used to measure temperature in active systems. An ongoing challenge is to generalize thermodynamic concepts to non-equilibrium by formulating generalized fluctuation-dissipation relations for active matter.[23,194,434,509,512,589,594,681,682] Here, it is an open question whether external forces or interaction forces have to be rescaled in order to find a generalized fluctuation-dissipation theorem. Such a force renormalization could also help to formulate generalized Langevin equations that contain a memory kernel and colored noise as recently done for passive particles in an active bath.[141] These generalized Langevin equations describe the motion of the particles effectively and could help to further understand the emergence of the two observed temperature classes.

To obtain a deeper understanding of the emergence of hot liquid-like droplets that coexist with a colder gas, the investigation of the local entropy production could provide important insights.[24,25,144,160,264,268,432,436,683] In particular, it would provide information about how far from equilibrium the system is locally. Here, the model-free method proposed in Ref. [431], which we plan to implement in AMEP in the near future, could be applied. In addition to entropy production, many more observables are planned to be included in AMEP. First, we plan to develop a cluster tracking algorithm, which is required to study the influence of cluster motion on MIPS.[146] Second, we plan to develop an algorithm that calculates the surface tension of arbitrarily shaped clusters. This is especially relevant to understand the observed negative surface tension at the interface between the dense and the dilute phase in MIPS.[684,685] In equilibrium, negative surface tension would imply that the interface is unstable. However, clusters formed by MIPS are stable, and the role of negative surface tension is controversially discussed.[446,686–690] Third, tools for finite-size scaling analysis are planned to be implemented as well.[198,486,691] These are especially important for answering the frequently discussed question to which universality class MIPS belongs.[168,443,692] Continuum theories for inertial active particles, which possibly include multiplicative noise, could provide one way to tackle this challenge. Alternatively, since the development of a continuum theory for inertial active matter is challenging as well, machine-learning techniques could be used to deduce suitable continuum models from particle-based simulations.[214,215,217,693]

It would also be interesting to explore our proposed concept for an active refrigerator within microscopic theories and experiments. The latter would open a route to explore possible applications such as trapping and absorption of large (toxic) molecules or viruses. These experiments could be realized with self-propelled particles that feature significant inertia. Examples range from activated micro-particles in a plasma[561,562] and vibrated granular particles[121,154,156,157,229,290,563–565] to drones,[37,566,601] mini-robots,[602] and dense animal collections.[186,603] More fundamentally, active particles might also be sensitive to frictional forces between each other, which could influence the refrigeration mechanism. Therefore, it would be interesting how frictional contacts in inertial active matter affect MIPS.[404,426,694] This could be explored by adding frictional forces to the inertial active Brownian particle model and exploring the phase space using Brownian dynamics simulations. In the overdamped limit, it has been shown that frictional forces

promote MIPS.[426] If the particles are inertial, the effect of friction is more complicated and not well understood. Especially, the fluctuation-dissipation relation, which determines the strength of the thermal noise, might have to be modified in the presence of frictional contacts.

With respect to the concept of temperature, our study of mixtures containing overdamped active and inertial passive Brownian particles has demonstrated that temperature differences in coexisting phases can emerge in a broader class of systems. In particular, we have shown that a cold non-equilibrium gas can coexist with a hotter liquid. In further studies, it might be helpful to also consider the surrounding heat bath, which absorbs the dissipated energy. Moreover, we have observed that large inertial passive particles tend to accumulate in the dilute phase when they are mixed with small overdamped active particles at large Péclet number. This effect could be further explored using Brownian dynamics simulations. Our results also open a route to create persistent temperature profiles in various experimental systems. This could be realized by inserting overdamped active particles such as bacteria, algae, or synthetic colloidal microswimmers into inertial passive systems such as dusty plasmas or passive granulates. More generally, the results of our studies help to design and to control active matter systems such as hybrid materials, which contain some active components to perform predefined tasks, or programmable active matter that can change its material characteristics due to external stimuli.[695] Furthermore, the understanding of the influence of inertia helps to program robot swarms for health-care applications such as targeted drug delivery, underwater or planetary exploration, cargo delivery and traffic control, or environmental applications such as the control of bacterial contamination.[38,44]

Finally, our explored technique to write into water can be realized using many different technical methods in order to develop possible applications. For example, instead of the resin bead, a photo-switchable chemical source could be used as a pen to separate between words or to draw dashed lines. Moreover, different steering techniques could be implemented. For example, faint chemical traces left by other objects could be visualized when steering the pen by chemical gradients.[680] Other steering techniques could be developed based on mechanical guiding,[678] optical forces,[576] or magnetic forces for example.[679] Such techniques would open the route to even draw 3D objects into water, e.g., by steering the pen with optical tweezers in 3D buoyant ink dispersions. In addition, suitable chemicals such as mixtures of photo-initiators, monomers, and cross-linker molecules could be co-assembled to fix the drawn objects by UV curing. To overcome the challenge of finding suitable pen trajectories to reach a target drawing, machine-learning techniques could be utilized.

Bibliography

[1] M. Glotzer, "The 3Ms of central spindle assembly: microtubules, motors and MAPs", *Nat. Rev. Mol. Cell Biol.* **10**, 9 (2009).

[2] R. G. Winkler and G. Gompper, "The physics of active polymers and filaments", *J. Chem. Phys.* **153**, 040901 (2020).

[3] S. Banerjee, M. L. Gardel, and U. S. Schwarz, "The Actin Cytoskeleton as an Active Adaptive Material", *Annu. Rev. Condens. Matter Phys.* **11**, 421 (2020).

[4] J. Elgeti, R. G. Winkler, and G. Gompper, "Physics of microswimmers—single particle motion and collective behavior: a review", *Rep. Prog. Phys.* **78**, 056601 (2015).

[5] H. Jeckel, E. Jelli, R. Hartmann, P. K. Singh, R. Mok, J. F. Totz, L. Vidakovic, B. Eckhardt, J. Dunkel, and K. Drescher, "Learning the space-time phase diagram of bacterial swarm expansion", *Proc. Natl. Acad. Sci.* **116**, 1489 (2019).

[6] H. C. Berg, *E. coli in Motion*, edited by H. C. Berg, Biological and Medical Physics, Biomedical Engineering (Springer, New York, NY, 2004).

[7] L. Tweedy, P. A. Thomason, P. I. Paschke, K. Martin, L. M. Machesky, M. Zagnoni, and R. H. Insall, "Seeing around corners: Cells solve mazes and respond at a distance using attractant breakdown", *Science* **369**, 1075 (2020).

[8] X. Yang, D. Dormann, A. E. Münsterberg, and C. J. Weijer, "Cell Movement Patterns during Gastrulation in the Chick Are Controlled by Positive and Negative Chemotaxis Mediated by FGF4 and FGF8", *Dev. Cell* **3**, 425 (2002).

[9] B. A. David and P. Kubes, "Exploring the complex role of chemokines and chemoattractants in vivo on leukocyte dynamics", *Immunol. Rev.* **289**, 9 (2019).

[10] M. Tennenbaum, Z. Liu, D. Hu, and A. Fernandez-Nieves, "Mechanics of fire ant aggregations", *Nat. Mater.* **15**, 54 (2016).

[11] G. Yang, W. Zhou, W. Qu, W. Yao, P. Zhu, and J. Xu, "A Review of Ant Nests and Their Implications for Architecture", *Buildings* **12**, 2225 (2022).

[12] J. Buhl, D. J. T. Sumpter, I. D. Couzin, J. J. Hale, E. Despland, E. R. Miller, and S. J. Simpson, "From Disorder to Order in Marching Locusts", *Science* **312**, 1402 (2006).

[13] T. Vicsek and A. Zafeiris, "Collective motion", *Phys. Rep.* **517**, 71 (2012).

[14] A. Attanasi, A. Cavagna, L. Del Castello, I. Giardina, T. S. Grigera, A. Jelić, S. Melillo, L. Parisi, O. Pohl, E. Shen, et al., "Information transfer and behavioural inertia in starling flocks", *Nat. Phys.* **10**, 691 (2014).

[15] M. Ballerini, N. Cabibbo, R. Candelier, A. Cavagna, E. Cisbani, I. Giardina, V. Lecomte, A. Orlandi, G. Parisi, A. Procaccini, et al., "Interaction ruling animal collective behavior depends on topological rather than metric distance: Evidence from a field study", *Proc. Natl. Acad. Sci.* **105**, 1232 (2008).

[16] J. Toner and Y. Tu, "Flocks, herds, and schools: A quantitative theory of flocking", *Phys. Rev. E* **58**, 4828 (1998).

[17]C. K. Hemelrijk and H. Hildenbrandt, "Schools of fish and flocks of birds: their shape and internal structure by self-organization", *Interface Focus* **2**, 726 (2012).

[18]S. Behera, D. P. Dogra, M. K. Bandyopadhyay, and P. P. Roy, "Understanding crowd flow patterns using active-Langevin model", *Pattern Recognit.* **119**, 108037 (2021).

[19]N. Bain and D. Bartolo, "Dynamic response and hydrodynamics of polarized crowds", *Science* **363**, 46 (2019).

[20]M. Das, C. F. Schmidt, and M. Murrell, "Introduction to Active Matter", *Soft Matter* **16**, 7185 (2020).

[21]C. Bechinger, R. Di Leonardo, H. Löwen, C. Reichhardt, G. Volpe, and G. Volpe, "Active Particles in Complex and Crowded Environments", *Rev. Mod. Phys.* **88**, 045006 (2016).

[22]A. M. Menzel, "Tuned, driven, and active soft matter", *Phys. Rep.* **554**, 1 (2015).

[23]D. Chaudhuri, "Active Brownian particles: Entropy production and fluctuation response", *Phys. Rev. E* **90**, 022131 (2014).

[24]J. O'Byrne, Y. Kafri, J. Tailleur, and F. van Wijland, "Time irreversibility in active matter, from micro to macro", *Nat. Rev. Phys.* **4**, 167 (2022).

[25]S. Shankar and M. C. Marchetti, "Hidden entropy production and work fluctuations in an ideal active gas", *Phys. Rev. E* **98**, 020604(R) (2018).

[26]M. te Vrugt and R. Wittkowski, "A review of active matter reviews", *arXiv:2405.15751v1 [cond-mat.soft]* (2024).

[27]M. C. Marchetti, J. F. Joanny, S. Ramaswamy, T. B. Liverpool, J. Prost, M. Rao, and R. A. Simha, "Hydrodynamics of soft active matter", *Rev. Mod. Phys.* **85**, 1143 (2013).

[28]G. Gompper, R. G. Winkler, T. Speck, A. P. Solon, C. Nardini, F. Peruani, H. Löwen, R. Golestanian, U. B. Kaupp, L. Alvarez, et al., "The 2020 motile active matter roadmap", *J. Phys. Condens. Matter* **32**, 193001 (2020).

[29]Y. Fu, H. Yu, X. Zhang, P. Malgaretti, V. Kishore, and W. Wang, "Microscopic Swarms: From Active Matter Physics to Biomedical and Environmental Applications", *Micromachines* **13**, 295 (2022).

[30]G. Volpe, N. A. M. Araújo, M. Guix, M. Miodownik, A. Sen, S. Sanchez, N. Martin, L. Alvarez, J. Simmchen, R. Di Leonardo, et al., "Roadmap for Animate Matter", *arXiv:2407.10623 [cond-mat.mtrl-sci]* (2024).

[31]M. Bär, R. Großmann, S. Heidenreich, and F. Peruani, "Self-Propelled Rods: Insights and Perspectives for Active Matter", *Annu. Rev. Condens. Matter Phys.* **11**, 441 (2020).

[32]A. Zöttl and H. Stark, "Emergent behavior in active colloids", *J. Phys. Condens. Matter* **28**, 253001 (2016).

[33]A. Cavagna and I. Giardina, "Bird Flocks as Condensed Matter", *Annu. Rev. Condens. Matter Phys.* **5**, 183 (2014).

[34]J. Grauer, H. Löwen, and B. Liebchen, "Strategic spatiotemporal vaccine distribution increases the survival rate in an infectious disease like Covid-19", *Sci. Rep.* **10**, 21594 (2020).

[35]P. Forgács, A. Libál, C. Reichhardt, N. Hengartner, and C. J. O. Reichhardt, "Using active matter to introduce spatial heterogeneity to the susceptible infected recovered model of epidemic spreading", *Sci. Rep.* **12**, 11229 (2022).

[36]M. te Vrugt, J. Jeggle, and R. Wittkowski, "Passive and active field theories for disease spreading", *J. Phys. A Math. Theor.* **57**, 315003 (2024).

[37]G. Vásárhelyi, C. Virágh, G. Somorjai, T. Nepusz, A. E. Eiben, and T. Vicsek, "Optimized flocking of autonomous drones in confined environments", *Sci. Robot.* **3**, eaat3536 (2018).

[38]M. M. Shahzad, Z. Saeed, A. Akhtar, H. Munawar, M. H. Yousaf, N. K. Baloach, and F. Hussain, "A Review of Swarm Robotics in a NutShell", *Drones* **7**, 269 (2023).

[39]A. Ghosh, W. Xu, N. Gupta, and D. H. Gracias, "Active matter therapeutics", *Nano Today* **31**, 100836 (2020).

[40]M. Luo, Y. Feng, T. Wang, and J. Guan, "Micro-/Nanorobots at Work in Active Drug Delivery", *Adv. Funct. Mater.* **28**, 1706100 (2018).

[41]M. Hu, X. Ge, X. Chen, W. Mao, X. Qian, and W.-E. Yuan, "Micro/Nanorobot: A Promising Targeted Drug Delivery System", *Pharmaceutics* **12**, 665 (2020).

[42]J. Wang and W. Gao, "Nano/Microscale Motors: Biomedical Opportunities and Challenges", *ACS Nano* **6**, 5745 (2012).

[43]S. Palagi and P. Fischer, "Bioinspired microrobots", *Nat. Rev. Mater.* **3**, 113 (2018).

[44]F. Soto, E. Karshalev, F. Zhang, B. Esteban Fernandez de Avila, A. Nourhani, and J. Wang, "Smart Materials for Microrobots", *Chem. Rev.* **122**, 5365 (2022).

[45]A. Sokolov, M. M. Apodaca, B. A. Grzybowski, and I. S. Aranson, "Swimming bacteria power microscopic gears", *Proc. Natl. Acad. Sci.* **107**, 969 (2010).

[46]R. Di Leonardo, L. Angelani, D. Dell'Arciprete, G. Ruocco, V. Iebba, S. Schippa, M. P. Conte, F. Mecarini, F. De Angelis, and E. Di Fabrizio, "Bacterial ratchet motors", *Proc. Natl. Acad. Sci.* **107**, 9541 (2010).

[47]L. Angelani, R. Di Leonardo, and G. Ruocco, "Self-Starting Micromotors in a Bacterial Bath", *Phys. Rev. Lett.* **102**, 048104 (2009).

[48]F. Vernerey, E. Benet, L. Blue, A. Fajrial, S. Lalitha Sridhar, J. Lum, G. Shakya, K. Song, A. Thomas, and M. Borden, "Biological active matter aggregates: Inspiration for smart colloidal materials", *Adv. Colloid Interface Sci.* **263**, 38 (2019).

[49]H. Levine and D. I. Goldman, "Physics of smart active matter: integrating active matter and control to gain insights into living systems", *Soft Matter* **19**, 4204 (2023).

[50]F. Peruani, J. Starruß, V. Jakovljevic, L. Søgaard-Andersen, A. Deutsch, and M. Bär, "Collective Motion and Nonequilibrium Cluster Formation in Colonies of Gliding Bacteria", *Phys. Rev. Lett.* **108**, 098102 (2012).

[51]I. Theurkauff, C. Cottin-Bizonne, J. Palacci, C. Ybert, and L. Bocquet, "Dynamic clustering in active colloidal suspensions with chemical signaling", *Phys. Rev. Lett.* **108**, 1 (2012).

[52]P. Kushwaha, V. Semwal, S. Maity, S. Mishra, and V. Chikkadi, "Phase separation of passive particles in active liquids", *Phys. Rev. E* **108**, 034603 (2023).

[53]I. Buttinoni, J. Bialké, F. Kümmel, H. Löwen, C. Bechinger, and T. Speck, "Dynamical Clustering and Phase Separation in Suspensions of Self-Propelled Colloidal Particles", *Phys. Rev. Lett.* **110**, 238301 (2013).

[54]J. Zhang, R. Alert, J. Yan, N. S. Wingreen, and S. Granick, "Active phase separation by turning towards regions of higher density", *Nat. Phys.* **17**, 961 (2021).

[55]M. N. van der Linden, L. C. Alexander, D. G. Aarts, and O. Dauchot, "Interrupted Motility Induced Phase Separation in Aligning Active Colloids", *Phys. Rev. Lett.* **123**, 098001 (2019).

[56]M. Y. Ben Zion, Y. Caba, A. Modin, and P. M. Chaikin, "Cooperation in a fluid swarm of fuel-free micro-swimmers", *Nat. Commun.* **13**, 184 (2022).

[57]J. Palacci, S. Sacanna, A. P. Steinberg, D. J. Pine, and P. M. Chaikin, "Living Crystals of Light-Activated Colloidal Surfers", *Science* **339**, 936 (2013).

[58]I. Grobas, M. Polin, and M. Asally, "Swarming bacteria undergo localized dynamic phase transition to form stress-induced biofilms", *Elife* **10**, e62632 (2021).

[59]G. Liu, A. Patch, F. Bahar, D. Yllanes, R. D. Welch, M. C. Marchetti, S. Thutupalli, and J. W. Shaevitz, "Self-Driven Phase Transitions Drive Myxococcus xanthus Fruiting Body Formation", *Phys. Rev. Lett.* **122**, 248102 (2019).

[60]V. Schaller, C. Weber, C. Semmrich, E. Frey, and A. R. Bausch, "Polar patterns of driven filaments", *Nature* **467**, 73 (2010).

[61]L. Huber, R. Suzuki, T. Krüger, E. Frey, and A. R. Bausch, "Emergence of coexisting ordered states in active matter systems", *Science* **361**, 255 (2018).

[62]A. Be'er, S. K. Strain, R. A. Hernández, E. Ben-Jacob, and E.-L. Florin, "Periodic Reversals in Paenibacillus dendritiformis Swarming", *J. Bacteriol.* **195**, 2709 (2013).

[63]U. Börner, A. Deutsch, H. Reichenbach, and M. Bär, "Rippling Patterns in Aggregates of Myxobacteria Arise from Cell-Cell Collisions", *Phys. Rev. Lett.* **89**, 078101 (2002).

[64]E. Demir, Y. I. Yaman, M. Basaran, and A. Kocabas, "Dynamics of pattern formation and emergence of swarming in Caenorhabditis elegans", *Elife* **9**, e52781 (2020).

[65]B. Liebchen and A. K. Mukhopadhyay, "Interactions in active colloids", *J. Phys. Condens. Matter* **34**, 083002 (2022).

[66]E. Sesé-Sansa, G.-J. Liao, D. Levis, I. Pagonabarraga, and S. H. L. Klapp, "Impact of dipole–dipole interactions on motility-induced phase separation", *Soft Matter* **18**, 5388 (2022).

[67]Y. Yang, J. Elgeti, and G. Gompper, "Cooperation of sperm in two dimensions: Synchronization, attraction, and aggregation through hydrodynamic interactions", *Phys. Rev. E* **78**, 061903 (2008).

[68]F. Fadda, D. A. Matoz-Fernandez, R. van Roij, and S. Jabbari-Farouji, "The interplay between chemo-phoretic interactions and crowding in active colloids", *Soft Matter* **19**, 2297 (2023).

[69]M. Durve, A. Saha, and A. Sayeed, "Active particle condensation by non-reciprocal and time-delayed interactions", *Eur. Phys. J. E* **41**, 49 (2018).

[70]F. A. Lavergne, H. Wendehenne, T. Bäuerle, and C. Bechinger, "Group formation and cohesion of active particles with visual perception–dependent motility", *Science* **364**, 70 (2019).

[71]J. U. Klamser, S. C. Kapfer, and W. Krauth, "Thermodynamic phases in two-dimensional active matter", *Nat. Commun.* **9**, 5045 (2018).

[72]P. Digregorio, D. Levis, A. Suma, L. F. Cugliandolo, G. Gonnella, and I. Pagonabarraga, "Full Phase Diagram of Active Brownian Disks: From Melting to Motility-Induced Phase Separation", *Phys. Rev. Lett.* **121**, 098003 (2018).

[73]R. S. Negi, R. G. Winkler, and G. Gompper, "Collective behavior of self-steering active particles with velocity alignment and visual perception", *Phys. Rev. Res.* **6**, 013118 (2024).

[74]B. Liebchen and H. Löwen, "Synthetic Chemotaxis and Collective Behavior in Active Matter", *Acc. Chem. Res.* **51**, 2982 (2018).

[75]A. V. Zampetaki, B. Liebchen, A. V. Ivlev, and H. Löwen, "Collective self-optimization of communicating active particles", *Proc. Natl. Acad. Sci.* **118**, 1 (2021).

[76]M. R. Shaebani, A. Wysocki, R. G. Winkler, G. Gompper, and H. Rieger, "Computational models for active matter", *Nat. Rev. Phys.* **2**, 181 (2020).

[77]L. Hecht, J. C. Ureña, and B. Liebchen, "An Introduction to Modeling Approaches of Active Matter", *arXiv:2102.13007 [cond-mat.soft]* (2021).

[78]A. Zöttl and H. Stark, "Modeling Active Colloids: From Active Brownian Particles to Hydrodynamic and Chemical Fields", *Annu. Rev. Condens. Matter Phys.* **14**, 109 (2023).

[79]B. Liebchen and H. Löwen, "Modeling Chemotaxis of Microswimmers: From Individual to Collective Behavior", in *Chemical Kinetics* (World Scientific, Singapore, 2019), p. 493.

[80]C. S. Dias, "Molecular Dynamics Simulations of Active Matter using LAMMPS", *arXiv:2102.10399 [cond-mat.soft]* **2**, 1 (2021).

[81]F. Toschi and M. Sega, *Flowing Matter*, edited by F. Toschi and M. Sega, Soft and Biological Matter (Springer International Publishing, Cham, 2019).

[82]G. Volpe, S. Gigan, and G. Volpe, "Simulation of the active Brownian motion of a microswimmer", *Am. J. Phys.* **82**, 659 (2014).

[83]M. E. Cates and J. Tailleur, "Motility-Induced Phase Separation", *Annu. Rev. Condens. Matter Phys.* **6**, 219 (2015).

[84]H. Chaté, "Dry Aligning Dilute Active Matter", *Annu. Rev. Condens. Matter Phys.* **11**, 189 (2020).

[85]J. Barré, R. Chétrite, M. Muratori, and F. Peruani, "Motility-Induced Phase Separation of Active Particles in the Presence of Velocity Alignment", *J. Stat. Phys.* **158**, 589 (2015).

[86]G. Gonnella, D. Marenduzzo, A. Suma, and A. Tiribocchi, "Motility-induced phase separation and coarsening in active matter", *C. R. Phys.* **16**, 316 (2015).

[87]J. Bickmann and R. Wittkowski, "Predictive local field theory for interacting active Brownian spheres in two spatial dimensions", *J. Phys. Condens. Matter* **32**, 214001 (2020).

[88]P. Degond, S. Henkes, and H. Yu, "Self-organized hydrodynamics with density-dependent velocity", *Kinet. Relat. Model.* **10**, 193 (2017).

[89]S. Steffenoni, G. Falasco, and K. Kroy, "Microscopic derivation of the hydrodynamics of active-Brownian-particle suspensions", *Phys. Rev. E* **95**, 052142 (2017).

[90]A. M. Menzel, A. Saha, C. Hoell, and H. Löwen, "Dynamical density functional theory for microswimmers", *J. Chem. Phys.* **144**, 024115 (2016).

[91]M. te Vrugt, H. Löwen, and R. Wittkowski, "Classical dynamical density functional theory: from fundamentals to applications", *Adv. Phys.* **69**, 121 (2020).

[92]M. te Vrugt, J. Bickmann, and R. Wittkowski, "How to derive a predictive field theory for active Brownian particles: a step-by-step tutorial", *J. Phys. Condens. Matter* **35**, 313001 (2023).

[93]G. Szamel, "Mode-coupling theory for the steady-state dynamics of active Brownian particles", *J. Chem. Phys.* **150**, 124901 (2019).

[94]A. Liluashvili, J. Ónody, and T. Voigtmann, "Mode-coupling theory for active Brownian particles", *Phys. Rev. E* **96**, 062608 (2017).

[95]B. Rallabandi, F. Yang, and H. A. Stone, "Motion of hydrodynamically interacting active particles", *arXiv:1901.04311v1 [physics.flu-dyn]*, 1 (2019).

[96]R. G. Winkler and G. Gompper, "Hydrodynamics in Motile Active Matter", in *Handbook of Materials Modeling*, edited by W. Andreoni and S. Yip (Springer International Publishing, Cham, 2018), p. 1.

[97]A. Tiribocchi, R. Wittkowski, D. Marenduzzo, and M. E. Cates, "Active Model H: Scalar Active Matter in a Momentum-Conserving Fluid", *Phys. Rev. Lett.* **115**, 188302 (2015).

[98]J. de Graaf, H. Menke, A. J. T. M. Mathijssen, M. Fabritius, C. Holm, and T. N. Shendruk, "Lattice-Boltzmann hydrodynamics of anisotropic active matter", *J. Chem. Phys.* **144**, 134106 (2016).

[99]M. E. Cates and J. Tailleur, "When are active Brownian particles and run-and-tumble particles equivalent? Consequences for motility-induced phase separation", *Europhys. Lett.* **101**, 20010 (2013).

[100]A. Suma, G. Gonnella, D. Marenduzzo, and E. Orlandini, "Motility-induced phase separation in an active dumbbell fluid", *Europhys. Lett.* **108**, 56004 (2014).

[101]T. Speck, A. M. Menzel, J. Bialké, and H. Löwen, "Dynamical mean-field theory and weakly non-linear analysis for the phase separation of active Brownian particles", *J. Chem. Phys.* **142**, 224109 (2015).

[102]D. Marenduzzo, "An introduction to the statistical physics of active matter: motility-induced phase separation and the "generic instability" of active gels", *Eur. Phys. J. Spec. Top.* **225**, 2065 (2016).

[103]S. Mandal, B. Liebchen, and H. Löwen, "Motility-Induced Temperature Difference in Coexisting Phases", *Phys. Rev. Lett.* **123**, 228001 (2019).

[104]E. Sesé-Sansa, I. Pagonabarraga, and D. Levis, "Velocity alignment promotes motility-induced phase separation", *Europhys. Lett.* **124**, 30004 (2018).

[105]R. van Damme, J. Rodenburg, R. van Roij, and M. Dijkstra, "Interparticle torques suppress motility-induced phase separation for rodlike particles", *J. Chem. Phys.* **150**, 164501 (2019).

[106]D. Levis and L. Berthier, "From single-particle to collective effective temperatures in an active fluid of self-propelled particles", *Europhys. Lett.* **111**, 60006 (2015).

[107]L. Caprini, U. M. B. Marconi, and A. Puglisi, "Spontaneous Velocity Alignment in Motility-Induced Phase Separation", *Phys. Rev. Lett.* **124**, 078001 (2020).

[108]J. Wang, M.-J. Huang, and R. Kapral, "Self-propelled torus colloids", *J. Chem. Phys.* **153**, 014902 (2020).

[109]G.-J. Liao, C. K. Hall, and S. H. L. Klapp, "Dynamical self-assembly of dipolar active Brownian particles in two dimensions", *Soft Matter* **16**, 2208 (2020).

[110]G. S. Redner, M. F. Hagan, and A. Baskaran, "Structure and Dynamics of a Phase-Separating Active Colloidal Fluid", *Phys. Rev. Lett.* **110**, 055701 (2013).

[111]D. Levis, J. Codina, and I. Pagonabarraga, "Active Brownian equation of state: metastability and phase coexistence", *Soft Matter* **13**, 8113 (2017).

[112]B. Liebchen, D. Marenduzzo, I. Pagonabarraga, and M. E. Cates, "Clustering and Pattern Formation in Chemorepulsive Active Colloids", *Phys. Rev. Lett.* **115**, 258301 (2015).

[113]S. Ramaswamy, "The Mechanics and Statistics of Active Matter", *Annu. Rev. Condens. Matter Phys.* **1**, 323 (2010).

[114]M. Zeitz, K. Wolff, and H. Stark, "Active Brownian particles moving in a random Lorentz gas", *Eur. Phys. J. E* **40**, 23 (2017).

[115]H. Stark, "Artificial Chemotaxis of Self-Phoretic Active Colloids: Collective Behavior", *Acc. Chem. Res.* **51**, 2681 (2018).

[116]J. Stürmer, M. Seyrich, and H. Stark, "Chemotaxis in a binary mixture of active and passive particles", *J. Chem. Phys.* **150**, 214901 (2019).

[117]R. C. Maloney, G.-J. Liao, S. H. L. Klapp, and C. K. Hall, "Clustering and phase separation in mixtures of dipolar and active particles", *Soft Matter* **16**, 3779 (2020).

[118]G.-J. Liao and S. H. L. Klapp, "Clustering and phase separation of circle swimmers dispersed in a monolayer", *Soft Matter* **14**, 7873 (2018).

[119]H. Löwen, "Inertial effects of self-propelled particles: From active Brownian to active Langevin motion", *J. Chem. Phys.* **152**, 040901 (2020).

[120]R. Chatterjee, N. Rana, R. A. Simha, P. Perlekar, and S. Ramaswamy, "Inertia Drives a Flocking Phase Transition in Viscous Active Fluids", *Phys. Rev. X* **11**, 031063 (2021).

[121]C. A. Weber, T. Hanke, J. Deseigne, S. Léonard, O. Dauchot, E. Frey, and H. Chaté, "Long-Range Ordering of Vibrated Polar Disks", *Phys. Rev. Lett.* **110**, 208001 (2013).

[122]H. D. Vuijk, J. U. Sommer, H. Merlitz, J. M. Brader, and A. Sharma, "Lorentz forces induce inhomogeneity and flux in active systems", *Phys. Rev. Res.* **2**, 013320 (2020).

[123]I. Petrelli, L. F. Cugliandolo, G. Gonnella, and A. Suma, "Effective temperatures in inhomogeneous passive and active bidimensional Brownian particle systems", *Phys. Rev. E* **102**, 012609 (2020).

[124]C. Dai, I. R. Bruss, and S. C. Glotzer, "Phase separation and state oscillation of active inertial particles", *Soft Matter* **16**, 2847 (2020).

[125]L. F. Cugliandolo, G. Gonnella, and I. Petrelli, "Effective Temperature in Active Brownian Particles", *Fluct. Noise Lett.* **18**, 1940008 (2019).

[126]L. L. Gutierrez-Martinez and M. Sandoval, "Inertial effects on trapped active matter", *J. Chem. Phys.* **153**, 044906 (2020).

[127]I. Petrelli, P. Digregorio, L. F. Cugliandolo, G. Gonnella, and A. Suma, "Active dumbbells: Dynamics and morphology in the coexisting region", *Eur. Phys. J. E* **41**, 128 (2018).

[128]W.-j. Zhu, X.-q. Huang, and B.-q. Ai, "Transport of underdamped self-propelled particles in active density waves", *J. Phys. A Math. Theor.* **51**, 115101 (2018).

[129]Z. Mokhtari, T. Aspelmeier, and A. Zippelius, "Collective rotations of active particles interacting with obstacles", *Europhys. Lett.* **120**, 14001 (2017).

[130]D. R. Parisi, R. Cruz Hidalgo, and I. Zuriguel, "Active particles with desired orientation flowing through a bottleneck", *Sci. Rep.* **8**, 9133 (2018).

[131]D. Arold and M. Schmiedeberg, "Active phase field crystal systems with inertial delay and underdamped dynamics", *Eur. Phys. J. E* **43**, 47 (2020).

[132]W.-Z. Fang, S. Ham, R. Qiao, and W.-Q. Tao, "Magnetic Actuation of Surface Walkers: The Effects of Confinement and Inertia", *Langmuir* **36**, 7046 (2020).

[133]M. Sandoval, "Pressure and diffusion of active matter with inertia", *Phys. Rev. E* **101**, 012606 (2020).

[134]P Chiarantoni, F Cagnetta, F Corberi, G Gonnella, and A Suma, "Work fluctuations of self-propelled particles in the phase separated state", *J. Phys. A Math. Theor.* **53**, 36LT02 (2020).

[135]K. R. Prathyusha, S. Henkes, and R. Sknepnek, "Dynamically generated patterns in dense suspensions of active filaments", *Phys. Rev. E* **97**, 022606 (2018).

[136]A. Manacorda and A. Puglisi, "Lattice Model to Derive the Fluctuating Hydrodynamics of Active Particles with Inertia", *Phys. Rev. Lett.* **119**, 208003 (2017).

[137]B.-q. Ai and F.-g. Li, "Transport of underdamped active particles in ratchet potentials", *Soft Matter* **13**, 2536 (2017).

[138]S. C. Takatori and J. F. Brady, "Inertial effects on the stress generation of active fluids", *Phys. Rev. Fluids* **2**, 094305 (2017).

[139]R. Mandal, P. J. Bhuyan, P. Chaudhuri, C. Dasgupta, and M. Rao, "Extreme active matter at high densities", *Nat. Commun.* **11**, 2581 (2020).

[140]L. Caprini, U. Marini Bettolo Marconi, A. Puglisi, and H. Löwen, "Entropons as collective excitations in active solids", *J. Chem. Phys.* **159**, 041102 (2023).

[141]J. Shea, G. Jung, and F. Schmid, "Force renormalization for probes immersed in an active bath", *Soft Matter* **20**, 1767 (2024).

[142]A. K. Omar, K. Klymko, T. GrandPre, P. L. Geissler, and J. F. Brady, "Tuning nonequilibrium phase transitions with inertia", *J. Chem. Phys.* **158**, 42 (2023).

[143]A. R. Sprenger, L. Caprini, H. Löwen, and R. Wittmann, "Dynamics of active particles with translational and rotational inertia", *J. Phys. Condens. Matter* **35**, 305101 (2023).

[144]D. Frydel, "Entropy production of active particles formulated for underdamped dynamics", *Phys. Rev. E* **107**, 014604 (2023).

[145]N. P. Kryuchkov, A. D. Nasyrov, K. D. Gursky, and S. O. Yurchenko, "Inertia changes evolution of motility-induced phase separation in active matter across particle activity", *Phys. Rev. E* **107**, 044601 (2023).

[146]C. B. Caporusso, L. F. Cugliandolo, P. Digregorio, G. Gonnella, D. Levis, and A. Suma, "Dynamics of Motility-Induced Clusters: Coarsening beyond Ostwald Ripening", *Phys. Rev. Lett.* **131**, 068201 (2023).

[147]K. Goswami, "Inertial particle under active fluctuations: Diffusion and work distributions", *Phys. Rev. E* **105**, 044123 (2022).

[148]G. H. P. Nguyen, R. Wittmann, and H. Löwen, "Active Ornstein–Uhlenbeck model for self-propelled particles with inertia", *J. Phys. Condens. Matter* **34**, 035101 (2022).

[149]J. Mayer Martins and R. Wittkowski, "Inertial dynamics of an active Brownian particle", *Phys. Rev. E* **106**, 034616 (2022).

[150]L. Caprini, R. K. Gupta, and H. Löwen, "Role of rotational inertia for collective phenomena in active matter", *Phys. Chem. Chem. Phys.* **24**, 24910 (2022).

[151]M. Patel and D. Chaudhuri, "Exact moments for trapped active particles: inertial impact on steady-state properties and re-entrance", *New J. Phys.* **26**, 073048 (2024).

[152]J. Su, H. Jiang, and Z. Hou, "Inertia-induced nucleation-like motility-induced phase separation", *New J. Phys.* **23**, 013005 (2021).

[153]G. Junot, G. Briand, R. Ledesma-Alonso, and O. Dauchot, "Active versus Passive Hard Disks against a Membrane: Mechanical Pressure and Instability", *Phys. Rev. Lett.* **119**, 028002 (2017).

[154]O. Dauchot and V. Démery, "Dynamics of a Self-Propelled Particle in a Harmonic Trap", *Phys. Rev. Lett.* **122**, 068002 (2019).

[155]S. Mayya, G. Notomista, D. Shell, S. Hutchinson, and M. Egerstedt, "Non-Uniform Robot Densities in Vibration Driven Swarms Using Phase Separation Theory", in 2019 IEEE/RSJ International Conference on Intelligent Robots and Systems (IROS) (2019), p. 4106.

[156]G. A. Patterson, P. I. Fierens, F. Sangiuliano Jimka, P. G. König, A. Garcimartín, I. Zuriguel, L. A. Pugnaloni, and D. R. Parisi, "Clogging Transition of Vibration-Driven Vehicles Passing through Constrictions", *Phys. Rev. Lett.* **119**, 248301 (2017).

[157]C. Scholz, S. Jahanshahi, A. Ldov, and H. Löwen, "Inertial delay of self-propelled particles", *Nat. Commun.* **9**, 5156 (2018).

[158]L. Caprini and U. M. B. Marconi, "Inertial self-propelled particles", *J. Chem. Phys.* **154**, 024902 (2021).

[159]E. A. Lisin, O. S. Vaulina, I. I. Lisina, and O. F. Petrov, "Active Brownian particle in homogeneous media of different viscosities: numerical simulations", *Phys. Chem. Chem. Phys.* **23**, 16248 (2021).

[160]E. Crosato, M. Prokopenko, and R. E. Spinney, "Irreversibility and emergent structure in active matter", *Phys. Rev. E* **100**, 042613 (2019).

[161]Y. Fily, Y. Kafri, A. P. Solon, J. Tailleur, and A. Turner, "Mechanical pressure and momentum conservation in dry active matter", *J. Phys. A Math. Theor.* **51**, 044003 (2018).

[162]E. Schiltz-Rouse, H. Row, and S. A. Mallory, "Kinetic temperature and pressure of an active Tonks gas", *Phys. Rev. E* **108**, 064601 (2023).

[163]S. De Karmakar and R. Ganesh, "Phase transition and emergence of active temperature in an active Brownian system in underdamped background", *Phys. Rev. E* **101**, 032121 (2020).

[164]L. Caprini and U. Marini Bettolo Marconi, "Active matter at high density: Velocity distribution and kinetic temperature", *J. Chem. Phys.* **153**, 184901 (2020).

[165]L. Hecht, S. Mandal, H. Löwen, and B. Liebchen, "Active Refrigerators Powered by Inertia", *Phys. Rev. Lett.* **129**, 178001 (2022).

[166]U. M. B. Marconi, A. Puglisi, and C. Maggi, "Heat, temperature and Clausius inequality in a model for active Brownian particles", *Sci. Rep.* **7**, 46496 (2017).

[167]U. Marini Bettolo Marconi, L. Caprini, and A. Puglisi, "Hydrodynamics of simple active liquids: the emergence of velocity correlations", *New J. Phys.* **23**, 103024 (2021).

[168]C. Maggi, M. Paoluzzi, A. Crisanti, E. Zaccarelli, and N. Gnan, "Universality class of the motility-induced critical point in large scale off-lattice simulations of active particles", *Soft Matter* **17**, 3807 (2021).

[169]D. Geiß and K. Kroy, "Brownian Thermometry Beyond Equilibrium", *ChemSystemsChem* **2**, e1900041 (2020).

[170]A Puglisi, A Sarracino, and A Vulpiani, "Temperature in and out of equilibrium: A review of concepts, tools and attempts", *Phys. Rep.* **709-710**, 1 (2017).

[171]D. Wexler, N. Gov, K. Ø. Rasmussen, and G. Bel, "Dynamics and escape of active particles in a harmonic trap", *Phys. Rev. Res.* **2**, 013003 (2020).

[172]J Casas-Vázquez and D Jou, "Temperature in non-equilibrium states: a review of open problems and current proposals", *Rep. Prog. Phys.* **66**, 1937 (2003).

[173]K. Feitosa and N. Menon, "Breakdown of Energy Equipartition in a 2D Binary Vibrated Granular Gas", *Phys. Rev. Lett.* **88**, 198301 (2002).

[174]S. Saw, L. Costigliola, and J. C. Dyre, "Configurational temperature in active matter. II. Quantifying the deviation from thermal equilibrium", *Phys. Rev. E* **107**, 024610 (2023).

[175]G. Rickayzen and J. G. Powles, "Temperature in the classical microcanonical ensemble", *J. Chem. Phys.* **114**, 4333 (2001).

[176]O. G. Jepps, G. Ayton, and D. J. Evans, "Microscopic expressions for the thermodynamic temperature", *Phys. Rev. E* **62**, 4757 (2000).

[177]M. Baldovin, A. Puglisi, A. Sarracino, and A. Vulpiani, "About thermometers and temperature", *J. Stat. Mech. Theory Exp.* **2017**, 113202 (2017).

[178]B. Liebchen and H. Löwen, "Selbstgetriebene Teilchen", *Phys. J.* **21**, 31 (2022).

[179]C. Wolgemuth, E. Hoiczyk, D. Kaiser, and G. Oster, "How Myxobacteria Glide", *Curr. Biol.* **12**, 369 (2002).

[180]S. Rafaï, L. Jibuti, and P. Peyla, "Effective Viscosity of Microswimmer Suspensions", *Phys. Rev. Lett.* **104**, 098102 (2010).

[181]J. R. Howse, R. A. L. Jones, A. J. Ryan, T. Gough, R. Vafabakhsh, and R. Golestanian, "Self-Motile Colloidal Particles: From Directed Propulsion to Random Walk", *Phys. Rev. Lett.* **99**, 048102 (2007).

[182]L. Qiao, M.-J. Huang, and R. Kapral, "Active motion of synthetic nanomotors in filament networks", *Phys. Rev. Res.* **2**, 033245 (2020).

[183]C. Kurzthaler, Y. Zhao, N. Zhou, J. Schwarz-Linek, C. Devailly, J. Arlt, J.-D. Huang, W. C. Poon, T. Franosch, J. Tailleur, et al., "Characterization and Control of the Run-and-Tumble Dynamics of *Escherichia Coli*", *Phys. Rev. Lett.* **132**, 038302 (2024).

[184]G. Ramos, M. L. Cordero, and R. Soto, "Bacteria driving droplets", *Soft Matter* **16**, 1359 (2020).

[185]C. Kurzthaler, C. Devailly, J. Arlt, T. Franosch, W. C. Poon, V. A. Martinez, and A. T. Brown, "Probing the Spatiotemporal Dynamics of Catalytic Janus Particles with Single-Particle Tracking and Differential Dynamic Microscopy", *Phys. Rev. Lett.* **121**, 078001 (2018).

[186]D. Klotsa, "As above, so below, and also in between: mesoscale active matter in fluids", *Soft Matter* **15**, 8946 (2019).

[187]W. Bialek, A. Cavagna, I. Giardina, T. Mora, E. Silvestri, M. Viale, and A. M. Walczak, "Statistical mechanics for natural flocks of birds", *Proc. Natl. Acad. Sci.* **109**, 4786 (2012).

[188]J. L. Silverberg, M. Bierbaum, J. P. Sethna, and I. Cohen, "Collective Motion of Humans in Mosh and Circle Pits at Heavy Metal Concerts", *Phys. Rev. Lett.* **110**, 228701 (2013).

[189]A. Garcimartín, J. M. Pastor, L. M. Ferrer, J. J. Ramos, C. Martín-Gómez, and I. Zuriguel, "Flow and clogging of a sheep herd passing through a bottleneck", *Phys. Rev. E* **91**, 022808 (2015).

[190]I. Lachow, "The upside and downside of swarming drones", *Bull. At. Sci.* **73**, 96 (2017).

[191]V. Magdanz, M. Medina-Sánchez, L. Schwarz, H. Xu, J. Elgeti, and O. G. Schmidt, "Spermatozoa as Functional Components of Robotic Microswimmers", *Adv. Mater.* **29**, 1606301 (2017).

[192]W. Gao and J. Wang, "The Environmental Impact of Micro/Nanomachines: A Review", *ACS Nano* **8**, 3170 (2014).

[193]É. Fodor and M. Cristina Marchetti, "The statistical physics of active matter: From self-catalytic colloids to living cells", *Phys. A: Stat. Mech. Appl.* **504**, 106 (2018).

[194]S. D. Cengio, D. Levis, and I. Pagonabarraga, "Fluctuation–dissipation relations in the absence of detailed balance: formalism and applications to active matter", *J. Stat. Mech. Theory Exp.* **2021**, 043201 (2021).

[195]W. Fei, Y. Gu, and K. J. Bishop, "Active colloidal particles at fluid-fluid interfaces", *Curr. Opin. Colloid Interface Sci.* **32**, 57 (2017).

[196]M. F. Hagan and A. Baskaran, "Emergent self-organization in active materials", *Curr. Opin. Cell Biol.* **38**, 74 (2016).

[197]C. C. Maass, C. Krüger, S. Herminghaus, and C. Bahr, "Swimming Droplets", *Annu. Rev. Condens. Matter Phys.* **7**, 171 (2016).

[198]K. Binder and P. Virnau, "Phase transitions and phase coexistence: equilibrium systems versus externally driven or active systems - Some perspectives", *Soft Mater.* **00**, 1 (2021).

[199]A. Be'er and G. Ariel, "A statistical physics view of swarming bacteria", *Mov. Ecol.* **7**, 9 (2019).

[200]B. Liebchen and D. Levis, "Chiral active matter", *Europhys. Lett.* **139**, 67001 (2022).

[201]J. Blaschke, M. Maurer, K. Menon, A. Zöttl, and H. Stark, "Phase separation and coexistence of hydrodynamically interacting microswimmers", *Soft Matter* **12**, 9821 (2016).

[202]F. Bergmann, L. Rapp, and W. Zimmermann, "Active phase separation: A universal approach", *Phys. Rev. E* **98**, 020603 (2018).

[203]P. Dolai, A. Simha, and S. Mishra, "Phase separation in binary mixtures of active and passive particles", *Soft Matter* **14**, 6137 (2018).

[204]F. D. C. Farrell, M. C. Marchetti, D. Marenduzzo, and J. Tailleur, "Pattern Formation in Self-Propelled Particles with Density-Dependent Motility", *Phys. Rev. Lett.* **108**, 248101 (2012).

[205]B. Liebchen and D. Levis, "Collective Behavior of Chiral Active Matter: Pattern Formation and Enhanced Flocking", *Phys. Rev. Lett.* **119**, 058002 (2017).

[206]D. Saintillan and M. J. Shelley, "Instabilities and Pattern Formation in Active Particle Suspensions: Kinetic Theory and Continuum Simulations", *Phys. Rev. Lett.* **100**, 178103 (2008).

[207]A. P. Solon, J.-B. Caussin, D. Bartolo, H. Chaté, and J. Tailleur, "Pattern formation in flocking models: A hydrodynamic description", *Phys. Rev. E* **92**, 062111 (2015).

[208]J. Palacci, B. Abécassis, C. Cottin-Bizonne, C. Ybert, and L. Bocquet, "Colloidal Motility and Pattern Formation under Rectified Diffusiophoresis", *Phys. Rev. Lett.* **104**, 138302 (2010).

[209]D. Levis, I. Pagonabarraga, and B. Liebchen, "Activity induced synchronization: Mutual flocking and chiral self-sorting", *Phys. Rev. Res.* **1**, 023026 (2019).

[210]K. Zhang, X. Gong, and Y. Jiang, "Machine Learning in Soft Matter: From Simulations to Experiments", *Adv. Funct. Mater.* **34**, 2315177 (2024).

[211]M. Nasiri and B. Liebchen, "Reinforcement learning of optimal active particle navigation", *New J. Phys.* **24**, 073042 (2022).

[212]M. Nasiri, H. Löwen, and B. Liebchen, "Optimal active particle navigation meets machine learning", *Europhys. Lett.* **142**, 17001 (2023).

[213]M. Caraglio, H. Kaur, L. J. Fiderer, A. López-Incera, H. J. Briegel, T. Franosch, and G. Muñoz-Gil, "Learning how to find targets in the micro-world: the case of intermittent active Brownian particles", *Soft Matter* **20**, 2008 (2024).

[214]S. Maddu, B. L. Cheeseman, C. L. Müller, and I. F. Sbalzarini, "Learning physically consistent differential equation models from data using group sparsity", *Phys. Rev. E* **103**, 042310 (2021).

[215]R. Supekar, B. Song, A. Hastewell, G. P. T. Choi, A. Mietke, and J. Dunkel, "Learning hydrodynamic equations for active matter from particle simulations and experiments", *Proc. Natl. Acad. Sci.* **120**, 10.1073/pnas.2206994120 (2023).

[216]M. Golden, R. O. Grigoriev, J. Nambisan, and A. Fernandez-Nieves, "Physically informed data-driven modeling of active nematics", *Sci. Adv.* **9**, 10.1126/sciadv.abq6120 (2023).

[217]C. Joshi, S. Ray, L. M. Lemma, M. Varghese, G. Sharp, Z. Dogic, A. Baskaran, and M. F. Hagan, "Data-Driven Discovery of Active Nematic Hydrodynamics", *Phys. Rev. Lett.* **129**, 258001 (2022).

[218]M. Nasiri, E. Loran, and B. Liebchen, "Smart active particles learn and transcend bacterial foraging strategies", *Proc. Natl. Acad. Sci.* **121**, e2317618121 (2024).

[219]N. M. Boffi and E. Vanden-Eijnden, "Deep learning probability flows and entropy production rates in active matter", *Proc. Natl. Acad. Sci.* **121**, e2318106121 (2024).

[220]C. Dai and S. C. Glotzer, "Efficient Phase Diagram Sampling by Active Learning", *J. Phys. Chem. B* **124**, 1275 (2020).

[221]A. R. Dulaney and J. F. Brady, "Machine learning for phase behavior in active matter systems", *Soft Matter* **17**, 6808 (2021).

[222]T. Xue, X. Li, X. Chen, L. Chen, and Z. Han, "Machine learning phases in swarming systems", *Mach. Learn. Sci. Technol.* **4**, 015028 (2023).

[223]K. J. Verhey, N. Kaul, and V. Soppina, "Kinesin Assembly and Movement in Cells", *Annu. Rev. Biophys.* **40**, 267 (2011).

[224]I. Santiago, "Nanoscale active matter matters: Challenges and opportunities for self-propelled nanomotors", *Nano Today* **19**, 11 (2018).

[225]S. Ghosh, A. Somasundar, and A. Sen, "Enzymes as Active Matter", *Annu. Rev. Condens. Matter Phys.* **12**, 177 (2021).

[226]A. Ghosh and P. Fischer, "Controlled Propulsion of Artificial Magnetic Nanostructured Propellers", *Nano Lett.* **9**, 2243 (2009).

[227]G. Volpe, I. Buttinoni, D. Vogt, H.-J. Kümmerer, and C. Bechinger, "Microswimmers in patterned environments", *Soft Matter* **7**, 8810 (2011).

[228]V. Kantsler, J. Dunkel, M. Polin, and R. E. Goldstein, "Ciliary contact interactions dominate surface scattering of swimming eukaryotes", *Proc. Natl. Acad. Sci.* **110**, 1187 (2013).

[229]C. Scholz, S. D'Silva, and T. Pöschel, "Ratcheting and tumbling motion of Vibrots", *New J. Phys.* **18**, 123001 (2016).

[230]C. Anderson and A. Fernandez-Nieves, "Social interactions lead to motility-induced phase separation in fire ants", *Nat. Commun.* **13**, 6710 (2022).

[231]G. Wang, T. V. Phan, S. Li, M. Wombacher, J. Qu, Y. Peng, G. Chen, D. I. Goldman, S. A. Levin, R. H. Austin, et al., "Emergent Field-Driven Robot Swarm States", *Phys. Rev. Lett.* **126**, 108002 (2021).

[232]K. Drescher, J. Dunkel, L. H. Cisneros, S. Ganguly, and R. E. Goldstein, "Fluid dynamics and noise in bacterial cell-cell and cell-surface scattering", *Proc. Natl. Acad. Sci.* **108**, 10940 (2011).

[233]P. Zhang, S. Jana, M. Giarra, P. Vlachos, and S. Jung, "Paramecia swimming in viscous flow", *Eur. Phys. J. Spec. Top.* **224**, 3199 (2015).

[234]F. Morrison, "Electrophoresis of a particle of arbitrary shape", *J. Colloid Interface Sci.* **34**, 210 (1970).

[235]B. Liebchen and H. Löwen, "Which interactions dominate in active colloids?", *J. Chem. Phys.* **150**, 10.1063/1.5082284 (2019).

[236]E. Lauga and T. R. Powers, "The hydrodynamics of swimming microorganisms", *Rep. Prog. Phys.* **72**, 096601 (2009).

[237]M. Heidari, A. Bregulla, S. M. Landin, F. Cichos, and R. von Klitzing, "Self-Propulsion of Janus Particles near a Brush-Functionalized Substrate", *Langmuir* **36**, 7775 (2020).

[238]R. Niu and T. Palberg, "Modular approach to microswimming", *Soft Matter* **14**, 7554 (2018).

[239]B. Liebchen, R. Niu, T. Palberg, and H. Löwen, "Unraveling modular microswimmers: From self-assembly to ion-exchange-driven motors", *Phys. Rev. E* **98**, 052610 (2018).

[240]M. Manjare, F. Yang, R. Qiao, and Y. Zhao, "Marangoni Flow Induced Collective Motion of Catalytic Micromotors", *J. Phys. Chem. C* **119**, 28361 (2015).

[241]M. Schmitt and H. Stark, "Marangoni flow at droplet interfaces: Three-dimensional solution and applications", *Phys. Fluids* **28**, 10.1063/1.4939212 (2016).

[242]A. Domínguez, P. Malgaretti, M. Popescu, and S. Dietrich, "Effective Interaction between Active Colloids and Fluid Interfaces Induced by Marangoni Flows", *Phys. Rev. Lett.* **116**, 078301 (2016).

[243]D. Crowdy, "Collective viscous propulsion of a two-dimensional flotilla of Marangoni boats", *Phys. Rev. Fluids* **5**, 124004 (2020).

[244]M. Wittmann, M. N. Popescu, A. Domínguez, and J. Simmchen, "Active spheres induce Marangoni flows that drive collective dynamics", *Eur. Phys. J. E* **44**, 15 (2021).

[245]S. Thutupalli, R. Seemann, and S. Herminghaus, "Swarming behavior of simple model squirmers", *New J. Phys.* **13**, 073021 (2011).

[246]A. Domínguez and M. N. Popescu, "Phase coexistence in a monolayer of active particles induced by Marangoni flows", *Soft Matter* **14**, 8017 (2018).

[247]P. Langevin, "Sur la théorie du mouvement brownien", *C. R. Acad. Sci.* **146**, 530 (1908).

[248]D. S. Lemons and A. Gythiel, "Paul Langevin's 1908 paper "On the Theory of Brownian Motion" ["Sur la théorie du mouvement brownien," C. R. Acad. Sci. (Paris) 146 , 530–533 (1908)]", *Am. J. Phys.* **65**, 1079 (1997).

[249]P Romanczuk, M. Bär, W Ebeling, B Lindner, and L. Schimansky-Geier, "Active Brownian particles", *Eur. Phys. J. Spec. Top.* **202**, 1 (2012).

[250]P. Digregorio, D. Levis, L. F. Cugliandolo, G. Gonnella, and I. Pagonabarraga, "Unified analysis of topological defects in 2D systems of active and passive disks", *Soft Matter* **18**, 566 (2022).

[251]A. K. Omar, K. Klymko, T. GrandPre, and P. L. Geissler, "Phase Diagram of Active Brownian Spheres: Crystallization and the Metastability of Motility-Induced Phase Separation", *Phys. Rev. Lett.* **126**, 188002 (2021).

[252]S. S. Khali, F. Peruani, and D. Chaudhuri, "When an active bath behaves as an equilibrium one", *Phys. Rev. E* **109**, 024120 (2024).

[253]B ten Hagen, S van Teeffelen, and H. Löwen, "Brownian motion of a self-propelled particle", *J. Phys. Condens. Matter* **23**, 194119 (2011).

[254]S. Plimpton, "Fast Parallel Algorithms for Short-Range Molecular Dynamics", *J. Comput. Phys.* **117**, 1 (1995).

[255]A. P. Thompson, H. M. Aktulga, R. Berger, D. S. Bolintineanu, W. M. Brown, P. S. Crozier, P. J. in 't Veld, A. Kohlmeyer, S. G. Moore, T. D. Nguyen, et al., "LAMMPS - a flexible simulation tool for particle-based materials modeling at the atomic, meso, and continuum scales", *Comput. Phys. Commun.* **271**, 108171 (2022).

[256]J. D. Weeks, D. Chandler, and H. C. Andersen, "Role of Repulsive Forces in Determining the Equilibrium Structure of Simple Liquids", *J. Chem. Phys.* **54**, 5237 (1971).

[257]H. C. Berg and D. A. Brown, "Chemotaxis in Escherichia coli analysed by Three-dimensional Tracking", *Nature* **239**, 500 (1972).

[258]H. C. Berg, "Bacterial behaviour", *Nature* **254**, 389 (1975).

[259]J. Tailleur and M. E. Cates, "Statistical Mechanics of Interacting Run-and-Tumble Bacteria", *Phys. Rev. Lett.* **100**, 218103 (2008).

[260]A. P. Solon, M. E. Cates, and J. Tailleur, "Active brownian particles and run-and-tumble particles: A comparative study", *Eur. Phys. J. Spec. Top.* **224**, 1231 (2015).

[261]M. Khatami, K. Wolff, O. Pohl, M. R. Ejtehadi, and H. Stark, "Active Brownian particles and run-and-tumble particles separate inside a maze", *Sci. Rep.* **6**, 37670 (2016).

[262]S. M. Block, J. E. Segall, and H. C. Berg, "Adaptation kinetics in bacterial chemotaxis", *J. Bacteriol.* **154**, 312 (1983).

[263]T. F. F. Farage, P. Krinninger, and J. M. Brader, "Effective interactions in active Brownian suspensions", *Phys. Rev. E* **91**, 042310 (2015).

[264]É. Fodor, C. Nardini, M. E. Cates, J. Tailleur, P. Visco, and F. van Wijland, "How Far from Equilibrium Is Active Matter?", *Phys. Rev. Lett.* **117**, 038103 (2016).

[265]L. L. Bonilla, "Active Ornstein-Uhlenbeck particles", *Phys. Rev. E* **100**, 022601 (2019).

[266]D. Martin, J. O'Byrne, M. E. Cates, É. Fodor, C. Nardini, J. Tailleur, and F. van Wijland, "Statistical mechanics of active Ornstein-Uhlenbeck particles", *Phys. Rev. E* **103**, 032607 (2021).

[267]L. Caprini, A. R. Sprenger, H. Löwen, and R. Wittmann, "The parental active model: A unifying stochastic description of self-propulsion", *J. Chem. Phys.* **156**, 071102 (2022).

[268]L. Caprini, U. M. B. Marconi, A. Puglisi, and A. Vulpiani, "The entropy production of Ornstein–Uhlenbeck active particles: a path integral method for correlations", *J. Stat. Mech. Theory Exp.* **2019**, 053203 (2019).

[269]H. Löwen, "Chirality in microswimmer motion: From circle swimmers to active turbulence", *Eur. Phys. J. Spec. Top.* **225**, 2319 (2016).

[270]S. van Teeffelen and H. Löwen, "Dynamics of a Brownian circle swimmer", *Phys. Rev. E* **78**, 020101 (2008).

[271]M. Mijalkov and G. Volpe, "Sorting of chiral microswimmers", *Soft Matter* **9**, 6376 (2013).

[272]Z.-F. Huang, A. M. Menzel, and H. Löwen, "Dynamical Crystallites of Active Chiral Particles", *Phys. Rev. Lett.* **125**, 218002 (2020).

[273]R. J. Hernández, F. J. Sevilla, A. Mazzulla, P. Pagliusi, N. Pellizzi, and G. Cipparrone, "Collective motion of chiral Brownian particles controlled by a circularly-polarized laser beam", *Soft Matter* **16**, 7704 (2020).

[274]J. Bickmann, S. Bröker, J. Jeggle, and R. Wittkowski, "Analytical approach to chiral active systems: Suppressed phase separation of interacting Brownian circle swimmers", *J. Chem. Phys.* **156**, 10.1063/5.0085122 (2022).

[275]E. Lauga, W. R. DiLuzio, G. M. Whitesides, and H. A. Stone, "Swimming in Circles: Motion of Bacteria near Solid Boundaries", *Biophys. J.* **90**, 400 (2006).

[276]R. Di Leonardo, D. Dell'Arciprete, L. Angelani, and V. Iebba, "Swimming with an Image", *Phys. Rev. Lett.* **106**, 038101 (2011).

[277]T.-W. Su, I. Choi, J. Feng, K. Huang, E. McLeod, and A. Ozcan, "Sperm Trajectories Form Chiral Ribbons", *Sci. Rep.* **3**, 1664 (2013).

[278]J. Elgeti, U. B. Kaupp, and G. Gompper, "Hydrodynamics of Sperm Cells near Surfaces", *Biophys. J.* **99**, 1018 (2010).

[279]F. Kümmel, B. ten Hagen, R. Wittkowski, I. Buttinoni, R. Eichhorn, G. Volpe, H. Löwen, and C. Bechinger, "Circular Motion of Asymmetric Self-Propelling Particles", *Phys. Rev. Lett.* **110**, 198302 (2013).

[280]Y. Shelke, N. R. Srinivasan, S. P. Thampi, and E. Mani, "Transition from Linear to Circular Motion in Active Spherical-Cap Colloids", *Langmuir* **35**, 4718 (2019).

[281]B. Zhang, A. Sokolov, and A. Snezhko, "Reconfigurable emergent patterns in active chiral fluids", *Nat. Commun.* **11**, 4401 (2020).

[282]T. Vicsek, A. Czirók, E. Ben-Jacob, I. Cohen, and O. Shochet, "Novel Type of Phase Transition in a System of Self-Driven Particles", *Phys. Rev. Lett.* **75**, 1226 (1995).

[283]F. Ginelli, "The Physics of the Vicsek model", *Eur. Phys. J. Spec. Top.* **225**, 2099 (2016).

[284]F. Peruani, A. Deutsch, and M. Bär, "A mean-field theory for self-propelled particles interacting by velocity alignment mechanisms", *Eur. Phys. J. Spec. Top.* **157**, 111 (2008).

[285]O. Chepizhko and F. Peruani, "Diffusion, Subdiffusion, and Trapping of Active Particles in Heterogeneous Media", *Phys. Rev. Lett.* **111**, 160604 (2013).

[286]A. Ahmadi, T. B. Liverpool, and M. C. Marchetti, "Nematic and polar order in active filament solutions", *Phys. Rev. E* **72**, 060901 (2005).

[287]A. Ahmadi, M. C. Marchetti, and T. B. Liverpool, "Hydrodynamics of isotropic and liquid crystalline active polymer solutions", *Phys. Rev. E* **74**, 061913 (2006).

[288]H. Chaté, F. Ginelli, and R. Montagne, "Simple Model for Active Nematics: Quasi-Long-Range Order and Giant Fluctuations", *Phys. Rev. Lett.* **96**, 180602 (2006).

[289]Y. Lanoiselée, G. Briand, O. Dauchot, and D. S. Grebenkov, "Statistical analysis of random trajectories of vibrated disks: Towards a macroscopic realization of Brownian motion", *Phys. Rev. E* **98**, 062112 (2018).

[290]L. Walsh, C. G. Wagner, S. Schlossberg, C. Olson, A. Baskaran, and N. Menon, "Noise and diffusion of a vibrated self-propelled granular particle", *Soft Matter* **13**, 8964 (2017).

[291] C. B. Caporusso, P. Digregorio, D. Levis, L. F. Cugliandolo, and G. Gonnella, "Motility-Induced Microphase and Macrophase Separation in a Two-Dimensional Active Brownian Particle System", *Phys. Rev. Lett.* **125**, 178004 (2020).

[292] J. Stenhammar, A. Tiribocchi, R. J. Allen, D. Marenduzzo, and M. E. Cates, "Continuum Theory of Phase Separation Kinetics for Active Brownian Particles", *Phys. Rev. Lett.* **111**, 145702 (2013).

[293] J. Stenhammar, D. Marenduzzo, R. J. Allen, and M. E. Cates, "Phase behaviour of active Brownian particles: the role of dimensionality", *Soft Matter* **10**, 1489 (2014).

[294] B. Liebchen, D. Marenduzzo, and M. E. Cates, "Phoretic Interactions Generically Induce Dynamic Clusters and Wave Patterns in Active Colloids", *Phys. Rev. Lett.* **118**, 268001 (2017).

[295] S. Saha, R. Golestanian, and S. Ramaswamy, "Clusters, asters, and collective oscillations in chemotactic colloids", *Phys. Rev. E* **89**, 062316 (2014).

[296] O. Pohl and H. Stark, "Dynamic Clustering and Chemotactic Collapse of Self-Phoretic Active Particles", *Phys. Rev. Lett.* **112**, 238303 (2014).

[297] E. Kanso and S. Michelin, "Phoretic and hydrodynamic interactions of weakly confined autophoretic particles", *J. Chem. Phys.* **150**, 10.1063/1.5065656 (2019).

[298] P. C. Hohenberg and B. I. Halperin, "Theory of dynamic critical phenomena", *Rev. Mod. Phys.* **49**, 435 (1977).

[299] R. Wittkowski, A. Tiribocchi, J. Stenhammar, R. J. Allen, D. Marenduzzo, and M. E. Cates, "Scalar ϕ4 field theory for active-particle phase separation", *Nat. Commun.* **5**, 4351 (2014).

[300] E. Tjhung, C. Nardini, and M. E. Cates, "Cluster Phases and Bubbly Phase Separation in Active Fluids: Reversal of the Ostwald Process", *Phys. Rev. X* **8**, 031080 (2018).

[301] J. Bialké, H. Löwen, and T. Speck, "Microscopic theory for the phase separation of self-propelled repulsive disks", *Europhys. Lett.* **103**, 30008 (2013).

[302] H. Risken, *The Fokker-Planck Equation*, Springer Series in Synergetics (Springer, Berlin, Heidelberg, 1984).

[303] J.-P. Hansen and I. R. McDonald, *Theory of Simple Liquids*, 3rd (Elsevier, Burlington, 2006).

[304] E. Bertin, M. Droz, and G. Grégoire, "Hydrodynamic equations for self-propelled particles: microscopic derivation and stability analysis", *J. Phys. A Math. Theor.* **42**, 445001 (2009).

[305] D. S. Dean, "Langevin equation for the density of a system of interacting Langevin processes", *J. Phys. A. Math. Gen.* **29**, L613 (1996).

[306] E. Bertin, H. Chaté, F. Ginelli, S. Mishra, A. Peshkov, and S. Ramaswamy, "Mesoscopic theory for fluctuating active nematics", *New J. Phys.* **15**, 085032 (2013).

[307] C. W. Gardiner, *Stochastic Methods*, 4th ed. (Springer, Berlin, Heidelberg, 2009).

[308] S. Chibbaro and J. P. Minier, *Stochastic Methods in Fluid Mechanics*, edited by S. Chibbaro and J. P. Minier, Vol. 548, CISM International Centre for Mechanical Sciences (Springer, Vienna, 2014).

[309] T. Ihle, "Kinetic theory of flocking: Derivation of hydrodynamic equations", *Phys. Rev. E* **83**, 030901 (2011).

[310] T. Ihle, "Chapman–Enskog expansion for multi-particle collision models", *Phys. Chem. Chem. Phys.* **11**, 9667 (2009).

[311] G. Wolschin, *Hydrodynamik* (Springer, Berlin, Heidelberg, 2016).

[312] E. M. Purcell, "Life at low Reynolds number", *Am. J. Phys.* **45**, 3 (1977).

[313]T. Qiu, T.-C. Lee, A. G. Mark, K. I. Morozov, R. Münster, O. Mierka, S. Turek, A. M. Leshansky, and P. Fischer, "Swimming by reciprocal motion at low Reynolds number", *Nat. Commun.* **5**, 5119 (2014).

[314]N. R. Fuller, *How Escherichia coli Move*, https://www.nsf.gov/news/mmg/media/images/ecoli_h1.jpg, (accessed 2020-12-08).

[315]L. Howard, *Green algae Chlamydomonas reinhardtii (Image 3)*, https://www.nsf.gov/news/mmg/media/images/PF3393_03_h.jpg, (accessed 2020-12-08).

[316]R. Golestanian and A. Ajdari, "Analytic results for the three-sphere swimmer at low Reynolds number", *Phys. Rev. E* **77**, 036308 (2008).

[317]F. Alouges, A. DeSimone, and A. Lefebvre, "Optimal strokes for axisymmetric microswimmers", *Eur. Phys. J. E* **28**, 279 (2009).

[318]B. Nasouri, A. Vilfan, and R. Golestanian, "Efficiency limits of the three-sphere swimmer", *Phys. Rev. Fluids* **4**, 073101 (2019).

[319]A. Daddi-Moussa-Ider, M. Lisicki, C. Hoell, and H. Löwen, "Swimming trajectories of a three-sphere microswimmer near a wall", *J. Chem. Phys.* **148**, 10.1063/1.5021027 (2018).

[320]A. Daddi-Moussa-Ider, M. Lisicki, A. J. T. M. Mathijssen, C. Hoell, S. Goh, J. Bławzdziewicz, A. M. Menzel, and H. Löwen, "State diagram of a three-sphere microswimmer in a channel", *J. Phys. Condens. Matter* **30**, 254004 (2018).

[321]Q. Wang and H. G. Othmer, "Analysis of a model microswimmer with applications to blebbing cells and mini-robots", *J. Math. Biol.* **76**, 1699 (2018).

[322]O. Silverberg, E. Demir, G. Mishler, B. Hosoume, N. Trivedi, C. Tisch, D. Plascencia, O. S. Pak, and I. E. Araci, "Realization of a push-me-pull-you swimmer at low Reynolds numbers", *Bioinspir. Biomim.* **15**, 064001 (2020).

[323]J. M. Yeomans, "The hydrodynamics of active systems", *Riv. Nuovo Cim.* **40**, 1 (2017).

[324]M. D. Graham, *Microhydrodynamics, Brownian Motion, and Complex Fluids* (Cambridge University Press, Cambridge, 2018).

[325]S. Kim and S. J. Karrila, *Microhydrodynamics* (Elsevier, 1991).

[326]J. S. Guasto, K. A. Johnson, and J. P. Gollub, "Oscillatory Flows Induced by Microorganisms Swimming in Two Dimensions", *Phys. Rev. Lett.* **105**, 168102 (2010).

[327]D. Saintillan and M. J. Shelley, "Emergence of coherent structures and large-scale flows in motile suspensions", *J. R. Soc. Interface* **9**, 571 (2012).

[328]S. Babel, H. Löwen, and A. M. Menzel, "Dynamics of a linear magnetic "microswimmer molecule"", *Europhys. Lett.* **113**, 58003 (2016).

[329]R. W. Nash, R. Adhikari, J. Tailleur, and M. E. Cates, "Run-and-Tumble Particles with Hydrodynamics: Sedimentation, Trapping, and Upstream Swimming", *Phys. Rev. Lett.* **104**, 258101 (2010).

[330]S. E. Spagnolie and E. Lauga, "Hydrodynamics of self-propulsion near a boundary: predictions and accuracy of far-field approximations", *J. Fluid Mech.* **700**, 105 (2012).

[331]R. W. Nash, R. Adhikari, and M. E. Cates, "Singular forces and pointlike colloids in lattice Boltzmann hydrodynamics", *Phys. Rev. E* **77**, 026709 (2008).

[332]M. T. Downton and H. Stark, "Simulation of a model microswimmer", *J. Phys. Condens. Matter* **21**, 204101 (2009).

[333]I. O. Götze and G. Gompper, "Mesoscale simulations of hydrodynamic squirmer interactions", *Phys. Rev. E* **82**, 041921 (2010).

[334]K. Ishimoto and E. A. Gaffney, "Squirmer dynamics near a boundary", *Phys. Rev. E* **88**, 062702 (2013).

[335]A. Zöttl and H. Stark, "Hydrodynamics Determines Collective Motion and Phase Behavior of Active Colloids in Quasi-Two-Dimensional Confinement", *Phys. Rev. Lett.* **112**, 118101 (2014).

[336]J.-T. Kuhr, J. Blaschke, F. Rühle, and H. Stark, "Collective sedimentation of squirmers under gravity", *Soft Matter* **13**, 7548 (2017).

[337]A. Zöttl and H. Stark, "Simulating squirmers with multiparticle collision dynamics", *Eur. Phys. J. E* **41**, 61 (2018).

[338]M. Kuron, P. Stärk, C. Burkard, J. de Graaf, and C. Holm, "A lattice Boltzmann model for squirmers", *J. Chem. Phys.* **150**, 144110 (2019).

[339]K. Qi, E. Westphal, G. Gompper, and R. G. Winkler, "Enhanced Rotational Motion of Spherical Squirmer in Polymer Solutions", *Phys. Rev. Lett.* **124**, 068001 (2020).

[340]A. W. Zantop and H. Stark, "Squirmer rods as elongated microswimmers: flow fields and confinement", *Soft Matter* **16**, 6400 (2020).

[341]M. N. Popescu, W. E. Uspal, Z. Eskandari, M. Tasinkevych, and S. Dietrich, "Effective squirmer models for self-phoretic chemically active spherical colloids", *Eur. Phys. J. E* **41**, 145 (2018).

[342]M. Kuron, P. Stärk, C. Holm, and J. de Graaf, "Hydrodynamic mobility reversal of squirmers near flat and curved surfaces", *Soft Matter* **15**, 5908 (2019).

[343]I. Llopis and I. Pagonabarraga, "Hydrodynamic interactions in squirmer motion: Swimming with a neighbour and close to a wall", *J. Nonnewton. Fluid Mech.* **165**, 946 (2010).

[344]I. Pagonabarraga, "Lattice Boltzmann Modeling of Complex Fluids: Colloidal Suspensions and Fluid Mixtures", in *Novel Methods in Soft Matter Simulations*, edited by M. Karttunen, A. Lukkarinen, and I. Vattulainen (Springer, Berlin, Heidelberg, 2004), p. 279.

[345]T. Krüger, H. Kusumaatmaja, A. Kuzmin, O. Shardt, G. Silva, and E. M. Viggen, *The Lattice Boltzmann Method*, Graduate Texts in Physics (Springer International Publishing, Cham, 2017).

[346]L. N. Carenza, G. Gonnella, A. Lamura, G. Negro, and A. Tiribocchi, "Lattice Boltzmann methods and active fluids", *Eur. Phys. J. E* **42**, 81 (2019).

[347]J.-C. Desplat, I. Pagonabarraga, and P. Bladon, "LUDWIG: A parallel Lattice-Boltzmann code for complex fluids", *Comput. Phys. Commun.* **134**, 273 (2001).

[348]S. Ramachandran, P. B. Sunil Kumar, and I. Pagonabarraga, "A Lattice-Boltzmann model for suspensions of self-propelling colloidal particles", *Eur. Phys. J. E* **20**, 151 (2006).

[349]M. E. Cates, K Stratford, R Adhikari, P Stansell, J.-C. Desplat, I Pagonabarraga, and A. J. Wagner, "Simulating colloid hydrodynamics with lattice Boltzmann methods", *J. Phys. Condens. Matter* **16**, S3903 (2004).

[350]G. M. Kremer, *An Introduction to the Boltzmann Equation and Transport Processes in Gases*, Interaction of Mechanics and Mathematics (Springer, Berlin, Heidelberg, 2010).

[351]P. L. Bhatnagar, E. P. Gross, and M. Krook, "A Model for Collision Processes in Gases. I. Small Amplitude Processes in Charged and Neutral One-Component Systems", *Phys. Rev.* **94**, 511 (1954).

[352]G. Gompper, T. Ihle, D. M. Kroll, and R. G. Winkler, "Multi-Particle Collision Dynamics: A Particle-Based Mesoscale Simulation Approach to the Hydrodynamics of Complex Fluids", in *Advanced Computer Simulation Approaches for Soft Matter Sciences III*, edited by C. Holm and K. Kremer (Springer Berlin Heidelberg, Berlin, Heidelberg, 2009), p. 1.

[353]A. Malevanets and R. Kapral, "Mesoscopic Multi-particle Collision Model for Fluid Flow and Molecular Dynamics", in *Novel Methods in Soft Matter Simulations*, edited by M. Karttunen, A. Lukkarinen, and I. Vattulainen (Springer, Berlin, Heidelberg, 2004), p. 116.

[354]J. Ruiz-Franco, D. Jaramillo-Cano, M. Camargo, C. N. Likos, and E. Zaccarelli, "Multi-particle collision dynamics for a coarse-grained model of soft colloids", *J. Chem. Phys.* **151**, 074902 (2019).

[355]R. G. Winkler, M. Ripoll, K. Mussawisade, and G. Gompper, "Simulation of complex fluids by multi-particle-collision dynamics", *Comput. Phys. Commun.* **169**, 326 (2005).

[356]R. G. Winkler, K. Mussawisade, M. Ripoll, and G. Gompper, "Rod-like colloids and polymers in shear flow: a multi-particle-collision dynamics study", *J. Phys. Condens. Matter* **16**, S3941 (2004).

[357]M. Ripoll, K. Mussawisade, R. G. Winkler, and G. Gompper, "Low-Reynolds-number hydrodynamics of complex fluids by multi-particle-collision dynamics", *Europhys. Lett.* **68**, 106 (2004).

[358]A Lamura, G Gompper, T Ihle, and D. M Kroll, "Multi-particle collision dynamics: Flow around a circular and a square cylinder", *Europhys. Lett.* **56**, 319 (2001).

[359]A. Zöttl, "Simulation of microswimmer hydrodynamics with multiparticle collision dynamics", *Chinese Phys. B* **29**, 074701 (2020).

[360]M.-J. Huang, J. Schofield, and R. Kapral, "Chemotactic and hydrodynamic effects on collective dynamics of self-diffusiophoretic Janus motors", *New J. Phys.* **19**, 125003 (2017).

[361]P. de Buyl and R. Kapral, "Phoretic self-propulsion: a mesoscopic description of reaction dynamics that powers motion", *Nanoscale* **5**, 1337 (2013).

[362]S. Thakur and R. Kapral, "Dynamics of self-propelled nanomotors in chemically active media", *J. Chem. Phys.* **135**, 024509 (2011).

[363]D. A. Fedosov, A. Sengupta, and G. Gompper, "Effect of fluid–colloid interactions on the mobility of a thermophoretic microswimmer in non-ideal fluids", *Soft Matter* **11**, 6703 (2015).

[364]P. J Hoogerbrugge and J. M. V. A Koelman, "Simulating Microscopic Hydrodynamic Phenomena with Dissipative Particle Dynamics", *Europhys. Lett.* **19**, 155 (1992).

[365]R. D. Groot and P. B. Warren, "Dissipative particle dynamics: Bridging the gap between atomistic and mesoscopic simulation", *J. Chem. Phys.* **107**, 4423 (1997).

[366]A. Panchenko, D. F. Hinz, and E. Fried, "Spatial averaging of a dissipative particle dynamics model for active suspensions", *Phys. Fluids* **30**, 033301 (2018).

[367]S. Eloul, W. C. K. Poon, O. Farago, and D. Frenkel, "Reactive Momentum Transfer Contributes to the Self-Propulsion of Janus Particles", *Phys. Rev. Lett.* **124**, 188001 (2020).

[368]K. Tokunaga and R. Akiyama, "Molecular dynamics study of a solvation motor in a Lennard-Jones solvent", *Phys. Rev. E* **100**, 062608 (2019).

[369]S. Heidenreich, J. Dunkel, S. H. L. Klapp, and M. Bär, "Hydrodynamic length-scale selection in microswimmer suspensions", *Phys. Rev. E* **94**, 020601 (2016).

[370]D. Saintillan and M. J. Shelley, "Active suspensions and their nonlinear models", *C. R. Phys.* **14**, 497 (2013).

[371]J. Stenhammar, C. Nardini, R. W. Nash, D. Marenduzzo, and A. Morozov, "Role of Correlations in the Collective Behavior of Microswimmer Suspensions", *Phys. Rev. Lett.* **119**, 028005 (2017).

[372]H. H. Wensink, J. Dunkel, S. Heidenreich, K. Drescher, R. E. Goldstein, H. Löwen, and J. M. Yeomans, "Meso-scale turbulence in living fluids", *Proc. Natl. Acad. Sci.* **109**, 14308 (2012).

[373]Z. Hao, S. Mayya, G. Notomista, S. Hutchinson, M. Egerstedt, and A. Ansari, "Controlling Collision-Induced Aggregations in a Swarm of Micro Bristle Robots", *IEEE Trans. Robot.* **39**, 590 (2022).

[374]T. Speck, J. Bialké, A. M. Menzel, and H. Löwen, "Effective Cahn-Hilliard Equation for the Phase Separation of Active Brownian Particles", *Phys. Rev. Lett.* **112**, 218304 (2014).

[375]C. R. Harris, K. J. Millman, S. J. van der Walt, R. Gommers, P. Virtanen, D. Cournapeau, E. Wieser, J. Taylor, S. Berg, N. J. Smith, et al., "Array programming with NumPy", *Nature* **585**, 357 (2020).

[376]S. van der Walt, S. C. Colbert, and G. Varoquaux, "The NumPy Array: A Structure for Efficient Numerical Computation", *Comput. Sci. Eng.* **13**, 22 (2011).

[377]P. Virtanen, R. Gommers, T. E. Oliphant, M. Haberland, T. Reddy, D. Cournapeau, E. Burovski, P. Peterson, W. Weckesser, J. Bright, et al., "SciPy 1.0: fundamental algorithms for scientific computing in Python", *Nat. Methods* **17**, 261 (2020).

[378]J. D. Hunter, "Matplotlib: A 2D Graphics Environment", *Comput. Sci. Eng.* **9**, 90 (2007).

[379]S. van der Walt, J. L. Schönberger, J. Nunez-Iglesias, F. Boulogne, J. D. Warner, N. Yager, E. Gouillart, and T. Yu, "scikit-image: image processing in Python", *PeerJ* **2**, e453 (2014).

[380]L. Hecht, K.-R. Dormann, K. L. Spanheimer, M. Ebrahimi, M. Cordts, S. Mandal, A. K. Mukhopadhyay, and B. Liebchen, "AMEP: The Active Matter Evaluation Package for Python", *arXiv:2404.16533 [cond-mat.soft]* (2024).

[381]M. Karplus and J. A. McCammon, "Molecular dynamics simulations of biomolecules", *Nat. Struct. Biol.* **9**, 646 (2002).

[382]I. Kumari, P. Sandhu, M. Ahmed, and Y. Akhter, "Molecular Dynamics Simulations, Challenges and Opportunities: A Biologist's Prospective", *Curr. Protein Pept. Sci.* **18**, 1163 (2017).

[383]P. R. L. Markwick and J. A. McCammon, "Studying functional dynamics in bio-molecules using accelerated molecular dynamics", *Phys. Chem. Chem. Phys.* **13**, 20053 (2011).

[384]S. Mogurampelly, O. Borodin, and V. Ganesan, "Computer Simulations of Ion Transport in Polymer Electrolyte Membranes", *Annu. Rev. Chem. Biomol. Eng.* **7**, 349 (2016).

[385]N. Yao, X. Chen, Z.-H. Fu, and Q. Zhang, "Applying Classical, Ab Initio , and Machine-Learning Molecular Dynamics Simulations to the Liquid Electrolyte for Rechargeable Batteries", *Chem. Rev.* **122**, 10970 (2022).

[386]J. B. Haskins, W. R. Bennett, J. J. Wu, D. M. Hernández, O. Borodin, J. D. Monk, C. W. Bauschlicher, and J. W. Lawson, "Computational and Experimental Investigation of Li-Doped Ionic Liquid Electrolytes: [pyr14][TFSI], [pyr13][FSI], and [EMIM][BF_4]", *J. Phys. Chem. B* **118**, 11295 (2014).

[387]M. R. Wilson, "Progress in computer simulations of liquid crystals", *Int. Rev. Phys. Chem.* **24**, 421 (2005).

[388]Y. Huang, W. Wang, J. K. Whitmer, and R. Zhang, "Structures, thermodynamics and dynamics of topological defects in Gay–Berne nematic liquid crystals", *Soft Matter* **19**, 483 (2023).

[389]G. Watanabe, A. Yamazaki, and J. Yoshida, "The Missing Relationship between the Miscibility of Chiral Dopants and the Microscopic Dynamics of Solvent Liquid Crystals: A Molecular Dynamics Study", *Symmetry* **15**, 1092 (2023).

[390]R. Horstmann, L. Hecht, S. Kloth, and M. Vogel, "Structural and Dynamical Properties of Liquids in Confinements: A Review of Molecular Dynamics Simulation Studies", *Langmuir* **38**, 6506 (2022).

[391]T. Pal, C. Beck, D. Lessnich, and M. Vogel, “Effects of Silica Surfaces on the Structure and Dynamics of Room-Temperature Ionic Liquids: A Molecular Dynamics Simulation Study”, *J. Phys. Chem. C* **122**, 624 (2018).

[392]S. Mandal, S. Lang, M. Gross, M. Oettel, D. Raabe, T. Franosch, and F. Varnik, “Multiple reentrant glass transitions in confined hard-sphere glasses”, *Nat. Commun.* **5**, 4435 (2014).

[393]S. Mandal and T. Franosch, “Diverging Time Scale in the Dimensional Crossover for Liquids in Strong Confinement”, *Phys. Rev. Lett.* **118**, 065901 (2017).

[394]F. Guarra and G. Colombo, “Computational Methods in Immunology and Vaccinology: Design and Development of Antibodies and Immunogens”, *J. Chem. Theory Comput.* **19**, 5315 (2023).

[395]S. Rafi, S. Yasmin, and R. Uddin, “A molecular dynamic simulation approach: development of dengue virus vaccine by affinity improvement techniques”, *J. Biomol. Struct. Dyn.* **40**, 61 (2022).

[396]A. Smith, X. Dong, and V. Raghavan, “An Overview of Molecular Dynamics Simulation for Food Products and Processes”, *Processes* **10**, 119 (2022).

[397]G. De Magistris and D. Marenduzzo, “An introduction to the physics of active matter”, *Physica A* **418**, 65 (2015).

[398]S. De Karmakar and R. Ganesh, “Motility-induced phase separation of self-propelled soft inertial disks”, *Soft Matter* **18**, 7301 (2022).

[399]J. Su, M. Feng, Y. Du, H. Jiang, and Z. Hou, “Motility-induced phase separation is reentrant”, *Commun. Phys.* **6**, 58 (2023).

[400]G. S. Redner, C. G. Wagner, A. Baskaran, and M. F. Hagan, “Classical Nucleation Theory Description of Active Colloid Assembly”, *Phys. Rev. Lett.* **117**, 148002 (2016).

[401]S. C. Takatori and J. F. Brady, “Towards a thermodynamics of active matter”, *Phys. Rev. E* **91**, 032117 (2015).

[402]M. Rojas-Vega, P. de Castro, and R. Soto, “Mixtures of self-propelled particles interacting with asymmetric obstacles”, *Eur. Phys. J. E* **46**, 95 (2023).

[403]Z. Ma and R. Ni, “Dynamical clustering interrupts motility-induced phase separation in chiral active Brownian particles”, *J. Chem. Phys.* **156**, 10.1063/5.0077389 (2022).

[404]P. Nie, J. Chattoraj, A. Piscitelli, P. Doyle, R. Ni, and M. P. Ciamarra, “Stability phase diagram of active Brownian particles”, *Phys. Rev. Res.* **2**, 023010 (2020).

[405]J. Yang, R. Ni, and M. P. Ciamarra, “Interplay between jamming and motility-induced phase separation in persistent self-propelling particles”, *Phys. Rev. E* **106**, L012601 (2022).

[406]S. Saw, L. Costigliola, and J. C. Dyre, “Configurational temperature in active matter. I. Lines of invariant physics in the phase diagram of the Ornstein-Uhlenbeck model”, *Phys. Rev. E* **107**, 024609 (2023).

[407]M. Sandoval, “Free and enclosed inertial active gas”, *Soft Matter* **19**, 6287 (2023).

[408]P.-C. Chen, K. Kroy, F. Cichos, X. Wang, and V. Holubec, “Active particles with delayed attractions form quaking crystallites”, *Europhys. Lett.* **142**, 67003 (2023).

[409]S. Mishra, A. Baskaran, and M. C. Marchetti, “Fluctuations and pattern formation in self-propelled particles”, *Phys. Rev. E* **81**, 061916 (2010).

[410]H. Zhao, A. Košmrlj, and S. S. Datta, “Chemotactic Motility-Induced Phase Separation”, *Phys. Rev. Lett.* **131**, 118301 (2023).

[411]J. Berx, A. Bose, R. Golestanian, and B. Mahault, “Reentrant condensation transition in a model of driven scalar active matter with diffusivity edge”, *Europhys. Lett.* **142**, 67004 (2023).

[412]C. Hoell, H. Löwen, and A. M. Menzel, "Particle-scale statistical theory for hydrodynamically induced polar ordering in microswimmer suspensions", *J. Chem. Phys.* **149**, 144902 (2018).

[413]C. Hoell, H. Löwen, and A. M. Menzel, "Dynamical density functional theory for circle swimmers", *New J. Phys.* **19**, 125004 (2017).

[414]R. Soto, M. Pinto, and R. Brito, "Kinetic Theory of Motility Induced Phase Separation for Active Brownian Particles", *Phys. Rev. Lett.* **132**, 208301 (2024).

[415]Y. Fily and M. C. Marchetti, "Athermal Phase Separation of Self-Propelled Particles with No Alignment", *Phys. Rev. Lett.* **108**, 235702 (2012).

[416]J. Grauer, H. Löwen, A. Be'er, and B. Liebchen, "Swarm Hunting and Cluster Ejections in Chemically Communicating Active Mixtures", *Sci. Rep.* **10**, 5594 (2020).

[417]X. Jiang, H. Jiang, and Z. Hou, "Nonlinear chemical reaction induced abnormal pattern formation of chemotactic particles", *Soft Matter* **19**, 3946 (2023).

[418]A. Fischer, A. Chatterjee, and T. Speck, "Aggregation and sedimentation of active Brownian particles at constant affinity", *J. Chem. Phys.* **150**, 10.1063/1.5081115 (2019).

[419]E. F. Keller and L. A. Segel, "Model for chemotaxis", *J. Theor. Biol.* **30**, 225 (1971).

[420]A. R. Sprenger, C. Bair, and H. Löwen, "Active Brownian motion with memory delay induced by a viscoelastic medium", *Phys. Rev. E* **105**, 044610 (2022).

[421]E. A. Lisin, O. S. Vaulina, I. I. Lisina, and O. F. Petrov, "Motion of a self-propelled particle with rotational inertia", *Phys. Chem. Chem. Phys.* **24**, 14150 (2022).

[422]J. Reichert and T. Voigtmann, "Tracer dynamics in crowded active-particle suspensions", *Soft Matter* **17**, 10492 (2021).

[423]D. Breoni, M. Schmiedeberg, and H. Löwen, "Active Brownian and inertial particles in disordered environments: Short-time expansion of the mean-square displacement", *Phys. Rev. E* **102**, 062604 (2020).

[424]E. Lemaitre, I. M. Sokolov, R. Metzler, and A. V. Chechkin, "Non-Gaussian displacement distributions in models of heterogeneous active particle dynamics", *New J. Phys.* **25**, 013010 (2023).

[425]T. Debnath, S. Nayak, P. Bag, D. Debnath, and P. K. Ghosh, "Structure and diffusion of active-passive binary mixtures in a single-file", *J. Chem. Sci.* **135**, 38 (2023).

[426]P. Nie, J. Chattoraj, A. Piscitelli, P. Doyle, R. Ni, and M. P. Ciamarra, "Frictional active Brownian particles", *Phys. Rev. E* **102**, 032612 (2020).

[427]H. Wang, F. H. Stillinger, and S. Torquato, "Sensitivity of pair statistics on pair potentials in many-body systems", *J. Chem. Phys.* **153**, 124106 (2020).

[428]E. Gavagnin, J. P. Owen, and C. A. Yates, "Pair correlation functions for identifying spatial correlation in discrete domains", *Phys. Rev. E* **97**, 062104 (2018).

[429]G. Szamel, E. Flenner, and L. Berthier, "Glassy dynamics of athermal self-propelled particles: Computer simulations and a nonequilibrium microscopic theory", *Phys. Rev. E* **91**, 062304 (2015).

[430]S. Bröker, M. te Vrugt, J. Jeggle, J. Stenhammar, and R. Wittkowski, "Pair-distribution function of active Brownian spheres in three spatial dimensions: simulation results and analytical representation", *Soft Matter* **20**, 224 (2024).

[431]S. Ro, B. Guo, A. Shih, T. V. Phan, R. H. Austin, D. Levine, P. M. Chaikin, and S. Martiniani, "Model-Free Measurement of Local Entropy Production and Extractable Work in Active Matter", *Phys. Rev. Lett.* **129**, 220601 (2022).

[432]T. GrandPre, K. Klymko, K. K. Mandadapu, and D. T. Limmer, "Entropy production fluctuations encode collective behavior in active matter", *Phys. Rev. E* **103**, 012613 (2021).

[433]É. Fodor and M. E. Cates, "Active engines: Thermodynamics moves forward", *Europhys. Lett.* **134**, 10003 (2021).

[434]D. Mandal, K. Klymko, and M. R. DeWeese, "Entropy Production and Fluctuation Theorems for Active Matter", *Phys. Rev. Lett.* **119**, 258001 (2017).

[435]Z. Zhang and R. Garcia-Millan, "Entropy production of nonreciprocal interactions", *Phys. Rev. Res.* **5**, L022033 (2023).

[436]L. Dabelow, S. Bo, and R. Eichhorn, "How irreversible are steady-state trajectories of a trapped active particle?", *J. Stat. Mech. Theory Exp.* **2021**, 033216 (2021).

[437]L. F. Cugliandolo, "The effective temperature", *J. Phys. A Math. Theor.* **44**, 483001 (2011).

[438]G. Szamel, "Stochastic thermodynamics for self-propelled particles", *Phys. Rev. E* **100**, 050603(R) (2019).

[439]T. Herpich, K. Shayanfard, and M. Esposito, "Effective thermodynamics of two interacting underdamped Brownian particles", *Phys. Rev. E* **101**, 022116 (2020).

[440]P. Gaspard and R. Kapral, "Active Matter, Microreversibility, and Thermodynamics", *Research* **2020**, 9739231 (2020).

[441]V. Venkatasubramanian, A. Sivaram, and L. Das, "A unified theory of emergent equilibrium phenomena in active and passive matter", *Comput. Chem. Eng.* **164**, 107887 (2022).

[442]F. Dittrich, T. Speck, and P. Virnau, "Critical behavior in active lattice models of motility-induced phase separation", *Eur. Phys. J. E* **44**, 53 (2021).

[443]J. T. Siebert, F. Dittrich, F. Schmid, K. Binder, T. Speck, and P. Virnau, "Critical behavior of active Brownian particles", *Phys. Rev. E* **98**, 030601(R) (2018).

[444]N. Gnan and C. Maggi, "Critical behavior of quorum-sensing active particles", *Soft Matter* **18**, 7654 (2022).

[445]A. Sinha and D. Chaudhuri, "How reciprocity impacts ordering and phase separation in active nematics?", *Soft Matter* **20**, 788 (2024).

[446]X.-q. Shi, G. Fausti, H. Chaté, C. Nardini, and A. Solon, "Self-Organized Critical Coexistence Phase in Repulsive Active Particles", *Phys. Rev. Lett.* **125**, 168001 (2020).

[447]M. Paoluzzi, D. Levis, and I. Pagonabarraga, "From motility-induced phase-separation to glassiness in dense active matter", *Commun. Phys.* **5**, 111 (2022).

[448]L. Caprini, U. M. B. Marconi, C. Maggi, M. Paoluzzi, and A. Puglisi, "Hidden velocity ordering in dense suspensions of self-propelled disks", *Phys. Rev. Res.* **2**, 023321 (2020).

[449]J. U. Klamser, S. C. Kapfer, and W. Krauth, "A kinetic-Monte Carlo perspective on active matter", *J. Chem. Phys.* **150**, 144113 (2019).

[450]D. Rogel Rodriguez, F. Alarcon, R. Martinez, J. Ramírez, and C. Valeriani, "Phase behaviour and dynamical features of a two-dimensional binary mixture of active/passive spherical particles", *Soft Matter* **16**, 1162 (2020).

[451]V. Ramasubramani, B. D. Dice, E. S. Harper, M. P. Spellings, J. A. Anderson, and S. C. Glotzer, "freud: A software suite for high throughput analysis of particle simulation data", *Comput. Phys. Commun.* **254**, 107275 (2020).

[452]R. Gowers, M. Linke, J. Barnoud, T. Reddy, M. Melo, S. Seyler, J. Domański, D. Dotson, S. Buchoux, I. Kenney, et al., "MDAnalysis: A Python Package for the Rapid Analysis of Molecular Dynamics Simulations", in Proceedings of the 15th Python in Science Conference (2016), p. 98.

[453]N. Michaud-Agrawal, E. J. Denning, T. B. Woolf, and O. Beckstein, "MDAnalysis: A toolkit for the analysis of molecular dynamics simulations", *J. Comput. Chem.* **32**, 2319 (2011).

[454]W. Humphrey, A. Dalke, and K. Schulten, "VMD: Visual molecular dynamics", *J. Mol. Graph.* **14**, 33 (1996).

[455]R. T. McGibbon, K. A. Beauchamp, M. P. Harrigan, C. Klein, J. M. Swails, C. X. Hernández, C. R. Schwantes, L.-P. Wang, T. J. Lane, and V. S. Pande, "MDTraj: A Modern Open Library for the Analysis of Molecular Dynamics Trajectories", *Biophys. J.* **109**, 1528 (2015).

[456]A. Stukowski, "Visualization and analysis of atomistic simulation data with OVITO–the Open Visualization Tool", *Model. Simul. Mater. Sci. Eng.* **18**, 015012 (2010).

[457]M. Sega, G. Hantal, B. Fábián, and P. Jedlovszky, "Pytim: A python package for the interfacial analysis of molecular simulations", *J. Comput. Chem.* **39**, 2118 (2018).

[458]T. Romo and A. Grossfield, "LOOS: An extensible platform for the structural analysis of simulations", in 2009 Annual International Conference of the IEEE Engineering in Medicine and Biology Society (2009), p. 2332.

[459]T. D. Romo, N. Leioatts, and A. Grossfield, "Lightweight object oriented structure analysis: Tools for building tools to analyze molecular dynamics simulations", *J. Comput. Chem.* **35**, 2305 (2014).

[460]K. Hinsen, "The molecular modeling toolkit: A new approach to molecular simulations", *J. Comput. Chem.* **21**, 79 (2000).

[461]The HDF Group, *Hierarchical Data Format, version 5*, https://github.com/HDFGroup/hdf5, (accessed 2024-10-09).

[462]A. Collette, *Python and HDF5* (O'Reilly Media, Sebastopol, 2013).

[463]P. de Buyl, P. H. Colberg, and F. Höfling, "H5MD: A structured, efficient, and portable file format for molecular data", *Comput. Phys. Commun.* **185**, 1546 (2014).

[464]W. M. Elhaddad and B. N. Alemdar, "Efficient Management of Big Datasets Using HDF and SQLite: A Comparative Study Based on Building Simulation Data", in Computing in Civil Engineering 2015 (2015), p. 249.

[465]J. Su, Z. Cao, J. Wang, H. Jiang, and Z. Hou, "Dynamical and thermodynamical origins of motility-induced phase separation", *Cell Reports Phys. Sci.* 101817 (2024).

[466]C. W. Stewart and R. van der Ree, "A Voronoi diagram based population model for social species of wildlife", *Ecol. Modell.* **221**, 1554 (2010).

[467]C. Arcelli and G. Sanniti di Baja, "Computing Voronoi diagrams in digital pictures", *Pattern Recognit. Lett.* **4**, 383 (1986).

[468]L. Chen, G. Mukerjee, R. Dorfman, and S. M. Moghadas, "Disease Risk Assessment Using a Voronoi-Based Network Analysis of Genes and Variants Scores", *Front. Genet.* **8**, 10.3389/fgene.2017.00029 (2017).

[469]I. Vavilova, A. Elyiv, D. Dobrycheva, and O. Melnyk, "The Voronoi Tessellation Method in Astronomy", in *Intelligent Astrophysics* (Springer Nature Switzerland, Cham, 2021), p. 57.

[470]H. Hu, X. Liu, and P. Hu, "Voronoi diagram generation on the ellipsoidal earth", *Comput. Geosci.* **73**, 81 (2014).

[471]F. Aurenhammer, "Voronoi diagrams—a survey of a fundamental geometric data structure", *ACM Comput. Surv.* **23**, 345 (1991).

[472]J. Burns, *Centroidal Voronoi Tesselations*, http://www.whitman.edu/Documents/Academics/Mathematics/burns.pdf, (accessed 2024-02-21).

[473]D. R. Nelson, M. Rubinstein, and F. Spaepen, "Order in two-dimensional binary random arrays", *Philos. Mag. A* **46**, 105 (1982).

[474]L. F. Cugliandolo and G. Gonnella, "Phases of active matter in two dimensions", *arXiv:1810.11833 [cond-mat.stat-mech]* (2018).

[475]E. P. Bernard and W. Krauth, "Two-Step Melting in Two Dimensions: First-Order Liquid-Hexatic Transition", *Phys. Rev. Lett.* **107**, 155704 (2011).

[476]V. M. Kendon, M. E. Cates, I. Pagonabarraga, J.-C. Desplat, and P. Bladon, "Inertial effects in three-dimensional spinodal decomposition of a symmetric binary fluid mixture: a lattice Boltzmann study", *J. Fluid Mech.* **440**, 147 (2001).

[477]Y. Zhang, A. Xu, G. Zhang, Y. Gan, Z. Chen, and S. Succi, "Entropy production in thermal phase separation: a kinetic-theory approach", *Soft Matter* **15**, 2245 (2019).

[478]S. Maneewongvatana and D. M. Mount, "Analysis of approximate nearest neighbor searching with clustered point sets", *arXiv:cs/9901013v1 [cs.CG]* (1999).

[479]D. Levis and L. Berthier, "Clustering and heterogeneous dynamics in a kinetic Monte Carlo model of self-propelled hard disks", *Phys. Rev. E* **89**, 062301 (2014).

[480]L. F. Cugliandolo, P. Digregorio, G. Gonnella, and A. Suma, "Phase Coexistence in Two-Dimensional Passive and Active Dumbbell Systems", *Phys. Rev. Lett.* **119**, 268002 (2017).

[481]F. Peruani and M. Bär, "A kinetic model and scaling properties of non-equilibrium clustering of self-propelled particles", *New J. Phys.* **15**, 065009 (2013).

[482]I. Palaia and A. Šarić, "Controlling cluster size in 2D phase-separating binary mixtures with specific interactions", *J. Chem. Phys.* **156**, 194902 (2022).

[483]F. Peruani, L. Schimansky-Geier, and M. Bär, "Cluster dynamics and cluster size distributions in systems of self-propelled particles", *Eur. Phys. J. Spec. Top.* **191**, 173 (2010).

[484]F. Peruani, A. Deutsch, and M. Bär, "Nonequilibrium clustering of self-propelled rods", *Phys. Rev. E* **74**, 030904 (2006).

[485]T. A. Witten and L. M. Sander, "Diffusion-Limited Aggregation, a Kinetic Critical Phenomenon", *Phys. Rev. Lett.* **47**, 1400 (1981).

[486]N. Kyriakopoulos, H. Chaté, and F. Ginelli, "Clustering and anisotropic correlated percolation in polar flocks", *Phys. Rev. E* **100**, 022606 (2019).

[487]M. Sanoria, R. Chelakkot, and A. Nandi, "Percolation transition in phase-separating active fluid", *Phys. Rev. E* **106**, 034605 (2022).

[488]S. Fehlinger and B. Liebchen, "Collective behavior of active molecules: Dynamic clusters, holes, and active fractalytes", *Phys. Rev. Res.* **5**, L032038 (2023).

[489]A. Ghosh, Z. Budrikis, V. Chikkadi, A. L. Sellerio, S. Zapperi, and P. Schall, "Direct Observation of Percolation in the Yielding Transition of Colloidal Glasses", *Phys. Rev. Lett.* **118**, 148001 (2017).

[490]D. Johansen, J. Trewhella, and D. P. Goldenberg, "Fractal dimension of an intrinsically disordered protein: Small-angle X-ray scattering and computational study of the bacteriophage λ N protein", *Protein Sci.* **20**, 1955 (2011).

[491]A. M. Brasil, T. L. Farias, and M. G. Carvalho, "Evaluation of the Fractal Properties of Cluster? Cluster Aggregates", *Aerosol Sci. Technol.* **33**, 440 (2000).

[492]J. M. Tenti, S. N. Hernández Guiance, and I. M. Irurzun, "Fractal dimension of diffusion-limited aggregation clusters grown on spherical surfaces", *Phys. Rev. E* **103**, 012138 (2021).

[493]M. Tokuyama and K. Kawasaki, "Fractal dimensions for diffusion-limited aggregation", *Phys. Lett. A* **100**, 337 (1984).

[494]H. G. E. Hentschel, "Fractal Dimension of Generalized Diffusion-Limited Aggregates", *Phys. Rev. Lett.* **52**, 212 (1984).

[495]M. Paoluzzi, M. Leoni, and M. C. Marchetti, "Fractal aggregation of active particles", *Phys. Rev. E* **98**, 052603 (2018).

[496]L. Bai and D. Breen, "Calculating Center of Mass in an Unbounded 2D Environment", *J. Graph. Tools* **13**, 53 (2008).

[497]A. Bray, "Theory of phase-ordering kinetics", *Adv. Phys.* **43**, 357 (1994).

[498]K. Wu, E. Otoo, and A. Shoshani, "Optimizing connected component labeling algorithms", in Proc. SPIE 5747, Medical Imaging 2005: Image Processing, edited by J. M. Fitzpatrick and J. M. Reinhardt (2005), p. 1965.

[499]C. Fiorio and J. Gustedt, "Two linear time Union-Find strategies for image processing", *Theor. Comput. Sci.* **154**, 165 (1996).

[500]R. Romero-Zaliz and J. Reinoso-Gordo, "An Updated Review on Watershed Algorithms", in *Stud. fuzziness soft comput.* Vol. 358 (Springer Verlag, 2018), p. 235.

[501]L. Hecht, L. Caprini, H. Löwen, and B. Liebchen, "How to define temperature in active systems", *J. Chem. Phys.* **161**, 224904 (2024).

[502]Wikipedia Contributors, *Temperature — Wikipedia, The Free Encyclopedia*, https://en.wikipedia.org/w/index.php?title=Temperature&oldid=1181931812, (accessed 2023-11-06), 2023.

[503]Wikimedia Foundation Inc., *Wikipedia: The free encyclopedia*, https://www.wikipedia.org, (accessed 2023-11-06), 2004.

[504]D. V. Schroeder, *An Introduction to Thermal Physics* (Oxford University Press, Oxford, 2021).

[505]P. A. Mello and R. F. Rodríguez, "The equipartition theorem revisited", *Am. J. Phys.* **78**, 820 (2010).

[506]R. Clausius, "Ueber einen auf die Wärme anwendbaren mechanischen Satz", *Ann. Phys.* **217**, 124 (1870).

[507]L. Berthier and J.-L. Barrat, "Nonequilibrium dynamics and fluctuation-dissipation relation in a sheared fluid", *J. Chem. Phys.* **116**, 6228 (2002).

[508]L. Berthier and J.-L. Barrat, "Shearing a Glassy Material: Numerical Tests of Nonequilibrium Mode-Coupling Approaches and Experimental Proposals", *Phys. Rev. Lett.* **89**, 095702 (2002).

[509]A Sarracino and A Vulpiani, "On the fluctuation-dissipation relation in non-equilibrium and non-Hamiltonian systems", *Chaos1* **29**, 083132 (2019).

[510]S. R. De Groot and P. Mazur, *Non-Equilibrium Thermodynamics* (Dover Publications, Inc., 1984).

[511]J. C. Mauro, R. J. Loucks, and P. K. Gupta, "Fictive Temperature and the Glassy State", *J. Am. Ceram. Soc.* **92**, 75 (2009).

[512]L. Dabelow, S. Bo, and R. Eichhorn, "Irreversibility in Active Matter Systems: Fluctuation Theorem and Mutual Information", *Phys. Rev. X* **9**, 021009 (2019).

[513]Z. Preisler and M. Dijkstra, "Configurational entropy and effective temperature in systems of active Brownian particles", *Soft Matter* **12**, 6043 (2016).

[514]F. J. Schwarzendahl and H. Löwen, "Anomalous Cooling and Overcooling of Active Colloids", *Phys. Rev. Lett.* **129**, 138002 (2022).

[515]M. Han, J. Yan, S. Granick, and E. Luijten, "Effective temperature concept evaluated in an active colloid mixture", *Proc. Natl. Acad. Sci.* **114**, 7513 (2017).

[516]D. Loi, S. Mossa, and L. F. Cugliandolo, "Effective temperature of active matter", *Phys. Rev. E* **77**, 051111 (2008).

[517]S. C. P. and A. Joy, "Effective temperature and Einstein relation for particles in active matter flows", *Phys. Rev. E* **105**, 065114 (2022).

[518]G. Szamel, "Self-propelled particle in an external potential: Existence of an effective temperature", *Phys. Rev. E* **90**, 012111 (2014).

[519]I. Goldhirsch, "Introduction to granular temperature", *Powder Technol.* **182**, 130 (2008).

[520]A. Puglisi, A. Baldassarri, and V. Loreto, "Fluctuation-dissipation relations in driven granular gases", *Phys. Rev. E* **66**, 061305 (2002).

[521]V. Kumaran, "Temperature of a granular material "fluidized" by external vibrations", *Phys. Rev. E* **57**, 5660 (1998).

[522]A Baldassarri, A Barrat, G D'Anna, V Loreto, P Mayor, and A Puglisi, "What is the temperature of a granular medium?", *J. Phys. Condens. Matter* **17**, S2405 (2005).

[523]L. F. Cugliandolo, J. Kurchan, and L. Peliti, "Energy flow, partial equilibration, and effective temperatures in systems with slow dynamics", *Phys. Rev. E* **55**, 3898 (1997).

[524]R. Di Leonardo, L. Angelani, G. Parisi, and G. Ruocco, "Off-Equilibrium Effective Temperature in Monatomic Lennard-Jones Glass", *Phys. Rev. Lett.* **84**, 6054 (2000).

[525]W. Kob and J.-L. Barrat, "Fluctuations, response and aging dynamics in a simple glass-forming liquid out of equilibrium", *Eur. Phys. J. B* **13**, 319 (2000).

[526]D. Loi, S. Mossa, and L. F. Cugliandolo, "Effective temperature of active complex matter", *Soft Matter* **7**, 3726 (2011).

[527]M. Himpel and A. Melzer, "Configurational temperature in dusty plasmas", *Phys. Rev. E* **99**, 063203 (2019).

[528]Y. Han and D. G. Grier, "Configurational temperatures and interactions in charge-stabilized colloid", *J. Chem. Phys.* **122**, 064907 (2005).

[529]Y. Grasselli, G. Bossis, and R. Morini, "Translational and rotational temperatures of a 2D vibrated granular gas in microgravity", *Eur. Phys. J. E* **38**, 8 (2015).

[530]Y. Komatsu and H. Tanaka, "Roles of Energy Dissipation in a Liquid-Solid Transition of Out-of-Equilibrium Systems", *Phys. Rev. X* **5**, 031025 (2015).

[531]A. Prevost, P. Melby, D. A. Egolf, and J. S. Urbach, "Nonequilibrium two-phase coexistence in a confined granular layer", *Phys. Rev. E* **70**, 050301 (2004).

[532]A. Lobkovsky, F. V. Reyes, and J. Urbach, "The effects of forcing and dissipation on phase transitions in thin granular layers", *Eur. Phys. J. Spec. Top.* **179**, 113 (2009).

[533]P Melby, F. V. Reyes, A Prevost, R Robertson, P Kumar, D. A. Egolf, and J. S. Urbach, "The dynamics of thin vibrated granular layers", *J. Phys. Condens. Matter* **17**, S2689 (2005).

[534]F. V. Reyes and J. S. Urbach, "Effect of inelasticity on the phase transitions of a thin vibrated granular layer", *Phys. Rev. E* **78**, 051301 (2008).

[535]K. Roeller, J. P. D. Clewett, R. M. Bowley, S. Herminghaus, and M. R. Swift, "Liquid-Gas Phase Separation in Confined Vibrated Dry Granular Matter", *Phys. Rev. Lett.* **107**, 048002 (2011).

[536]C. S. Campbell, "Granular material flows – An overview", *Powder Technol.* **162**, 208 (2006).

[537]A. Ivlev, H. Löwen, G. Morfill, and C. P. Royall, *Complex Plasmas and Colloidal Dispersions*, Series in Soft Condensed Matter (World Scientific, Singapore, 2012).

[538]A. V. Ivlev, J. Bartnick, M. Heinen, C.-R. Du, V. Nosenko, and H. Löwen, "Statistical Mechanics where Newton's Third Law is Broken", *Phys. Rev. X* **5**, 011035 (2015).

[539]J. C. Maxwell, "V. Illustrations of the dynamical theory of gases. —Part I. On the motions and collisions of perfectly elastic spheres", *Lond. Edinb. Dubl. Phil. Mag.* **19**, 19 (1860).

[540]L. Boltzmann, "Über die Beziehung zwischen dem zweiten Hauptsatz der mechanischen Wärmetheorie und der Wahrscheinlichkeitsrechnung respektive den Sätzen über das Wärmegleichgewicht", *Wiener Berichte* **76**, 373 (1877).

[541]J. Shea, G. Jung, and F. Schmid, "Passive probe particle in an active bath: can we tell it is out of equilibrium?", *Soft Matter* **18**, 6965 (2022).

[542]L. Hecht, I. Dong, and B. Liebchen, "Motility-induced coexistence of a hot liquid and a cold gas", *Nat. Commun.* **15**, 3206 (2024).

[543]R. Becker, *Theory of Heat* (Springer, Berlin, Heidelberg, 1967).

[544]M. Caraglio and T. Franosch, "Analytic Solution of an Active Brownian Particle in a Harmonic Well", *Phys. Rev. Lett.* **129**, 158001 (2022).

[545]V. Démery and É. Fodor, "Driven probe under harmonic confinement in a colloidal bath", *J. Stat. Mech. Theory Exp.* **2019**, 033202 (2019).

[546]D. Chaudhuri and A. Dhar, "Active Brownian particle in harmonic trap: exact computation of moments, and re-entrant transition", *J. Stat. Mech. Theory Exp.* **2021**, 013207 (2021).

[547]C. Di Bello, R. Majumdar, R. Marathe, R. Metzler, and É. Roldán, "Brownian Particle in a Poisson-Shot-Noise Active Bath: Exact Statistics, Effective Temperature, and Inference", *Ann. Phys.* **536**, 2300427 (2024).

[548]A. Argun, A.-R. Moradi, E. Pinçe, G. B. Bagci, A. Imparato, and G. Volpe, "Non-Boltzmann stationary distributions and nonequilibrium relations in active baths", *Phys. Rev. E* **94**, 062150 (2016).

[549]A. Einstein, "Über die von der molekularkinetischen Theorie der Wärme geforderte Bewegung von in ruhenden Flüssigkeiten suspendierten Teilchen", *Ann. Phys.* **322**, 549 (1905).

[550]A. R. Sprenger, S. Jahanshahi, A. V. Ivlev, and H. Löwen, "Time-dependent inertia of self-propelled particles: The Langevin rocket", *Phys. Rev. E* **103**, 042601 (2021).

[551]D. Villamaina, A. Puglisi, and A. Vulpiani, "The fluctuation–dissipation relation in sub-diffusive systems: the case of granular single-file diffusion", *J. Stat. Mech. Theory Exp.* **2008**, L10001 (2008).

[552]G. Ciccotti, G. Jacucci, and I. R. McDonald, ""Thought-experiments" by molecular dynamics", *J. Stat. Phys.* **21**, 1 (1979).

[553]H. J. Metcalf and P. van der Straten, *Laser Cooling and Trapping*, Graduate Texts in Contemporary Physics (Springer, New York, 1999).

[554]A. Ziabari, M. Zebarjadi, D. Vashaee, and A. Shakouri, "Nanoscale solid-state cooling: a review", *Rep. Prog. Phys.* **79**, 095901 (2016).

[555]V. S. Letokhov, M. A. Ol'shanii, and Y. B. Ovchinnikov, "Laser cooling of atoms: a review", *Quant. Semiclass. Opt. Eur. Opt. Soc. Part B* **7**, 5 (1995).

[556]C. Van den Broeck and R. Kawai, "Brownian Refrigerator", *Phys. Rev. Lett.* **96**, 210601 (2006).

[557]M. J. Bowick, N. Fakhri, M. C. Marchetti, and S. Ramaswamy, "Symmetry, Thermodynamics, and Topology in Active Matter", *Phys. Rev. X* **12**, 010501 (2022).

[558]D. Schildknecht, A. N. Popova, J. Stellwagen, and M. Thomson, "Reinforcement learning reveals fundamental limits on the mixing of active particles", *Soft Matter* **18**, 617 (2022).

[559]F. Turci and N. B. Wilding, "Phase Separation and Multibody Effects in Three-Dimensional Active Brownian Particles", *Phys. Rev. Lett.* **126**, 038002 (2021).

[560]J. O'Byrne and J Tailleur, "Lamellar to Micellar Phases and Beyond: When Tactic Active Systems Admit Free Energy Functionals", *Phys. Rev. Lett.* **125**, 208003 (2020).

[561]G. E. Morfill and A. V. Ivlev, “Complex plasmas: An interdisciplinary research field”, *Rev. Mod. Phys.* **81**, 1353 (2009).

[562]V. Nosenko, F. Luoni, A. Kaouk, M. Rubin-Zuzic, and H. Thomas, “Active Janus particles in a complex plasma”, *Phys. Rev. Res.* **2**, 033226 (2020).

[563]A. Kudrolli, G. Lumay, D. Volfson, and L. S. Tsimring, “Swarming and Swirling in Self-Propelled Polar Granular Rods”, *Phys. Rev. Lett.* **100**, 058001 (2008).

[564]A. Deblais, T. Barois, T. Guerin, P. H. Delville, R. Vaudaine, J. S. Lintuvuori, J. F. Boudet, J. C. Baret, and H. Kellay, “Boundaries Control Collective Dynamics of Inertial Self-Propelled Robots”, *Phys. Rev. Lett.* **120**, 188002 (2018).

[565]L. Giomi, N. Hawley-Weld, and L. Mahadevan, “Swarming, swirling and stasis in sequestered bristle-bots”, *Proc. R. Soc. A Math. Phys. Eng. Sci.* **469**, 20120637 (2013).

[566]J. Deseigne, O. Dauchot, and H. Chaté, “Collective Motion of Vibrated Polar Disks”, *Phys. Rev. Lett.* **105**, 098001 (2010).

[567]I. Goldhirsch and G. Zanetti, “Clustering instability in dissipative gases”, *Phys. Rev. Lett.* **70**, 1619 (1993).

[568]D. Paolotti, A. Barrat, U. Marini Bettolo Marconi, and A. Puglisi, “Thermal convection in monodisperse and bidisperse granular gases: A simulation study”, *Phys. Rev. E* **69**, 061304 (2004).

[569]V. Garzó, A. Santos, and G. M. Kremer, “Impact of roughness on the instability of a free-cooling granular gas”, *Phys. Rev. E* **97**, 052901 (2018).

[570]W. D. Fullmer and C. M. Hrenya, “The Clustering Instability in Rapid Granular and Gas-Solid Flows”, *Annu. Rev. Fluid Mech.* **49**, 485 (2017).

[571]A. Puglisi, V. Loreto, U. M. B. Marconi, A. Petri, and A. Vulpiani, “Clustering and Non-Gaussian Behavior in Granular Matter”, *Phys. Rev. Lett.* **81**, 3848 (1998).

[572]C. Lozano, B. ten Hagen, H. Löwen, and C. Bechinger, “Phototaxis of synthetic microswimmers in optical landscapes”, *Nat. Commun.* **7**, 12828 (2016).

[573]C. Lozano, B. Liebchen, B. ten Hagen, C. Bechinger, and H. Löwen, “Propagating density spikes in light-powered motility-ratchets”, *Soft Matter* **15**, 5185 (2019).

[574]R. Golestanian, “Collective Behavior of Thermally Active Colloids”, *Phys. Rev. Lett.* **108**, 038303 (2012).

[575]H.-R. Jiang, N. Yoshinaga, and M. Sano, “Active Motion of a Janus Particle by Self-Thermophoresis in a Defocused Laser Beam”, *Phys. Rev. Lett.* **105**, 268302 (2010).

[576]I. Buttinoni, G. Volpe, F. Kümmel, G. Volpe, and C. Bechinger, “Active Brownian motion tunable by light”, *J. Phys. Condens. Matter* **24**, 284129 (2012).

[577]L. Caprini and U. Marini Bettolo Marconi, “Spatial velocity correlations in inertial systems of active Brownian particles”, *Soft Matter* **17**, 4109 (2021).

[578]R. Livi and P. Politi, *Nonequilibrium Statistical Physics* (Cambridge University Press, Cambridge, England, 2017).

[579]R. B. Bird, W. E. Stewart, and E. N. Lightfoot, *Transport Phenomena*, 2nd ed. (John Wiley & Sons, New York, 2002).

[580]G. Lebon, D. Jou, and J. Casas-Vázquez, *Understanding Non-equilibrium Thermodynamics* (Springer, Berlin, Heidelberg, 2008).

[581]G. Falasco, M. V. Gnann, D. Rings, and K. Kroy, “Effective temperatures of hot Brownian motion”, *Phys. Rev. E* **90**, 032131 (2014).

[582]U. D. Jentschura and J Sapirstein, “Green function of the Poisson equation: D = 2, 3, 4”, *J. Phys. Commun.* **2**, 015026 (2018).

[583]R. Zwanzig, *Nonequilibrium Statistical Mechanics* (Oxford University Press, New York, 2001).

[584]K. Cole, J. Beck, A. Haji-Sheikh, and B. Litkouhi, *Heat Conduction Using Greens Functions*, 2nd ed. (CRC Press, Boca Raton, 2010).

[585]E. N. Economou, *Green’s Functions in Quantum Physics* (Springer, Berlin, Heidelberg, 2006).

[586]N. A. Söker, S. Auschra, V. Holubec, K. Kroy, and F. Cichos, “How Activity Landscapes Polarize Microswimmers without Alignment Forces”, *Phys. Rev. Lett.* **126**, 228001 (2021).

[587]S. Auschra, V. Holubec, N. A. Söker, F. Cichos, and K. Kroy, “Polarization-density patterns of active particles in motility gradients”, *Phys. Rev. E* **103**, 062601 (2021).

[588]J. J. Brey, J. W. Dufty, C. S. Kim, and A. Santos, “Hydrodynamics for granular flow at low density”, *Phys. Rev. E* **58**, 4638 (1998).

[589]U. Seifert, “Stochastic thermodynamics, fluctuation theorems and molecular machines”, *Rep. Prog. Phys.* **75**, 126001 (2012).

[590]L. Onsager and S. Machlup, “Fluctuations and Irreversible Processes”, *Phys. Rev.* **91**, 1505 (1953).

[591]P. Pietzonka and U. Seifert, “Entropy production of active particles and for particles in active baths”, *J. Phys. A Math. Theor.* **51**, 01LT01 (2018).

[592]T. Nemoto, É. Fodor, M. E. Cates, R. L. Jack, and J. Tailleur, “Optimizing active work: Dynamical phase transitions, collective motion, and jamming”, *Phys. Rev. E* **99**, 022605 (2019).

[593]F. Cagnetta, F. Corberi, G. Gonnella, and A. Suma, “Large Fluctuations and Dynamic Phase Transition in a System of Self-Propelled Particles”, *Phys. Rev. Lett.* **119**, 158002 (2017).

[594]L. Caprini, A. Puglisi, and A. Sarracino, “Fluctuation–Dissipation Relations in Active Matter Systems”, *Symmetry* **13**, 81 (2021).

[595]B. Städler, A. D. Price, R. Chandrawati, L. Hosta-Rigau, A. N. Zelikin, and F. Caruso, “Polymer hydrogel capsules: en route toward synthetic cellular systems”, *Nanoscale* **1**, 68 (2009).

[596]T. M. S. Chang, “Semipermeable Microcapsules”, *Science* **146**, 524 (1964).

[597]N. Greinert, T. Wood, and P. Bartlett, “Measurement of Effective Temperatures in an Aging Colloidal Glass”, *Phys. Rev. Lett.* **97**, 265702 (2006).

[598]S. Ye, P. Liu, F. Ye, K. Chen, and M. Yang, “Active noise experienced by a passive particle trapped in an active bath”, *Soft Matter* **16**, 4655 (2020).

[599]C. Maggi, M. Paoluzzi, N. Pellicciotta, A. Lepore, L. Angelani, and R. Di Leonardo, “Generalized Energy Equipartition in Harmonic Oscillators Driven by Active Baths”, *Phys. Rev. Lett.* **113**, 238303 (2014).

[600]D. Arold and M. Schmiedeberg, “Mean field approach of dynamical pattern formation in underdamped active matter with short-ranged alignment and distant anti-alignment interactions”, *J. Phys. Condens. Matter* **32**, 315403 (2020).

[601]M. Duarte, S. Oliveira, and A. Christensen, “Hybrid Control for Large Swarms of Aquatic Drones”, in Artificial Life 14: Proceedings of the Fourteenth International Conference on the Synthesis and Simulation of Living Systems (2014), p. 785.

[602]M. Leyman, F. Ogemark, J. Wehr, and G. Volpe, “Tuning phototactic robots with sensorial delays”, *Phys. Rev. E* **98**, 052606 (2018).

[603]H. L. Devereux, C. R. Twomey, M. S. Turner, and S. Thutupalli, “Whirligig beetles as corralled active Brownian particles”, *J. R. Soc. Interface* **18**, 20210114 (2021).

[604]H. W. Dickinson, *A Short History of the Steam Engine* (Cambridge University Press, Cambridge, 2011).

[605]J. Stichlmair, H. Klein, and S. Rehfeldt, *Distillation* (Wiley, Hoboken, New Jersey, 2021).

[606]Z. Lei, C. Li, and B. Chen, "Extractive Distillation: A Review", *Sep. Purif. Rev.* **32**, 121 (2003).

[607]S. M. Rossnagel, "Thin film deposition with physical vapor deposition and related technologies", *J. Vac. Sci. Technol. A* **21**, S74 (2003).

[608]D. M. Mattox, *Handbook of Physical Vapor Deposition (PVD) Processing*, Second Edition (William Andrew Publishing, Boston, 2010).

[609]S. Hurwitz and M. Manga, "The Fascinating and Complex Dynamics of Geyser Eruptions", *Annu. Rev. Earth Planet. Sci.* **45**, 31 (2017).

[610]A. Patch, D. Yllanes, and M. C. Marchetti, "Kinetics of motility-induced phase separation and swim pressure", *Phys. Rev. E* **95**, 012601 (2017).

[611]T. Schindler and S. C. Kapfer, "Nonequilibrium steady states, coexistence, and criticality in driven quasi-two-dimensional granular matter", *Phys. Rev. E* **99**, 022902 (2019).

[612]C. Scholz and T. Pöschel, "Velocity Distribution of a Homogeneously Driven Two-Dimensional Granular Gas", *Phys. Rev. Lett.* **118**, 198003 (2017).

[613]T. Pöschel and S. Luding, *Granular Gases*, edited by T. Pöschel and S. Luding, Vol. 564, Lecture Notes in Physics (Springer, Berlin, Heidelberg, 2001).

[614]C. Valeriani, M. Li, J. Novosel, J. Arlt, and D. Marenduzzo, "Colloids in a bacterial bath: simulations and experiments", *Soft Matter* **7**, 5228 (2011).

[615]L. Angelani, C. Maggi, M. L. Bernardini, A. Rizzo, and R. Di Leonardo, "Effective Interactions between Colloidal Particles Suspended in a Bath of Swimming Cells", *Phys. Rev. Lett.* **107**, 138302 (2011).

[616]M. Huang, W. Hu, S. Yang, Q.-X. Liu, and H. P. Zhang, "Circular swimming motility and disordered hyperuniform state in an algae system", *Proc. Natl. Acad. Sci.* **118**, e2100493118 (2021).

[617]A. Ramamonjy, J. Dervaux, and P. Brunet, "Nonlinear Phototaxis and Instabilities in Suspensions of Light-Seeking Algae", *Phys. Rev. Lett.* **128**, 258101 (2022).

[618]S. Auschra, A. Bregulla, K. Kroy, and F. Cichos, "Thermotaxis of Janus particles", *Eur. Phys. J. E* **44**, 90 (2021).

[619]J. Stenhammar, R. Wittkowski, D. Marenduzzo, and M. E. Cates, "Activity-Induced Phase Separation and Self-Assembly in Mixtures of Active and Passive Particles", *Phys. Rev. Lett.* **114**, 018301 (2015).

[620]S. Dikshit and S. Mishra, "Activity-driven phase separation and ordering kinetics of passive particles", *Eur. Phys. J. E* **45**, 21 (2022).

[621]M. Baus and C. F. Tejero, *Equilibrium Statistical Physics* (Springer International Publishing, Cham, 2021).

[622]M. Zaeifi Yamchi and A. Naji, "Effective interactions between inclusions in an active bath", *J. Chem. Phys.* **147**, 194901 (2017).

[623]C. Wang and H. Jiang, "The inhibition of concentrated active baths", *J. Chem. Phys.* **152**, 184907 (2020).

[624]N. Möller, L. Hecht, R. Niu, B. Liebchen, and T. Palberg, "Writing Into Water", *Small* **19**, 2303741 (2023).

[625]N. Möller, "Active Motion of Colloids Driven by pH Gradients", Dissertation (Johannes Gutenberg-Universität Mainz, 2022).

[626]C. S. Henshilwood, F. D'Errico, K. L. van Niekerk, L. Dayet, A. Queffelec, and L. Pollarolo, "An abstract drawing from the 73,000-year-old levels at Blombos Cave, South Africa", *Nature* **562**, 115 (2018).

[627]S. D. Houston, *The First Writing: Script Invention as History and Process* (Cambridge University Press, Cambridge, 2004).

[628]F. D'Errico and C. B. Stringer, "Evolution, revolution or saltation scenario for the emergence of modern cultures?", *Philos. Trans. R. Soc. B* **366**, 1060 (2011).

[629]P. F. Bai, R. A. Hayes, M. Jin, L. Shui, Z. C. Yi, L. Wang, X. Zhang, and G. Zhou, "Review of Paper-like Display Technologies (Invited Review)", *Prog. Electromagn. Res.* **147**, 95 (2014).

[630]T. H. Newman, K. E. Williams, and R. F. W. Pease, "High resolution patterning system with a single bore objective lens", *J. Vac. Sci. Technol. B* **5**, 88 (1987).

[631]A. Levskaya, A. A. Chevalier, J. J. Tabor, Z. B. Simpson, L. A. Lavery, M. Levy, E. A. Davidson, A. Scouras, A. D. Ellington, E. M. Marcotte, et al., "Engineering Escherichia coli to see light", *Nature* **438**, 441 (2005).

[632]J. Li, E. H. Hill, L. Lin, and Y. Zheng, "Optical Nanoprinting of Colloidal Particles and Functional Structures", *ACS Nano* **13**, 3783 (2019).

[633]N. Vogel, M. Retsch, C.-A. Fustin, A. del Campo, and U. Jonas, "Advances in Colloidal Assembly: The Design of Structure and Hierarchy in Two and Three Dimensions", *Chem. Rev.* **115**, 6265 (2015).

[634]S. Kim, B. Marelli, M. A. Brenckle, A. N. Mitropoulos, E.-S. Gil, K. Tsioris, H. Tao, D. L. Kaplan, and F. G. Omenetto, "All-water-based electron-beam lithography using silk as a resist", *Nat. Nanotechnol.* **9**, 306 (2014).

[635]M. Imboden, H. Han, T. Stark, E. Lowell, J. Chang, F. Pardo, C. Bolle, P. G. del Corro, and D. J. Bishop, "Building a Fab on a Chip", *Nanoscale* **6**, 5049 (2014).

[636]"Ten years in images", *Nat. Nanotechnol.* **11**, 836 (2016).

[637]A. Aubret, Q. Martinet, and J. Palacci, "Metamachines of pluripotent colloids", *Nat. Commun.* **12**, 6398 (2021).

[638]M. Eda, T. Yamasaki, and M. Sakai, "Identifying the bird figures of the Nasca pampas: An ornithological perspective", *J. Archaeol. Sci. Reports* **26**, 101875 (2019).

[639]D. M. Eigler and E. K. Schweizer, "Positioning single atoms with a scanning tunnelling microscope", *Nature* **344**, 524 (1990).

[640]C. R. Moon, L. S. Mattos, B. K. Foster, G. Zeltzer, and H. C. Manoharan, "Quantum holographic encoding in a two-dimensional electron gas", *Nat. Nanotechnol.* **4**, 167 (2009).

[641]G.-Y. Liu, S. Xu, and Y. Qian, "Nanofabrication of Self-Assembled Monolayers Using Scanning Probe Lithography", *Acc. Chem. Res.* **33**, 457 (2000).

[642]M. Liu, N. A. Amro, and G.-y. Liu, "Nanografting for Surface Physical Chemistry", *Annu. Rev. Phys. Chem.* **59**, 367 (2008).

[643]J. Im, Y. Liu, Q. Hu, G. F. Trindade, C. Parmenter, M. Fay, Y. He, D. J. Irvine, C. Tuck, R. D. Wildman, et al., "Strategies for Integrating Metal Nanoparticles with Two-Photon Polymerization Process: Toward High Resolution Functional Additive Manufacturing", *Adv. Funct. Mater.* **33**, 2211920 (2023).

[644]J. Im, G. F. Trindade, T. T. Quach, A. Sohaib, F. Wang, J. Austin, L. Turyanska, C. J. Roberts, R. Wildman, R. Hague, et al., "Functionalized Gold Nanoparticles with a Cohesion Enhancer for Robust Flexible Electrodes", *ACS Appl. Nano Mater.* **5**, 6708 (2022).

[645]Y. Guo, J. A. Belgodere, Y. Ma, J. P. Jung, and B. Bharti, "Directed Printing and Reconfiguration of Thermoresponsive Silica-pNIPAM Nanocomposites", *Macromol. Rapid Commun.* **40**, 1900191 (2019).

[646]R. S. Roberts, *Art Smith: Pioneer Aviator* (McFarland, Jefferson, North Carolina, and London, 2003).

[647]J. Anderson, "Colloid Transport By Interfacial Forces", *Annu. Rev. Fluid Mech.* **21**, 61 (1989).

[648]J. L. Anderson and D. C. Prieve, "Diffusiophoresis: Migration of Colloidal Particles in Gradients of Solute Concentration", *Sep. Purif. Methods* **13**, 67 (1984).

[649]A. Würger, "Thermal non-equilibrium transport in colloids", *Rep. Prog. Phys.* **73**, 126601 (2010).

[650]P. O. Staffeld and J. A. Quinn, "Diffusion-induced banding of colloid particles via diffusiophoresis: 1. Electrolytes", *J. Colloid Interface Sci.* **130**, 69 (1989).

[651]J. Palacci, C. Cottin-Bizonne, C. Ybert, and L. Bocquet, "Osmotic traps for colloids and macromolecules based on logarithmic sensing in salt taxis", *Soft Matter* **8**, 980 (2012).

[652]A. Banerjee, H. Tan, and T. M. Squires, "Drop-in additives for suspension manipulation: Colloidal motion induced by sedimenting soluto-inertial beacons", *Phys. Rev. Fluids* **5**, 073701 (2020).

[653]A. Toyotama, T. Kanai, T. Sawada, J. Yamanaka, K. Ito, and K. Kitamura, "Gelation of Colloidal Crystals without Degradation in Their Transmission Quality and Chemical Tuning", *Langmuir* **21**, 10268 (2005).

[654]L. Lin, J. Zhang, X. Peng, Z. Wu, A. C. H. Coughlan, Z. Mao, M. A. Bevan, and Y. Zheng, "Opto-thermophoretic assembly of colloidal matter", *Sci. Adv.* **3**, e1700458 (2017).

[655]H. J. Keh, "Diffusiophoresis", in *Encyclopedia of Microfluidics and Nanofluidics* (Springer US, Boston, MA), p. 365.

[656]S. Marbach and L. Bocquet, "Osmosis, from molecular insights to large-scale applications", *Chem. Soc. Rev.* **48**, 3102 (2019).

[657]R. Niu, P. Kreissl, A. T. Brown, G. Rempfer, D. Botin, C. Holm, T. Palberg, and J. de Graaf, "Microfluidic pumping by micromolar salt concentrations", *Soft Matter* **13**, 1505 (2017).

[658]R. Niu, T. Palberg, and T. Speck, "Self-Assembly of Colloidal Molecules due to Self-Generated Flow", *Phys. Rev. Lett.* **119**, 028001 (2017).

[659]M. Ibele, T. Mallouk, and A. Sen, "Schooling Behavior of Light-Powered Autonomous Micromotors in Water", *Angew. Chemie* **121**, 3358 (2009).

[660]R. Niu, E. C. Oğuz, H. Müller, A. Reinmüller, D. Botin, H. Löwen, and T. Palberg, "Controlled assembly of single colloidal crystals using electro-osmotic micro-pumps", *Phys. Chem. Chem. Phys.* **19**, 3104 (2017).

[661]M. J. Esplandiu, K. Zhang, J. Fraxedas, B. Sepulveda, and D. Reguera, "Unraveling the Operational Mechanisms of Chemically Propelled Motors with Micropumps", *Acc. Chem. Res.* **51**, 1921 (2018).

[662]R. Niu and T. Palberg, "Seedless assembly of colloidal crystals by inverted micro-fluidic pumping", *Soft Matter* **14**, 3435 (2018).

[663]S. Michelin and E. Lauga, "Universal optimal geometry of minimal phoretic pumps", *Sci. Rep.* **9**, 10788 (2019).

[664]A. Reinmüller, H. J. Schöpe, and T. Palberg, "Self-Organized Cooperative Swimming at Low Reynolds Numbers", *Langmuir* **29**, 1738 (2013).

[665]R. Niu, D. Botin, J. Weber, A. Reinmüller, and T. Palberg, "Assembly and Speed in Ion-Exchange-Based Modular Phoretic Microswimmers", *Langmuir* **33**, 3450 (2017).

[666]A. Banerjee and T. M. Squires, "Long-range, selective, on-demand suspension interactions: Combining and triggering soluto-inertial beacons", *Sci. Adv.* **5**, eaax1893 (2019).

[667]N. Möller, B. Liebchen, and T. Palberg, "Shaping the gradients driving phoretic micro-swimmers: influence of swimming speed, budget of carbonic acid and environment", *Eur. Phys. J. E* **44**, 41 (2021).

[668]D. Veregol, *Colloidal Systems* (CreateSpace Independent Publishing Platform, 2016).

[669]R. Niu, S. Khodorov, J. Weber, A. Reinmüller, and T. Palberg, "Large scale micro-photometry for high resolution pH-characterization during electro-osmotic pumping and modular micro-swimming", *New J. Phys.* **19**, 115014 (2017).

[670]H. Yukawa and S. Sakata, "On the Interaction of Elementary Particles II", *Proc. Physico-Mathematical Soc. Japan. 3rd Ser.* **19**, 1084 (1937).

[671]*Mathematica, Version 13.0* (Wolfram Research, Inc., Champaign, IL, 2021).

[672]S. Hamdi, W. Schiesser, and G. Griffiths, "Method of lines", *Scholarpedia* **2**, 2859 (2007).

[673]W. Schiesser, *The Numerical Method of Lines* (Academic Press, Inc., San Diego, 1991).

[674]G. Dhatt, G. Touzot, and E. Lefrançois, *Finite Element Method* (ISTE, London, 2012).

[675]C. P. Winsor, "The Gompertz Curve as a Growth Curve", *Proc. Natl. Acad. Sci.* **18**, 1 (1932).

[676]H. Aceves and M. Colosimo, "An introduction to dynamical friction in stellar systems", *Am. J. Phys.* **75**, 139 (2007).

[677]W. Mulder, "Dynamical Friction on Extended Objects", *Astron. Astrophyiscs* **117**, 9 (1983).

[678]J. Palacci, S. Sacanna, A. Vatchinsky, P. M. Chaikin, and D. J. Pine, "Photoactivated Colloidal Dockers for Cargo Transportation", *J. Am. Chem. Soc.* **135**, 15978 (2013).

[679]A. Snezhko, M. Belkin, I. S. Aranson, and W.-K. Kwok, "Self-Assembled Magnetic Surface Swimmers", *Phys. Rev. Lett.* **102**, 118103 (2009).

[680]N. Möller, S. Seiffert, T. Palberg, and R. Niu, "Active and Passive Motion in Complex pH-Fields", *ChemNanoMat* **7**, 1145 (2021).

[681]C. Ganguly and D. Chaudhuri, "Stochastic thermodynamics of active Brownian particles", *Phys. Rev. E* **88**, 032102 (2013).

[682]E. W. Burkholder and J. F. Brady, "Fluctuation-dissipation in active matter", *J. Chem. Phys.* **150**, 184901 (2019).

[683]C. Nardini, É. Fodor, E. Tjhung, F. van Wijland, J. Tailleur, and M. E. Cates, "Entropy Production in Field Theories without Time-Reversal Symmetry: Quantifying the Non-Equilibrium Character of Active Matter", *Phys. Rev. X* **7**, 021007 (2017).

[684]A. Patch, D. M. Sussman, D. Yllanes, and M. C. Marchetti, "Curvature-dependent tension and tangential flows at the interface of motility-induced phases", *Soft Matter* **14**, 7435 (2018).

[685]E. Chacón, F. Alarcón, J. Ramírez, P. Tarazona, and C. Valeriani, "Intrinsic structure perspective for MIPS interfaces in two-dimensional systems of active Brownian particles", *Soft Matter* **18**, 2646 (2022).

[686]S. Hermann, D. de las Heras, and M. Schmidt, "Non-negative Interfacial Tension in Phase-Separated Active Brownian Particles", *Phys. Rev. Lett.* **123**, 268002 (2019).

[687]A. K. Omar, Z.-G. Wang, and J. F. Brady, "Microscopic origins of the swim pressure and the anomalous surface tension of active matter", *Phys. Rev. E* **101**, 012604 (2020).

[688]J. Bialké, J. T. Siebert, H. Löwen, and T. Speck, "Negative Interfacial Tension in Phase-Separated Active Brownian Particles", *Phys. Rev. Lett.* **115**, 098301 (2015).

[689]L. Li, Z. Sun, and M. Yang, "Surface Tension Between Coexisting Phases of Active Brownian Particles", *arXiv:2308.04917v1 [cond-mat.soft]* (2023).

[690]N. Lauersdorf, T. Kolb, M. Moradi, E. Nazockdast, and D. Klotsa, "Phase behavior and surface tension of soft active Brownian particles", *Soft Matter* **17**, 6337 (2021).

[691]V. Holubec, D. Geiss, S. A. M. Loos, K. Kroy, and F. Cichos, "Finite-Size Scaling at the Edge of Disorder in a Time-Delay Vicsek Model", *Phys. Rev. Lett.* **127**, 258001 (2021).

[692]B. Partridge and C. F. Lee, "Critical Motility-Induced Phase Separation Belongs to the Ising Universality Class", *Phys. Rev. Lett.* **123**, 068002 (2019).

[693]S. H. Rudy, S. L. Brunton, J. L. Proctor, and J. N. Kutz, "Data-driven discovery of partial differential equations", *Sci. Adv.* **3**, 1108 (2017).

[694]M. Han, M. Fruchart, C. Scheibner, S. Vaikuntanathan, J. J. de Pablo, and V. Vitelli, "Fluctuating hydrodynamics of chiral active fluids", *Nat. Phys.* **17**, 1260 (2021).

[695]H. Yu, Y. Fu, X. Zhang, L. Chen, D. Qi, J. Shi, and W. Wang, "Programmable active matter across scales", *Program. Mater.* **1**, e7 (2023).

[696]L. Caprini, U. Marini Bettolo Marconi, and A. Puglisi, "Activity induced delocalization and freezing in self-propelled systems", *Sci. Rep.* **9**, 1386 (2019).

[697]B. Dybiec, E. Gudowska-Nowak, and I. M. Sokolov, "Underdamped stochastic harmonic oscillator driven by Lévy noise", *Phys. Rev. E* **96**, 042118 (2017).

[698]L. Boltzmann, "Studien über das Gleichgewicht der lebendigen Kraft zwischen bewegten materiellen Punkten", *Wiener Berichte* **58**, 517 (1868).

[699]I. Bronshtein, K. Semendyayev, G. Musiol, and H. Mühlig, *Handbook of Mathematics*, 6th ed. (Springer, Berlin, Heidelberg, 2015).

[700]P. Vogel, N. Möller, M. N. Qaisrani, P. Bista, S. A. L. Weber, H.-J. Butt, B. Liebchen, M. Sulpizi, and T. Palberg, "Charging of Dielectric Surfaces in Contact with Aqueous Electrolytes - the Influence of CO 2", *J. Am. Chem. Soc.* **144**, 21080 (2022).

[701]D. Botin, J. Wenzl, R. Niu, and T. Palberg, "Colloidal electro-phoresis in the presence of symmetric and asymmetric electro-osmotic flow", *Soft Matter* **14**, 8191 (2018).

[702]A. Liberzon, T. Käufer, A. Bauer, P. Vennemann, and E. Zimmer, *OpenPIV/openpiv-python: OpenPIV-Python v0.23.6*, https://doi.org/10.5281/zenodo.5009150, 2021.

Appendices

Appendix A: Defining temperature in active systems

The following text is taken verbatim from my publication "How to define temperature in active systems" published as a preprint on *arXiv* (2024).[501]

Analytical results for the kinetic temperature

In Chap. 4, we discussed the analytical expression of the kinetic temperature for free non-interacting ABPs. Let us now consider a few more complicated setups. By confining the system through an external harmonic potential $U_{\text{ext}}(\mathbf{r}) = k\mathbf{r}^2/2$, for the AOUP case (Eq. (2.11)), one obtains[158]

$$\alpha = \frac{\tau_{\text{p}}\gamma_{\text{t}}/m}{1 + \tau_{\text{p}}\gamma_{\text{t}}/m + \tau_{\text{p}}^2 k/m}. \tag{A1}$$

Since the second moments of the distribution for ABPs and AOUPs are equal, this result holds also for ABPs. Equation (A1) shows that the harmonic confinement reduces the kinetic temperature. In the overdamped regime, i.e., $\tau_{\text{p}}\gamma_{\text{t}}/m \gg 1$, Eq. (A1) simplifies to

$$\alpha = \frac{1}{1 + \tau_{\text{p}}k/\gamma_{\text{t}}}. \tag{A2}$$

For a general external potential U_{ext}, exact analytical results are not known. However, naively, we can derive an approximate result based on an equilibrium-like approximation obtained in the overdamped regime, which reads[696]

$$\alpha \approx \left[1 + \frac{\tau_{\text{p}}}{\gamma_{\text{t}}}\nabla^2 U_{\text{ext}}(\mathbf{r})\right]^{-1}. \tag{A3}$$

Note that this result is consistent with Eq. (A2) for the harmonic external potential in the overdamped regime.

For interacting active particles, there are no simple analytical expressions for the kinetic temperature except in very dense systems displaying a solid configuration. In this case, for AOUPs, we obtain[577]

$$k_{\text{B}}T_{\text{kin}}^{\text{AOUP}} = k_{\text{B}}T_{\text{b}} + \frac{v_0^2\tau_{\text{p}}\gamma_{\text{t}}}{1 + \tau_{\text{p}}/\tau_I + 6\omega_E^2\tau_{\text{p}}^2}\frac{\mathcal{I}}{\pi}. \tag{A4}$$

The term ω_{E}^2 reads

$$\omega_{\text{E}}^2 = \frac{1}{2m}\left(u''(\bar{x}) + \frac{u'(\bar{x})}{\bar{x}}\right), \tag{A5}$$

where $\bar{x}$ is the average distance between different particles, i.e., the lattice constant of the crystal, u is the interaction potential, and $\mathcal{I}$ is a numerical factor that shows a non-trivial dependence on τ_p, m/γ_t, and ω_E.[577] We remark that the kinetic energy of a single active particle in a solid configuration is smaller than the kinetic energy of a free active particle: In the solid, the neighboring particles hinder the motion of a target particle and decrease its kinetic energy.

Virial temperature for inertial ABPs

For inertial ABPs (Eqs. (2.2) and (2.3)), the virial temperature can be calculated by inserting the total force, i.e., the right-hand side of Eq. (2.2), into the virial. This leads to four contributions: The first contribution comes from the drag force $-\gamma_\mathrm{t}\mathbf{v}_i$ and involves the correlation function $\langle \mathbf{r}_i \cdot \mathbf{v}_i \rangle$. In the steady state, it can be rewritten in terms of the effective diffusion coefficient:

$$2\langle \mathbf{r}_i \cdot \mathbf{v}_i \rangle = \partial_t \langle \mathbf{r}_i \cdot \mathbf{r}_i \rangle = \partial_t \mathrm{MSD}(t) \xrightarrow[t\gg 1]{} \partial_t (2dD_\mathrm{eff} t) = 2dD_\mathrm{eff}. \tag{A6}$$

This contribution is equal to the Einstein temperature as defined in Eq. (4.15). The second contribution comes from the effective self-propulsion force $\gamma_\mathrm{t} v_0 \hat{\mathbf{p}}_i$. It contains the correlation $\langle \mathbf{r}_i \cdot \hat{\mathbf{p}}_i \rangle$ between the position and orientation of the active particles. The third contribution involves the Gaussian white noise $\sqrt{2k_\mathrm{B}T_\mathrm{b}\gamma_\mathrm{t}}\boldsymbol{\xi}_i$. It leads to the correlation $\langle \mathbf{r}_i \cdot \boldsymbol{\xi}_i \rangle = 0$.[133] The remaining contribution involves the interaction forces $\mathbf{F}_{ij} = -\boldsymbol{\nabla}_{\mathbf{r}_i} u(r_{ij})$ and possible external forces. The contribution from the interaction forces can be written as

$$\begin{aligned}
\sum_{i=1}^{N} \langle \mathbf{r}_i \cdot \mathbf{F}_i \rangle &= \sum_{i=1}^{N} \sum_{j=1, j\neq i}^{N} \langle \mathbf{r}_i \cdot \mathbf{F}_{ij} \rangle \\
&= \sum_{i=2}^{N} \sum_{j=1}^{i-1} \mathbf{r}_i \cdot \mathbf{F}_{ij} + \sum_{i=2}^{N} \sum_{j=1}^{i-1} \mathbf{r}_j \cdot \mathbf{F}_{ji} \\
&= \sum_{i=2}^{N} \sum_{j=1}^{i-1} (\mathbf{r}_i - \mathbf{r}_j) \cdot \mathbf{F}_{ij} \\
&= \sum_{i=1}^{N} \sum_{j<i} \langle \mathbf{r}_{ij} \cdot \mathbf{F}_{ij} \rangle
\end{aligned} \tag{A7}$$

by applying Newton's third law and using $\mathbf{F}_i = \sum_{j=1, j\neq i}^{N} \mathbf{F}_{ij}$. Here, we use $\mathbf{r}_{ij} = \mathbf{r}_i - \mathbf{r}_j$. Finally, we can write the virial temperature for inertial ABPs as

$$k_\mathrm{B} T_\mathrm{vir}^\mathrm{ABP} = \gamma_\mathrm{t} \lim_{t\to\infty} \partial_t \mathrm{MSD}(t) - \frac{1}{2Nd} \sum_{i=1}^{N} \left\langle \sum_{j<i} \mathbf{r}_{ij} \cdot \mathbf{F}_{ij} + \gamma_\mathrm{t} v_0 \mathbf{r}_i \cdot \hat{\mathbf{p}}_i \right\rangle. \tag{A8}$$

Derivation of the oscillator temperature

Let us consider a passive tracer particle trapped in a harmonic potential and suspended in a bath of Brownian particles. Due to the collisions of the bath particles with the tracer, the latter is driven by these collisions, which can be modeled as random driving force following a Gaussian white noise process. Let x denote the displacement of the tracer particle with respect to its equilibrium position (here only in one spatial dimension for simplicity). Then, the equation of motion for the tracer particle of mass m reads

$$m\ddot{x} = -\gamma\dot{x} - kx + \sqrt{2k_\mathrm{B}T\gamma}\xi(t) \tag{A9}$$

with the drag coefficient γ of the bath, the force constant k, and Gaussian white noise $\xi(t)$ of zero mean and unit variance. Here, T denotes the temperature of the bath, which is related to the position fluctuations $\langle x^2 \rangle$ via

$$\langle x^2 \rangle = \frac{k_\mathrm{B}T}{k}. \tag{A10}$$

This relation can be derived as follows: First, we write down the Fokker-Planck equation for the probability density $\mathcal{P}(x, v, t)$ with $v = \dot{x}$ by following the standard text book:[302]

$$\frac{\partial \mathcal{P}}{\partial t} = \left\{ \frac{\gamma}{m} - v\frac{\partial}{\partial x} + \left(\frac{\gamma}{m}v + \frac{k}{m}x \right) \frac{\partial}{\partial v} + \frac{k_\mathrm{B}T\gamma}{m^2}\frac{\partial^2}{\partial v^2} \right\} \mathcal{P}. \tag{A11}$$

Now, it can be shown that the solution of the Fokker-Planck equation is given by [a]

$$\mathcal{P}(x, v) = \frac{1}{A} \exp\left\{ -\frac{1}{k_\mathrm{B}T} \left(\frac{1}{2}mv^2 + \frac{1}{2}kx^2 \right) \right\}, \tag{A12}$$

which is simply the Boltzmann distribution with normalization constant $A = \int \mathrm{d}x \int \mathrm{d}v\, \mathcal{P}(x, v)$.[698]

Then, the position fluctuations can be determined as

$$\begin{aligned} \langle x^2 \rangle &= \frac{\int \mathrm{d}x \int \mathrm{d}v\, x^2 \mathcal{P}(x, v)}{\int \mathrm{d}x \int \mathrm{d}v\, \mathcal{P}(x, v)} \\ &= \frac{\int \mathrm{d}x\, x^2 \exp\left\{ -\frac{kx^2}{2k_\mathrm{B}T} \right\}}{\int \mathrm{d}x\, \exp\left\{ -\frac{kx^2}{2k_\mathrm{B}T} \right\}} \\ &= \frac{\sqrt{\pi}}{2} \left(\frac{2k_\mathrm{B}T}{k} \right)^{(3/2)} \sqrt{\frac{k}{2\pi k_\mathrm{B}T}} = \frac{k_\mathrm{B}T}{k}, \end{aligned} \tag{A13}$$

where we have used Eqs. (21.24b) and (21.25) from Ref. [699, p. 1100].

[a] The solution can be derived from the condition $\partial_t \mathcal{P} = 0$ by using a Gaussian distribution as an ansatz for $\mathcal{P}(x, v)$. It is also given in Ref. [697].

The effective temperature

The effective temperature is based on linear response theory and the fluctuation dissipation theorem (FDT). It can be derived as follows: Let us consider a (weak) time-dependent perturbation that couples to an observable A. Then, the linear response function, which describes the response of an observable B to the time-dependent perturbation, is given by

$$R_{AB}(t,t') = -\frac{1}{k_\mathrm{B}T}\left\langle \dot{B}(t)A(t')\right\rangle, \tag{A14}$$

where the average $\langle\cdot\rangle$ is taken over the unperturbed system.[303] It is related to the time-integrated linear response (susceptibility) by

$$\chi_{AB}(t,0) = \int_0^t \mathrm{d}t'\, R_{AB}(t,t'), \tag{A15}$$

following the notation in Ref. [125]. By setting $A = B = x$, where x denotes the position of a particle in x direction, one can show that

$$\begin{aligned}\chi_{xx}(t,0) &= \int_0^t \mathrm{d}t'\, R_{xx}(t,t') \\ &= \frac{1}{2k_\mathrm{B}T}\int_0^t \mathrm{d}t' \int_0^t \mathrm{d}t''\, \langle \dot{x}(t')\dot{x}(t'')\rangle \\ &= \frac{1}{2k_\mathrm{B}T}\mathrm{MSD}(t)\end{aligned} \tag{A16}$$

with the mean-square displacement $\mathrm{MSD}(t) = \langle [x(t) - x(0)]^2\rangle$. Hence, the FDT for the time-integrated linear response reads

$$2k_\mathrm{B}T\chi_{xx}(t) = \mathrm{MSD}(t). \tag{A17}$$

Following Ref. [125], this can be generalized to d spatial dimensions:

$$2dk_\mathrm{B}T\chi(t) = \mathrm{MSD}(t), \tag{A18}$$

with

$$\chi(t) = \int_0^t \mathrm{d}t'' \sum_{\alpha=1}^{d} R_{\alpha\alpha}(t,t''). \tag{A19}$$

In order to define an effective temperature for systems out of equilibrium, one introduces a time-dependent effective temperature $T_\mathrm{eff}(t)$, which is defined by[123,125]

$$k_\mathrm{B}T_\mathrm{eff}(t) = \frac{\mathrm{MSD}(t)}{2d\chi(t)}. \tag{A20}$$

Appendix B: Active refrigerator

In the following, we show two additional figures related to the proposed active refrigerators in Chap. 5. Figure B1 shows numerical results of an active refrigerator, and Fig. B2 demonstrates the use of active refrigerators for trapping and absorbing passive tracer particles.

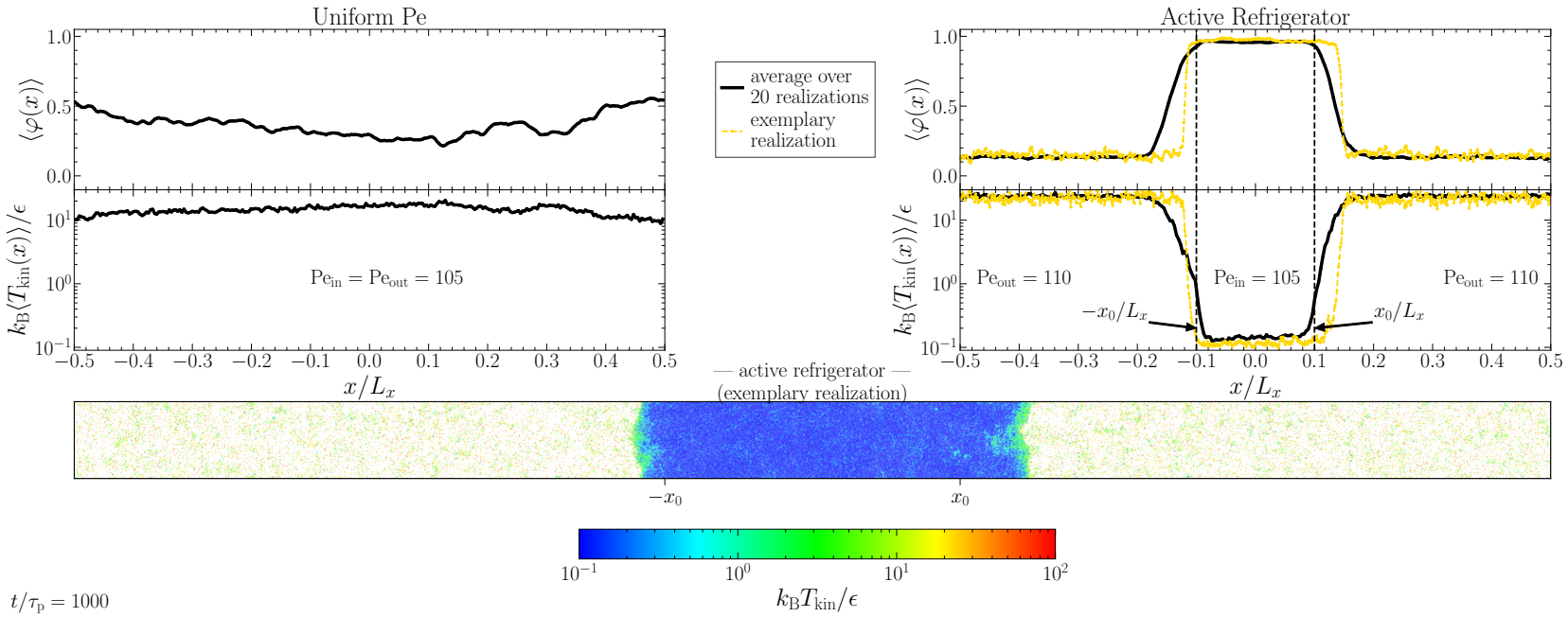

Fig. B1 Active refrigerator. The top panels show the profiles of the area fraction $\langle\varphi(x)\rangle$ and the temperature profiles $k_\mathrm{B}T_\mathrm{kin}(x) = m\langle|\mathbf{v}|^2\rangle_y/2$ averaged over the y coordinate and 20 realizations with $N = 16\,000$ particles for (i) uniform Pe (top left panels) with $\mathrm{Pe_{in}} = \mathrm{Pe_{out}} = 105$ and $\varphi_\mathrm{tot} = 0.35$ (see also Fig. 5.3a) and (ii) the active refrigerator (top right panels) with $\mathrm{Pe_{in}} = 105$, $\mathrm{Pe_{out}} = 110$, $\varphi_\mathrm{tot} = 0.35$, and $x_0/L_x = 0.1$ (see also Fig. 5.3c). The lower panel shows an exemplary realization of the active refrigerator with the same parameters as in the top right panels but with $N = 100\,000$ particles (the corresponding profile of the area fraction $\langle\varphi(x)\rangle$ and the temperature profile $k_\mathrm{B}T_\mathrm{kin}(x) = m\langle|\mathbf{v}|^2\rangle_y/2$ averaged over the y coordinate are shown as yellow dashed line in the top right panels). The other parameters are $m/(\gamma_\mathrm{t}\tau_\mathrm{p}) = 5\times10^{-2}$, $I/(\gamma_\mathrm{r}\tau_\mathrm{p}) = 5\times10^{-3}$, $\epsilon/(k_\mathrm{B}T_\mathrm{b}) = 10$, and $\sigma/\sqrt{D_\mathrm{t}/D_\mathrm{r}} = 1$.

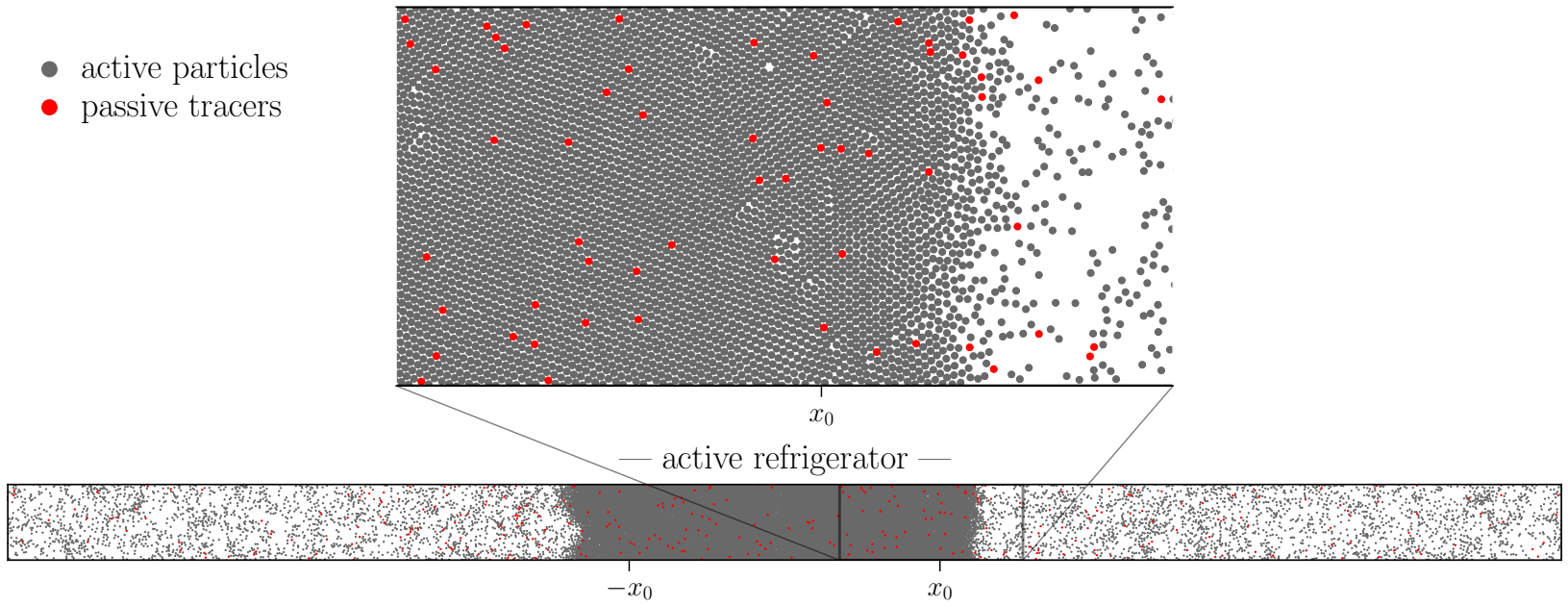

Fig. B2 Absorbing and trapping tracers. Example of the absorption and trapping of passive tracers (red) inside the active refrigerator with parameters $\mathrm{Pe_{in}} = 105$, $\mathrm{Pe_{out}} = 110$, $\varphi_\mathrm{tot} = 0.35$, and $x_0/L_x = 0.1$ (see also Fig. 5.12). The passive tracers have the same attributes as the active particles (gray) except $\mathrm{Pe} = 0$ and are initially placed outside the targeted cooling domain. The fraction of passive tracers is given by $N_\mathrm{passive}/N = 0.02$ with $N = 16\,000$. All other parameters are the same as in Fig. B1.

Appendix C: Mixtures of active and passive Brownian particles

The following figures are taken from the supplemental information of my publication "Motility-Induced Coexistence of a Hot Liquid and a Cold Gas" published in *Nature Communications* (2024).[542]

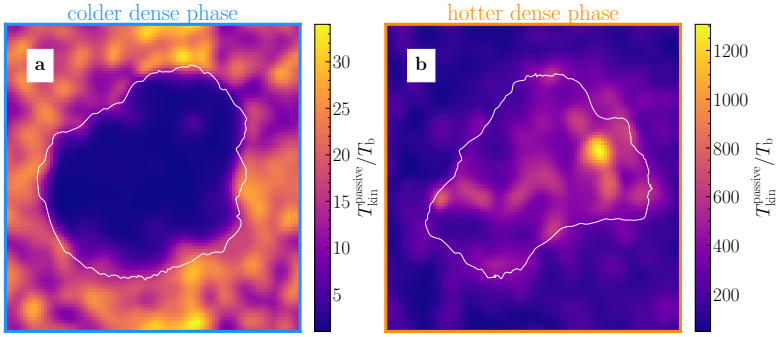

Fig. C1 Zero-inertia limit for active particles. To show that our results persist even when considering zero inertia for the active particles, we also made simulations using the overdamped Langevin equation for the active particles for the scenario **a** cold-liquid–hot-gas and the opposite scenario **b** hot-liquid–cold-gas. Here, we show the corresponding coarse-grained kinetic temperature fields. The white lines denote the border of the dense phase, which is located inside the area enclosed by the white lines. Parameters used in panels a and b are the same as in Fig. 6.2e–h and i–l in Chap. 6, respectively, but with $m_{\mathrm{a}}/(\gamma_{\mathrm{t}}\tau_{\mathrm{p}}) = 0$ and $I/(\gamma_{\mathrm{r}}\tau_{\mathrm{p}}) = 0$.

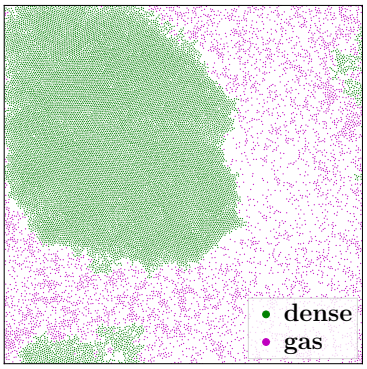

Fig. C2 Distinction between dense and dilute phase. Exemplary snapshot demonstrating the distinction between particles in the dense and the dilute phase obtained from the identification of the largest cluster. Here, a cluster is defined based on the distance between the particles such that two particles belong to the same cluster if their distance to each other is smaller than the cutoff distance $r_{\mathrm{c}} = 2^{1/6}\sigma$ of the repulsive pairwise interaction potential. Parameters: Pe $= 100$, $x_{\mathrm{a}} = 0.6$ (other parameters as in Fig. 6.4 in Chap. 6).

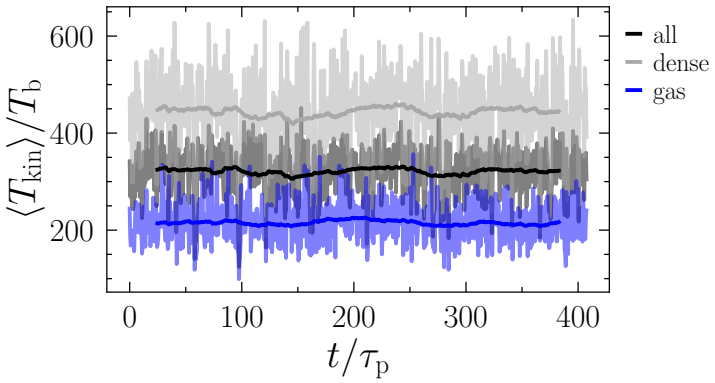

Fig. C3 Kinetic temperature over time. Kinetic temperature of the passive particles in the MIPS state over time averaged over all particles (black), particles in the dense phase (gray), and particles in the dilute phase (blue). The darker lines are moving averages. Parameters: Pe $= 400$, $x_{\rm a} = 0.9$ (other parameters as in Fig. 6.4 in Chap. 6).

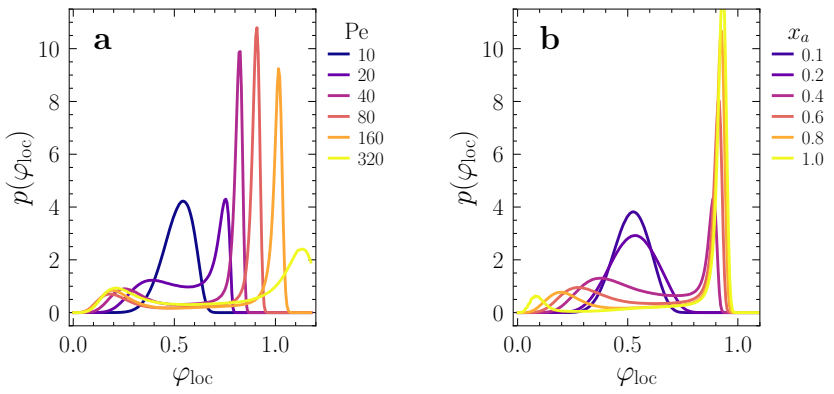

Fig. C4 Local area fraction. **a** Distribution of the local area fraction $\varphi_{\rm loc}$ at $x_{\rm a} = 0.8$ for different Pe values as given in the key. **b** Distribution of $\varphi_{\rm loc}$ at Pe $= 80$ for different $x_{\rm a}$ values as given in the key (other parameters as in Fig. 6.4 in Chap. 6). We calculated $p(\varphi_{\rm loc})$ via averages over circles of radius 5σ and over time in the steady state (see also Eq. (3.4) in Chap. 3).

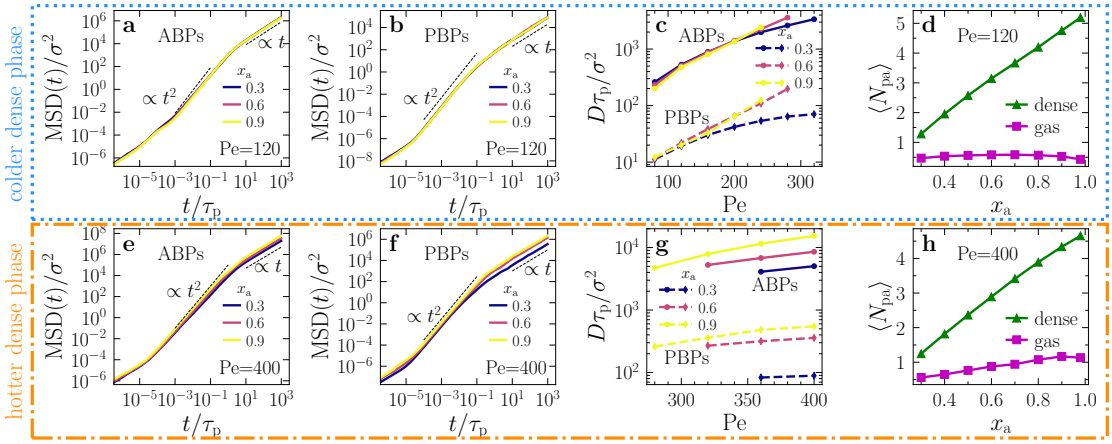

Fig. C5 Diffusive dynamics and number of active neighbors. a,b Mean square displacement (MSD; Eq. (3.1)) of the active and passive particles, respectively, for Pe $= 120$ and three values of x_a as shown in the key. **c** Long-time diffusion coefficients (obtained from a fit to the long-time MSD) of the ABPs (solid lines) and PBPs (dashed lines) in region ($\mathrm{II_a}$) of the phase diagram (cf. Fig. 6.8 in Chap. 6). **e,f** MSD of the active and passive particles, respectively, for Pe $= 400$ and three values of x_a given in the key. **g** Long-time diffusion coefficients of the ABPs (solid lines) and PBPs (dashed lines) in region ($\mathrm{II_b}$) of the phase diagram (cf. Fig. 6.8 in Chap. 6). **d,h** Mean number of active particles in contact with passive particles (i.e., with a distance smaller than the cutoff distance r_c of the WCA potential) for Pe $= 120$ and Pe $= 400$, respectively. All other parameters are the same as in Fig. 6.4 in Chap. 6.

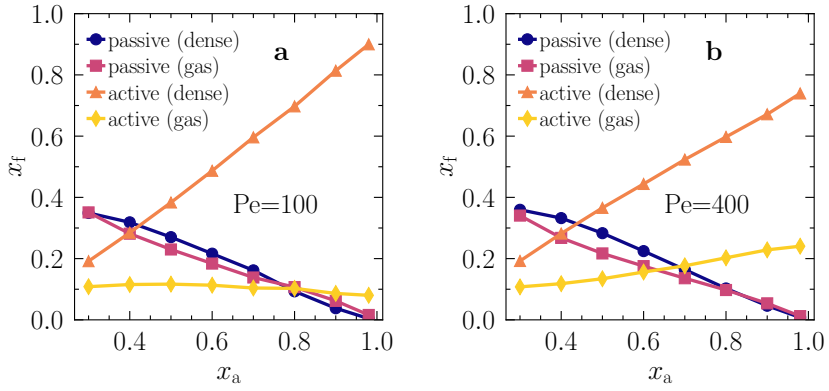

Fig. C6 Fraction of particles in dense and dilute phases. Fraction $x_f = N/(N_a + N_p)$, where N denotes the number of active or passive particles in the dense or dilute phase **a** at Pe $= 100$ and **b** at Pe $= 400$ (other parameters as in Fig. 6.4 in Chap. 6).

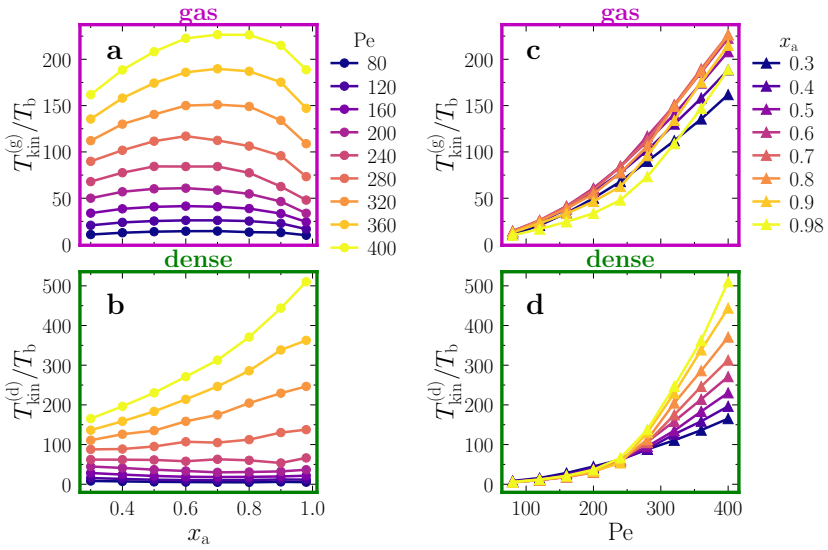

Fig. C7 Kinetic temperature. Kinetic temperature of the passive particles **a,c** in the dilute phase and **b,d** in the dense phase in the MIPS state for different values of Pe and x_a as given in the key. Parameters as in Fig. 6.4, Chap. 6.

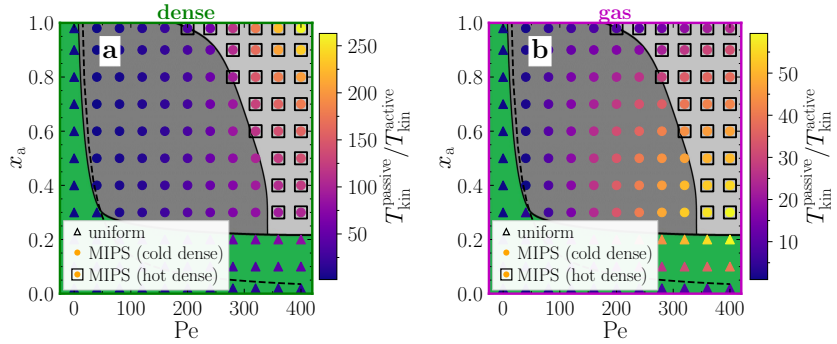

Fig. C8 Violation of the equipartition theorem. Same non-equilibrium state diagram as in Fig. 6.8, but the colors now denote the ratio of the kinetic temperature of the passive particles and the active particles **a** in the dense phase and **b** in the gas phase with values given in the key.

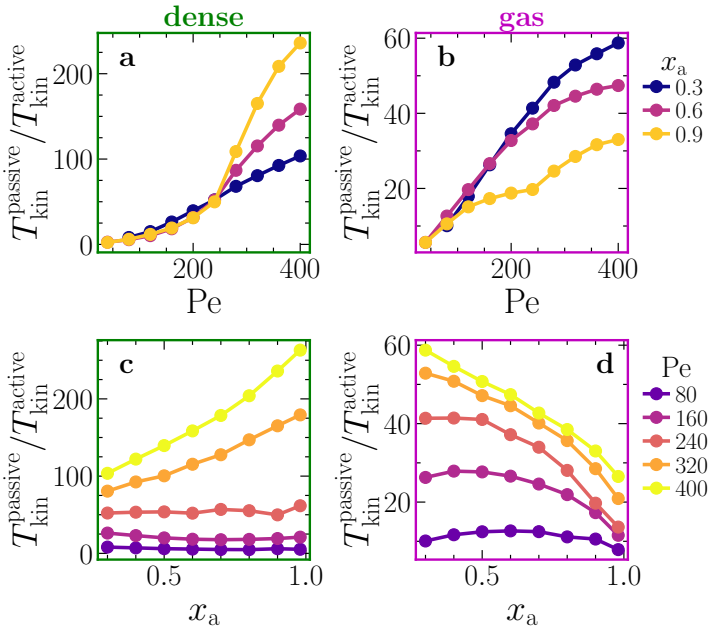

Fig. C9 Kinetic temperature ratios. Cuts through the non-equilibrium phase diagram in Fig. C8 showing the ratio of the kinetic temperature of the passive particles and the active particles **a**,**b** as function of Pe for three different values of x_{a} given in the key and **c**,**d** as function of x_{a} for different Pe (values are given in the key) in the dense and gas phase, respectively (other parameters as in Fig. 6.4).

Appendix D: Writing into water

This section contains additional information about the experiments from Nadir Möller and co-workers from the group of Prof. Thomas Palberg at Johannes Gutenberg-Universität Mainz as well as additional figures. Most parts are reprinted from our joint publication "Writing into water" published in *Small* (2023) with permission from John Wiley & Sons, Inc. (Ref. [624], © 2023 The Authors. Small published by Wiley-VCH GmbH.) or from its Supporting Information.

Experimental details

For completeness, the details about the experiments as published in my publication "Writing into Water" published in *Small* (2023) are reprinted here with permission from John Wiley & Sons, Inc. (Ref. [624], © 2023 The Authors. Small published by Wiley-VCH GmbH.).

Sample preparation: As pens, we mainly used micro-gel based cationic IEX beads (C-IEX45, Purolite Ltd, UK). The mean diameter ($2a_{\mathrm{IEX}} = 45 \pm 2.3\,\mu\mathrm{m}$) was measured by image analysis. The IEX beads were recharged with H+ ions by washing them twice in aqueous HCl ($20\,\mathrm{v/v\%}$) solutions and subsequently rinsing them with deionized water. The beads were then stored for $48\,\mathrm{h}$ in an exicator. For some experiments, we also used anionic resin-based IEX beads or splinters thereof (A-IEX15, Mitsubishi Chemical Corporation, Japan and A-IEX-L, Carl Roth + Co. KG. Karlsruhe, Germany). These were only rinsed with deionized water and subsequently dried.

Passive ink particles were sulphate-stabilized polystyrene (PS) or silica (Si) colloidal suspensions (Microparticles, GmbH, Germany). Table D1 denotes the lab codes, Manufacturer batch nos., sizes, and ζ-potentials where applicable. Prior to use, a part of the original stock ($32\,\mathrm{wt\%}$) was diluted with deionized water to $1\,\mathrm{wt\%}$ and conditioned for some weeks in a flask containing mixed-bed IEX (Amberjet, Carl Roth GmbH + Co. KG, Karlsruhe, Germany) to remove excess ions from the production process. After deionization, the IEX was removed, and the deionized suspensions stored in contact with ambient air. Thus conditioned, they show comparably low ζ-potential magnitudes due to CO_2 adsorption.[700] CO_2 absorption can be reversed and any absorbed CO_2 removed by further contact with mixed bed IEX in strictly gas-tight flasks.[700] As compared to the merely deionized state, the deionized and de-carbonized state shows an approximately doubled ζ-potential magnitude.

The sample cell was constructed by sandwiching a chemically inert PVC ring (inner radius $R = 12.5\,\mathrm{mm}$, height $H \approx 0.2\,\mathrm{mm}$) between two standard microscopy slides ($75 \times 25 \times 1\,\mathrm{mm}$, soda lime glass, hydrolytic class 3, VWR International, Germany). The ring was fixed to the bottom slide with epoxy glue (UHU plus sofortfest, UHU GmbH, Germany). Prior to cell assembly, the glass slides were thoroughly cleaned to remove coatings and organic contaminants (washing in $1\,\mathrm{v/v\%}$ Hellmanex®III-solution (Hellma Analytics, Germany), sonication in isopropanol for 30 minutes, rinsing with deionized water, and drying in N_2 flow). Right after cleaning, their ζ-potential was $\zeta = -138 \pm 8\,\mathrm{mV}$. If stored in the dry state under ambient conditions, the ζ-potential

Tab. D1 Tracer colloids and IEX beads. Parameters of tracer colloids and IEX beads used in the experiments. ζ-potentials were determined from electrokinetic experiments using a custom-built Doppler Velocimeter.[701]

Lab code	Manufacturer batch number	Diameter, $2a$ (µm)	ζ-potential under deionized conditions (mV)
Si444	Si02-F-SC54	0.442 ± 0.054	-70 ± 3 (ambient CO_2)
Si832	SiO2-F-L1287	0.839 ± 0.031	-68 ± 3 (ambient CO_2) -108 ± 5 (de-carbonized)
Si2.1	SiO2-F-L4255-1	2.11 ± 0.18	N/A
PS2.3	PS/Q-F-L2090	2.30 ± 0.22	-35 ± 3 (ambient CO_2) -65 ± 5 (de-carbonized)
C-IEX45	CGC50 x 8	45 ± 2	N/A
A-IEX-L	K306.2, Amberlite	250–400	N/A
A-IEX15	CA08S	$15.0 \pm 1,6$	N/A

magnitude decreases and equilibrates at $\zeta = -105 \pm 5$ mV. The magnitude can be reduced further to $\zeta = -70 \pm 5$ mV by immersing the slides for one hour in diluted deconex® cleaning solutions (5 v/v%, deconex®11, VWR, Germany).

Line imaging: Cells were mounted on the stage of an inverted microscope (DMIRBE, Leica, Germany) and writing was observed at 10x magnification with a 12.87 Mpx. consumer DSLR (D700, Nikon, Japan) using a 0.63x mounting tube. In the images, 100 px correspond to 0.93 µm. Images were captured in 14 bit RAW format at intervals of 4 s, converted to TIFF, and stored. Videos and cropped images for display were constructed from the TIFF color-images. Data for further evaluation were converted to gray-scale and analyzed using a custom-written Python script. For $c \leq 0.2$ wt% of Si832, the recorded intensity was proportional to the tracer concentration, showing the absence of multiple scattering effects (Fig. D1c). Line profiles are constructed from intensity readings perpendicular to the line axes. For an individual profile, each $I(y)$ is an x-average over ten neighboring pixels. Typically, 50 individual profiles obtained from locations distributed over a distance of approximately 100 µm along the written line were averaged to improve statistics. From fits of a Gaussian to the averaged profile, we extracted the line amplitude, standard deviation, and full width at half maximum.

Particle image velocimetry: For flow-field imaging, we studied the stationary-state motion of tracers using either the DSLR at 10x magnification and 20 fps or (for smaller tracers) a fast monochromatic camera (acA133-200um, Semi Python 1300, Basler, Germany) at 20x magnification and 100 fps. Flow fields were calculated from image pairs separated by $\Delta t = 100$ ms using the OpenPIV Python package.[702] For each location, the results were averaged over 50 successive image pairs.

pH microphotometry: For pH mapping, we employ a further refined version[667] of the general photometric approach reported by Niu et al.[669] A diluted mixture of two universal indicators (pH 4–10, Merck, Germany; pH 1–5, Sigma-Aldrich, USA, ratio 1:7) was injected into the sample dispersion ($c = 100$–$200\,\mu\text{mol}\,\text{L}^{-1}$). Images were recorded in transmission under Köhler illumination ($\Delta I(x,y)/\langle I\rangle = 0.015$) using the DSLR camera. The 4.256×2.832 pixels on the CMOS-sensor are arranged in a Bayer pattern for the three RGB-channels resulting in dots of four px each, defining the maximum spatial resolution. For each dot, we compared the recorded channel intensities to those of a reference sample (deionized water) to obtain the absorbance in each channel from the Beer-Lambert-Law. Calibration was performed using pH-buffer solutions ranging from pH $= 1.9$ to 8.9 in 0.5 pH steps. For intermediate values, we used bicubic interpolation. We improved the signal-to-noise ratio by binning to 6x6 dots, reducing the final resolution to 357x237 blocks. At 10x magnification, we have $5.8 \times 5.8\,\mu\text{m}^2$ per block. In the pH range of interest (4 to 6), a height averaged pH-gradient resolution of $0.02\,\text{pH steps}/6\,\mu\text{m}$ results. Results are modeled by numerical solutions of the three-dimensional advection–diffusion equation, which also yields the pH maps at specific locations, e.g., at the cell bottom.[667]

Line evolution past the line focus

The linewidth in the decay region depends on both the tracer concentration and the IEX speed. Figure D1a shows snapshots of C-IEX rolling through Si832. From top to bottom, the tracer concentration c increases, and the velocities vary in the range of $v_{\text{IEX}} = 6$–$12\,\mu\text{m}^{-1}$. With increasing c, the background intensity increases and the lines appear thicker.

For each line in Fig. D1a, we recorded the intensity profiles $80\,\text{s}$ after IEX passage, i.e., far past the line focus and show these in Fig. D1b. For better statistics, we averaged over a trail length of $50\,\mu\text{m}$. All five density profiles are well described by Gaussians superimposed on a flat background. The fits return the standard deviation σ, which relates to the Full Width at Half Maximum (FWHM) as $2.355\sigma = \text{FWHM}$. From independent measurements on Si832 layers equilibrated at $\vartheta = 0$ and performed under exactly identical illumination, we found the dark field scattered intensity to increase with a power law dependence as $I \propto c^a$ (Fig. D1c). Fitting a linear function to the data in the double logarithmic plot of Fig. D1c returns an exponent of $a = 0.85 \pm 0.04$. This is close to but below the expectation of light scattering theory for dilute suspensions of $a = 1$. The observed small deviation is attributed to tracer-tracer repulsion, which leads to the development of fluid order and in turn, decreases the forward-scattering. Figure D1d shows the time-dependent FWHM extracted from the concentration-dependent experiments in Fig. D1a. The black arrow marks $t = 80\,\text{s}$ used in Fig. D1b. All curves increase roughly linearly in this double-logarithmic plot. The feature marked by the blue arrow is caused by the passage of a blob also seen in Fig. D3a. As expected, the curves get wider for increasing concentrations, but the vertical spacing between the curves does not match exactly with the increase in weight fraction. This could be due to the different velocities of the IEX in Fig. D1a. We therefore determined the velocity dependence of line widths in independent measurements at constant tracer concentration.

Figure D1e shows the data for $c = 0.18\,\text{wt}\%$. Here, we averaged over five to ten IEX beads per adjusted tilt angle. The large standard deviation in the measured IEX speed

is attributed to the size dispersity of the IEX. The widths decrease systematically with increasing velocity. Data in this double logarithmic plot are well described by a power law with exponent -1.02 ± 0.09. This is remarkably close to -1. The comparably large uncertainty of the fit and the small deviation are again attributed to variations in IEX size. We use the result to rescale the data of Fig. D1d to $v_{\mathrm{IEX}} = 8\,\mu\mathrm{m\,s}^{-1}$. The velocity-scaled datasets are displayed in Fig. D1f. The datasets are now spaced more evenly. The velocity-scaled FWHM at $t = 80\,\mathrm{s}$ is shown in dependence on concentration in Fig. D1g. The data in this double-logarithmic plot are well described by a power law of exponent $a = 0.51 \pm 0.02$. We use the result to rescale the data in Fig. D1f to $c = 0.1\,\mathrm{wt}\%$. The velocity- and concentration-scaled data are plotted double-logarithmically in Fig. D1h versus time after IEX passage. All data arrange neatly along a single curve. Fitting a linear function to the data returns a power-law behavior FWHM $\propto t^{\lambda}$ with exponent $\lambda = 0.48 \pm 0.04$. This is close to the theoretical expectation of $\lambda = 0.5$ for free diffusion.

We stress that these data were taken by averaging over only a few IEX at each inspected set of boundary conditions. The observed scaling behavior should therefore be taken with due caution. However, even these preliminary data are well compatible with a simple scaling behavior for the line width as FWHM $\propto v_{\mathrm{IEX}}^{-1} c^{1/2} t^{1/2}$. The v-scaling would be expected as long as the IEX accretes the tracers with a constant solvent flux arriving at its surface. This is reasonable due to the large exchange capacity of the IEX and the low concentration of residual cations. The t-scaling is expected for a purely diffusive decay.

Shaping the formation zone

In this section, we consider the influences of tracer charge, substrate charge, and pH-gradient strength. For C-IEX45 rolling in Si832 (cf. Tab. D1), we observe significant changes of the shape of the formation zone but no effects for the decay zone. The changes in the formation zone relate to a systematic variation in the approach-distance of the tracers.

The pH gradient induces significant DO flows along a highly charged substrate, which transport low-charge tracers towards the IEX. The approach velocity measured between $200\,\mu\mathrm{m}$ and $50\,\mu\mathrm{m}$ distance from the IEX center was used to describe this approach in terms of an effective attraction exerted by the IEX (Fig. 7.5, Chap. 7). At shorter distances, the hydrodynamic flow pattern is significantly more complicated due to upward components in the solvent motion, the complex geometry of the wedge between IEX and substrate, hydrodynamic and direct tracer-tracer interactions, and the presence of an additional type of phoretic flow. In fact, low-charge or uncharged tracers are halted by these effects very close to or even underneath the IEX center. The exact stopping distance is not accessible in the flow field measurements due to shading by the IEX. We accounted for these phenomena in an effective way by adding a repulsive component to the total effective force in the particle model and the continuum model (see Subsec. 7.3.2 and Subsec. 7.3.3).

The situation differs for highly charged tracers due to the additional diffusio-phoretic slip existing at their surface.[647,648] For this case, the approach situation is sketched in Fig. D2. Relative to the tracer surface, the pH gradient induces an additional inward solvent flow (DPS, dark blue arrow), which results in an outward tracer motion (DPT, violet arrow). In the sketched situation, the tracer would still be swept further inward

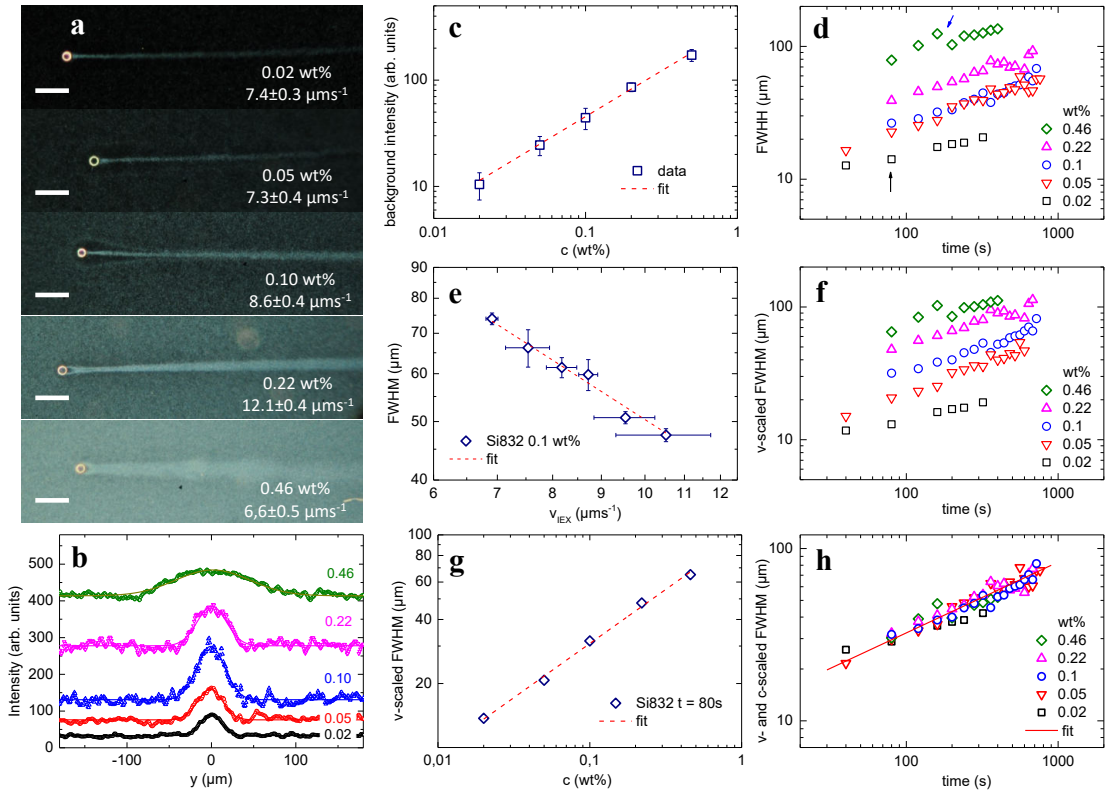

Fig. D1 Line width measurements. a Dark field snapshots of C-IEX45 (cf. Tab. D1) rolling with speeds in the range of 6–12 µm s^{-1} through Si832 of different concentrations as indicated. Scale bars: 200 µm. Concentrations and speeds are indicated in each image. **b** Line profiles recorded 80 s after IEX passage. The solid lines are fits of a Gaussian with an offset corresponding to the background scattering intensity. **c** Double-logarithmic plot of the concentration dependent scattering intensity in dark field images of tracers equilibrated on a horizontal substrate. The fit of a linear function to the data returned a power law exponent of $a = 0.85 \pm 0.04$. **d** Double-logarithmic plot of the time dependent FWHM for the five experiments shown in panel a. **e** Double-logarithmic plot of the dependence of linewidth on IEX speed for C-IEX45 rolling through Si832 at 0.18 wt%. The fit of a linear function to the data (dashed line) returns a power law exponent of -1.02 ± 0.09. **f** Double-logarithmic plot of the time-dependent FWHM scaled to $v_{\mathrm{IEX}} = 8\,\mu\mathrm{m\,s}^{-1}$. **g** Double-logarithmic plot of the v-scaled FWHM in dependence on the Si832 concentration. The fit of a linear function to the data (dashed line) returns a power law exponent of 0.51 ± 0.02. **h** Double-logarithmic plot of the time-dependent FWHM scaled to $v_{\mathrm{IEX}} = 8\,\mu\mathrm{m\,s}^{-1}$ and $c = 0.1$ wt%. The fit of a linear function to the complete data (solid line) returns a power law exponent of $\lambda = 0.48 \pm 0.04$.

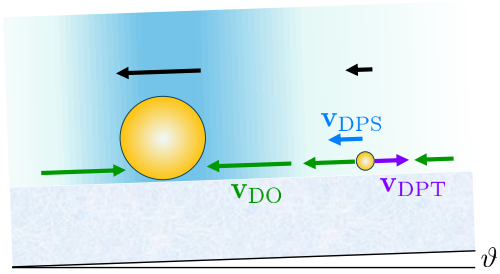

Fig. D2 Relevant velocities during tracer approach. Due to gravity, both IEX and tracers roll down the substrate tilted by an angle ϑ (black arrows). The incompressible solvent flows with local velocities $\mathbf{v}_{\mathrm{DO}}(x, y)$ under the influence of the pH field (indicated by the background shading). The DO flow accelerates as it converges at the IEX (green arrows). The pH gradient further induces a diffusio-phoretic (DP) slip at the charged tracer surfaces. This results in an inward solvent flow (DPS, dark blue arrow) relative to the tracer surface and an outward tracer motion (DPT, violet arrow).

towards the IEX. However, with increasing gradient strength, v_{DPT} will increase until it equals v_{DO}, and the tracer becomes stalled.

To vary the relative weight of the two phoretic flows, we systematically varied the charge ratio $\zeta_{\mathrm{T}}/\zeta_{\mathrm{S}}$ between tracers and substrate. The experiments discussed in Chap. 7 were performed with deionized tracer suspensions equilibrated in contact with ambient air. Due to CO_2 adsorption, their ζ-potential is low,[700] and diffusio-phoretic (DP) flows are of negligible magnitude except very close to the IEX surface, where the pH gradients are strongest. We de-carbonized the tracers and charged them up by prolonged batch deionization removing CO_2 through ion exchange of its dissociation products (carbonic acid). Further, a reduced substrate ζ-potential was obtained by storing the substrate slides in diluted deconex® cleaning solutions. A stepwise increase in charge ratio had a significant influence on the minimum approach distance. It drastically altered the shape of the formation zone but left the decay unaffected. This is shown in Fig. D3a-d. For charge ratios $\zeta_{\mathrm{T}}/\zeta_{\mathrm{S}} \leq 1$, we typically observe the single HDW-lines to start directly at the IEX (Fig. D3a). As the charge ratio increases, we observe the evolution of sharply bordered, more or less drop-shaped exclusion zones of increasing size.

Bright field images and tracer flow fields corresponding to the dark field images in Fig. D3a, b, and d are presented in Fig. D4. In Fig. D4a, we studied the low-charge tracers on a native substrate. Here, the tracer motion directly reflects the underlying DO-flow field. In Fig. D4b and c, we used larger charge ratios, but left all other boundary conditions unchanged (tracer concentration, exchange rate, IEX velocity). Therefore, the underlying solvent flow pattern must remain unaltered. In Fig. D4b and c, however, we now see a significant alteration of the tracer flow field.

With increasing charge ratio, DP flows gain in strength and importance. Hence, tracers approaching the IEX at its front are stalled already at some distance to the IEX, while tracers initially located in the immediate vicinity of the IEX move outward (Fig. D4c). A tracer depleted region forms. Comparison to the bright field images shows that tracers accumulate exactly where outward DP motion and inward DO flow balance and the tracer velocity vanishes: $v_{\mathrm{T}} = v_{\mathrm{DPT}} + v_{\mathrm{DO}} = 0$. As the IEX passes, the accumulation region first

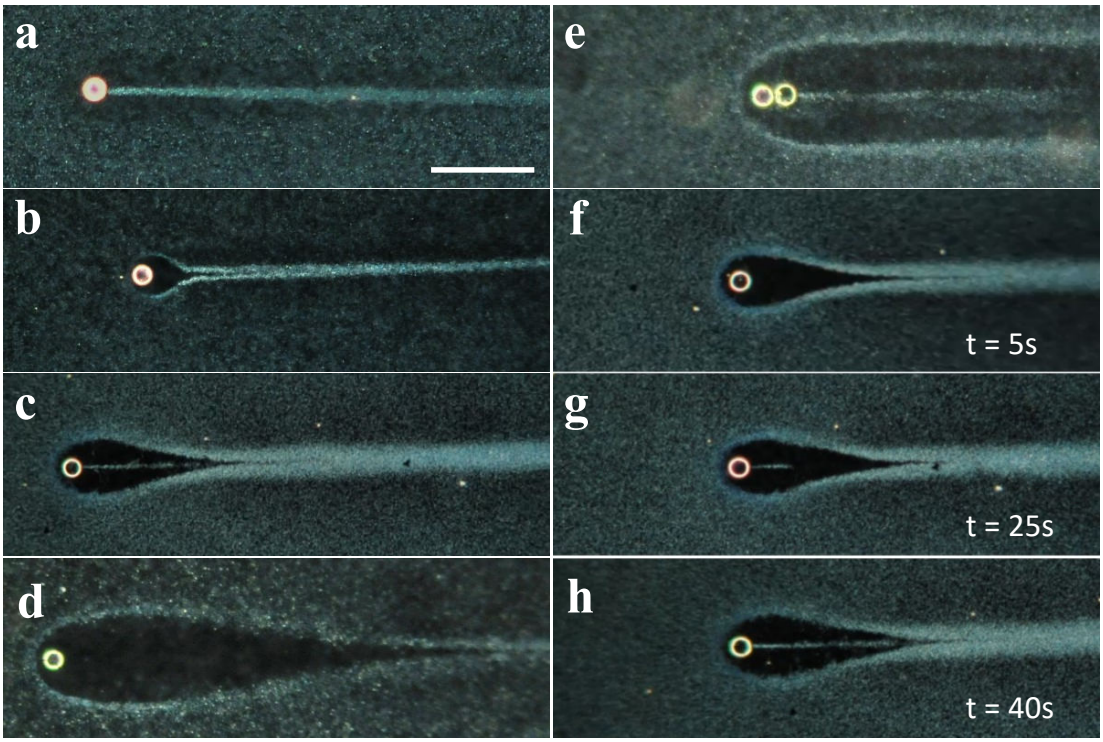

Fig. D3 Manipulating the shape of the line formation zone. Dark field images of C-IEX45 (cf. Tab. D1) rolling through Si832 at $\vartheta = 3.1$ ($v_{\mathrm{IEX}} = 7.7\,\mu\mathrm{m\,s^{-1}}$). Scale bars: $200\,\mu$m. Here, we changed the minimum approach distance by varying the charge ratio $\zeta_{\mathrm{T}}/\zeta_{\mathrm{S}}$. **a** $0.02\,\mathrm{wt\%}$ Si832, salt free but non-decarbonized ($\zeta_{\mathrm{T}} = -68\,\mathrm{mV}$) on a native substrate of $\zeta_{\mathrm{S}} = -105\,\mathrm{mV}$. Note the slight depletion of Si832 from the immediate IEX surroundings. **b** Same as in panel a, but after de-carbonizing Si832 for 1 h ($\zeta_{\mathrm{T}} = -80\,\mathrm{mV}$) and on a deconexed substrate ($\zeta_{\mathrm{S}} = -70\,\mathrm{mV}$). **c** Same as in panel a, but after de-carbonizing Si832 for 24 h ($\zeta_{\mathrm{T}} = -102\,\mathrm{mV}$) on a deconexed substrate ($\zeta_{\mathrm{S}} = -70\,\mathrm{mV}$). **d** Single IEX rolling in $0.16\,\mathrm{wt\%}$ Si832 deionized for 21 d ($\zeta_{\mathrm{T}} = -108\,\mathrm{mV}$) on a deconexed substrate ($\zeta_{\mathrm{S}} = -70\,\mathrm{mV}$). **e** IEX-pair rolling through $0.16\,\mathrm{wt\%}$ Si832 deionized for 21 d ($\zeta_{\mathrm{T}} = -108\,\mathrm{mV}$). **f–h** Temporal development of the pattern seen in panel c. Snapshots were taken at different times after the start of the experiment as indicated in the key.

shifts outward, then inward again. Tracers in this boundary are carried along as it shifts inward again (Fig. D4b). The evolution of the drop-shaped formation zone in Fig. D3a-d is thus seen to originate from changes in the location, where outward DP tracer motion and inward DO solvent flow balance.

Our observations can be rationalized considering that both DP and DO flows originate from the same electrophoretic effect (i.e., from the drop in chemical potential across a charged surface as induced by the increase in the pH of the adjacent solvent) but differ in the relevant type of surface and hydrodynamic boundary conditions. The DP flow originates on the tracer surface, i.e., it reacts to the tracer ζ-potential and the local pH gradient. Here, the theoretical concepts of bulk diffusio-phoresis in a quiescent solvent can be directly applied after suitable coordinate transformation.[647,648] By contrast, the DO flow in any volume element above the substrate originates from both the local contribution (depending on the substrate ζ-potential and the local pH gradient) and

the global hydrodynamic flow pattern. The latter depends on the difference in pH between IEX surface and the background solvent but is also subject to modifications by the hydrodynamic boundary conditions of an extended substrate (and of a closed cell of finite volume). Such a situation is not analytically accessible but may be addressed in numerical calculations.[657] Note that therefore, the DP tracer motion follows the local gradient direction, and the DO solvent motion does not need to be co-linear.[680] This can clearly be seen by comparing the solvent flow field of Fig. D4a to the tracer flow fields in Fig. D4b and c.

The differences in the position dependence of the two flows become relevant at increased tracer ζ-potentials. Irrespective of ζ_T, the tracer DP velocity drops quickly with increasing distance to the IEX, respectively the distance from the trail ridge. As the local pH gradient along and perpendicular to the trail ridge vanishes with increased distance to the IEX, it becomes negligibly small. By contrast, the DO flows —depending on the large-scale pH differences— are still active far past the IEX. They retain considerable strength, focus the line, and close the initial depletion zone (Fig. D4b). A single line results. With increasing tracer ζ-potential, the closing point shifts further away from the IEX. However, the splits always close and a single line is obtained past the line focus as long as a single C-IEX45 is used. By contrast, using a pair of IEX approximately doubles the local pH-gradient while leaving the global pH difference between IEX surface and background unchanged. This shifts the minimum approach distance still further outward. Tracers are now accumulated along a contour far off the IEX center, where the inward DO flow is still very slow (Fig. 7.2). Thus, they can avoid inward transport by the DO flow after IEX passage. The DP split becomes stabilized (Fig. D3e).

Quite frequently, an additional line is formed starting at the center of the IEX back (Fig. D3f–h). Interestingly, it starts with some delay. Presumably assisted by fluctuations, few tracers reach the IEX, beneath which they are trapped by the solvent flows and expelled once the loading capacity of the IEX is reached. In this type of tracer accumulation at the IEX, the feeding rate is way smaller than by direct DO flow causing the delay. Simultaneously, the IEX velocity slightly increases by some 5–$10\,\%$ and the depleted region slightly stretches. Both indicates a phoretic contribution of the trapped tracers to the propulsion, as well known from modular swimmers.[665] Due to a low feeding rate, this line type typically contributes only little to the merged line in the decay regime.

Alternative ink and alternative pens

The modularity of our approach allows facile testing of the effects introduced by alternative components. By varying the size of silica tracers, both line graininess and contrast can be varied. This is demonstrated in Fig. D5 for three species of Si tracers with different sizes as indicated. In all three cases, we used the same tracer concentration $c = 0.1\,\mathrm{wt}\%$. With decreasing tracer size, both graininess and contrast decrease. For the largest tracers, the lines obtain a “pointillistic” appearance. They become smoother at lower tracer size, but at the same time loose contrast, as scattering power scales with a_T^{-6}. Next, we exchanged the silica particles for polystyrene particles of lower mass density (PS2.3, $\rho_\mathrm{PS} = 1.05\,\mathrm{kg\,m^{-3}}$). Three representative images are shown in Fig. D6. The use of lighter tracers generally leads to lines blurred by convection. For tracers of low charge (Fig. D6a and b), regions of enhanced density form way above the focusing DO flows along the substrate. For

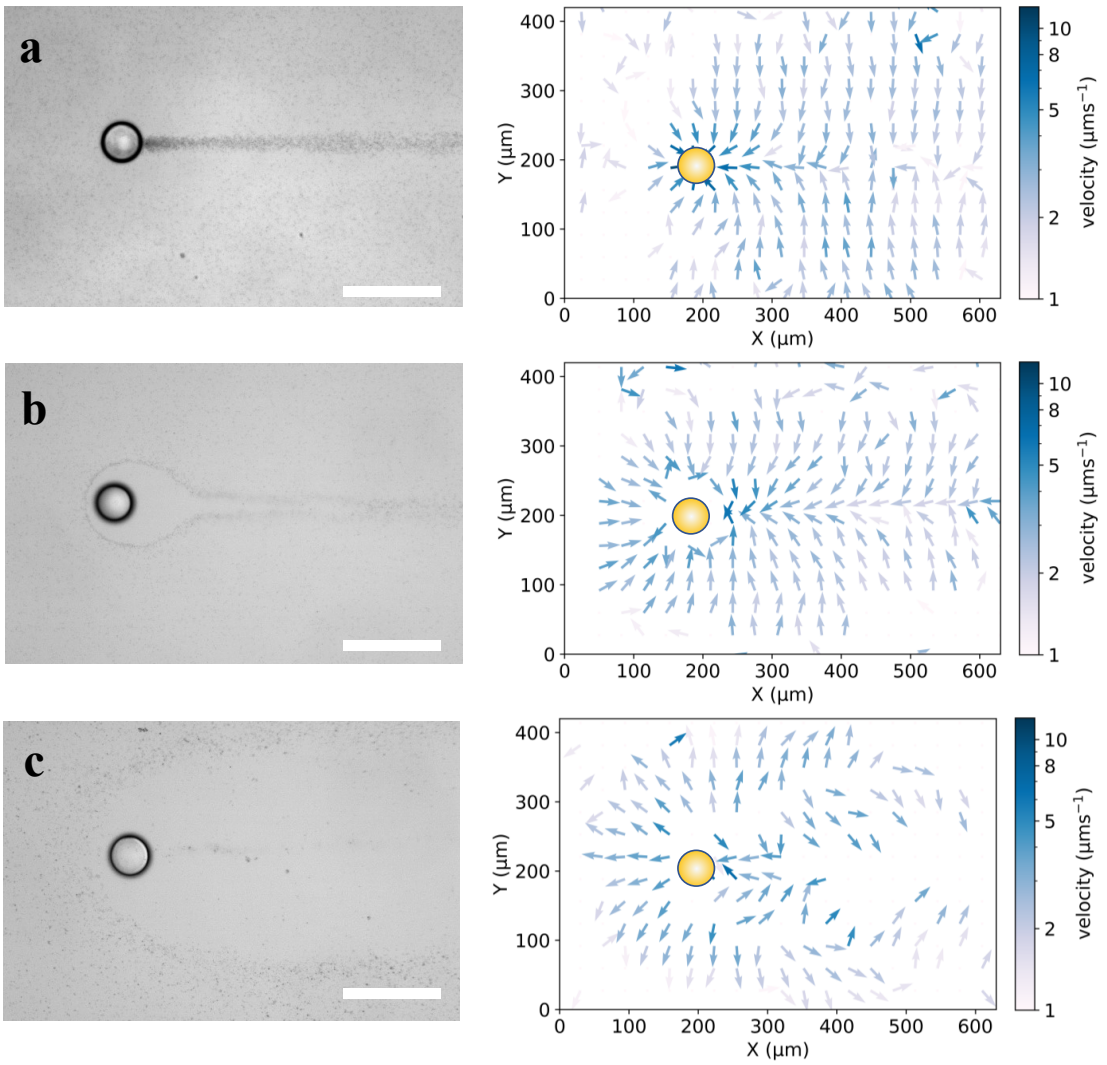

Fig. D4 Flow analysis. Bright field images (left, scale bar $100\,\mu m$) and tracer flow fields (right) for C-IEX45 (cf. Tab. D1) rolling at $3.1°$ inclination ($v_{IEX} = 7.7\,\mu m\,s^{-1}$). The flow direction is given by the orientation of the arrows and the instantaneous lab-frame velocity is encoded by the arrow color as indicated in the key. Images and maps were recorded for C-IEX45 rolling on differently charged glass substrates through $0.10\,wt\%$ Si832 tracers. **a** Salt free but not de-carbonized tracers ($\zeta_T = -68\,mV$) on a native substrate of $\zeta_S = -105\,mV$ (same conditions as in Fig. D3a). Under these conditions, DP flows are negligible and the tracer flow field coincides with the solvent flow field. **b** Si832 deionized for 1 h ($\zeta_T = -80\,mV$) on a deconexed substrate of $\zeta_S = -70\,mV$ (same conditions as in Fig. D3b). The tracer flow field shows significant differences when compared to the previous situation. **c** Si832 deionized for 21 d ($\zeta_S = -108\,mV$) on a deconexed substrate of $\zeta_S = -70\,mV$ (same conditions as in Fig. D3d). Note the now extended region of outward tracer motion next to the IEX in the velocity maps.

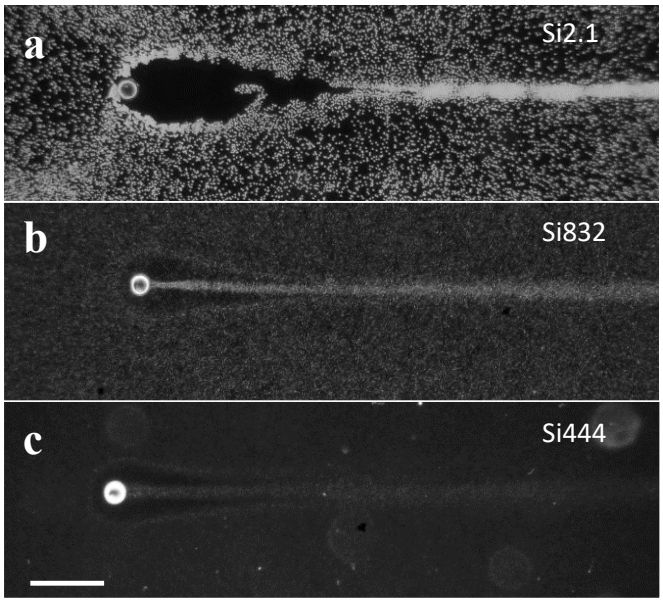

Fig. D5 Variation of graininess and optical line contrast. Moderately de-carbonized C-IEX45 (cf. Tab. D1) rolling at $v_{\mathrm{IEX}} = 8.4\,\mu\mathrm{m\,s^{-1}}$ on low-charge substrates. Scale bar: $250\,\mu\mathrm{m}$. **a** Si2.1 at $c = 0.1\,\mathrm{wt\%}$. **b** Si832 at $c = 0.1\,\mathrm{wt\%}$. **c** Si444 at $c = 0.1\,\mathrm{wt\%}$.

highly charged tracers (Fig. D6c), the broadening is additionally enhanced by outward DP motion, which leads to an upward motion already at some distance from the IEX surface. Overall, the use of tracers with low mass density leads to very low contrast and thus, is not useful for writing.

We next checked different types of pens for their capacity to write lines. The examples in Fig. D7 feature inert rafts of Si832 tracer particles. These were made by slowly drying Si832 suspensions. The rafts were either free to glide through Si832 or were fixed and passed by the tracers. This resulted in short trails, which mainly depend on the shape, orientation, and velocity of the rafts. Figure D7a shows a mobile raft simply ploughing through the tracer layer. Here, a region of enhanced tracer density forms at its front as well as a short tracer-depleted region in its wake. Figure D7b shows a triangular raft fixed in a hydrodynamically favorable orientation. As the tracers drift by, a short trail of slightly increased tracer density forms downstream. Lacking pH gradients, pens made of chemically passive rafts do not trigger DO flows. Line shape and contrast are therefore fully determined by the laminar flow field around these differently shaped and oriented objects. However, in all cases, only very short lines resulted, even at larger gliding velocities. Thus, without attraction, no useful lines are written.

We further replaced the cationic IEX by anionic IEX (A-IEX) and compiled the main results in Fig. D8. This resin type exchanges residual carbonate ions for OH^-. Thus, it increases the pH. A-IEX-L (cf. Tab. D1) features large exchange rates for CO_3H^- available at concentrations of several $\mu\mathrm{mol\,L^{-1}}$. They create a pronounced pH variation of complex shape featuring a pH maximum at some distance to the IEX surface (Fig. D8a).[680] On its outer side, i.e., pointing away from the IEX, the pH field is contoured by an inverted gradient (blue arrow in Fig. D8b). Small hydrogel-based A-IEX15 spheres (cf. Tab. D1)

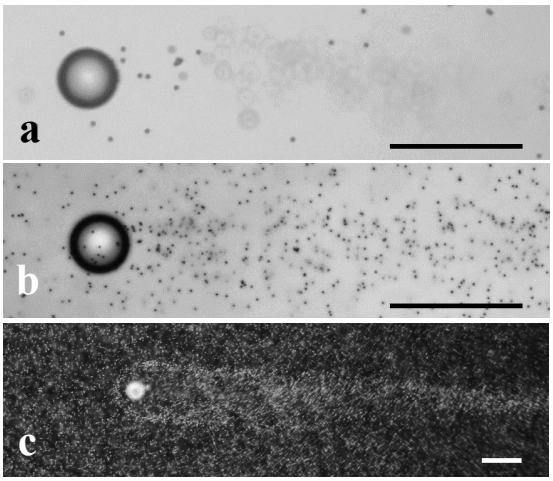

Fig. D6 Weak-contrast lines written by C-IEX45 in different suspensions of light tracers. Scale bars: $100\,\mu$m. **a** Bright field image of C-IEX45 (cf. Tab. D1) rolling on an inclined substrate ($\vartheta = 2.3°$) in a dilute suspension of PS2.3 ($\zeta_T = -35$ mV, Tab. D1). The tracers in focus approach the C-IEX along the substrate. The actual trail forms above (blurred tracer images). **b** The same situation but now focused to some $150\,\mu$m above the substrate. **c** Dark field images of C-IEX45 rolling on an inclined substrate ($\vartheta = 2.3°$) in suspension of decarbonized PS2.3 ($\zeta_T = -65$ mV, Tab. D1) at $0.10\,$wt%.

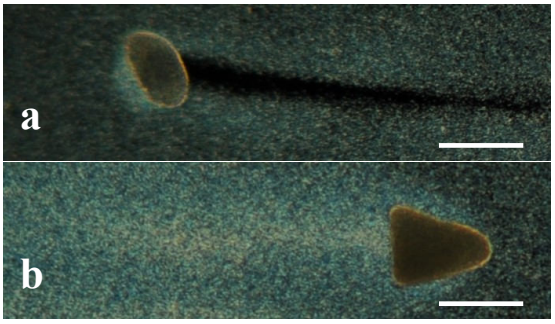

Fig. D7 Writing with inert objects. Dark field images of weak trails formed by inert objects moving through suspensions of tracer particles. Scale bars: $100\,\mu$m. **a** Chemically inert raft of dried Si832 gliding down an inclined substrate ($\vartheta = 7.6°$) in a suspension of Si832 at $0.10\,$wt%. **b** Chemically inert raft of dried Si832 fixed to an inclined substrate ($\vartheta = 7.6°$) in a suspension of Si832 at $0.10\,$wt%.

show somewhat lower exchange rates and lower capacities. These create a simpler pH field with only negative gradients but of much weaker amplitude and are well suited as pens. Negatively charged tracers approaching from the front are pushed away (both in rolling direction and sideways) by the corresponding outward DO flow (Fig. D8c). A tracer-depleted region past the A-IEX results. For combination with Si832, we found small A-IEX-L splinters to be most suitable. This combination leads to a high-contrast inverted line (Fig. D8d). Like the positive lines discussed above, also this line of negative optical contrast appears to be very stable in time (Fig. D8e).

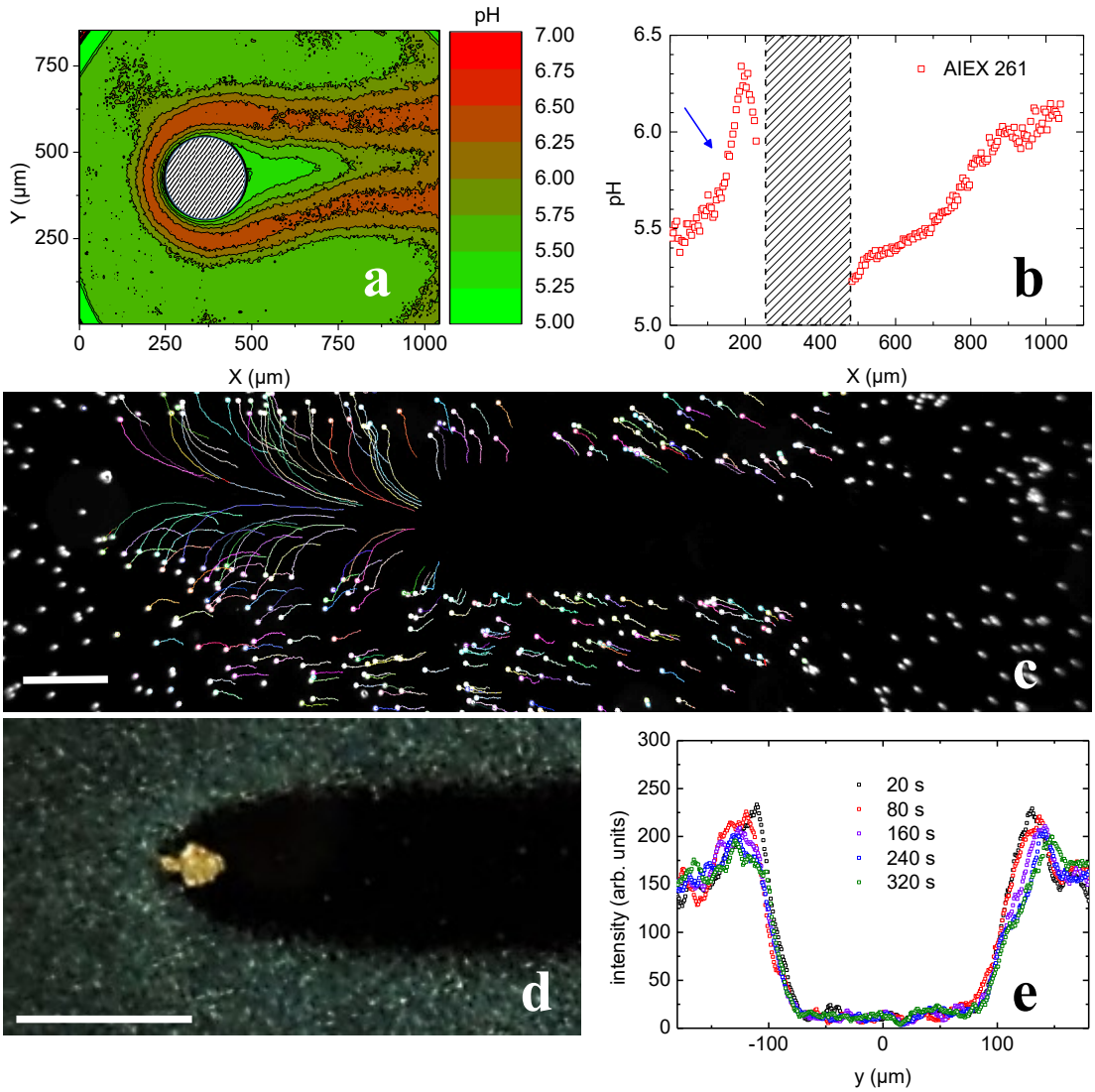

Fig. D8 Contrast inversion by inversion of the pH gradient direction. a pH map of a resin-type anionic A-IEX-L of 261 µm diameter (cf. Tab. D1). Due to the high exchange rate, a complex pH pattern evolves. **b** pH profile recorded along the rolling direction. The inverted gradient to the front of the A-IEX is indicated by the blue arrow. Note however, that the whole pH field is bordered by such an outward-decreasing pH field in panel a. **c** Tracer trajectories recorded in darkfield for a hydrogel-based A-IEX15 (cf. Tab. D1). Scale bar: 200 µm. The ensuing pH field is similar but less pronounced for this smaller resin species. Tracers are swept away from the A-IEX in forward direction and sideways. **d** Small resin-type A-IEX-L splinter gliding down an inclined substrate in Si832 at 0.1 wt% and creating a line of negative optical contrast. Scale bar: 250 µm. **e** Line profiles of the inverted line drawn in panel d for different times after A-IEX passage as indicated.

Alternative drive

In Fig. D9, we again used a cationic IEX and tracers which are gravitationally bound to the substrate. We here studied modular microswimmers, which propel on a horizontal substrate driven by the DP flow along the surfaces of assembled tracers.[665] In all three cases, we observe a characteristic shape of the formation zone, featuring a blob-like region of enhanced tracer density in the immediate back of the IEX. From that blob, a much finer line of tracers is expelled, which only slowly broadens by diffusion. Figure D9a shows a line written by tracers with different sizes past a cationic IEX resin splinter obtained from crushing a larger IEX bead.[664] It demonstrates that a spherical IEX geometry is not essential for writing, nor is a uniform tracer size. Figure D9b shows that, due to mutual repulsion between the negatively charged tracers, the raft past the IEX may take a crystalline structure. However, this has little influence on line formation. In Fig. D9c, a modular swimmer is formed by exactly the same components as used in the writing experiments discussed in Chap. 7. Again, a nice line is written past a short formation zone of enhanced tracer density.

Figure D9 demonstrates that writing does not depend on the type of steering chosen. Rather, it requires the presence of an effective attraction (here realized by DO flows). However, modular swimmers lack the ability of precise steering, they steer by statistical rearrangements of their load. Therefore, these freely propelling modular swimmers write curves instead of straight lines or prescribed patterns. In the approach presented in Chap. 7, propulsion by gravity was essential for writing straight lines as prerequisite for drawing more complex patterns.

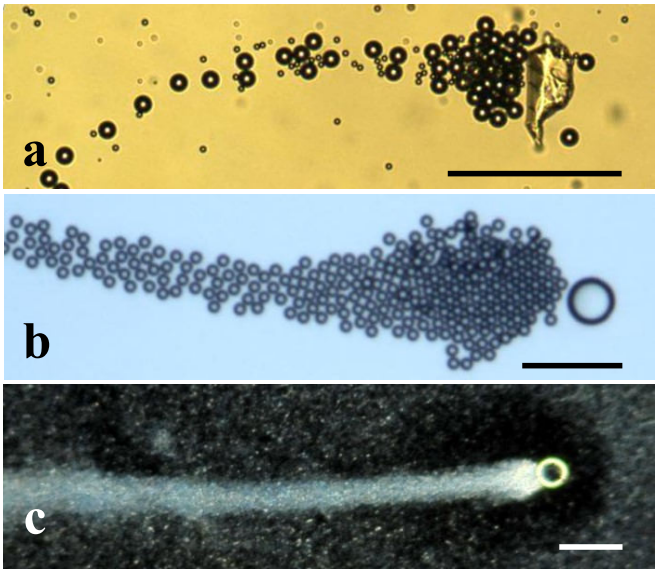

Fig. D9 Writing with self-propelling pens. Images of lines formed by different cationic IEX types on horizontal native substrates in different tracer suspensions. These objects move as modular phoretic swimmers. Scale bars: $100\,\mu$m. **a** Swimmer formed by a resin type C-IEX splinter in a dilute binary suspension of PS15, PS5.2, and PS1.7. **b** Swimmer formed by microgel-type C-IEX45 in a dilute suspension of PS10. **c** Swimmer formed by C-IEX45 in a suspension of Si832 at $0.10\,\mathrm{wt}\%$ on a horizontal substrate. Note the diffusely bordered depletion zone close to the C-IEX demonstrating the effect of the DO flows.

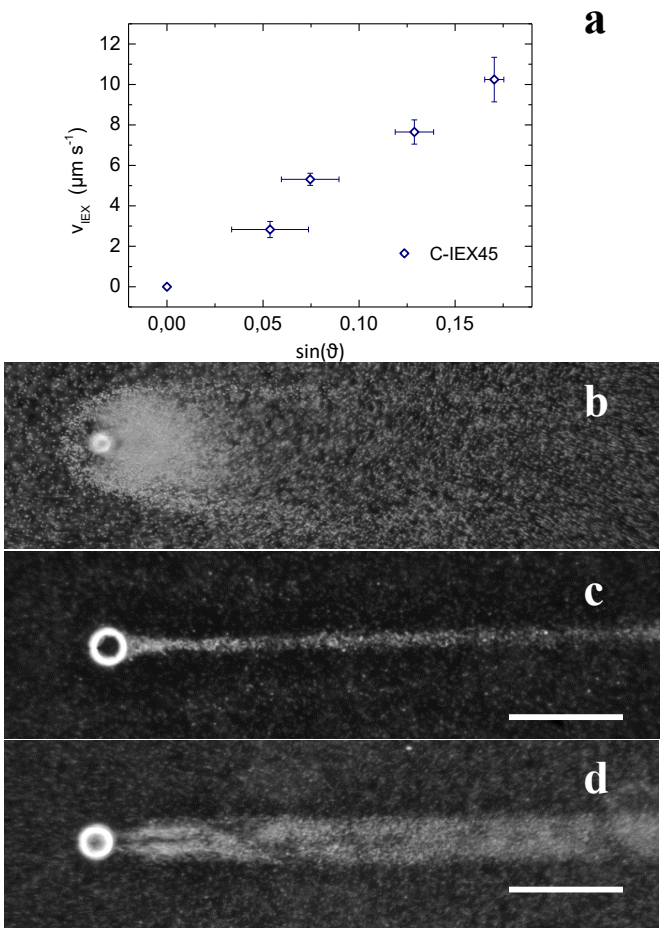

Fig. D10 Tuning the inclination. **a** Speed of C-IEX45 (cf. Tab. D1) rolling through tracer free water as a function of substrate inclination. **b–d** Dark filed images taken at different velocities of C-IEX45. Scale bars: $200\,\mu\text{m}$. **b** C-IEX45 rolling through $0.1\,\text{wt}\%$ Si2.1 at very low $v_{\text{IEX}} \approx 0.28\,\mu\text{m}\,\text{s}^{-1}$. Note the extended asymmetric accretion zone. No useful line is written. **c** C-IEX45 rolling through $0.1\,\text{wt}\%$ Si832 at $v_{\text{IEX}} \approx 7.2\,\mu\text{m}\,\text{s}^{-1}$. A straight, narrow line is obtained. **d** C-IEX45 rolling through $0.16\,\text{wt}\%$ Si832 at $v_{\text{IEX}} \approx 14\,\mu\text{m}\,\text{s}^{-1}$. Note the initial line split, which quickly washes out due to diffusion.

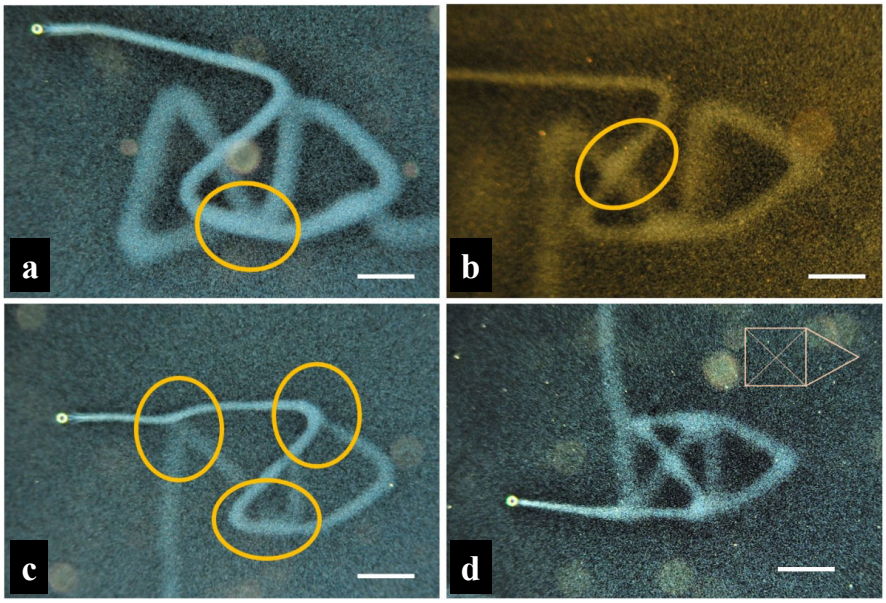

Fig. D11 Approaching a perfect drawing in experiment. By trial and error, we successively improved the adjustment of the stage programming. Scale bar: 250 µm. **a–c** Results obtained at intermediate stages. The encircled regions highlight deviations from the ideal pattern shape (line length variations, lateral line shifts, line bending, and blobbing). **d** Final result.

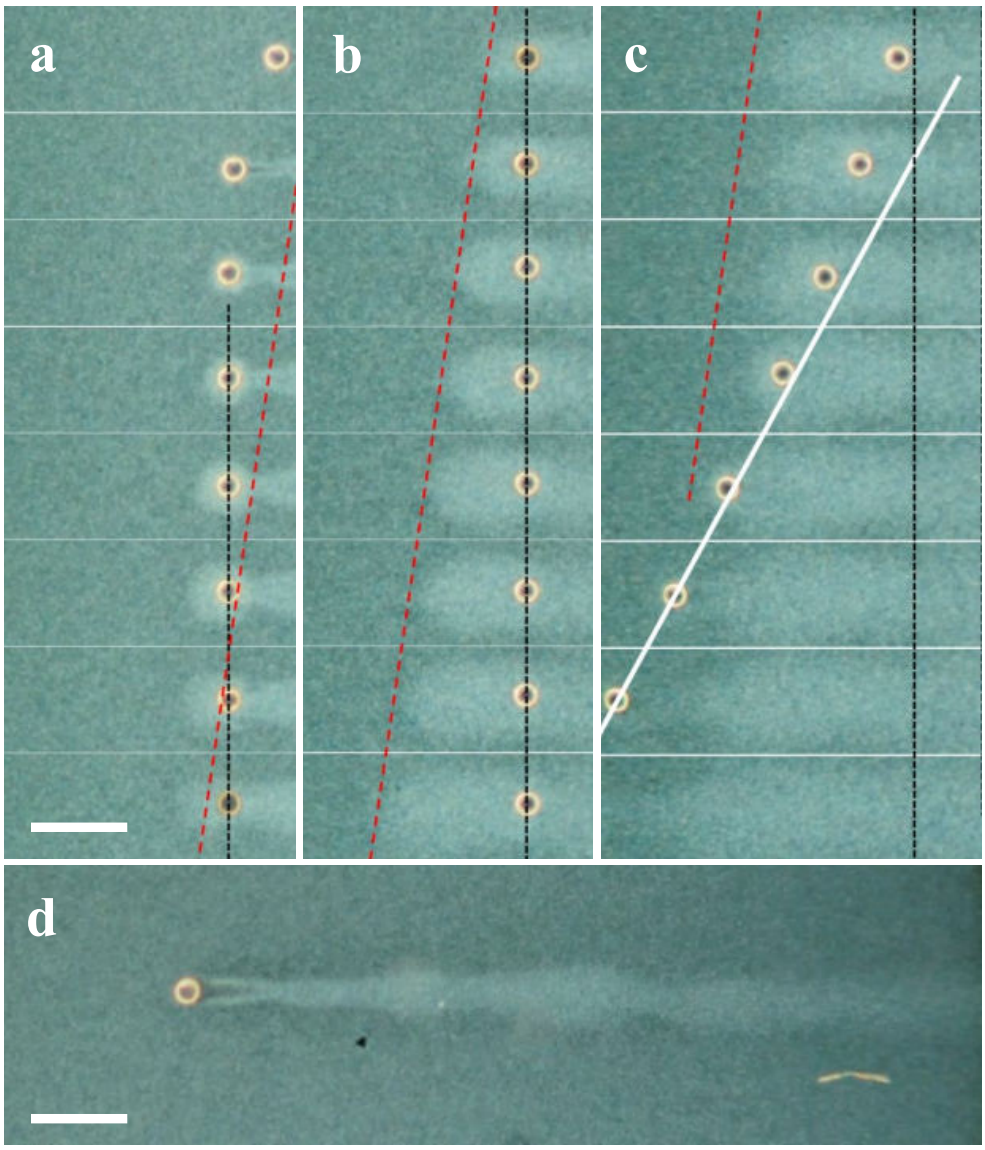

Fig. D12 Formation of a blotted line. Time series of dark field images of blob formation due to a transient sticking of the IEX to the substrate. C-IEX45 rolling through Si832 at $c = 0.2\,\mathrm{wt}\%$ (cf. Tab. D1). Scale bars: $250\,\mu\mathrm{m}$. **a–c** Development of a blob. Time increases from top to bottom and from panel a to c. Images are separated by $800\,\mathrm{ms}$. The dashed black line marks the position at which the IEX stuck to the substrate. The red line is a guide to the eye, marking the location of the blob tip, which continues to move leftward at roughly constant velocity, until the IEX is detached again. The solid white line denoted the constant velocity of the IEX after escaping the blob. Note the acceleration stage immediately after detachment. **d** Frequent sticking results in blotted lines.

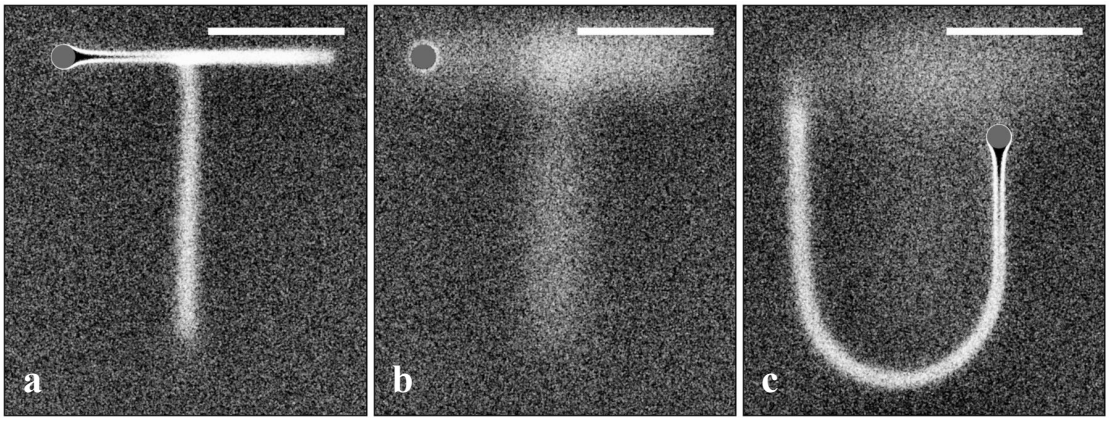

Fig. D13 Erasing and rewriting. Demonstration of erasing written letters by globally heating the system and recycling the ink in a Brownian dynamics simulation at $v_{\mathrm{IEX}} = 12\,\mu\mathrm{m\,s}^{-1}$. Other parameters as given in Tab. 7.1 in Chap. 7. Scale bar: $250\,\mu\mathrm{m}$. **a** Snapshot after the letter T has been written and before heating the system. **b** During heating, the written lines broaden by diffusion and slowly disappear. **c** Rewritten letter U after erasing the previously written letter T.

Academic Career

2021–2024	PhD Scholarship of the German Academic Scholarship Foundation (**Studienstiftung des deutschen Volkes**)
2020–2024	Doctoral research assistant (Wissenschaftlicher Mitarbeiter) at the Institute for Condensed Matter Physics, **Technical University of Darmstadt** (Germany) in the group of Prof. Dr. Benno Liebchen
Dec. 2019	**Master of Science, Physics** Thesis: "Charge and Composition Scaling of Binary Glass-Forming Liquids"
2018	Student teaching assistant for computational physics at **Technical University of Darmstadt** (Germany).
2017–2019	Master student (Physics) at **Technical University of Darmstadt** (Germany)
2017–2018	Student research assistant at **Technical University of Darmstadt** (Germany) in the group of Prof. Dr. Michael Vogel (Institute for Condensed Matter Physics)
Aug. 2017	**Bachelor of Science, Physics** Thesis: "^{1}H and ^{7}Li NMR: Relaxometry and Diffusometry on PPG-Based Polymer Electrolytes"
2014–2017	Bachelor student (Physics) at **Technical University of Darmstadt** (Germany)

Acknowledgements

The time I was working on this thesis was a great but also stressful period filled with numerous challenges and adventures. I learned a lot during this time, and I enjoyed working on this thesis. However, this thesis would not have been possible without the support of great people around me.

First and foremost, I would like to thank my supervisor Prof. Benno Liebchen. I am grateful for your patience, your support, and the freedom to pursue my own ideas. Thank you for listening to my concerns, ideas, and questions, and for giving me the opportunity to create AMEP and to build a great development team.

Second, I am very thankful for the financial and academic support from the German Academic Scholarship Foundation (Studienstiftung des deutschen Volkes), which gave me the opportunity to meet many interesting people from different disciplines.

Third, I gratefully acknowledge the computing time provided to me at the NHR Center NHR4CES at TU Darmstadt (project number p0020259).

Next, I would like to thank all collaborators: Prof. Hartmut Löwen, Prof. Thomas Palberg, Prof. Lorenzo Caprini, Prof. Steffen Hardt, Prof. Ran Niu, Prof. Micheal Vogel, Dr. Nadir Möller, Dr. Henning Bonart, Dr. Florian Gebhard, Dr. Suvendu Mandal, Dr. Tamal Roy, Dr. Robin Horstmann, and Sebastian Kloth. It was a pleasure to work with you. A special thanks goes to Prof. Thomas Palberg for agreeing to be the second referee of my thesis.

I would also like to thank the students who I was able to supervise during their Bachelor's or Master's thesis: Iris, Zino, and Kay-Ro. I enjoyed working with you and you did a great job.

Moreover, I want to thank the whole group of Prof. Benno Liebchen for their support, for many fruitful discussions, and for the great time. Special thanks go to Kay-Ro, my former student and now a fantastic colleague. Thank you for our long and intensive discussions and for your valuable feedback. Special thanks also go to Dennis, Aritra, and Mahdi for intensive discussions and helpful advice. I would also like to thank Mahdi for exploring great restaurants with me. Additionally, I am grateful to all people that supported me in the development of AMEP. Special thanks go to Kay-Ro and Kai. I am grateful for your amazing support in publishing AMEP and in organizing the AMEP project week 2023. Special thanks also go to all participants of the project week and to the co-authors of the corresponding publication: Aritra, Kai, Kay-Ro, Mahdieh, Malte, and Suvendu. Your support helped to improve AMEP.

Furthermore, I would like to thank all people that read preliminary parts of my thesis for proofreading purposes: Aritra, Daniel, Dennis, Kay-Ro, Sebastian, and Teresa.

Last but not least, there are many people which I haven't mentioned so far but which are responsible for the success of this thesis in their own unique ways. These are my friends, my band mates, and, of course, my family. Thank you for your ongoing support.

Erklärungen laut Promotionsordnung

§ 8 Abs. 1 lit. c PromO

Ich versichere hiermit, dass die elektronische Version meiner Dissertation mit der schriftlichen Version übereinstimmt.

§ 8 Abs. 1 lit. d PromO

Ich versichere hiermit, dass zu einem vorherigen Zeitpunkt noch keine Promotion versucht wurde. In diesem Fall sind nähere Angaben über Zeitpunkt, Hochschule, Dissertationsthema und Ergebnis dieses Versuchs mitzuteilen.

§ 9 Abs. 1 PromO

Ich versichere hiermit, dass die vorliegende Dissertation selbstständig und nur unter Verwendung der angegebenen Quellen verfasst wurde.

§ 9 Abs. 2 PromO

Die Arbeit hat bisher noch nicht zu Prüfungszwecken gedient.

Darmstadt, 14.10.2024

L. Hecht